

**Observation of Very High Energy γ -rays from Active Galactic
Nuclei and characterization of their non-thermal emission
mechanisms**

DISSERTATION

zur Erlangung des akademischen Grades

DOCTOR RERUM NATURALIUM

(Dr. rer. nat.) im Fach Physik

Spezialisierung: Experimentalphysik

eingereicht an der

Mathematisch-Naturwissenschaftlichen Fakultät
der Humboldt-Universität zu Berlin

von

M.Sc. Wrijupan Bhattacharyya

Präsidentin der Humboldt-Universität zu Berlin

Prof. Dr.-Ing. Dr. Sabine Kunst

Dekan der Mathematisch-Naturwissenschaftlichen Fakultät

Prof. Dr. Elmar Kulke

Gutachter/innen: 1. Prof. Dr. Elisa Bernardini
2. Prof. Dr. David Berge
3. Prof. Dr. Pratik Majumdar

Tag der mündlichen Prüfung: 24 September 2019

Abstract

Cosmic rays are a stream of charged energetic particles that constantly shower upon the Earth from all directions. Since cosmic rays are electrically charged, they are deflected by the cosmic magnetic fields during their propagation and completely lose directional information before reaching the Earth. Hence identifying their sources of origin is a difficult task. The astrophysical engines producing them are the most powerful particle accelerators in the universe, capable of accelerating particles up to extremely high energies ($> 10^{20}$ eV). The main aim of this thesis is to characterize such extremely powerful sources that are most likely accelerating cosmic rays. Cosmic-ray sources are also believed to produce photons and neutrinos that can travel undeflected towards the Earth and thus act as direct tracers of their sources of origin. The combined information from both these cosmic messengers have been used in this thesis in the context of the recent observations and theoretical models.

The primary astrophysical objects under investigation in this thesis are called blazars, a sub-class of Active Galactic Nuclei having an ultra-relativistic jet oriented towards our line of sight. Blazars exhibit a wide range of interesting physical characteristics throughout the entire electromagnetic spectrum, most notably in the Very High Energy (VHE) γ -ray band. In this thesis VHE γ -ray observations by the Major Atmospheric Gamma-ray Imaging Cherenkov (MAGIC) telescopes were used to study the spectral and temporal properties of blazars. The VHE emission was combined with multi-wavelength photon and neutrino observations to characterize blazar jets, constrain their emission mechanisms and draw implications for cosmic-ray acceleration.

To investigate the mechanisms giving rise to the broadband emission from blazars, a stationary lepto-hadronic code is developed using a simple semi-analytical framework. The high-energy emission from blazar jets can arise due to both leptonic as well as hadronic processes. A simultaneous neutrino observation (via the so-called multi-messenger observation strategy) is required to break this ambiguity and confirm the occurrence of hadronic particle acceleration inside the jets. Hence along with the leptonic interactions, the code also implements the relevant hadronic interaction channels: proton synchrotron radiation, photo-meson interactions, proton-proton interactions and pair cascades. The code allows a self-consistent scan over a wide parameter space required for the interpretation of multi-messenger observations, that is fundamental to identify plausible cosmic-ray accelerators.

The thesis presents the results from the MAGIC and multi-wavelength monitoring campaign of the blazar 1ES 1959+650 during 2016. The blazar has long been anticipated as a potential cosmic-ray source, following its "orphan" flaring behaviour in 2002. In 2016 the source again underwent into an extremely active phase and exhibited three remarkably bright VHE γ -ray flares on 13th June, 14th June and 1st July of 2016. On two of these nights, signs of rapid flux variability within sub-hour timescales was clearly resolved by the MAGIC observations. The observed VHE variability was used to constrain the size of the emission region. In order to investigate the broadband spectra of the source during the remarkable flaring activities, three different theoretical models were adopted: leptonic, hadronic and mixed lepto-hadronic. The flat VHE spectra extending up to several TeV energies during the flares, required high values of Doppler factor to explain the observations using the leptonic model. The observations could be explained using the hadronic model with relatively smaller values of Doppler factor and high magnetic field strength. In order to constrain the level of neutrino emission from the source a mixed lepto-hadronic scenario was also investigated. Both the hadronic and mixed lepto-hadronic models yielded neutrino fluxes during the intense activity period, that falls below the sensitivity of the current generation of neutrino telescopes. This is consistent with the non-detection of significant neutrino excess from the source location by the most recent IceCube analysis.

In 2017, the observation of a high-energy neutrino by IceCube in spatial and temporal coincidence with a flaring blazar named TXS 0506+056 yielded for the first time, hints towards identification of an extragalactic cosmic-ray source. These multi-messenger observations, combined together with a wider electromagnetic data set were

interpreted in this thesis adopting a lepto-hadronic theoretical framework. The modelling of the electromagnetic data and the predicted neutrino flux implies that the source could indeed be a potential neutrino emitter and hence an accelerator of high-energy cosmic rays. The spectral steepening observed in the VHE γ -ray band by MAGIC could be attributed in the modelling to internal γ - γ absorption, in the same target photon field responsible for production of the high-energy neutrino event. Model-derived constraints on the maximum proton energy suggests an upper limit, that could be well compatible with ultra-high-energy cosmic rays.

Zusammenfassung

Die Kosmische Strahlung ist ein Strom geladener, energetischer Teilchen, die kontinuierlich aus allen Richtungen auf die Erde schauern. Da die Teilchen der kosmischen Strahlung elektrisch geladen sind, werden sie während ihrer Propagation durch kosmische Magnetfelder abgelenkt und verlieren vor dem Erreichen der Erde vollständig ihre Richtungsinformation. Die Identifizierung ihrer Herkunft ist daher eine herausfordernde Aufgabe. Die astrophysikalischen Quellen, in welchen sie produziert werden, sind die stärksten Teilchenbeschleuniger des Universums und damit in der Lage, Teilchen bis zu extrem hohen Energien ($> 10^{20}$ eV) zu beschleunigen. Das Hauptziel dieser Arbeit ist die Charakterisierung solcher extrem leistungsfähigen Quellen, die höchstwahrscheinlich kosmische Strahlung beschleunigen. Es wird weiterhin angenommen, dass kosmische Strahlungsquellen Photonen und Neutrinos produzieren, die sich unabgelenkt zur Erde bewegen können und somit direkt zu ihren Ursprungsquellen weisen. Die kombinierten Informationen aus diesen beiden kosmischen Botenteilchen wurde in dieser Arbeit im Rahmen jüngster Beobachtungen sowie theoretischer Modelle zu Nutze gemacht.

Die primären astrophysikalischen Objekte, die in dieser Arbeit untersucht werden, werden Blazare genannt, eine Unterklasse der aktiven galaktischen Kerne, bei welcher ein ultra-relativistischer Jet in unsere Blickrichtung zeigt. Blazare weisen im gesamten elektromagnetischen Spektrum eine Bandbreite interessanter physikalischer Eigenschaften auf, insbesondere im sehr hochenergetischen (very high energy: VHE) Bereich der Gammastrahlung. In dieser Arbeit wurden Beobachtungen von VHE-Strahlung durch die Major Atmospheric Gamma-ray Imaging Cherenkov (MAGIC) Teleskope verwendet, um die spektralen und zeitlichen Eigenschaften von Blazaren zu untersuchen. Die VHE-Emission wurde mit Observationen von sowohl Multiwellenlängen-Photonen als auch Neutrinos kombiniert, um Blazar-Jets zu charakterisieren, ihre Emissionsmechanismen einzuschränken und Rückschlüsse auf die Beschleunigung kosmischer Strahlung zu ziehen. Um die Mechanismen zu untersuchen, die zur Breitbandemission von Blazaren führen, wurde ein zeitunabhängiger lepto-hadronischer Code mit einer einfachen, semi-analytischen Struktur entwickelt.

Die hochenergetische Emission von Blazar-Jets kann sowohl durch leptonische als auch durch hadronische Prozesse entstehen. Eine simultane Neutrino-Beobachtung (über die sogenannte Multi-Messenger-Observationsstrategie) ist erforderlich, um diese Unbestimmtheit zu durchbrechen und das Auftreten der hadronischen Teilchenbeschleunigung innerhalb der Jets zu bestätigen. Daher bietet der Code neben den leptonischen Interaktionen auch die relevanten hadronischen Wechselwirkungskanäle: Protonensynchrotronstrahlung, Photomeson-Interaktionen, Proton-Proton-Interaktionen und Paarkaskaden. Des Weiteren ermöglicht der Code einen Scan über einen großen Parameterraum zur Interpretation von Multi-Messenger-Beobachtungen, was zur Identifikation plausibler kosmischer Strahlungsbeschleuniger grundlegend ist.

Die Arbeit präsentiert die Ergebnisse der MAGIC- und Multiwellenlängen-Observationskampagne des Blazars 1ES 1959+650 aus dem Jahr 2016. Der Blazar gilt seit langem als potentielle kosmische Strahlungsquelle, nachdem ein starker Strahlenausbruch, ein sogenannter Flare, bisher einmalig 2002 gemessen wurde. Im Jahr 2016 durchlief die Quelle erneut eine äußerst aktive Phase und zeigte am 13. Juni, 14. Juni und 1. Juli 2016 drei bemerkenswert helle VHE-Gamma-Flares. In zwei dieser Nächte wurden die Anzeichen einer schnellen Flussvariabilität innerhalb von Sub-Stunden-Zeiträumen mit MAGIC-Beobachtungen eindeutig festgestellt. Die beobachtete VHE-Variabilität wurde verwendet, um die Größe des entsprechenden Emissionsbereichs der Quelle einzugrenzen. Um die Breitbandspektren der Quelle während der bemerkenswerten Flare-Aktivitäten zu untersuchen, wurden drei verschiedene theoretische Modelle angewendet: leptonisch, hadronisch und kombiniert lepto-hadronisch. Um die flachen VHE-Spektren, die sich während der Flares bis zu Energien von mehreren TeV ausbreiten, mit dem leptonischen Modell zu erklären, wurden jedoch hohe Werte für den Dopplerfaktor benötigt. Mit dem hadronischen Modell hingegen konnten die Beobachtungen mit relativ kleinen Dopplerfaktorwerten und

hoher Magnetfeldstärke erklärt werden. Um die Neutrinoemission aus der Quelle zu begrenzen, wurde auch ein kombiniertes Szenario, ein lepto-hadronisches Modell, untersucht. Sowohl die hadronischen als auch die lepto-hadronischen Modelle sagten während der intensiven Aktivitätsphase Neutrinoflüsse vorher, die unter die Sensitivität der aktuellen Generation von Neutrinoobservatorien fällt. Dies ist vereinbar mit dem Nichtnachweis eines signifikanten Neutrinoüberschusses aus Richtung der Quellposition durch die neueste IceCube-Analyse.

Im Jahr 2017 ergab die Beobachtung eines hochenergetischen Neutrinos durch IceCube in räumlicher und zeitlicher Übereinstimmung mit dem Flare eines Blazars namens TXS 0506+056 erstmals Hinweise auf die Identifizierung einer extragalaktischen, kosmischen Strahlungsquelle. Diese Multi-Messenger-Beobachtungen, kombiniert mit einem breiten elektromagnetischen Datensatz, wurden in dieser Arbeit in einem lepto-hadronischen theoretischen Rahmen interpretiert. Die Modellierung der elektromagnetischen Daten und des vorhergesagten Neutrinoflusses impliziert, dass die Quelle in der Tat eine potenzielle Neutrinoquelle und damit ein Beschleuniger der hochenergetischen kosmischen Strahlung sein könnte. Das im VHE-Gammabereich steil abfallende Spektrum, wie von MAGIC beobachtet, konnte in der Modellierung auf die interne Annihilation von Gammaphotonen zurückgeführt werden, die im gleichen Ziel-Photonenfeld stattfindet, das für die Produktion des hochenergetischen Neutrinoereignisses verantwortlich ist. Modellbasierte Einschränkungen der maximalen Protonenenergie deuten auf eine Obergrenze hin, welche mit der Messung ultrahochenergetischer kosmischer Strahlen vereinbar ist.



Acknowledgements

First of all I would like to thank Prof. Dr. Elisa Bernardini, the supervisor of this thesis for her support of the research work, motivation and constant encouragement. The faith she kept in me helped me to stay focused and motivated me to delve into challenging research topics, that ultimately yielded fruitful results.

I express my heartfelt gratitude to Dr. Konstancja Satalecka for all her advices, scientific discussions and for always being there. Academic interactions with her helped me a lot to improve my understanding in various topics of Astroparticle Physics. A special thanks to her for a detailed proof-reading of this thesis. I also sincerely thank my current and past group members Giovanna Pedaletti, Cosimo Nigro and Dariusz Gora for making me feel comfortable and helping me in various academic and personal aspects.

I am extremely grateful to Dr. Fabrizio Tavecchio, Dr. Matteo Cerruti and Dr. Susumu Inoue for their inputs and discussions that helped me a lot to implement models for blazar non-thermal emission. A special thanks to Fabrizio for always being available for help whenever needed and providing comments for my research works and thesis.

Many thanks to all the members of the MAGIC Collaboration for giving me an opportunity to learn in a very supportive environment. Being a member of the MAGIC Collaboration has been the best three years of my academic life.

I am thankful to all my colleagues and friends in Zeuthen for helping me to survive through various difficult phases during my PhD life. Without your presence, my life in Berlin would not have been as interesting and colourful.

Thumbs up to my father, mother and elder sister for always believing in me. Even though you are far away, I can always feel your support and love.

No words would be sufficient to thank Debarati, who beared with me with immense patience through all the hard times and always motivated me to get-going in life. The mental support and comfort that I received from her, was my key source of inspiration throughout my academic career and life. Thank you!

Contents

Abstract	1
Zusammenfassung	3
Acknowledgements	7
1 Introduction	11
2 Distant cosmic messengers: cosmic rays, γ rays, and neutrinos	13
2.1 Cosmic rays	13
2.1.1 Cosmic-ray spectrum	14
2.1.2 Chemical composition of cosmic rays	16
2.1.3 Production mechanisms of cosmic rays	16
2.1.4 Sources of cosmic rays	18
2.2 Photons from outer space	20
2.2.1 Production mechanisms of γ rays	20
2.2.2 Main detection techniques of γ rays	23
2.2.3 Sources of γ rays	25
2.3 Astrophysical neutrinos	26
2.3.1 High-energy neutrino detectors	26
2.3.2 Sources of background	28
2.3.3 Sources of astrophysical neutrinos	28
2.4 Multi-messenger astronomy	30
3 Imaging Atmospheric Cherenkov telescopes	33
3.1 Cherenkov light production	33
3.2 Extensive Air Showers and its types	35
3.3 Imaging Air Cherenkov Technique	37
3.4 The MAGIC telescopes	38
3.4.1 Brief description of hardware, trigger and readout system	38
3.4.2 Data-taking procedure	41
3.4.3 Data analysis chain	41
3.4.4 High level analysis	47
3.4.5 Moon-adapted analysis	52
3.4.6 Systematic uncertainties	54
3.5 Cherenkov Telescope Array	55
3.5.1 Types of IACTs in the CTA array	56
3.5.2 The CTA Key Science Projects	57

4	Active galactic nuclei and blazars	58
4.1	Active galactic nuclei	58
4.1.1	Morphology of AGNs	58
4.1.2	The different kinds of AGNs	61
4.1.3	The unification model	62
4.2	Blazars	64
4.2.1	Classification of blazars	64
4.2.2	Emission models	65
4.2.3	The cosmic gamma-ray horizon	68
4.2.4	The blazar sequence	69
5	Broadband characterization of the blazar 1ES 1959+650	74
5.1	The blazar 1ES 1959+650	74
5.1.1	The discovery and basic properties	74
5.1.2	The observational history	76
5.2	Observation and data analysis for 2016	79
5.2.1	MAGIC observations and data analysis	79
5.2.2	Multi-wavelength observations	84
5.3	Long-term analysis results	86
5.3.1	The MAGIC light curve	86
5.3.2	The multi-wavelength light curve	88
5.3.3	Spectral index vs flux correlation in VHE γ -ray and X-rays	90
5.4	The remarkably bright VHE flares	90
5.4.1	The spectra during the highest flux nights	90
5.4.2	Intra-night variability	96
5.4.3	Size of the emission region	100
5.4.4	Broadband emission modeling	100
5.5	Summary	108
6	Development of a new stationary lepto-hadronic SED modelling tool	110
6.1	Leptonic emission processes	110
6.1.1	Introduction of an emission volume	111
6.1.2	Relativistic beaming effect	111
6.1.3	Implementation of Synchrotron-Self Absorption	113
6.1.4	Implementation of γ - γ pair production	115
6.2	Hadronic emission processes	116
6.2.1	Implementation of the proton-synchrotron radiation	118
6.2.2	Implementation of the photo-meson interactions	118
6.2.3	Implementation of proton-proton interactions	122
6.2.4	Implementation of photo-meson pair cascades	124
6.3	Test applications	125
6.3.1	PKS 2155-304	125
6.4	Summary	126
7	Multi-messenger association of a high-energy neutrino event with a flaring blazar TXS 0506+056	130
7.1	The neutrino and electromagnetic observations	130
7.1.1	The IceCube detection of the astrophysical neutrino event IC 170922A	131
7.1.2	The γ -ray and multi-wavelength observations	132
7.2	Multi-messenger interpretation	133
7.2.1	The spine-layer framework	133
7.2.2	Model description	135
7.3	Results	136
7.3.1	Radiative components and their contribution to the overall SED	136
7.3.2	The neutrino event rates and neutrino energy	138

7.3.3	Constraints on the maximum proton energy	138
8	Summary and conclusions	141
A	γ-ray and multi-wavelength tables for 1ES 1959+650 2016 monitoring campaign	144
A.1	Multi-wavelength long-term light curves during 2016	144
A.2	Spectra in the optical, X-ray, HE and VHE γ -ray bands during the brightest flaring nights from 2016	152
B	Supplementary materials for the lepto-hadronic code development	155
B.1	The Naima package	155
B.2	Energy spectra of leptons from photo-meson interactions	155
B.2.1	Energy spectra for positrons, muon anti-neutrinos and electron neutrinos	156
B.2.2	Energy spectra of muon neutrinos	156
B.2.3	Energy spectra for electrons and electron anti-neutrinos	156
C	Parametrization of Cherenkov shower images	157
C.1	Image parametrization:	157
	Bibliography	160
	List of Figures	175
	List of Tables	181

Chapter 1

Introduction

Astroparticle Physics is a branch of science that bridges the gap between Astrophysics and Particle Physics, investigating the highest energy phenomenon occurring in our universe. One of the biggest open questions in the field of Astroparticle Physics is the mystery behind the origin of high-energy cosmic rays. At Earth we can detect such high energy particles but their origin still remains a mystery. Since cosmic rays are electrically charged, they are deflected by the intergalactic magnetic field during their propagation towards the Earth and hence their arrival direction appears random. Hence to pin-point cosmic-ray sources, other astrophysical messengers such as photons and neutrinos are required, that are by-products of cosmic-ray interactions with the nearby gas or radiation fields. Such secondary by-products are electrically neutral and can reach the Earth undeviated, thus acting as direct tracers of the progenitor sources.

The extreme astrophysical powerhouse located at the center of active galaxies are considered as one of the prime candidates for cosmic-ray acceleration. The central engine of such active galaxies are powered by super-massive black holes that accretes matter onto its core and produces extremely powerful non-thermal radiation, that can outshine the emission from the host galaxy. Some of these Active Galactic Nuclei eject powerful outflows composed of plasma, known as jets. Blazars are a sub-class of Active Galactic Nuclei, having their ultra-relativistic jets closely aligned to the line of site of an observer on Earth. Although numerous observational evidences suggest acceleration of highest energy particles inside these extremely powerful sources, the exact acceleration and emission processes at play are still one of the hottest questions in Astroparticle Physics.

Active galactic nuclei and blazars are known to emit photons spanning the entire electromagnetic spectrum, ranging from radio up to γ ray energies. Due to the favourable geometry of the jet, the intrinsic emission from blazars appear highly boosted in the frame of the observer due to relativistic beaming effects. The non-thermal spectral energy distribution of blazars typically consists of two humps. The first lower energy hump is usually attributed to synchrotron radiation of accelerated electrons inside the jet. The origin of the second hump is debatable and can be attributed to both leptonic and hadronic emission processes. The key ingredient to fully characterize the second hump in the spectral energy distribution, are very-high-energy γ -ray observations. Very-high-energy γ rays are by-products of highest energy particle acceleration in the jets of Active Galactic Nuclei. Such observations are possible through ground-based Cherenkov photon detectors installed on Earth, that offers excellent sensitivity, energy and angular resolution to observe very-high-energy γ -ray sources. At such energies, these objects appear highly variable and the size of the emission region can be constrained from the characteristic flux variability time scale. Micro-scale variability as fast as a few minutes have recently been detected by the ground-based detectors observing in the very-high-energy regime (Aharonian et al. (2007), Albert et al. (2007b)).

Recently, on September 2017 a high-energy neutrino event was detected in coincidence with a blazar named TXS 0506+056 that was also observed to be in an active electromagnetic emission state across various wavebands, especially in γ rays (IceCube Collaboration et al., 2018b). These observations for the first time indicated that active galaxies especially blazars, due to the relativistic boosting effect of the intrinsic emission component, can produce detectable high-energy neutrino emission within the sensitivity of the current generation of instruments.

A powerful probe to identify and unveil the properties of high-energy cosmic-ray accelerators is multi-messenger astronomy: coordinated joint observations of high energy neutrinos and photons. While extremely energetic photons can originate from both leptonic and hadronic processes inside the jets of Active Galactic Nuclei, neutrinos which can be only produced in hadronic interactions, provide an unambiguous signature of cosmic-ray

acceleration within the source. Thus simultaneous multi-messenger neutrino and photon observations are the key to identify potential cosmic-ray sources and probe their underlying physical characteristics.

The ultimate aim of this thesis is to characterize the non-thermal emission mechanisms in the jets of Active Galactic Nuclei/blazars and investigate physical conditions under which cosmic rays and neutrinos can be produced in such extreme environments. This is achieved using multi-wavelength photon observations (from radio up to very-high-energy γ rays) together with high-energy neutrino observations. The recent observations are then interpreted within the framework of the current theoretical models. Two sources are investigated in detail in this context, namely the blazars 1ES 1959+650 and TXS 0506+056.

Overview of the contents

The thesis is divided into the following parts. Chapter 2 gives a brief overview of the three primary messengers in Astroparticle Physics, namely cosmic rays, photons and neutrinos. Chapter 3 introduces the main detection techniques of very-high-energy γ rays by ground-based experiments on Earth, with a special emphasis on the Major Atmospheric Gamma-ray Imaging Cherenkov (MAGIC) telescopes. In Chapter 4, the concept of Active Galactic Nuclei and blazars is discussed along with their properties, classification and the current unification model. Chapter 5 discusses about the very-high-energy and multi-wavelength observations of the blazar 1ES 1959+650. 1ES 1959+650 is a very powerful nearby object and a possible site of high-energy cosmic-ray acceleration. Special emphasis is given to the characterization of the rapid, bright γ -ray flares observed from this source by MAGIC during 2016. In Chapter 6, the development of a new lepto-hadronic code is discussed. The code aims to model the broadband non-thermal emission spectra from Active Galactic Nuclei and investigate the conditions for neutrino and cosmic-ray production. In Chapter 7, the first potential multi-messenger association of a high-energy neutrino event with a flaring blazar named TXS 0506+056 is described in terms of a stationary lepto-hadronic model. Consistent interpretation of the electromagnetic and neutrino observations from this object provides, for the first time, potential evidence towards identification of the first extragalactic cosmic-ray source. Finally, Chapter 8 closes this thesis with summary and conclusions.

Chapter 2

Distant cosmic messengers: cosmic rays, γ rays, and neutrinos

The field of non-thermal Astroparticle Physics was established by Viktor Hess in 1912 and it deals with the highest energy phenomenon occurring in the universe. In 1912 Hess discovered the presence of charged particles that comes from outside the Earth's atmosphere (Hess, 1912), which were later termed as "cosmic rays" due to their extraterrestrial origin. Cosmic rays are believed to be produced by non-thermal processes in astrophysical sources that can accelerate particles to extremely high energies up to 10^{21} eV. These particles then propagate through the universe interacting both inside and outside the source of origin, with the intervening molecular clouds, intergalactic magnetic fields and cosmological radiation fields such as the cosmic microwave background (CMB). Ultimately the cosmic rays and the secondary particles produced in cosmic-ray interactions are detected by satellite-borne instruments or detectors placed at Earth. The most important goal of non-thermal Astroparticle Physics is to identify the sources of high-energy cosmic rays and investigate the production mechanisms and physical characteristics of the progenitor sources, through the detection of the cosmic messengers from such distant objects.

There are mainly four types of messengers originating from distant astrophysical sources:

- cosmic rays
- photons (γ)
- neutrinos (ν)
- gravitational waves

This chapter gives a brief description of the different messengers in Astroparticle Physics that are used to explore the distant corners of the universe. The thesis demonstrates the importance of multi-messenger astronomy, i.e. synergistic observations of the different astrophysical messengers that can play a crucial role to probe new Physics and understand the properties of the extreme particle accelerators of the universe. Along with cosmic rays, photons and neutrinos, another messenger called gravitational wave (GW) events can also be used to gain complete knowledge of especially various transient phenomenon in the sky, such as merger of neutron stars and/or black holes, gamma-ray bursts, core collapse supernovae. However GWs are out of scope of this thesis and hence not discussed in details here.

An important part of this thesis deals with the study of very-high-energy (VHE; $E > 100$ GeV) γ -ray emission from Active Galactic Nuclei and characterization of their broadband emission spectra, especially in connection to the search for cosmic-ray and neutrino sources.

2.1 Cosmic rays

The term cosmic ray was first coined by Robert Millikan in 1926 (Millikan and Cameron, 1926) following the discovery by Viktor Hess in 1912, presuming them to be a new type of energetic radiation. However, the cosmic rays are now believed to be composed of known type of particle - protons and helium nuclei compose the bulk of

the cosmic rays (97-98%). A tiny fraction is composed of heavier elements, electrons, positrons, neutrinos and also γ rays.

In 1938, Pierre Auger discovered that the energetic cosmic rays can initiate extended air showers (EAS) by interacting with the Earth's atmosphere. An EAS generates a cascade of secondary particles that can reach the ground. Hence cosmic rays can be indirectly detected by air shower experiments installed on Earth through the millions of charged particles generated in an EAS, or directly through balloon and satellite experiments. One of the biggest open questions in the field of Astroparticle Physics is to identify the sources of the ultra-high-energy-cosmic rays (UHECRs; $E > 3 \times 10^{18}$ eV). Extraterrestrial particles of energies exceeding 10^{18} eV are detected at Earth, but their arrival directions from the sky appear randomly distributed. Particle acceleration to such ultra high energies are beyond the reach of the energies attainable by solar particles or artificial particle accelerators. Hence to understand the particle acceleration mechanisms for UHECR production is one of the important goals in Astroparticle Physics.

The largest cosmic-ray detector operating in the 1990s were the 100 km² ground-based array known as Akeno Giant Air Shower Array (AGASA) (Chiba et al., 1992) and the High Resolution Fly's Eye (HiRes) (Boyer et al., 2002) until 2006. The Pierre Auger Observatory built in 2008, is the largest cosmic-ray observatory at present covering an area of 3000 km² (Abraham et al., 2004), located in Argentina. The largest observatory in the northern hemisphere is the Telescope Array (TA) (Nonaka et al., 2009) experiment (area of 762 km²), situated in Utah.

2.1.1 Cosmic-ray spectrum

Since cosmic rays are charged particles, they are deflected by the intergalactic magnetic fields leading to a complete loss of their directional information. From their spectral shape, indirect conclusions can be drawn about its source population. The all-particle spectrum of cosmic rays as seen from the Earth is shown in Fig. 2.1. The spectrum below 1 GeV is mainly composed of particles from within our solar system, since the solar magnetic field blocks lesser energetic particles coming from outside.

The spectral shape of the particle flux of cosmic rays ($\frac{dN}{dE}$) can be described by a series of power law functions (Wiebel-Sooth et al. (1998), Voigt et al. (1999)):

$$\frac{dN}{dE} = \begin{cases} E^{-2.67} & 100 \text{ GeV} < E < 3 \text{ PeV} \\ E^{-3.10} & 3 \text{ PeV} < E < 3 \text{ EeV} \\ E^{-2.75} & E > 3 \text{ EeV} \end{cases}$$

The transition near 1 PeV is known as the "knee". The cosmic rays below the knee are believed to be of Galactic origin while the transition from the Galactic to the extragalactic component is expected to be somewhere between 1 PeV and 1 EeV. The progress of the study on this transition depends on the search for the highest energy Galactic particle accelerators as well as the search for extragalactic sources capable of producing UHECRs. The second spectral break near 1 EeV is termed as the "ankle". The cosmic ray spectrum beyond a few tens of EeV undergo a severe cutoff due to the interaction with the CMB photons, that will be discussed below.

Cosmic-ray interaction with the CMB

The interaction of the cosmic rays far beyond the knee with the CMB radiation limits the highest energies up to which the cosmic rays can be observed. If a cosmic ray of energy $> 5 \times 10^{19}$ eV interacts with the CMB, it undergoes photo-hadronic interactions to produce unstable delta resonances that further decay into less energetic particles:



The absorption of cosmic rays above 5×10^{19} eV by the CMB photons leads to the sharp cutoff in their energy spectrum known as the GZK-cutoff after the name of its discoverers (Greisen (1966), Zatsepin and Kuz'min (1966)). Later, hints of confirmation of their prediction was given by the HiRes experiment (Abbasi et al., 2005). However the presence of the GZK-cutoff was under debate due to the measurement of the so-called "trans-Greisen events" measured above the GZK limit by the AGASA experiment (Yoshida et al., 1995). In 2007-2008, new measurements by HiRes experiment detected the presence of a cutoff in the spectrum at an approximate energy of 60 EeV,

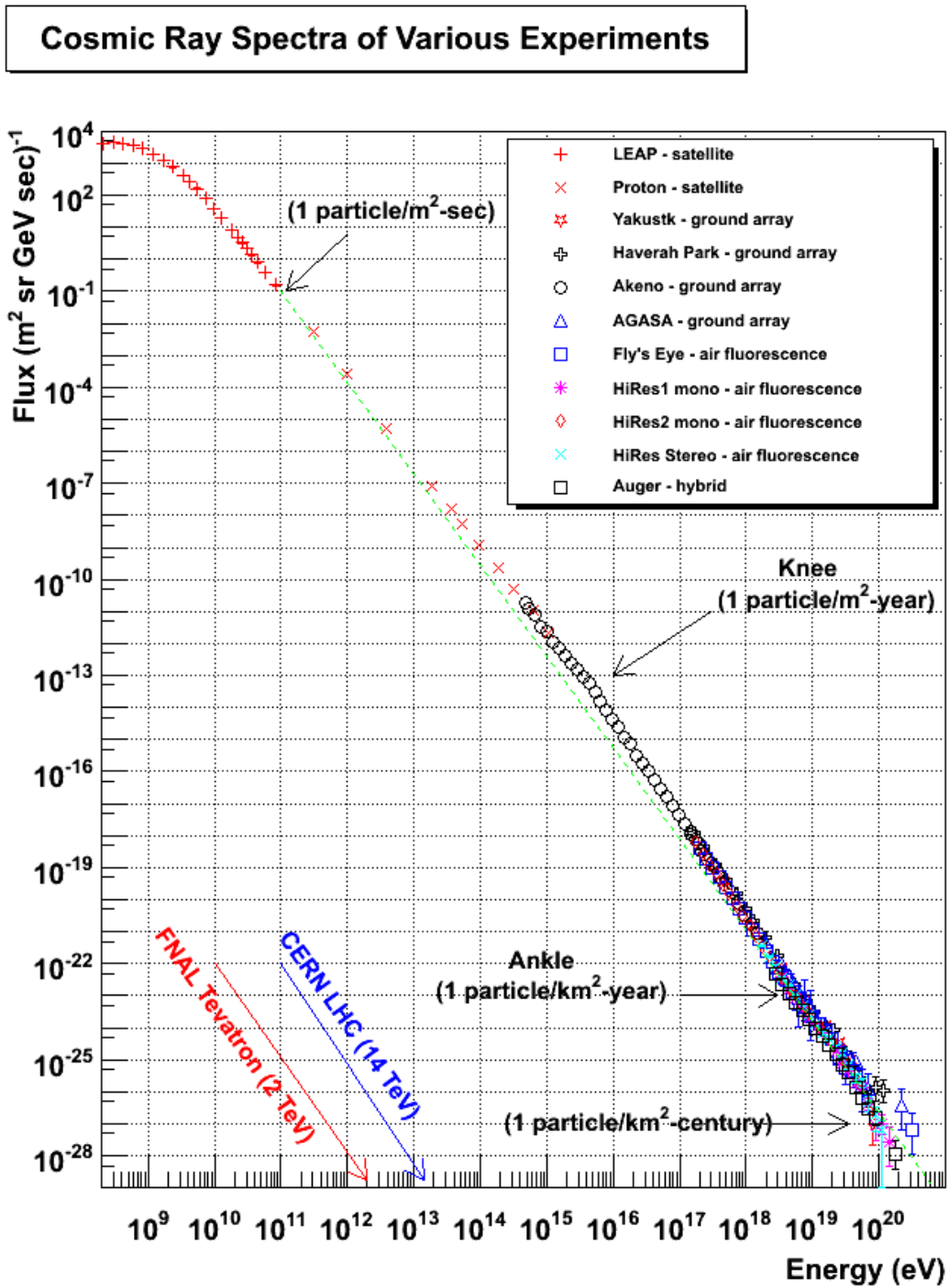


Figure 2.1: Spectrum of cosmic rays as observed from the Earth (Hanlon, 2010)

with a statistical significance greater than 5σ (Abbasi et al., 2008). The results reported by the HiRes Collaboration soon gained support from the new measurements by the Pierre Auger Observatory (Yamamoto, 2008). Later, the measurements by the Telescope Array (TA) collaboration showed the presence of a steepening in the UHECR spectrum at ~ 54 EeV (Abu-Zayyad et al. (2013); see also Verzi et al. (2017), Ivanov (2015), Unger et al. (2018)) corroborating the presence of the cutoff, consistent with the expectations by Greisen, Zatsepin and Kuz'min.

2.1.2 Chemical composition of cosmic rays

A small fraction of cosmic rays is composed of uncharged particles such as γ rays and neutrinos while the major composition consists of charged particles. Above ~ 1 GeV, it is mainly composed of protons (85%) and helium nuclei (12%) and small fraction of electron-positron pairs (2%) and heavier nuclei (1%).

Below 1 PeV, the chemical composition of cosmic rays can be directly measured. Above these energies, the chemical composition measurement relies upon indirect detection by ground-based detectors such as the HiRes, Pierre Auger, TA observatories and it is debatable whether the main constituents are protons or heavier nuclei (Pierre Auger Collaboration et al. (2011), Abbasi et al. (2010)). Fig. 2.2 shows the UHECR spectrum overlaid with different cosmic-ray models of Galactic to extragalactic transition and different injected chemical composition. The mixed composition and iron-dominated models (Allard et al., 2007) predict that the ankle represents the Galactic to extragalactic transition. The proton-dominated models (known as dip models; Berezhinsky et al. (2006)) indicate that the ankle is due to pair production propagation losses.

The cosmic-ray mass fractions reported from the most recent measurements (Unger et al., 2018) by the Pierre Auger Collaboration is shown in Fig. 2.3. The composition is dominated by protons below the ankle, while the contribution from He and N increases with energy. A small proton contribution can also exist at ultra high energies, as can be seen from the figure. An Fe contribution arises at energies $E > 10^{19}$ eV. A hint of Fe contribution at lower energies ($E > \sim 10^{17}$ eV) was also found, which falls sharply with increasing energy. The proton fraction between $E \sim 2 \times 10^{17} - 5 \times 10^{17}$ eV was found to be roughly constant. The reported mass compositions by the Pierre Auger Collaboration are in agreement with the results from the KASCADE-GRANE Collaboration (Apel et al. (2011), Apel et al. (2013)).

2.1.3 Production mechanisms of cosmic rays

The spectrum of the cosmic rays consist of only a few features and hence it is believed that the bulk of them share the same acceleration mechanism. The most commonly believed mechanism was proposed by Fermi (Fermi, 1949) which states that the cosmic rays are accelerated by repeatedly crossing shock fronts. This is also commonly referred to as "shock" acceleration. Depending on the characteristics of the shock, we can distinguish between the first-order and second-order Fermi acceleration.

First-order Fermi acceleration occurs when a cosmic ray travelling through a shock wave encounters magnetic field inhomogeneities. The particle bounces back and forth through the shock and gains energy. The energy gained by the particle ($\Delta E/E$) after each crossing of the shock is of the order of $\Delta E/E \propto \beta$, where β represents the average velocity of the shock in units of the velocity of light c .

Second-order Fermi acceleration occurs when the cosmic ray interacts with a moving magnetized cloud. In this case, the energy gained by the cosmic ray at each interaction with the magnetized clouds is proportional to the square of the shock velocity, i.e. $\Delta E/E \propto \beta^2$.

The presence of shock waves are quite common in the universe. The shocks from SNRs are believed to accelerate the Galactic cosmic rays via the first-order Fermi mechanism. The commonly believed shock regions capable of accelerating UHECRs are the GRB shocks, jets of active galactic nuclei (AGNs; see Chapter 4) containing knots and hotspots, etc. The energy spectrum of the accelerated charged particles produced by Fermi first-order acceleration, are predicted to have a simple power law form (Gaisser, 1991).

If cosmic rays are accelerated via the Fermi mechanism, the particle's gyroradius cannot exceed the physical dimensions of the acceleration region, otherwise the particle cannot be confined within the region. For a particle with charge Z , accelerated inside a region of radius R (cm) and containing a tangled magnetic field of strength B (G), the maximum reachable energy to respect the above condition (the so-called Hillas criterion) is given by the following equation:

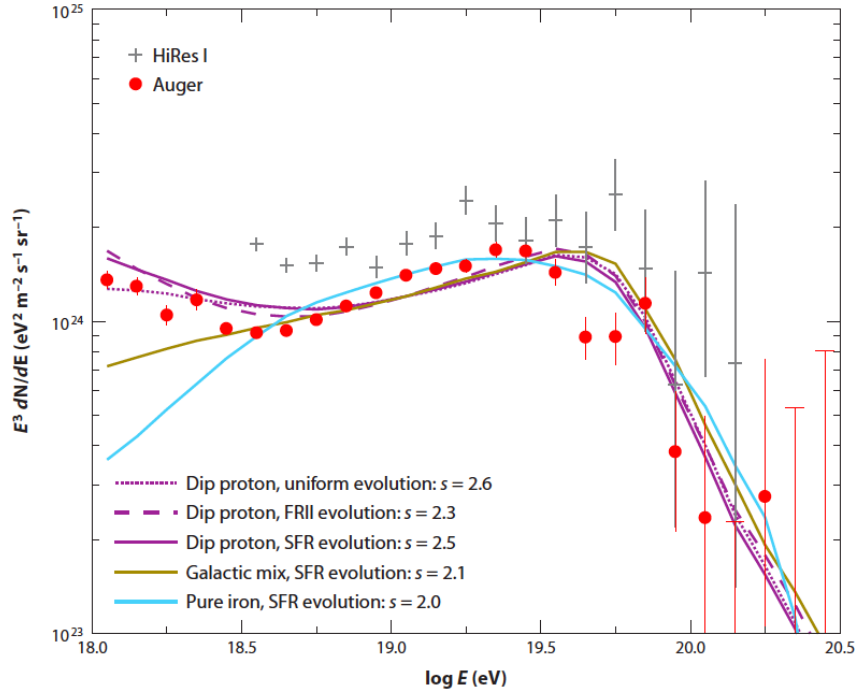


Figure 2.2: Spectrum of UHECRs measured by HiRes and Pierre Auger experiments overlaid with different cosmic-ray models of Galactic to extragalactic transition and different injected chemical composition. Image taken from [Kotera et al. \(2010\)](#) and the references therein.

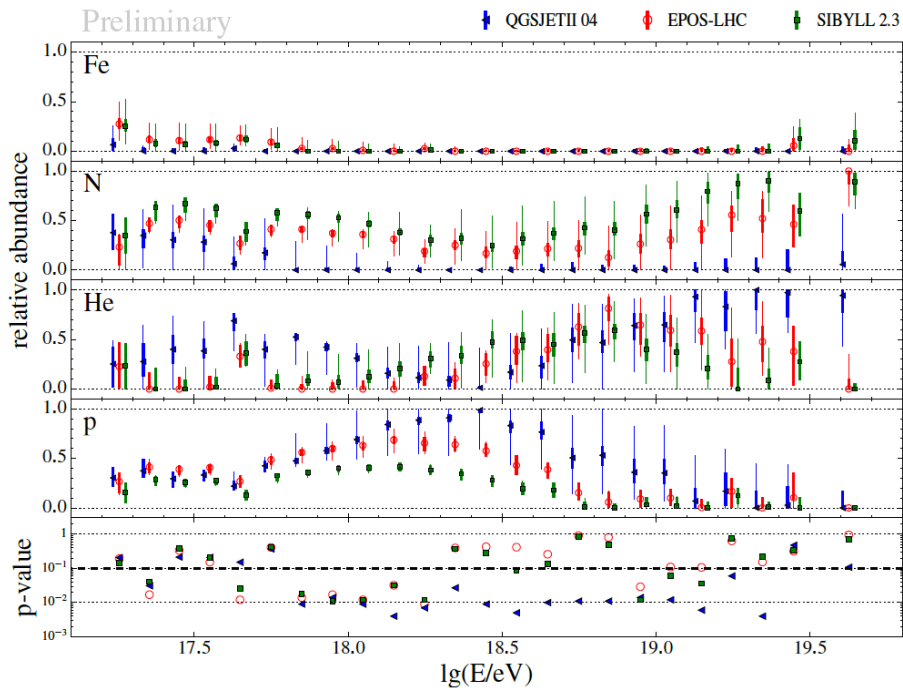


Figure 2.3: The mass fractions of cosmic rays obtained by fitting the distribution of atmospheric depth (height at which the number of particles in the cosmic-ray induced air shower reaches its maximum) obtained from simulations of proton (p), helium (He), nitrogen (N) and iron (Fe)-induced air showers to the data (goodness of fit is shown in the lowest panel). Image taken from [Unger et al. \(2018\)](#).

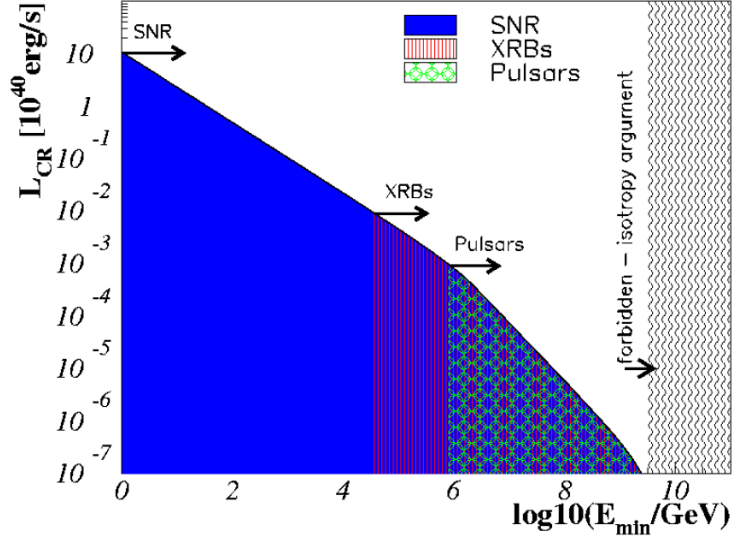


Figure 2.4: The contribution of various galactic sources to the cosmic-ray luminosity from the Milky Way. The solid black curve provides the cosmic-ray luminosity above the minimum energy, $E > E_{min}$. The blue shaded region shows the contribution from SNRs, the red hatched region (lines) shows the contribution from X-ray binaries and the green hatched region (open circles) show the contribution from pulsars. Figure taken from [Becker \(2008\)](#).

$$B(\text{G}) = \frac{30}{Z} \frac{E_{max}}{10^{19} \text{ eV}} \frac{10^{15}}{R \text{ cm}} \quad (2.2)$$

2.1.4 Sources of cosmic rays

Galactic sources:

The possible Galactic sources of cosmic rays include supernova remnants (SNRs), Pulsar Wind Nebulae (PWNs), X-ray binaries and young stars. [Becker \(2008\)](#) have used the electromagnetic luminosity of non-thermal Galactic sources to estimate their contribution to the cosmic-ray spectrum. Fig. 2.4 shows the contribution of SNRs, X-ray binaries and pulsars to the total cosmic-ray luminosity from the galaxy. The SNRs can be the most dominant contributors to the cosmic-ray flux at the lowest energies up to 30 TeV. The X-ray binaries and pulsars can give contribution to the cosmic-ray flux below and above the knee.

Extragalactic sources:

The cosmic rays above the knee and ankle are predominantly believed to be of extragalactic origin, since the experimental data do not show any significant anisotropy in their arrival direction towards the Galactic plane. Moreover to confine the gyro-radius of the UHECRs within the Galaxy, extremely low magnetic field of the order of tens of μG are required, that is in tension with the current predictions (see for example, [Crocker et al. \(2010\)](#) which predicts a lower limit on the magnetic field near the Galactic center of the order of 50-100 μG). These measurements also suggest a predominantly extragalactic origin of the highest energy cosmic rays.

The so-called *Hillas plot* shown in Fig. 2.5 displays the magnetic field of the source as a function of its dimensions for different possible sources of cosmic rays. As can be seen from the figure, the extragalactic sources of cosmic-ray acceleration can be neutron stars, gamma-ray bursts (GRBs) and different regions of active galaxies. AGNs are considered to be one of the most promising sources of UHECRs ([Dermer and Razzaque \(2010\)](#), [Biermann et al. \(2009\)](#)). Jetted AGNs or blazars, which are the main topics in this thesis can contain strong magnetic fields ($\sim 10^2 - 10^3 \text{ G}$) that can accelerate protons close to 10^{20} eV .

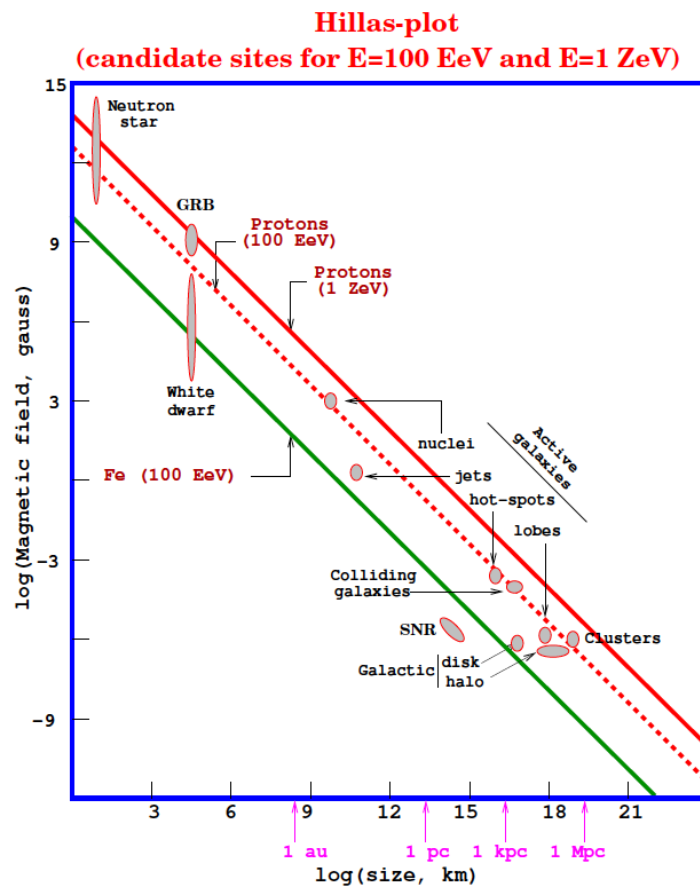


Figure 2.5: Magnetic field strength as a function of the typical size of various potential cosmic-ray sources. The lines indicate the upper bound to the energy up to which cosmic rays (protons or heavier nuclei such as iron (Fe)) can be accelerated while still remaining confined within the source (Hillas, 1984).

The Pierre Auger observatory reported a correlation of 69% between the arrival direction of extremely energetic ($E > 10^{19}$ eV) cosmic rays with the position of nearby AGNs and rejected the hypothesis of isotropic distribution of these cosmic rays at 99% confidence level (Pierre Auger Collaboration et al. (2007), Pierre Auger Collaboration et al. (2008)). In contrast, the measurements with the HiRes observatory could not find any significant correlation of cosmic-ray arrival direction with AGNs and their most significant correlation had a chance probability of 24% (High Resolution Fly'S Eye Collaboration et al., 2008). Later the Pierre Auger collaboration reported a more precise measurement with a larger data sample where the correlation factor with nearby AGNs were reduced to 38%, compared to the expectation of 21% for isotropic distribution of cosmic rays (Abreu et al., 2010). The most recent measurements by the Pierre Auger Collaboration detected an anisotropy in the arrival direction of cosmic rays (having energies above 8×10^{18} eV) at a level of 5.2σ (Aab et al., 2017). The direction of the anisotropy indicates an extragalactic origin of the UHECRs. Hence AGNs which are the most numerous extragalactic objects in the universe, still remain one of the most exciting sources for accelerating the highest energy cosmic rays.

UHECR acceleration in AGNs should leave an observable imprint in their γ -ray spectrum through various emission mechanisms (proton synchrotron, photo-meson pair cascades, muon synchrotron etc). With future generation of γ -ray telescopes such as the Cherenkov Telescope Array, that will be sensitive up to 100 TeV energies, it will be possible to break the degeneracy between the hadronic and leptonic emission mechanisms and shed more light on UHECR acceleration.

2.2 Photons from outer space

Photons are the most abundantly available tracers of distant astrophysical sources. Unlike cosmic rays that are charged and undergo deviations in the intergalactic magnetic fields, photons can travel undeviated towards the Earth and can precisely pin-point back to the source of origin. Astrophysical photons cover a wide range of energies spanning the entire electromagnetic spectrum and can be produced by both thermal and non-thermal emission processes. In case of thermal emission, the process can be described by the Planckian formula for black body radiation connecting the photon fluxes to the surface temperature of the emitting object. The non-thermal processes can give rise to a broadband energy spectrum of photons from the radio band up to several TeV of γ rays. Due to the wavelength-dependence of the penetration depth of photons in the Earth's atmosphere, only the radio to optical photons can be directly detected using detectors built on Earth. The direct detection of higher energy photons in the X-ray and γ -ray regime is only possible by satellite-borne instruments as shown in the schematic representation of Fig. 2.6. Although not shown in Fig. 2.6, VHE γ -ray photons can be detected by experiments installed on the ground by various indirect measurement techniques, as will be described shortly in this section.

Since the main focus of this thesis will be on the observation of γ rays, the next subsections will give a more detailed introduction to γ rays.

γ -ray astronomy is the study of the most energetic photons in the electromagnetic spectrum that are produced in various non-thermal processes in astrophysical environments. γ -ray astrophysics can be sub-divided into several sub-categories based on the energy range of interest: low-energy (1 MeV - 30 MeV), high-energy (30 MeV - 100 GeV), very-high-energy (100 GeV - 100 TeV). The main focus of this thesis will be investigation of the very-high-energy γ -ray domain.

2.2.1 Production mechanisms of γ rays

γ rays can be produced by various emission mechanisms which can be both hadronic and leptonic in nature. The main non-thermal emission mechanisms are briefly discussed below. For more details please see the following references: Longair (1992), Dermer and Menon (2009), Aharonian (2000).

Leptonic non-thermal emission mechanisms

- **Inverse Compton scattering**

This is the major leptonic interaction channel by which γ rays are produced in a large number of astrophysical sources. In this process, the ultra-relativistic leptons up-scatter low-energy target photons up to γ -ray energies. The sources of low-energy target photons can be both intrinsic (e.g.: synchrotron photons emitted by the same lepton population) or external to the γ -ray source. Based on the energy of the primary electron

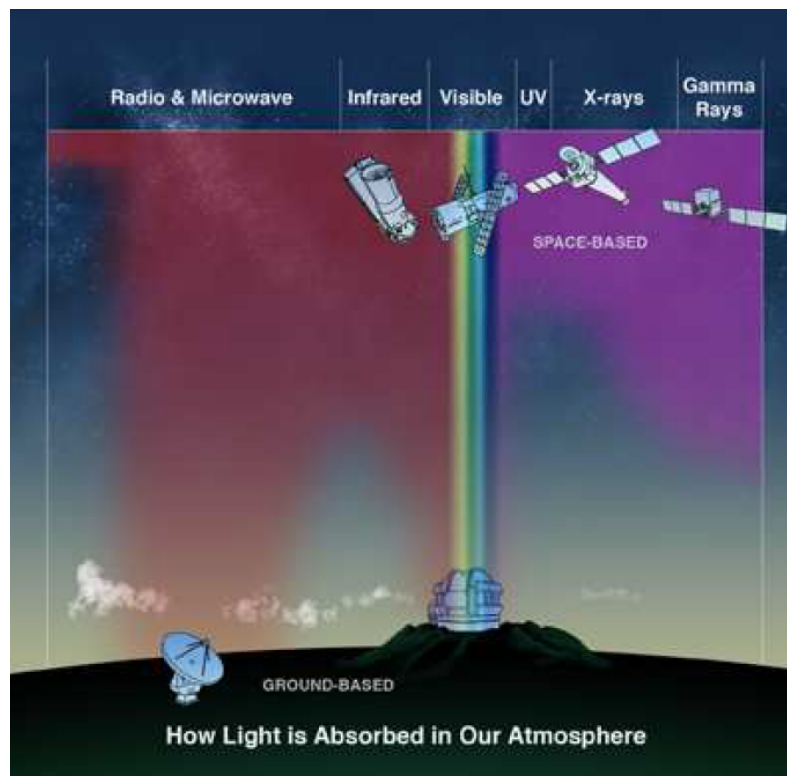


Figure 2.6: Schematic representation of the penetration depth of photons to the Earth's atmosphere as a function of wavelength, for satellite or ground-based detection methods. Figure taken from [Backes \(2011\)](#).

E_e and primary photon E_γ , two interaction regime can be identified - the classical or Thomson regime and the Klein Nishina regime. The interaction cross-section in each energy regime is given by:

$$\sigma_T = \frac{8}{3}\pi r_e^2; \quad E_e E_\gamma \ll m_e^2 c^4 \quad (\text{Thomson regime}) \quad (2.3)$$

$$\sigma_{KN} = 2\pi r_e^2 \frac{1+e}{e} \left[\frac{2+2e}{1+2e} - \frac{\ln(1+2e)}{e} \right] + \frac{\ln(1+2e)}{e} - \frac{1+3e}{(1+2e)^2}; \quad (2.4)$$

$$E_e E_\gamma \approx m_e^2 c^4 \quad (\text{Klein - Nishina regime})$$

where r_e is the classical electron radius. When $E_e E_\gamma \gg m_e^2 c^4$, the cross-section takes the following approximate form:

$$\sigma = \frac{\pi r_e^2}{e} \left[\ln(2\varepsilon) + \frac{1}{2} \right] \quad (2.5)$$

where $\varepsilon = E_e E_\gamma / m_e^2 c^4$. The photons emitted in the Thomson regime follow the spectral distribution of the seed photon field, while for those emitted in the Klein-Nishina regime, the photon spectra encounters a sharp cutoff at the highest energies due to relativistic effects, known as the "Klein-Nishina effect".

- **Pair production**

Another leptonic interaction channel by which γ -ray photons can be produced in astrophysical sources is γ - γ pair production. Through this mechanism, an extremely energetic photon can interact with a lower energy target photon to produce a γ -ray photon if the following threshold criterion is satisfied:

$$E_{th} = \frac{m_e^2 c^4}{h\nu}$$

where m_e denotes the rest mass of an electron and ν represents the frequency of the target photon. The process can be a relevant channel in case of hadronic cascade interactions, that will be described in Chapter 6. Moreover, this mechanism is also responsible for the attenuation of γ rays during their propagation towards Earth due to interaction with the Extragalactic Background Light (EBL; for more details see Chapter 4).

Hadronic non-thermal emission mechanisms

- **Photo-meson interactions**

In some astrophysical environments the density of low-energy photons often exceeds the density of matter. In such environments, the interaction of a relativistic protons with the ambient soft photon field is a more favoured channel to produce γ rays compared to proton-proton collisions. The soft photon target can be provided intrinsically by the emission region or may originate outside the γ -ray production zone. The relativistic protons after interacting with the lower energy photons produce charged (π^+ , π^-) and neutral (π^0) pions with equal probability. The neutral pions subsequently decay to produce two γ -ray photons. The interaction channel is schematically explained below:

$$p + \gamma \rightarrow n_0 \pi^0 + n_+ \pi^+ + n_- \pi^- \rightarrow \pi^0 = \gamma + \gamma$$

where n_0, n_+, n_- denote the number of generated π^0, π^+, π^- respectively. Often the produced γ -ray photons are energetic enough to be overcome the threshold for pair production in the optically thick regime by interacting with the low-energy photons present in the environment. In such cases the primary γ -ray photon trigger an electromagnetic cascade by redistributing its energy to lower energetic particles and photons until it emerges in the optically thin regime for γ rays.

The photo-meson interactions also give rise to neutrinos and anti-neutrinos of different flavour ($\nu_\mu, \bar{\nu}_\mu, \nu_e, \bar{\nu}_e$) through the prompt decay of charged pions (π^\pm) and muons (μ^\pm):

$$\begin{aligned} \pi^+ &\rightarrow \mu^+ + \nu_\mu \\ \pi^- &\rightarrow \mu^- + \bar{\nu}_\mu \\ \mu^+ &\rightarrow e^+ + \nu_e + \bar{\nu}_\mu \\ \mu^- &\rightarrow e^- + \bar{\nu}_e + \nu_\mu \end{aligned}$$

The typical energy carried by a neutrino is ($E_\nu \sim 0.05E_p$), where E_p is the energy of the parent proton. Thus in the hadronic emission scenarios, γ -ray emission through π^0 decay is always accompanied by simultaneous neutrino production. In the simplest scenarios, the expected neutrino flux F_ν from a source population can be calculated if the γ -ray flux F_γ is known, by assuming a proportionality between them: $F_\nu \propto F_\gamma$ (see for e.g.: [Righi et al. \(2017\)](#)).

- **Proton-proton interactions**

One of the principle production mechanisms of γ rays in astrophysical environments is through inelastic proton-proton collision. The target matter density for interaction with a relativistic proton can be provided by the accelerating region or the Interstellar Medium (ISM) which produces many secondary unstable particles such as pions, kaons and hyperons. For the production of γ rays the main contribution comes from the production and decay of neutral pions and η mesons. The main interaction channels are briefly described below:

$$\begin{aligned}\pi^0 &= \gamma + \gamma & (99\%) \\ \pi^0 &= \gamma + e^+ + e^- & (1\%) \\ \eta &= \gamma + \gamma & (39.4\%) \\ \eta &= 3\pi^0 = 6\gamma & (32.5\%) \\ \eta &= \pi^+ + pi^- + pi^0 = 2\gamma & (22.6\%) \\ \eta &= pi^+ + pi^- + \gamma & (5\%)\end{aligned}$$

Similar to the photo-meson interaction scenario, the proton-proton interactions also generate neutrinos through charged pion decay along with the γ rays produced from the decay of the neutral particles.

- **Proton synchrotron radiation**

The ultra-relativistic protons present in various astrophysical environments are accelerated by the tangled magnetic fields present inside the emission region. They spiral around the magnetic fields and emit synchrotron radiation through a process similar to the electron synchrotron radiation. For a proton of energy E interacting with a magnetic field B , the synchrotron cooling time and the characteristic energy of the emitted synchrotron photon ϵ_c is given by the following formulae:

$$t_{sy} = \frac{6\pi m_p^4 c^3}{\sigma_T m_e^2 E B^2} = 4.5 \times 10^4 B_{100}^{-1} E_{19}^{-2} \text{ s} \quad (2.6)$$

$$\epsilon_c = \sqrt{\frac{3}{2}} \frac{heBE^2}{2\pi m_p^3 c^5} = 87 B_{100} E_{19}^2 \text{ GeV} \quad (2.7)$$

where $B_{100} = B/100$ G and $E_{19} = E/10^{19}$ eV. m_p, m_e represent the mass of a proton and an electron respectively and σ_T represents the Thomson's cross-section. The average energy of a synchrotron photon produced by a proton of energy E is given by $\epsilon_m = 0.29\epsilon_c$. Under dense magnetic environments where protons can be accelerated to extremely high energies, it is possible to observe signatures of γ -ray photons produced through proton synchrotron interactions.

- **Bremsstrahlung radiation**

It is produced when a charged particle is deflected in an electric field. γ rays can be produced due to Bremsstrahlung by the deflection of extremely energetic cosmic rays.

2.2.2 Main detection techniques of γ rays

Based on the energy domain of observation, the γ -ray detection techniques can be broadly classified into two categories:

- Satellited-based detection, that is usually relevant for γ rays in the high-energy and low-energy regime
- Ground-based detection, which is an indirect detection method mainly for γ rays in the VHE regime.

The main detection principles of both these techniques will be briefly discussed below. For a review of the γ -ray detection techniques, the reader is referred to [De Angelis and Mallamaci \(2018\)](#).

Table 2.1: A comparison of the characteristics of the *Fermi* satellite, IACTs and EAS arrays.

Characteristics	<i>Fermi</i>	IACTs	EAS arrays
Duty cycle	80%	20%	>90%
Field of view	$4\pi/5$	$5^\circ \times 5^\circ$	$4\pi/5$
Energy range	20 MeV-300 GeV	50 GeV-50 TeV	400 GeV-100 TeV
Energy resolution	5-10%	15-20%	$\sim 50\%$
Angular resolution	0.1°	0.07°	0.5°
Sensitivity	1% Crab ¹ (1 GeV)	1% Crab (500 GeV)	0.5 Crab (5 TeV)

Space-based satellites

Satellite-borne instruments can directly measure the γ -ray flux from distant astrophysical sources. They are mainly used to detect γ rays in the energy range of few MeV up to ~ 300 GeV. The detection of high-energy γ rays are limited by their flux. Higher energetic photon implies much lower flux which thus cannot be measured with the limited collection area ($\sim 1\text{m}^2$) of satellites and requires larger detector arrays (see the section below). To measure the direction and energy of the incoming γ rays, their interaction products are detected by means of a tracker and a calorimeter. In addition, an anti-coincidence detector (ACD) is used to eliminate the cosmic-ray background. The main detection principle relies upon pair production (for photons with energy above 30 MeV) and inverse Compton scattering (for photons below 30 MeV).

One of the major advantages of space-based γ -ray detectors is their high duty cycle and ability to survey the entire sky. They also provide a good energy resolution and good discrimination power of γ -like events and hadron-like events but have a poor angular resolution at low energies ($> 0.5^\circ$ below \sim few GeV).

In 2008, space-based γ -ray astronomy entered into a new era due to the launch of the *Fermi* γ -ray satellite (<https://fermi.gsfc.nasa.gov/>), which is by far the largest space-based instrument measuring γ rays. It consists of two sub-instruments: the Large Area Telescope (LAT) and the Gamma-ray Burst Monitor (GBM). The *Fermi*-LAT instrument is sensitive in the energy range 20 MeV to 300 GeV. A comparison of the characteristics between the *Fermi* satellite and other ground-based instruments such as Imaging Air Cherenkov Telescopes (IACTs) and Extensive Air shower arrays (discussed in the next sub-section) is given in Table 2.1.

Lower energy γ rays up to 10 MeV are measured by the INTEGRAL satellite (<http://sci.esa.int/integral/>), that has been operational since 2002.

Imaging Atmospheric Cherenkov Telescopes (IACTs)

Ground-based telescope arrays are used to detect VHE ($E > 100\text{GeV}$) γ rays up to energies of 50 TeV. The detection technique is called Imaging Air Cherenkov Technique, that will be described in Chapter 3, Sec. 3.3. The main advantages of ground-based telescope arrays are: the collection area can be increased to $> 1\text{km}^2$ enabling the detection of γ rays up to tens of TeV despite the low flux. They also have a very good angular resolution and good discriminating power for γ and hadrons compared to the satellite-borne instruments. One of the main drawbacks is that they are sensitive to the background light and hence can be only operated during complete or partial darkness of the night sky, thereby reducing the duty cycle of operations compared to satellite instruments. Since IACTs are pointing instruments², they also have a smaller field of view (FoV) compared to satellite-borne instruments (see Table 2.1). The major IACTs currently under operation are: the High-Energy Stereoscopic System (H.E.S.S.) (<https://www.mpi-hd.mpg.de/hfm/HESS/>) in Namibia, Major Atmospheric Gamma-ray Imaging Cherenkov (MAGIC) telescope in the Canary Islands, La Palma (<https://magic.mpp.mpg.de/>) and Very Energetic Radiation Imaging Telescope Array System (VERITAS) in Arizona (<https://veritas.sao.arizona.edu/>). MAGIC in the current date is a stereoscopic system of two IACTs, which started its operation in 2004 with a single telescope (more details about the telescope, its hardware and data analysis chain will be given in Chapter 3). H.E.S.S. has been operational since 2004 with an array of four telescopes and a fifth one was built in 2012. VERITAS started its operation since 2007 and consists of an array of four IACTs. In addition, First G-APD Cherenkov Telescope (FACT) (<https://www.isdc.unige.ch/fact/>) is a single IACT located beside the MAGIC telescopes in La Palma. The future generation of Cherenkov telescopes, the Cherenkov Telescope

²They point towards a particular source direction to observe it

Array (CTA) (<https://www.cta-observatory.org/>) is under construction, which will have more than 100 telescopes distributed in the northern and southern hemispheres and will offer unprecedented improvement in performance compared to the current instruments (more details will be given in Chapter 3).

Extended Air Shower arrays

EAS arrays rely upon the indirect detection of γ rays through the secondary particles generated in a γ -ray-induced air shower, that reaches the ground. EAS detectors have a much higher energy threshold and possess worse sensitivity, angular and energy resolution compared to the IACTs. The main advantages of such detection techniques is that they have a large FoV and are not sensitive to the background light of the sky. Hence they can even be operated during daytime almost all year round (see Table 2.1). Since they have a much larger collection area compared to IACTs, they can detect higher energetic photons up to ~ 100 TeV which have much lower fluxes. A past example of such ground-based detectors is MILAGRO (<https://physics.nyu.edu/experimentalparticle/milagro.html>), a water Cherenkov detector that was located in New Mexico. One of the current generation instruments using such detection techniques is the High Altitude Water Cherenkov (HAWC) observatory (<https://www.hawc-observatory.org/>) located in Mexico. It consists of an array of 300 water Cherenkov detectors each of which has a tank filled with purified water. When VHE photons pass through the tank, they generate secondary pairs that can emit Cherenkov light, which in turn are detected by means of photo-multiplier tubes installed in the tank.

2.2.3 Sources of γ rays

Galactic sources

One of the known Galactic γ -ray sources are pulsars, which are rapidly rotating highly magnetized neutron stars. Due to the rotational effect, they produce a pulsed γ -ray emission observed from Earth. PWNs are luminous structures visible around pulsars and form the largest population of known Galactic γ -ray sources. Also γ -ray binaries, which are binary systems of a pulsar rotating around a massive companion star, are known to emit γ -rays. Another possible source of Galactic γ -ray emission are the SNRs which result from explosion of stars in supernova. SNRs are also believed to accelerate cosmic rays during the shock after a supernova explosion, which can in principle interact with the interstellar medium to generate γ rays.

Based on the fourth *Fermi* Large Area Telescope (LAT) source catalog (4FGL) (Fermi-LAT Collaboration et al., 2019) after 8 years of operation, the majority of the identified Galactic sources are pulsars (~ 241). The H.E.S.S. Collaboration performed a deep survey of the Galactic plane from 2004-2013 and identified 78 VHE γ -ray emitting objects, 16 of which were previously unknown (Abdalla et al., 2018). A large population of the detected sources can be associated to pulsars or PWNs and some of them to SNRs and γ -ray binaries. Abeysekara et al. (2017) provides a catalog of 39 TeV-emitting sources measured in a survey by the HAWC telescope, most of which lie near the Galactic plane. 20 out of these 39 objects could be associated to TeVCat sources: 10 are PWNs or SNRs, 2 are blazars and the remaining 8 are unidentified.

Extragalactic sources

Amongst the known extragalactic sources of γ rays are AGNs, starburst galaxies and GRBs. The later are extremely rare events of short duration bursts of γ rays and correspond to the most energetic γ -ray flares. Very recently the first GRB at the VHE γ -ray regime was detected by the MAGIC telescopes on 15th January, 2019 (Mirzoyan, 2019).

The main topic of discussion in this thesis will be AGNs as γ -ray and cosmic-ray emitters. AGNs are powered by supermassive black holes at the center of the galaxy that can emit ultra-relativistic jets, in some cases very closely aligned to the line of sight of an observer on Earth. The AGN jets are believed to accelerate particles to extremely high energies that can produce very strong γ -ray emission. AGNs will be discussed in details in Chapter 4.

About 80% of the sources in the *Fermi* 4FGL catalog are associated to extragalactic objects most of which are active galaxies of the blazar class. At higher energies ($E > 100$ GeV), more than 200 sources have been detected and are catalogued in the TeVCat webpage (<http://tevcat.uchicago.edu/>). About half of them belong to

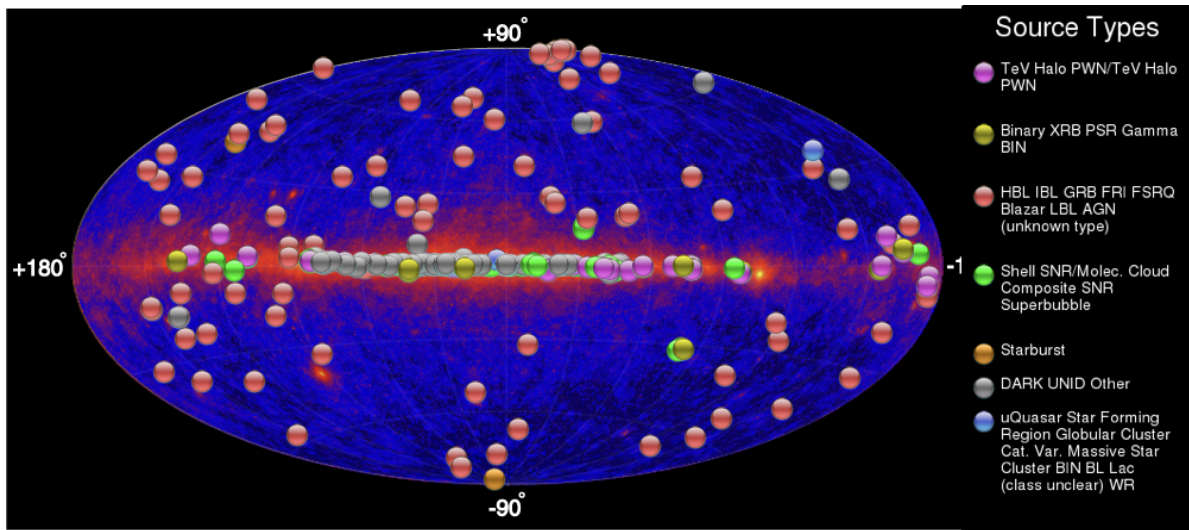


Figure 2.7: List of the VHE ($E > 100$ GeV) γ -ray emitting sources (Galactic and extragalactic) from the TeV catalog. Image taken from <http://tevcat.uchicago.edu/>.

our Galaxy (SNRs, pulsars, PWNs) and the remaining half are extragalactic sources. A map of the VHE γ -ray emitting sources from the TeV catalog is given in Fig. 2.7.

2.3 Astrophysical neutrinos

Neutrinos are electrically neutral particles that can be produced by hadronic processes in astrophysical environments by photo-meson and proton-proton interactions, through charged pion (and muon) decay (as described in Sec. 2.2.1). Neutrinos interact only weakly with matter and hence can escape dense environments easily, that are not transparent to cosmic rays or photons. Since they are uncharged and are not deflected by the cosmic magnetic fields while travelling towards the Earth, they can be traced back to their sources of origin and serve as a direct indication of hadronic interactions inside the source. Neutrinos can change identities while travelling through space, i.e. they can oscillate amongst different flavours (Fukuda et al. (1998); Ahmad et al. (2001); Ahmad et al. (2002)). In 2015, Takaaki Kajita and Arthur McDonald were jointly awarded the Nobel Prize in Physics for this remarkable discovery.

2.3.1 High-energy neutrino detectors

Neutrinos are very difficult to detect since they have a very small interaction cross-section. To overcome this difficulty huge effective detector volumes are required. The large volumes of ice in Antarctica and large water bodies present on Earth provide naturally occurring detector media, that can be used as a part of the neutrino telescopes. The current generation of neutrino detectors include IceCube (<https://icecube.wisc.edu/>) deployed in the antarctic ice with a large detector volume of 1 km^3 and ANTARES (<http://antares.in2p3.fr/0verview/index.html>), a large water Cherenkov detector located in the Mediterranean Sea. A substantial expansion of the IceCube detector is planned (IceCube-Gen2; IceCube-Gen2 Collaboration et al. (2014)) that will enlarge the instrumented detector volume by nearly one order of magnitude, offer unprecedented sensitivity, wider energy coverage and improved angular resolution. Also, two giant sea water Cherenkov detectors that will constitute the KM3Net experiment (<http://www.km3net.org/>), are already under construction in the Mediterranean Sea which will also increase the detector volume tens times compared to ANTARES. Fig. 2.8 shows a schematic representation of the IceCube detector installed in Antarctica.

Neutrinos can be detected indirectly from the secondary particles they produce upon interaction with the detector. There are two main interaction channels: charged current (CC) and neutral current (NC) interactions. In a CC interaction a neutrino interacts with a nucleon by exchanging W^\pm bosons to produce a lepton of the same

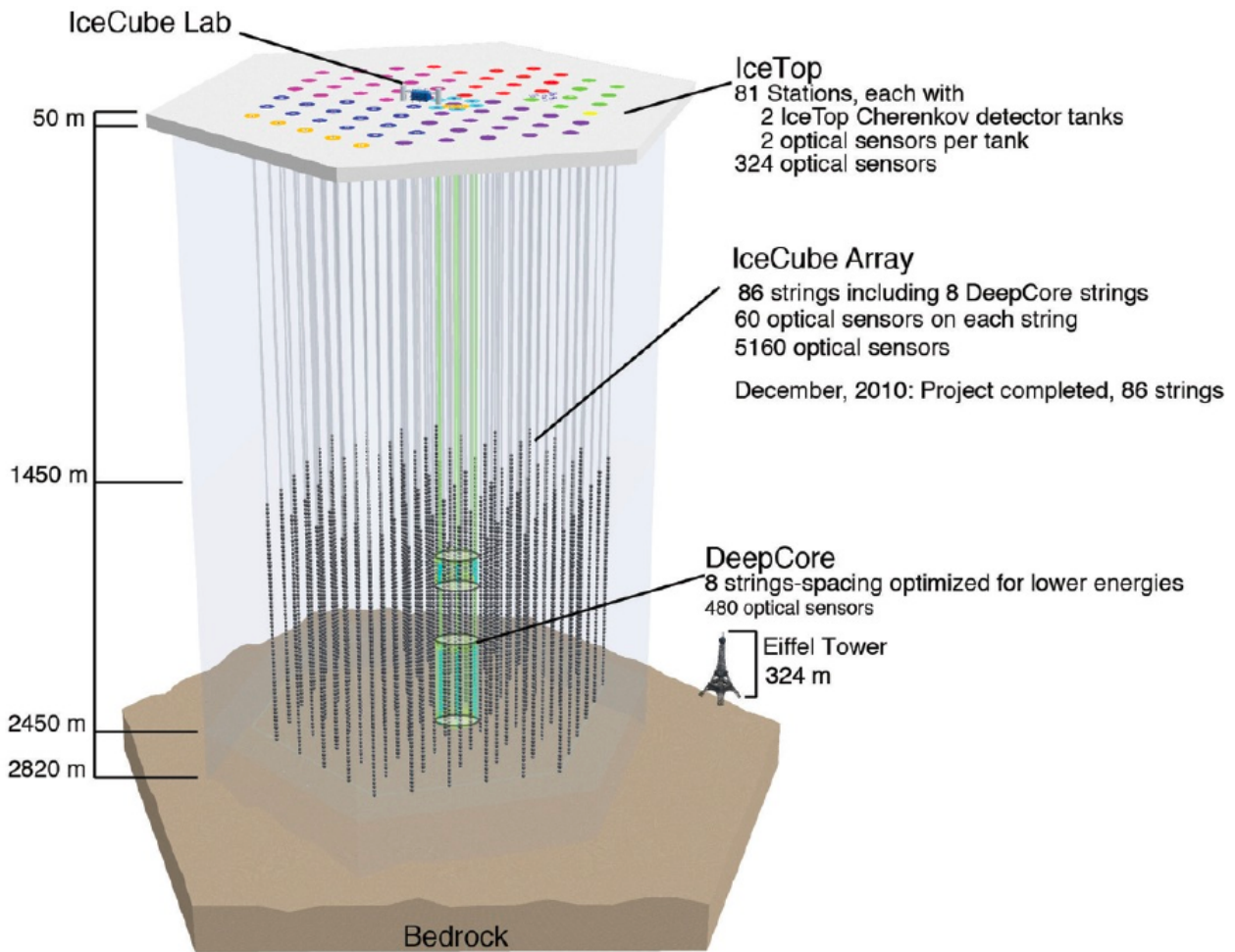


Figure 2.8: The IceCube neutrino detector located at South Pole, Antarctica. Image taken from [Taboada \(2018\)](#).

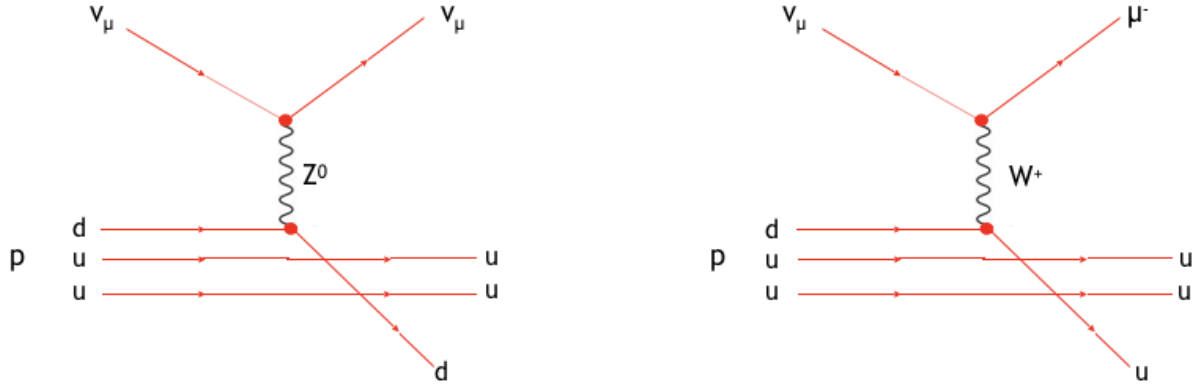


Figure 2.9: Left: Neutral current interaction of a muon neutrino and a proton. Right: Charged current interaction of a muon neutrino and a proton. Image adapted from [Satalecka \(2010\)](#).

flavour and the nucleon transforms to a new hadronic state (H). In a NC interaction a neutrino exchanges Z^0 upon interaction with a nucleon and produces a neutrino of the same flavour and a hadron. Fig. 2.9 shows the CC and NC interactions of a muon neutrino (μ_ν) with a proton (p).

There are two main detection channels in a neutrino telescope: a track channel (through the leptons produced in CC interactions) and a cascade channel (through the secondary showers by leptons and hadron produced in CC/NC interactions). The charged particles produced in CC and NC reactions, trigger a cascade of secondary particles by interacting with the detector. Showers triggered by charged leptons (from CC) are known as electromagnetic showers and that triggered by hadrons (from both CC and NC) are known as hadronic showers. The main interaction mechanisms are Bremsstrahlung, pair production and photo-nuclear processes. These charged particles travelling faster than the speed of light, can emit Cherenkov photons which is used to detect them. In the IceCube neutrino detector, the interaction medium is ice while in water Cherenkov detectors such as ANTARES, the interaction medium is water. A charged particle-induced cascade deposit most of their energy within a short distance (few meters) and hence provides a very precise determination of the parent neutrino energy, however the direction information is lost (angular uncertainty $3\text{-}10^\circ$). On the other hand, high-energy muons can travel a large distance without energy loss and hence provide a good direction estimation of the parent neutrino (angular uncertainty 0.5°), at the cost of poor energy estimation.

2.3.2 Sources of background

The search for astrophysical point sources of neutrinos is strongly influenced by the background arising from cosmic-ray air showers in the Earth's atmosphere. The main source of background in the neutrino observations are the down-going atmospheric muons events. These muons are detected by an outer veto layer of the IceCube detector and tagged as background. The atmospheric neutrinos, produced along with the muons from cosmic-ray interactions with the atmosphere, provide another strong source of background. At energies above 100 GeV, an additional background component of atmospheric muons and neutrinos arise from the decay of charm-containing mesons. It is difficult to distinguish between muon tracks in the detector generated by an atmospheric or a cosmogenic neutrino. Only the up-going muon tracks are thus treated as a probable signal. Some of the down-going atmospheric neutrinos are also vetoed because of the muons produced in the same cosmic-ray air shower. Hence this reduces the atmospheric neutrino background to some extent in the southern sky.

2.3.3 Sources of astrophysical neutrinos

The Sun is one of the prime sources to produce low-energy neutrinos (up to few tens of MeV). Electron neutrinos are produced in the nuclear fusion reactions in the Sun, that occur via two thermonuclear reaction chains: the pp cycle (produces $\sim 98\%$ of the solar neutrino flux) and the CNO cycle (contributes $\sim 1.5\%$ to the total solar neutrino flux).

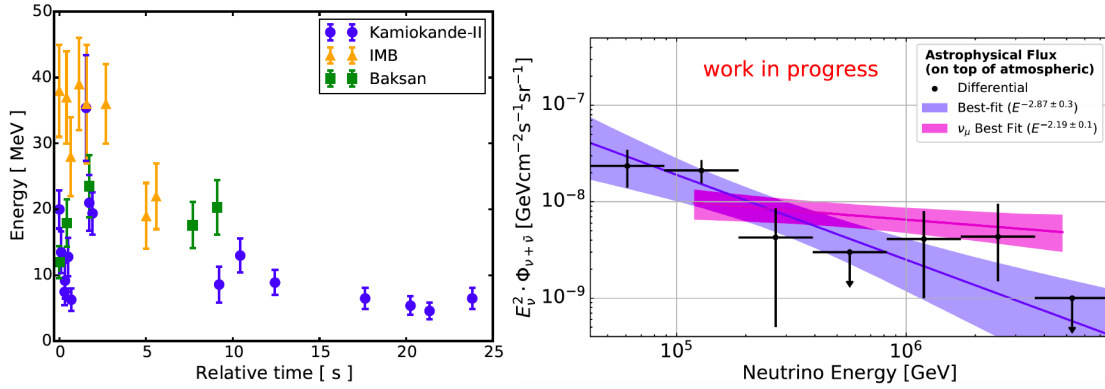


Figure 2.10: Left panel: The arrival time and energies of the neutrinos observed from SN1987A by Kamiokande, IMB and Baksan. The figure is taken from the thesis of Andrii Terliuk (Terliuk, 2018). Right panel: Flux of the astrophysical neutrinos measured in 7.5 years of IceCube data (Wandkowsky, 2018). The blue band shows a single power law fit to the data and the pink band denotes the 8 years up-going muons best fit.

Another source of astrophysical neutrinos are supernovae. A flux of low-energy neutrinos were detected from the supernova SN1987A by Kamiokande, IMB and Baksan in 1987 (Hirata et al. (1988), Bionta et al. (1987), Alexeyev et al. (1988)). The arrival time and the energies of the detected neutrinos after the supernova explosion is shown in Fig. 2.10, left panel.

The IceCube neutrino experiment measured a diffuse flux of astrophysical neutrinos (in the TeV-PeV range) in 2013 (IceCube Collaboration et al. (2013), Aartsen et al. (2014b)). After 7.5 years of operation, IceCube detected >100 astrophysical neutrino events (Taboada, 2018). Their energy spectrum follows a power law shape with spectral index $\Gamma = 2.87 \pm 0.3$ (Wandkowsky, 2018), but no clear correlation (in space or time) with known astrophysical point sources (Aartsen et al., 2017f) or the Galactic plane could be found. The energy spectrum of astrophysical neutrinos is shown in Fig. 2.10, right panel.

The main observational challenges to identify sources of astrophysical neutrinos are the limited event rates and large positional uncertainty ($\sim 1^\circ$ for muon track events and even larger uncertainty for cascade events). The Galactic contribution to the diffuse neutrino flux was estimated to be small (Aartsen et al., 2017e). A part of the diffuse flux was believed to be contributed by blazars. Padovani et al. (2016) has reported positional correlation (at a random expectation level of $\sim 0.4 - 1\%$) between 5 neutrino events detected by IceCube with γ -ray emitting blazars of BL Lac type (defined in Chapter 4). Kadler et al. (2016) reported a spatial and temporal coincidence (probability of chance coincidence is $\sim 5\%$) between a neutrino event having highest reconstructed energy of ~ 2 PeV (but having a large positional uncertainty), with a γ -ray outburst of the blazar PKS B1424-418. The overall contribution of blazars from the 2nd *Fermi*-LAT blazar catalog (2LAC) to the diffuse neutrino flux was constrained to be $< 27\%$ (Aartsen et al., 2017d). The contributions from GRBs was constrained by a more stringent limit of $< 1\%$ (Aartsen et al., 2017c). The diffuse neutrino flux measured by IceCube is expected to have a close to equal ratio amongst the different neutrino flavours ($\nu_\mu : \nu_e : \nu_\tau = 1 : 1 : 1$) due to flavour mixing while travelling through space. Interestingly, first hints of identification of possible tau neutrino events were reported in Usner et al. (2018) (see also Wille et al. (2018)), that can only be produced by neutrino oscillations on its path towards the Earth.

Recently on 23rd September 2017, IceCube detected an astrophysical neutrino with energy ~ 290 TeV from a direction coincident with a blazar called TXS 0506+056 (IceCube Collaboration et al., 2018b). Chance coincidence was disfavoured at a confidence level of 3.5σ . During the same time, the blazar was also flaring in γ -rays as observed by the *Fermi*-LAT and MAGIC telescopes at different energy ranges (Tanaka et al. (2017), Mirzoyan (2017)). This is a remarkable discovery since it is the first potential association of a high-energy neutrino event with a known extragalactic astrophysical source. An independent confirmation of the source as a high-energy neutrino emitter came from a-posteriori measurements by IceCube (IceCube Collaboration et al., 2018a), when an excess of high-energy neutrino events over the atmospheric background were detected from the source direction in 2014/2015. More details on this topic including the interpretation of the neutrino signal and the simultaneously observed electromagnetic spectrum during 2017 will be discussed in Chapter 7.

2.4 Multi-messenger astronomy

In order to understand the nature of our non-thermal universe we need to "look" at its very distant corners. We rely on the detection of cosmic messenger particles coming from distant astrophysical objects that can provide crucial information regarding the particle acceleration and emission mechanisms occurring inside the sources of origin, their particle composition, energetics, propagation of secondary messengers towards the Earth and structure of the universe. Such studies form the core of multi-messenger astronomy (Santander, 2017) and are extremely important to understand some of the fundamental unanswered questions in Astroparticle Physics, such as investigating the production mechanisms and sources of the mysterious UHECRs.

Cosmic rays are the highest energy messenger particles known in our universe. They can reach energies greater than 10^{20} eV. However since they are not electrically neutral, they are deflected in their path towards the Earth by the cosmic magnetic fields and thus completely lose the direction information. Therefore they cannot act as the direct messengers of their sources of origin unless they reach ultra-high-energies ($E > 10^{19}$ eV). But at such ultra-high-energies, the cosmic-ray energy spectrum undergoes the GZK cutoff (Sec. 2.1.1). Consequently, for a detailed understanding of the extreme non-thermal universe, the information obtained only from cosmic-ray measurements are insufficient. Cosmic-ray interactions with the ambient matter or radiation fields during their acceleration or propagation, also produce photons and neutrinos (see Sec. 2.2.1). Both of these particles are electrically neutral and can be directly traced back to their sources of origin. Hence coordinated observations of the three messengers in Astroparticle Physics - cosmic rays, photons and neutrinos form the core of multi-messenger astronomy and are of paramount importance to characterize extreme astrophysical particle accelerators that might be linked to the sources of UHECRs.

GWs can also act as messengers of the inner regions of the astrophysical engines, alongside photons, neutrinos and cosmic rays. In 2015, the LIGO gravitational wave detector measured a GW signal from a binary black hole merger system (Abbott et al., 2016). In 2017, the LIGO and Virgo experiments detected GWs from a pair of colliding neutron stars (GW170817; Abbott et al. (2017b)). The GW event also had an accompanying electromagnetic transient GRB 170817A (Goldstein et al. (2017); Abbott et al. (2017c); Abbott et al. (2017a)) that showed a long afterglow at various wavelengths (Evans et al. (2017); Alexander et al. (2017); Arcavi et al. (2017); Chornock et al. (2017); Kasen et al. (2017); Kasliwal et al. (2017); Pian et al. (2017); Valenti et al. (2017); Pozanenko et al. (2018)). These observations corroborate the significance of GW detections and search for counterpart objects in multi-messenger astronomy. A detailed discussion on GWs in multi-messenger astronomy is beyond the scope of this thesis and for more details, the reader is referred to Branchesi (2016).

Photons reaching the Earth from distant astrophysical objects span a wide range of frequencies from radio to VHE γ rays and can provide a wealth of information regarding the nature of the emitting particles, particle composition, acceleration and emission mechanisms operating inside the source. The mechanism of production of the highest energy observable photons can be both leptonic (for eg: by inverse Compton scattering) and hadronic (for eg: from proton-proton or photo-meson interactions, proton synchrotron radiation etc) in origin. However one of the most important drawbacks is that the observation of the highest energy part of the electromagnetic spectrum is limited by the opacity of the universe to VHE γ -rays. The VHE γ -ray photons interacts with the EBL to produce e^+e^- pairs and thus gets attenuated.

On the other hand, the neutrinos of extremely high energy can travel large cosmological distances without getting absorbed and hence can be tracers of very distant corners of the universe. Moreover unlike photons, neutrinos can only be produced in hadronic particle interactions and thus bear an unambiguous signature of cosmic-ray acceleration and interaction inside the source. However neutrinos are not easily detectable due to their low cross-section and the large background produced by cosmic-ray interactions with the Earth's atmosphere. On the other hand, photon observations are much more abundant compared to neutrino observations since they are easily detectable by direct or indirect detection methods.

Thus globally coordinated measurements of the different messenger particles coming from the same astrophysical source is of paramount importance for a complete understanding of the source dynamics. IceCube has a real-time alert system (Aartsen et al., 2017g), which sends an alert to multi-wavelength instruments observing in different energy bands, immediately after detecting an interesting event or an increase in the event rates from a sky direction (within a few seconds). The electromagnetic detectors then start follow-up observations in the direction of the issued trigger. Such coordinated observation campaign are extremely important to look for electromagnetic counterparts of neutrino sources which maximizes the chances of identifying a high-energy cosmic-ray source.

The most important multi-messenger observation campaign of this kind till date, has been performed in

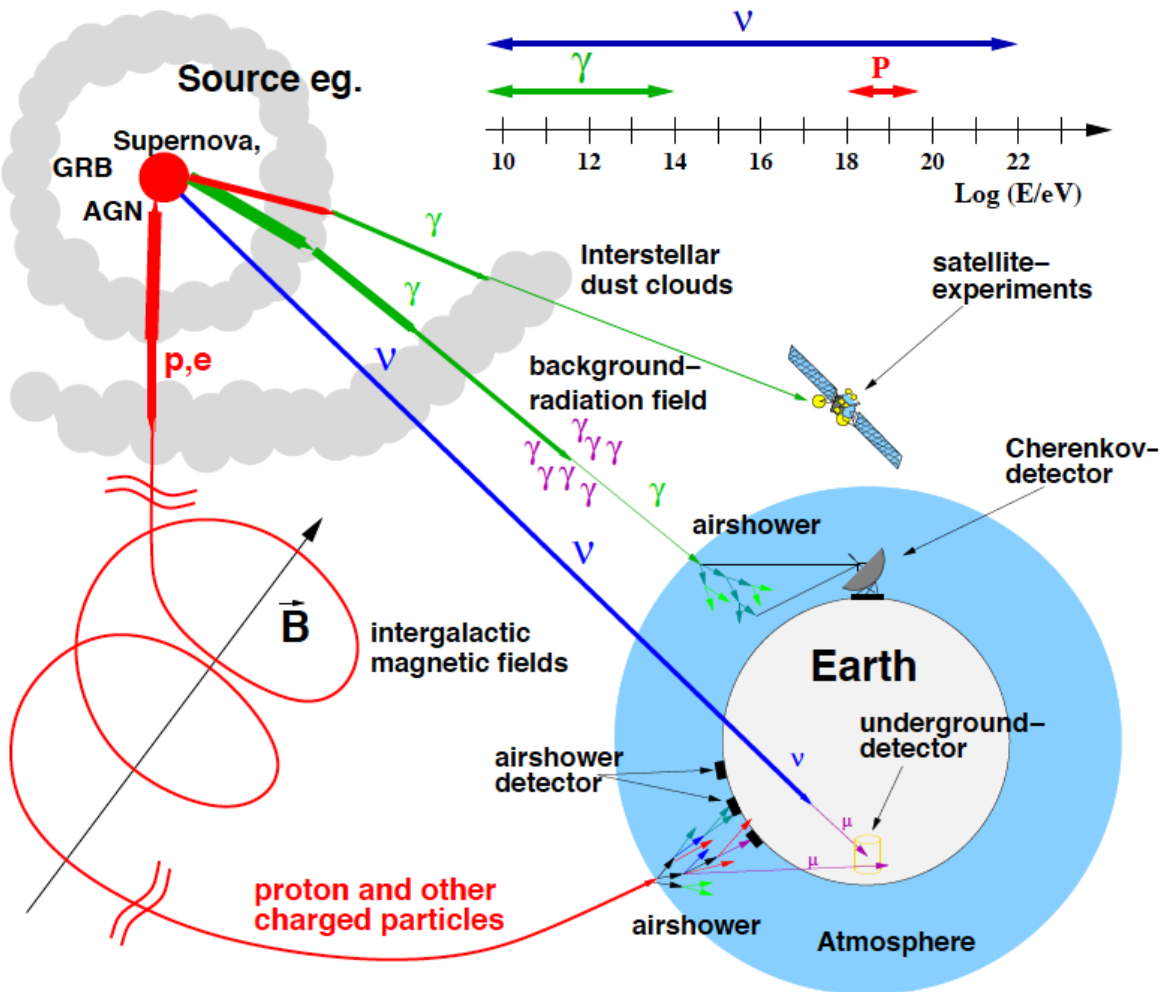


Figure 2.11: A schematic sketch of multi-messenger astronomy: the different messengers of Astroparticle Physics, their propagation towards the Earth and detection methods. Figure taken from Backes (2011).

September 2017, when a high-energy neutrino event detected by IceCube (dubbed IC 170922A) was found to be in spatial coincidence (within 0.1°) with a known γ -ray emitting blazar, TXS 0506+056. These observations triggered a series of theoretical studies to understand the nature of the emission mechanisms, linking them to high-energy cosmic-ray acceleration (more details will be given in Chapter 7).

The main contributions of the author in the field of multi-messenger astronomy are discussed in the context of two sources: the blazars 1ES 1959+650 and TXS 0506+056 (see Chapter 5 and 7). The multi-messenger observations of TXS 0506+056 from 2017 are interpreted in terms of a lepto-hadronic theoretical model, which corroborates that TXS 0506+056 could indeed be a potential source of the high-energy neutrino detected by Icecube and hence a site of high-energy cosmic-ray acceleration. For the source 1ES 1959+650, it was verified a-posteriori from the theoretical modelling of the multi-wavelength data, that the source cannot produce detectable neutrino emission within the limits of the current generation of instruments, even during very high activity states.

The strength of multi-messenger astronomy to identify and characterize plausible cosmic-ray sources has already been established. Efforts are ongoing amongst various GW, cosmic-ray, neutrino and photon communities to develop new multi-messenger observational strategies and data analysis techniques. Such interdisciplinary studies to explain the observations and constrain theoretical models will soon become one of the most dominant approaches to understand the distant and powerful astrophysical particle accelerators in the universe.

Chapter 3

Imaging Atmospheric Cherenkov telescopes

In this chapter the principle detection techniques of VHE γ rays will be discussed. Since the main instrument used for the data analysis in this thesis are the Major Atmospheric Gamma-ray Imaging Cherenkov (MAGIC) telescopes, our focus will be primarily on the description of the hardware, data-taking and software used for the data analysis of MAGIC. Since the Earth's atmosphere is not transparent to VHE γ rays, they are detected indirectly from Earth by a method called imaging atmospheric Cherenkov technique, using the atmosphere as part of the detector. Before going into the description of the MAGIC telescopes and its operational details, I will briefly review the concept of Cherenkov light production and the detection technique used by the current experiments.

3.1 Cherenkov light production

The Cherenkov effect was first proposed by Pavel Cherenkov in 1934 (Cherenkov, 1934), who was jointly awarded the Nobel Prize in 1958 with Ilya Frank and Igor Tamm. If a charged particle travels through a dielectric medium such as air with a velocity greater than the speed of light in the medium, then it produces Cherenkov light.

If velocity of the charged particle is v , which is greater than the velocity of light in the medium c/n , where n is the refractive index of the dielectric medium, it induces an asymmetric polarization along its direction of motion in the medium. This effect is demonstrated in Fig. 3.1. The image on the left-hand-side of fig. 3.1 shows the case of $v < c/n$ and the one on the right-hand-side shows the case of $v > c/n$. In the former the polarization induced in the dielectric medium is symmetric and no net electric field is induced. In the later case, the polarization is asymmetric and a net electric field is induced along the direction of the moving particle. To compensate the effect of the asymmetric polarization, an electromagnetic shock wave is generated which is called Cherenkov light. It is always emitted in a cone of angle θ given by:

$$\theta = \frac{c}{vn(\lambda)} \quad (3.1)$$

where $n(\lambda)$ is the spectral index of the medium which is dependent on the wavelength λ of the emitted Cherenkov photon. The minimum particle velocity required for the production of Cherenkov light can be derived as:

$$\beta_m(\lambda) = \frac{1}{n(\lambda)}$$

The Cherenkov cone formation is schematically explained in Fig. 3.2, where one can see the cone of emitted Cherenkov light with respect to the primary moving charged particle and the instantaneous wavefront created by the emission.

When a VHE γ ray enters the atmosphere, it interacts with an atmospheric nuclei to produce shower of charged electromagnetic secondary particles known as Extensive Air Showers (EAS; Sec. 3.2). Some of them travel with a speed greater than that of light in air and thus emit Cherenkov radiation. The typical Cherenkov angle in air has a value of 1° and illuminates the Earth's surface in the form of a circle known as the "Cherenkov light pool". The

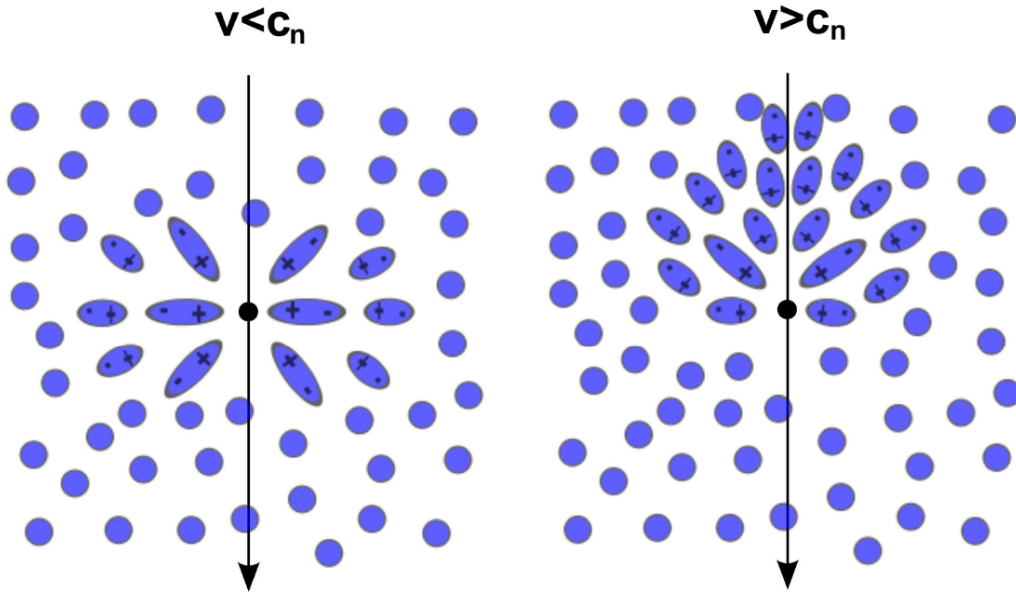


Figure 3.1: Polarization induced by a charged particle moving inside a dielectric medium with a certain velocity v . If this velocity is lower than the speed of light in the medium (denoted by c_n in the figure), the polarization induced is symmetric (left). If on the other hand the velocity is greater than the velocity of light in the medium, the polarization is asymmetric along the direction of the particle (right) and Cherenkov light is emitted. Figure taken from [Weekes \(2003\)](#).

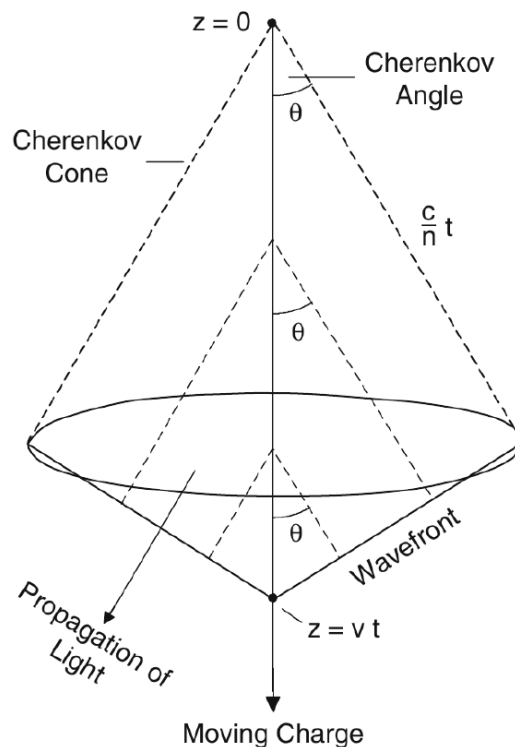


Figure 3.2: Schematic representation of the Cherenkov cone formation. A relativistic particle with a velocity v moves down the z -axis through a medium of refractive index n and emits Cherenkov light with a cone of angle θ . Image taken from [Grieder \(2010\)](#).

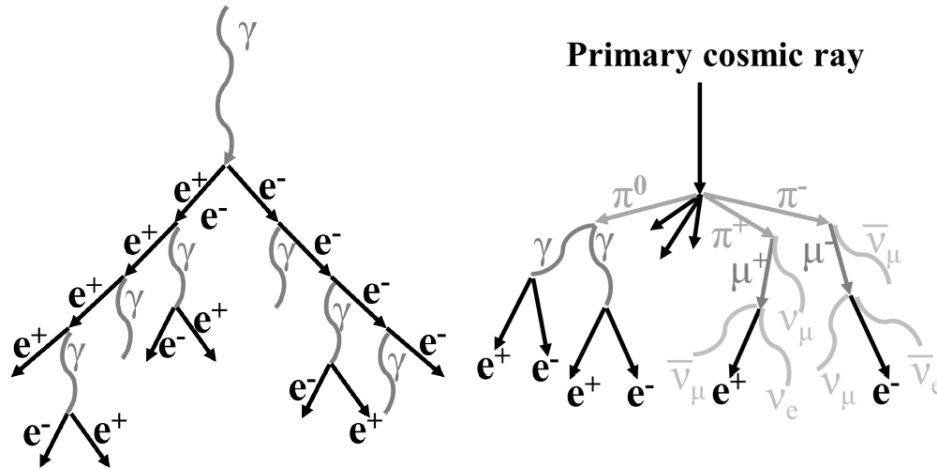


Figure 3.3: Left panel: Schematic representation of electromagnetic shower development. Right panel: Schematic representation of hadronic shower development. Image credit: [Weekes \(2003\)](#).

density of photons on the ground depends on the energy of the primary particle and gets marginally affected by various scattering processes like the Rayleigh and Mie scattering and absorption by the atmospheric molecules. The observed Cherenkov spectra lie in the visible-UV region and peaks at ~ 320 nm. The duration of Cherenkov flashes are very short (\sim few ns) and fast sampling electronics is necessary to detect them and limit the background contamination from the night sky.

Apart from VHE γ rays, hadrons can also generate particle cascades by interacting with the atmosphere and emit Cherenkov light. Such hadron-initiated showers are much more abundant compared to γ -ray-induced showers and forms the main source of background in VHE γ -ray observations. Hence understanding the characteristics of both types of showers is necessary to discriminate between the two and get rid of the background.

3.2 Extensive Air Showers and its types

As discussed in the previous section, when a VHE γ ray or a hadron interacts with an atmospheric nuclei, it generates a cascade shower of charged electromagnetic secondary particles that form the EAS. The EAS generated by a primary γ ray is known as electromagnetic shower and that generated by a primary hadron is known as hadronic shower. A schematic representation of the development of the two types of showers is given in Fig. 3.3.

If a γ ray with energy ≥ 20 MeV enters the Earth's atmosphere, it interacts with the atmospheric molecules to produce an e^+/e^- pair. The first interaction occurs at an altitude of about 20 km above sea level. The pairs then travel roughly along the same direction as the initial photon. Radiation length χ_0 is defined as the distance which a particle travels before its energy is reduced by a factor of $\frac{1}{e}$:

$$\frac{dN}{dE} = -\frac{E}{\chi_0}$$

After travelling a distance equivalent to $7/9 \chi_0$, where $\chi_0 = 36.664 \text{g/cm}^2$ is the radiation length of electrons in air, the pairs lose energy via Bremsstrahlung process and secondary γ rays are emitted. The secondaries may be energetic enough to further produce e^+/e^- pairs and thus a cascade of secondary particles are generated. The cascade development stops when the critical energy $E_c \sim 80$ MeV is reached. At this energy the ionization losses and the Bremsstrahlung losses are equal for the pairs and below this energy no new secondary particles are generated. This occurs roughly at a height of 10 km above the sea level (depending on the energy of the progenitor γ ray) where the number of generated secondary pairs is maximum. The altitude is known as the "height of shower maximum". Fig. 3.4 (left panel) shows a simulation of electromagnetic shower development.

In a similar way, a hadron (mainly protons, which are the primary components of cosmic rays) can also interact with an air nuclei and generate secondary particles that can emit Cherenkov light. The mean free path for inelastic

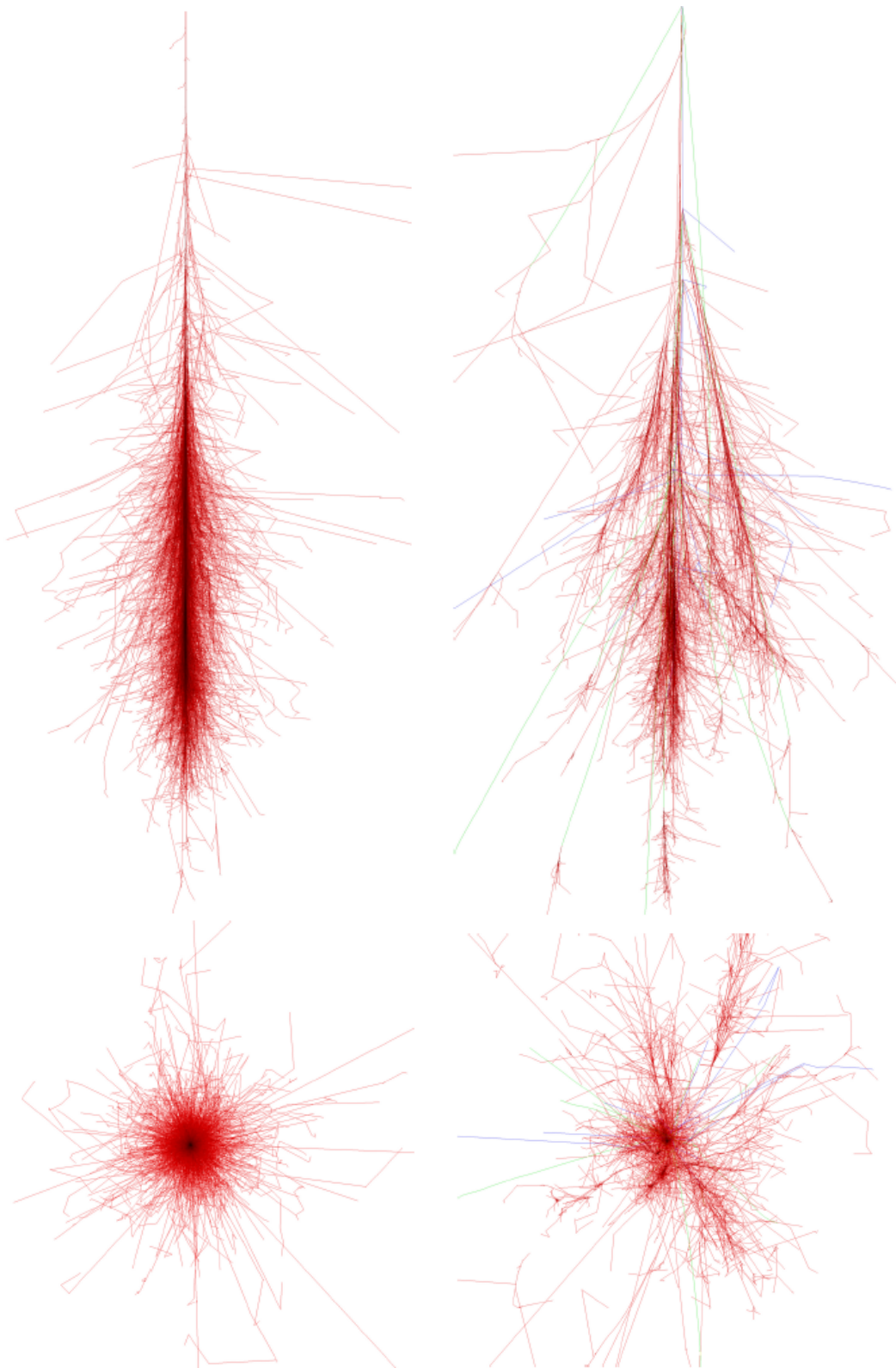


Figure 3.4: Left panel: A Monte Carlo simulation of an electromagnetic cascade generated by a 100 GeV γ ray. Right panel: A Monte Carlo simulation of a cascade generated by a 100 GeV proton. Top panel: The vertical profile of the showers. Bottom panel: The transverse profile of the showers. The red lines correspond to e^\pm or γ -ray tracks and the green and blue lines correspond to muons and hadrons respectively. Image taken from [López Coto \(2015\)](#).

scattering off an air nuclei is roughly 80 g cm^{-2} , which is larger than the radiation length for electromagnetic showers. Thus hadronic showers penetrate deeper into the atmosphere before the first interaction. Upon interaction, the proton mostly generates charged and neutral pions (π^0, π^\pm). The π^0 further decays into two photons while the π^\pm decays into secondary muons and neutrinos. The unstable secondary muons further decay to produce e^+ and e^- . The pairs lose energy by Bremsstrahlung and generate secondary photons in a similar way as the electromagnetic shower. Hence the background Cherenkov photons produced in hadronic shower consists of two types of components - a pionic component (the ones produced through direct pion decay) and an electromagnetic component (the ones produced through the decay of secondary leptons). The later is very difficult to distinguish from pure electromagnetic showers. Fig. 3.4 (right panel) shows a simulation of hadronic shower development.

The electromagnetic showers develop quite fast, within $\sim 3 \text{ ns}$. The secondary particles generated in an electromagnetic shower do not scatter off too much from the shower axis. Hence γ -ray initiated showers are roughly axis-symmetric with respect to their initial direction, as depicted in the longitudinal and transverse profiles of the shower shown in Fig. 3.4 (left panel).

The hadronic showers are more asymmetric and spread out compared to the electromagnetic showers (right panel, Fig. 3.4) since the transverse momentum received by the secondary pions are larger than those of e^+/e^- . Moreover, the hadronic showers take a longer time ($\sim 10 \text{ ns}$) for their development compared to electromagnetic showers.

3.3 Imaging Air Cherenkov Technique

Imaging Air Cherenkov Technique is a method used by ground-based VHE γ -ray experiments for the indirect detection of VHE γ ray events. An Imaging Air Cherenkov Telescope (IACTs) detects the Cherenkov light produced in an EAS initiated by a VHE γ ray, upon interaction with the Earth's atmosphere. Hence the atmosphere forms an important component of the detector. The main purpose of this technique is to collect the maximum amount of Cherenkov light from EAS that forms an image in the camera, extract the spatial and temporal information of the shower from the image, suppress the hadronic background and reconstruct the direction and energy of the progenitor particle.

The first IACT built was the Whipple observatory (Kildea et al., 2007) followed by the HEGRA observatory (Mirzoyan et al., 1994). At present there are three working IACTs, H.E.S.S. (Aharonian et al., 2006), MAGIC and VERITAS (Holder, 2007) and the upcoming next generation telescope array CTA (Actis et al., 2011) is under active development.

To maximize the photon collection efficiency, the IACTs are equipped with large reflector surfaces. If the telescopes are inside the Cherenkov light pool, the photons are reflected by the mirrors attached to the reflector, into fast-response pixelized cameras where they project an image of the EAS.

As discussed in Sec. 3.2, along with the VHE γ -ray initiated shower there are also hadronic showers which can produce Cherenkov photons. The background contribution from hadronic showers is ~ 1000 times larger than the signal. The difference in the geometry and temporal characteristics of the two types of images produced by electromagnetic and hadronic cascades are used to discriminate the background events from the signal and suppress them. Apart from the Cherenkov light generated by the hadronic showers, another major source of background in the VHE γ -ray observations is the isotropically distributed Night Sky Background (NSB) photons, which are relics from the star light, the moon, artificial lights etc. The atmospheric muons, which arises from cosmic-ray air showers form another source of background. The muonic background can be easily distinguished due to the ring-like shape that it produces in the camera. To detect Cherenkov flashes from EAS that develop within a very short time, highly sensitive and fast-response photo-multiplier tubes (PMTs) are usually used in the cameras of the IACTs. The fast response is also essential to detect the faint signal while integrating as little background as possible. During IACT operations, the atmospheric parameters such as temperature, humidity, aerosol abundance, presence of clouds etc. are also monitored since turbulence in the atmosphere can affect the data quality and sensitivity of the telescopes. The optimal location for an IACT is therefore a dark site far away from artificial lights, where the atmospheric conditions are expected to be comparatively stable.

Fig. 3.5 shows a schematic representation of the imaging technique. More than one telescopes are often used in order to better reconstruct the arrival direction of the incoming photon and better suppress the background light. Usually the telescope system operate in stereoscopic mode i.e. only when the number of events crosses a desired threshold in two or more telescopes, a signal trigger is issued.

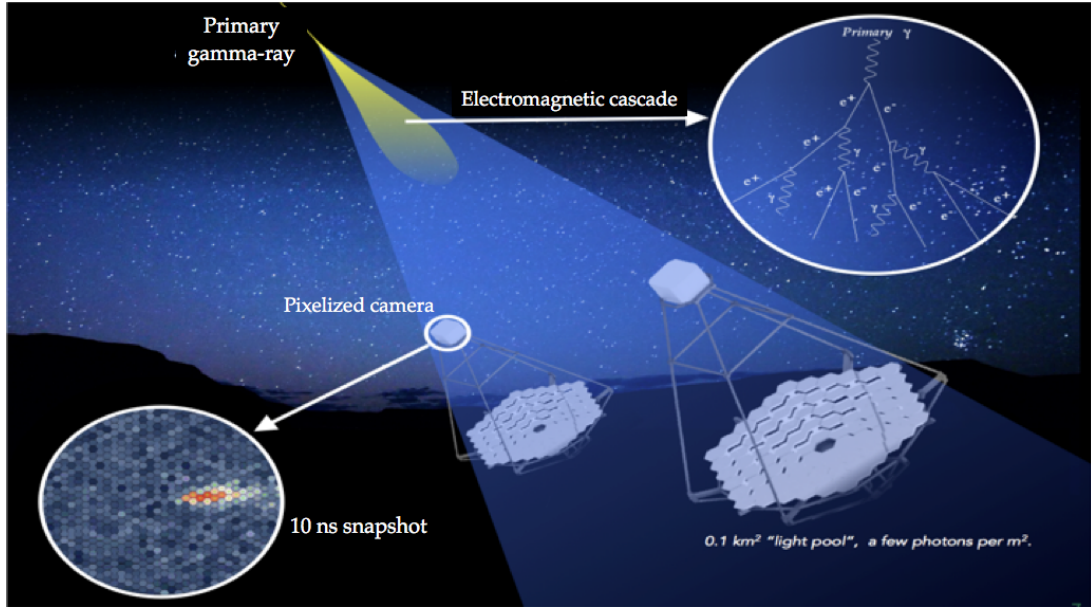


Figure 3.5: Schematic representation of the Imaging Air Cherenkov Technique. Image adapted from www.ctaobservatory.org

3.4 The MAGIC telescopes

The MAGIC telescopes are a stereoscopic system of two IACTs, located in El Roque de los Muchachos in the Canary island of La Palma, Spain. The construction of the first telescope (MAGIC I) was completed in 2004 and the second telescope (MAGIC II) was commissioned in 2009. Since 2009, they are operating in stereoscopic mode. The stereo system could achieve a sensitivity of $0.76 \pm 0.03\%$ of the Crab Nebula flux above 290 GeV for 50 hours of observation (Aleksić et al., 2012a) and energy threshold of 50 GeV for low zenith angle observations. The system underwent a major hardware upgrade between the summer of 2011-2012 (Aleksić et al., 2016b) which further improved the sensitivity to $0.66 \pm 0.03\%$ of the Crab Nebula flux above 220 GeV for 50 hours of observation. The data analyzed in this thesis were observed in stereoscopic mode after the upgrade. The MAGIC telescopes are equipped to observe under moon light conditions, which helps to increase the duty cycle compared to only dark night observations up to 40%. This allows for a better time coverage which can be crucial especially to study transient events such as flares from active galactic nuclei, gamma-ray bursts or neutrino and gravitational wave follow-up observations.

3.4.1 Brief description of hardware, trigger and readout system

The hardware of both MAGIC I and II can be considered identical and consists of three main components - a supporting structure, a reflector and a camera. An image of the MAGIC telescopes is shown in Fig. 3.6.

The telescope structure is rigid and light-weight (less than 20 tons) made of carbon fiber, enabling fast movement of the telescopes especially important for prompt follow-up observations of transient γ -ray sources such as GRBs. The structure holds the reflector dish, the camera and the drive system that moves the telescopes. The effect of gravitational loading on the structure is corrected by means of an active mirror control (AMC) that adjusts the mirrors in the reflector dish according to the zenith angle of pointing and a CCD camera known as Starguider which uses the number of stars in the field of view as reference to monitor the pointing accuracy. The focusing of the mirrors by the AMC helps to reduce the aberration in the shower image, by adjusting each mirror after every repositioning of the telescopes.

The large reflector dish has a parabolic shape and a diameter of 17 m. To increase the photon collection statistics, the reflector has a Davis-Cotton design (Davies and Cotton, 1957), where its radius of curvature is equal to the focal length. The advantage of the parabolic mirror surface is that the time spread for the asynchronous



Figure 3.6: The MAGIC telescopes. Images credit: Daniel López

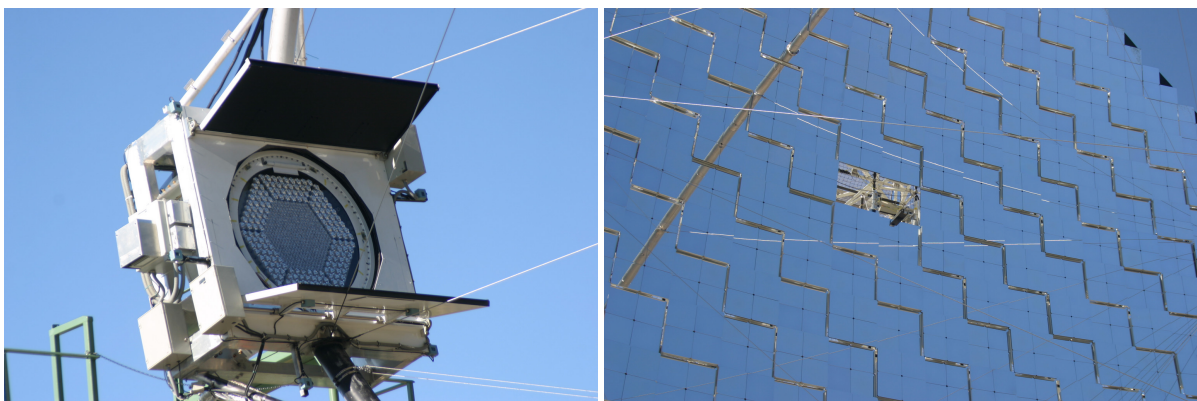


Figure 3.7: Left panel: An image of one of the MAGIC cameras. Right panel: An image of the MAGIC I mirror panels. Images taken from <https://magic.mpp.mpg.de/>.

photon pulses is negligible compared to time spread of Cherenkov pulses and as a result no significant broadening of the image is introduced. The point spread function (PSF), defined as the 39% containment radius of a reflected spot in the focal plane of the mirror for a point-like source, is less than 10 mm. As an example, the image of the reflector surface of the MAGIC I telescope is shown in Fig. 3.7 (right panel).

The MAGIC cameras are composed of 1039 high quantum efficiency (QE), low gain and UV-sensitive PMTs, each coupled to a light collector called Winston cone to increase the collection efficiency. Each camera has a total field of view of (FoV) of 3.5° . The anode current flowing through the PMTs is proportional to the NSB level. Hence the low-gain configuration is specifically designed to reduce the amount of charge hitting the anode and thus prevent fast-ageing of the PMTs, which can happen during bright NSB conditions such as moon light. This also helps in increasing the duty cycle of observations, which ideally should be done under dark conditions. For observations under moderate moon light, the gain of the PMTs can be reduced by a factor of 1.7 (reduced HV settings; (Chmill et al., 2017)). For higher moon levels UV-pass filters are used in the MAGIC cameras (since the PMT gain cannot be decreased indefinitely as it reduces the collection efficiency). For more details regarding MAGIC observations under moon light, see Ahnen et al. (2017). The signals recorded by the PMTs are converted into optical pulses by means of vertical-cavity surface-emitting lasers (VCSELs) and sent to the counting house (CH) via fiber optic cables. In the CH, the analog signal is converted into digital signal. The receiver boards convert the optical pulses into electronic ones via photodiodes and splits the signal into two - one for the readout system and other for the trigger system.

The trigger and readout system

The standard MAGIC trigger system consists of three levels. The first level (L0) is an amplitude discriminator that operates on individual PMTs and only accepts pixels with charge above a certain threshold. All the pixels that are chosen by the L0 level are then sent to the L1 level. At L1 level, the trigger system operating on individual telescopes search for time-coincident L0 triggers above a certain boundary threshold for a minimum number of neighbouring pixels (usually 3). The pixels that are accepted by the L1 trigger are then sent to the L3 level where the system looks for time coincidence of the L1 triggers from each telescope (Paoletti et al., 2008). Since the two MAGIC telescopes are roughly 80 m apart, the shower front reaches them at different times. Thus the L1 trigger signals are delayed by an amount depending on the pointing direction of the telescopes, which allows a coincidence window of width 100 ns.

The trigger rate depends on the discriminator threshold (DT) set at the L0 level for each PMT. The DTs are controlled by the Individual Pixel Rate Control (IPRC) software which tries to keep a stable L0 rate for each pixel within a desired limit. The limits are so chosen in order to keep a low energy threshold and to keep the trigger rates at a level which can be handled by the data acquisition system (DAQ). If the trigger rate of an individual pixel goes temporarily out of these limits, the IPRC adjusts the DT immediately until the rates are back within the desired range. When a lot of accidental triggers are induced into the camera, especially during observations under moon, the DTs are increased by the IPRC leading to an increase of the trigger-level energy threshold (Ahnen et al., 2017).

The MAGIC telescopes also have two alternative trigger systems to improve the performance at the lowest energies, namely the Sum Trigger (García et al., 2014) and Topo Trigger (López-Coto et al., 2016). Since they were not used for the work done in this thesis, the reader is referred to the given references for more details about these trigger systems.

The readout of both the MAGIC telescopes consists of a Domino Ring Sampler version 4 (DRS4) analog memory chip. The analog signal from the receiver boards is connected to an array of 1024 capacitors, which are charged by the signal up to a time proportional to the period of a clock (Domino wave). When the trigger conditions are fulfilled, the clock stops and the charge accumulated by some of the capacitors is digitized by means of an Analog-to-Digital Converter (ADC). The signal in each pixel is recorded into a 30 ns waveform (the so-called DAQ window) in the form of raw ADC counts. In between two events, the readout system of MAGIC I has a dead time of 25 μs and that of MAGIC II has a dead time of 27 μs (Bitossi, 2009).

3.4.2 Data-taking procedure

Data acquisition

During each observation night of the MAGIC telescopes, different kinds of data are collected: pedestal run, pedestal subtraction run, calibration runs and the actual data runs. The purpose of the pedestal run is to record the number of background events caused by the NSB, the detector and electronic noise which are later subtracted during data calibration. The baseline of the capacitors in the readout system are calibrated by means of an additional measurement once per night, known as the pedestal subtraction run. After the pedestal run, artificial light pulses from the calibration box are used to illuminate the camera uniformly and the triggered events are recorded, for the purpose of the calibration run. The calibration run is mainly performed to calculate the conversion factor from digital counts into number of photo-electrons. After these special runs, the actual data run begins. The data runs are typically of 15-20 minutes duration and divided into a number of sub-runs. During the data run, the events are triggered by the three-step digital system described in Sec. 3.4.1. In addition to the pedestal and calibration runs taken at the beginning of each source observation, interleaved pedestal and calibration events are recorded in between the data acquisition at a rate of 25 Hz to monitor the detector and electronic noise changes within short time scales.

Observational pointing mode

The default pointing mode for MAGIC observations is the so-called *wobble* mode (shown in Fig. 3.8). In this mode each telescope tracks a sky position which is 0.4° away from the celestial coordinates of the source. After the end of each data run, the telescopes change the wobble position to a new location same distance away from the source. This is done to eliminate possible inhomogeneities in the camera. For observations using two wobble positions, an OFF region is defined diametrically opposite to the position which the telescope is tracking (ON region) and the background is recorded simultaneously. It saves observation time since no dedicated OFF pointing is required for the background estimation. During background estimation, the number of OFF regions can be chosen from one to five (typically chosen three). More than one OFF regions help in better background estimation since systematic effects in the FoV and due to PMT response can be reduced. The schematic representation in Fig. 3.8 shows the observations using wobble mode with one (left) and three (right) OFF positions.

However this process has some drawbacks. Since the telescopes are pointed 0.4° away from the source, it decreases the γ -ray detection efficiency because some fraction of the electromagnetic cascades lie outside the trigger region of the camera. Moreover, since the background is evaluated from a different region of the camera (OFF regions) than the data, it can be affected by inhomogeneous response of the camera components (for e.g.: different levels of electronic noise and gain of the PMTs, dead pixels in parts of the camera etc.).

Apart from the wobble mode, MAGIC can also perform observations in the so-called ON/OFF mode (for more details, refer to [Fernández Barral \(2017\)](#)), where it points directly to the source position. The background data is taken during a separate OFF pointing, from a region without any γ -ray source. The data that is analyzed in this thesis, were taken using the wobble mode.

3.4.3 Data analysis chain

The standard data analysis chain for MAGIC is known as Magic Analysis and Reconstruction Software (MARS) ([Zanin, 2013](#)). The software extracts the charge and timing information of every pixel, separates the γ -like events from the hadron-initiated events and reconstructs the energy and arrival direction of the primary particle. In the following subsections a brief description of the analysis software is given starting from the calibration of the raw events up to the high level analysis to produce spectra and light curves. A part of the data analyzed for this thesis were taken under moon light conditions. In subsection 3.4.5 a short description is given of the special adaptations required for such an analysis.

Signal extraction and calibration

The very first step of the data analysis is to extract the raw ADC counts from the 30 ns waveform recorded by the DAQ. The data acquisition system stores the intensity of each individual pixel and the arrival time of the Cherenkov

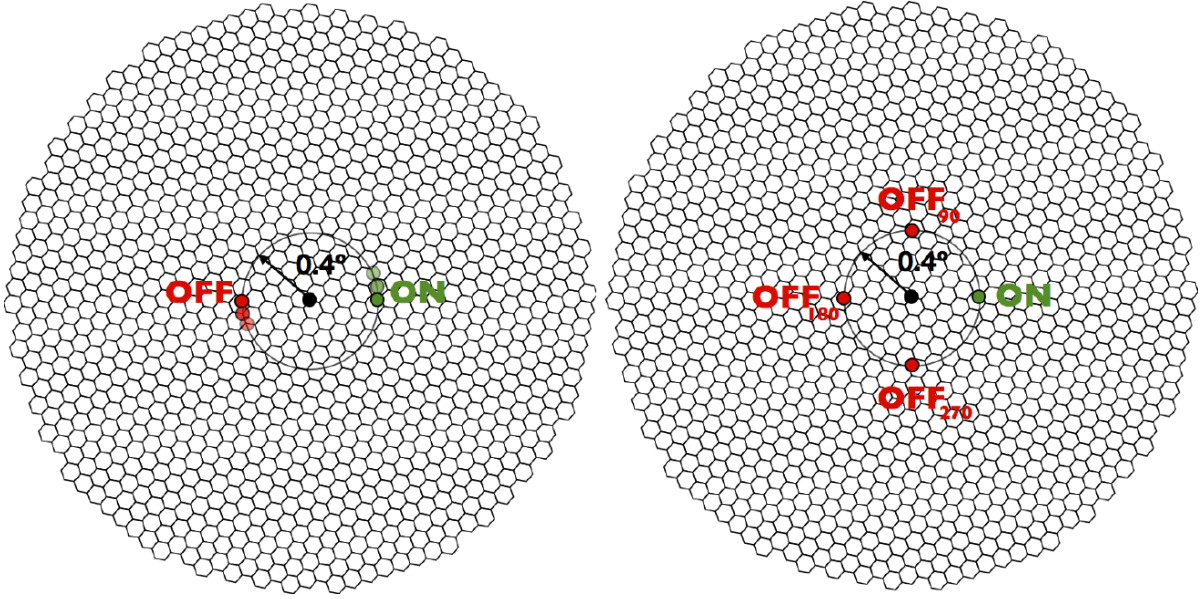


Figure 3.8: Schematic representation of the wobble mode of observation. The camera center (black dot) is located 0.4° away from the source (green dot). As the source moves in the camera plane it follows a circular trajectory. The OFF is calculated simultaneously to the data from a region / regions 0.4° at the same distance from the camera center as the source. The chosen number of OFF regions can be one (left panel) or three (right panel) and up to five. Figure taken from [López Coto \(2015\)](#).

light. The program which does this job is known as *Sorcerer* (Simple Outright Raw Calibration; Easy Reliable Extraction Routines).

First, the baseline of the capacitors in the readout system is estimated. For this purpose, a Gaussian fit is made to all the slices recorded during the pedestal run (the recorded events arise due to various noise processes) and the mean value is chosen for the baseline subtraction. The next step is charge extraction. For this purpose an algorithm looks for the largest integrated charge in the DAQ waveform by a sliding window of 3 ns. In absence of a genuine signal, the sliding window algorithm picks up the largest integrated noise fluctuation. Once the window containing the highest integrated charge distribution is found, the signal arrival time can be calculated as the mid-point of the window. After signal extraction, the raw ADC counts are converted into number of photo-electrons using the so-called F-factor method over the calibration runs ([Mirzoyan, 1997](#)). The calibration laser is assumed to generate a Poissonian distribution of the number of photo-electrons. The distribution of the calibration events is then parametrized in terms of the mean and standard deviation. The distribution of the observed pulses in the form of ADC counts can similarly be parametrized in terms of mean and standard deviation. Both the distributions can be connected by means of a conversion factor F, that can be measured in the laboratory and is different for each pixel. The ADC counts are then converted into the number of photo-electrons using the measured conversion factor. The program *Sorcerer* takes as input the DAQ waveform and provides the charge in photo-electrons and the arrival time as output for all the pixels, for every triggered event.

Image cleaning

After extracting the charge and arrival time for each individual pixel of the camera, the next step is cleaning the resultant image, to remove the pixels which do not contain useful information about the shower. The image is mostly dominated by noise i.e. events triggered purely by background fluctuations. Hence an image cleaning procedure is required to reduce the background contamination to the image and keep mostly the pixels that are most probably triggered by the γ -ray shower. Image cleaning is done in the MAGIC software by a program called *Star*. The standard image cleaning procedure is briefly stated below.

The pixels containing the events from γ -ray showers are often brighter than the pixels containing only noise.

Hence to choose the core pixels (i.e. the brightest pixels triggered by the γ -ray shower), first only the pixels which have a charge above a certain threshold Q_c are inspected. An additional criterion that is imposed during core pixel selection is that each core pixel should have a minimum number of other core pixels as neighbours (the number of neighbours can be two, three, four etc.). This is done in order to eliminate random pixels with high charge values which are not part of the shower. After the core pixel selection is complete, a set of boundary pixels (i.e. slightly dimmer pixels which still belong to the γ -ray shower) are chosen which should have a minimum charge above a second threshold Q_b and contain at least one core pixel as neighbour. The choices of Q_c and Q_b have to be optimized so that the background is suppressed and at the same time important information about the shower is retained. The cleaning thresholds cannot be too high since it results in an increase in the energy threshold at analysis level and loss of lower energy photons. At the same time a too low threshold implies a lot of noise fluctuations in the cleaned image. The typical and specially adapted values of the cleaning thresholds Q_c and Q_b for data taken under dark and moon light conditions respectively, are tabulated in Table 3.1 and discussed in subsection 3.4.5. In order to keep the energy threshold low, the program also uses the arrival time information of the pixels and combines it with the fact that the Cherenkov pulses last for a very short time (~ 3 ns) compared to the NSB photons. The arrival time of individual core pixels cannot be extremely different from the mean arrival time of all the core pixels. Hence a time window Δt_c is set and all pixels with arrival time outside this window are rejected. The boundary pixels also have to arrive within a time window of Δt_b compared to the core pixels. The timing thresholds used in MAGIC are $\Delta t_c = 4.5$ ns and $\Delta t_b = 1.5$ ns.

Hillas parametrization

The cleaned image from the γ -ray induced shower forms an elliptical shape in the plane of the camera. The next step of the analysis is to parametrize the image formed in the camera and reconstruct the shower parameters such as nature of the primary emitting particle, its energy and arrival direction. This step is also done by the program *Star*. In order to parametrize the shower image, an ellipse (the so-called Hillas ellipse) is fit to the surviving pixels after image cleaning and the moments of the ellipse (up to third order) are calculated, which are known as the Hillas parameters (Hillas, 1985). The author contributed to the Cherenkov shower image parametrization for the ctapipe software (a brief description is given in Appendix C). The software is being developed in Github and will be used for low-level data processing for the future generation Cherenkov Telescope Array (briefly described in Sec. 3.5).

The main Hillas parameters are shown in Fig. 3.9. A short description of each of the parameters are given below.

Source-independent parameters These parameters are independent of the position of the source.

- **Size:** Size is the sum of charge (in photo-electrons) of the surviving pixels in the image. It is related to the energy of the primary particle.
- **Center of gravity (c.o.g.):** It is the weighted mean of the X and Y coordinates of the shower image in the camera plane.
- **Length:** It is the length of the semi-major axis of the Hillas ellipse. Length is related to the longitudinal development profile of the shower.
- **Width:** It is the length of the semi-minor axis of the Hillas ellipse. Width is related to the lateral development profile of the shower.
- **Conc(N):** It is the fraction of charged contained in the N brightest pixels. In MAGIC the value of N is chosen to be 2. For electromagnetic showers the value of Conc(2) is much higher than for the hadronic showers.

Source-dependent parameters These parameters are dependent on the position of the source in the camera.

- **Dist:** Dist is the angular distance between the expected position of the source in the camera and c.o.g of the shower image.
- **Alpha:** Alpha is the angle between the major axis of the Hillas ellipse and the line connecting the expected source position in the camera to the c.o.g of the image.

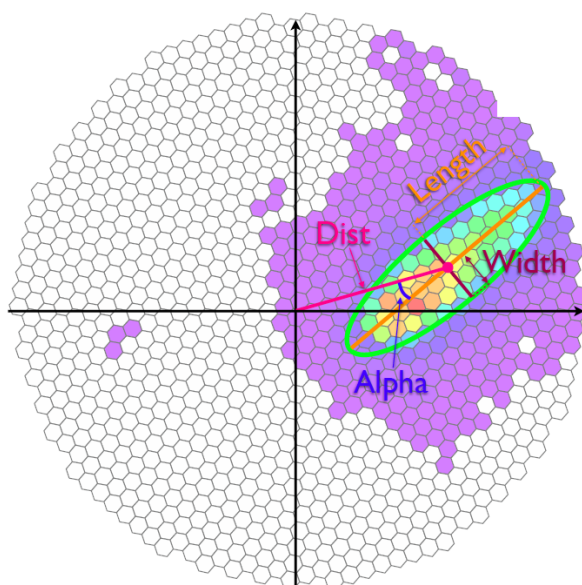


Figure 3.9: The Hillas ellipse fitted to the surviving pixels after image cleaning and a schematic view of the main Hillas parameters. For simplicity, the image represents an ON-mode observation where the source is expected to be at the center of the camera. Image taken from [Fernández Barral \(2017\)](#).

Timing parameters The timing parameters are very useful, especially to discriminate the electromagnetic showers from the hadronic showers due to the difference in their temporal development (~ 3 ns development time for electromagnetic showers compared to ~ 10 ns for hadronic showers).

- **TimeRMS:** It is the RMS of the time of arrival for the surviving pixels after image cleaning.
- **Time gradient:** It is the slope of a linear fit to the projection of the arrival times of the pixels along the major axis of the Hillas ellipse.

Directional parameters These parameters are essential to infer the head (corresponds to the point of origin of the EAS) and the tail (corresponds to the bottom part of the EAS) of the shower.

- **Asymmetry:** It gives the sign of the direction between the image c.o.g and the brightest pixel (pixel with the highest charge). The brightest pixel should be located close to the head of the image since particles at the top of the shower have higher energies.
- **M3Long:** It is the third moment of the Hillas ellipse fit and has the same sign as the asymmetry parameter.

Stereoscopic parameters

Up to this point, the data collected by each telescope are treated individually. At the stereoscopic reconstruction level, the individual telescope parameters are merged to obtain the stereo parameters by a program called *Superstar*. For the standard MAGIC analysis chain, the image cleaning and the Hillas parametrization for each telescope is done by the on-site analysis i.e. the analysis done on the MAGIC site immediately after the data-taking ([Fidalgo et al., 2016](#)) (note however, that for moon data the image cleaning levels have to be tuned; see Sec. 3.4.5). The standard off-site analysis chain begins at the *Superstar* level. The main stereo parameters are described below and shown schematically Fig. 3.10, which allow a 3-dimensional reconstruction of the shower.

- **Shower axis:** The shower axis is calculated by the intersection method of two major axes of the Hillas ellipses from MAGIC I and II, combined with the information of the position and pointing of the telescope ([Aharonian et al. \(1997\)](#), [Hofmann et al. \(1999\)](#)). It gives the direction of the shower.

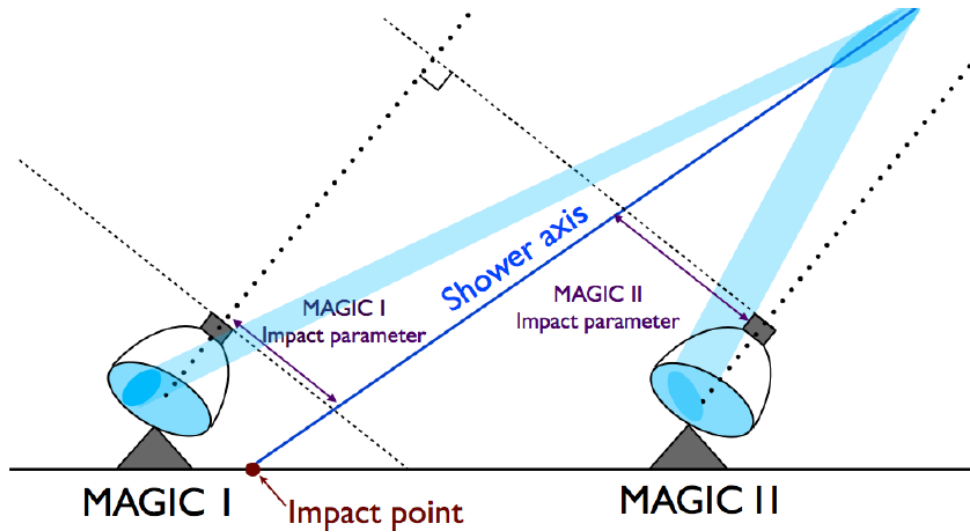


Figure 3.10: Schematic representation of the stereoscopic parameters. Image taken from [Guberman \(2018\)](#).

- **Impact parameter:** It corresponds to the distance between the shower axis and the pointing direction of the telescope.
- **Impact point:** It is the point in the ground where the shower axis hits.
- **Height of the shower maximum:** It is the height at which the number of particles in the EAS is maximal. This parameter strongly depends on the energy of the primary particle - a particle with higher energy penetrates deeper into the atmosphere and produces the maximum number of secondary particles closer to the telescope.

Data quality selection

The data from the Cherenkov showers can be affected by the weather conditions, technical problems or various unwanted noise (like a car flashing the MAGIC cameras during data-taking). In those cases the affected data can be rejected or in some cases corrected (such as data affected by clouds and dust).

Various auxiliary instruments to monitor the atmospheric conditions were installed in the MAGIC observation site. A weather station is installed at the roof of the counting house (from where the shifters operate the telescope), which continuously measures the typical atmospheric variables such as temperature, wind, gusts, humidity, pressure etc. Additionally an instrument called Pyrometer is installed at the dish of MAGIC I, which points parallel to the direction of observation. The Pyrometer measures the sky temperature. The presence of clouds or dust affect the atmospheric transparency and absorbs/scatters Cherenkov light causing a loss of photons. This leads to wrong energy and flux estimation of the shower. Hence monitoring the atmospheric transparency is crucial. If there are clouds present, it reflects the thermal radiation from Earth and a higher sky temperature is recorded by the Pyrometer. The *cloudiness* parameter is evaluated by comparing the sky temperature measured by Pyrometer with a reference sky temperature under good weather conditions.

The main instrument used by MAGIC to measure the atmospheric transparency is called Laser Imaging Detection And Ranging (LIDAR). The LIDAR shoots a laser and measures the back-scattered light from the atmosphere to estimate its transparency at different heights. If the transparency is not too low, the data can be corrected using the method described in [Fruck et al. \(2014\)](#). Also data taken under bad weather conditions can be rejected by placing a cut on the LIDAR transparency. In case the LIDAR data is not available (for e.g.: LIDAR cannot operate under high moon intensity), the Pyrometer data is used to evaluate the atmospheric transmission.

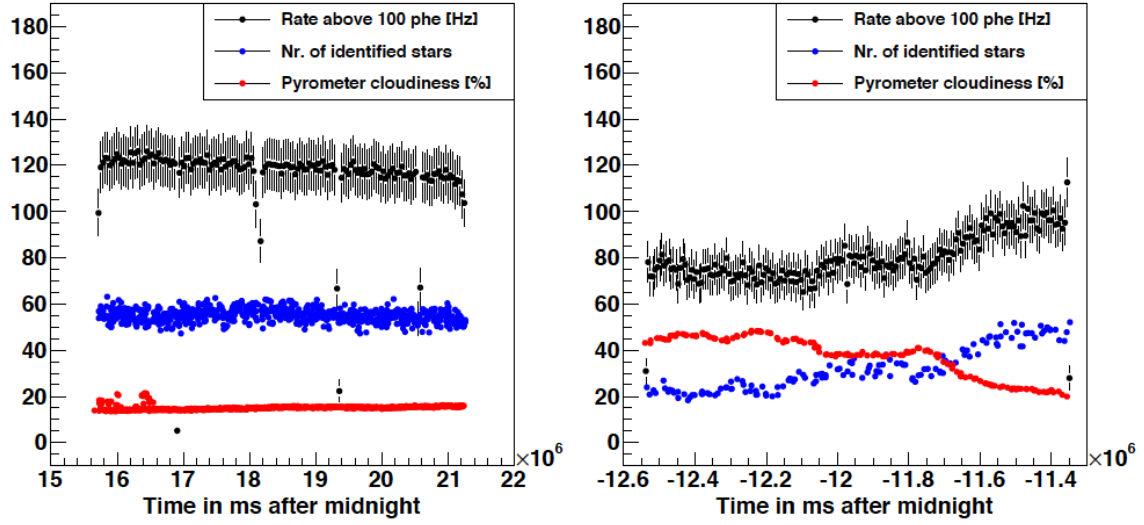


Figure 3.11: Dependence of the MAGIC data on weather conditions on the MAGIC site. Left: The measured event rates (black points) by MAGIC under good weather conditions, indicated by low "cloudiness" parameter (red) (obtained from Pyrometer) and high number of stars (obtained by the Starguider camera). Right (the color code is same): The measured events under bad weather conditions (resulting in low event rates, high clouds and low number of detected stars in the field of view). Image credit: [Glawion \(2014\)](#).

The trigger rates or the rate of events above a certain frequency (say 100 Hz) can be used to measure the stability of the atmospheric transparency. High rate fluctuations can indicate more noise level and such a data can be rejected by setting a range of acceptable event rates.

For visual inspection of the sky during data-taking, an All-Sky camera is mounted in the MAGIC site which takes long exposure images every 2 minutes. If there are clouds, it can be easily seen by the shifters on duty of data-taking from the All-sky image. Also the number of stars in the MAGIC field of view measured by the Starguider instrument can act as a complimentary method to detect the presence of clouds, by comparing the detected number of stars with a reference number of stars under dark and perfect weather conditions. Fig. 3.11 shows the dependence of the detected event rates by MAGIC on the weather conditions (indicated by the "cloudiness" parameter measured by Pyrometer and the detected number of stars measured by the Starguider camera). Apart from the transparency, data selection cuts can also be placed on the mean DC level which increases with the NSB, to reject data taken under high NSB. This can be useful to lower the analysis energy threshold.

Gamma-hadron separation, direction and energy reconstruction

At this step of the analysis a final background suppression to the data is performed and the arrival direction and energy of the primary particle is reconstructed. Algorithms such as Random Forests or Look-Up Tables (LUTS) are used for this purpose. In the MARS analysis chain, a program called *Coach* is used to train the Random Forests and build the LUTs.

In order to separate hadronic showers from γ -ray showers (the so-called gamma-hadron separation), multi-dimensional decision trees known as Random Forest are trained using a sample of Monte Carlo-generated γ rays and a sample of hadronic events. The Monte Carlo sample used for training the Random Forest has to be statistically independent of the sample that will be used later for flux estimation. Hence the total Monte Carlo sample is divided into two subsets - a train sample that is used to train the Random Forest and a test sample that is used to calculate the effective area and migration matrix. The hadronic sample is collected from real data itself. Hadronic event rates are always dominant over the γ -ray event rates. So any data where there has been no significant γ -ray detection can be used as a hadronic (or OFF) sample.

The Random Forest training begins with the entire sample of events, containing the Monte Carlo γ rays and hadronic background events. A set of pre-selected parameters (such as image length, width, arrival time etc) are

used to discriminate γ rays and hadrons. The algorithm starts by splitting the total number of events into two sub-samples, γ rays and hadrons based on optimized cuts on a randomly selected parameter. The cut optimization is done by minimization of the Gini coefficient (for more details, please see [Gini \(1921\)](#)). The separation into gammas and hadrons continues for each sub-sample depending on a new randomly selected parameter at each step, until one of the branches contains only γ rays or hadrons. The training of the Random Forest grows up to 100 trees.

The trained Random Forest is applied to the real data by a program called *Melibea*. Each event in the real data sample has to pass through all the decision trees of the trained Random Forest, which help to classify it as a γ ray or a hadron. After an event has gone through all the decision trees, it is assigned a value called *hadronness*, which gives a measure of how likely it is that the event is hadron-like. The value of *hadronness* lies between 0 and 1: 0 indicates that the event is γ -like and 1 indicates that the event is hadron-like. The final background rejection is done by placing a cut on the *hadronness* parameter.

For the direction reconstruction, the crossing of the shower major axes method can be used (for more details, see [Aharonian et al. \(1997\)](#), [Hofmann et al. \(1999\)](#)). However this method cannot work for small-sized or parallel images. For such cases the *DispRF* method ([Aleksić et al., 2010](#)) used in MAGIC can be more suitable. The major axis of the Hillas ellipse represents the incoming direction of the shower. Thus the source position should also lie in the major axis of the ellipse, at a certain distance (defined as a new parameter called *disp*) from the image c.o.g. Since the *disp* parameter for Monte Carlo γ rays is known, a Random Forest is trained in order to find a correlation between the *disp* value and a selected set of parameters. The trained Random Forest is then used to estimate the *disp* value of the real shower image. For each telescope image, there can be two different reconstructed positions on either side of the image along the shower axis (as shown in the left panel of [Fig. 3.12](#)). By combining the images from the two telescopes, there emerges four possibilities of the source position in the camera plane. In order to reconstruct the source direction, the angular distance between two pairs of positions is calculated for all possible pair combinations and the two closest pairs are chosen. The final reconstructed source position is the average of the two closest points, weighted with the number of pixels in each image. The stereo *disp* reconstruction method is schematically shown in [Fig. 3.12](#) (right panel).

For the energy estimation, LUTs are used. A LUT is built using Monte Carlo γ rays whose true energy is known. The LUT is filled with the true energy E_{true} and RMS of each event, binning them in size and impact parameter, for each of the two telescopes separately. The estimated energy (E_{est}) of an event is calculated by averaging the corresponding values of E_{true} for each image of both the telescopes, weighted by the RMS of each energy bin.

3.4.4 High level analysis

After the event reconstruction step, every event has been assigned a value of *hadronness*, a reconstructed energy and a reconstructed direction. In this section the high level analysis products are discussed, that is: evaluation of the signal significance, calculation of energy spectra and light curves for the source under investigation.

Signal detection

After the estimation of *hadronness*, energy and arrival direction of the shower, we can evaluate whether the data contains a signal. For this purpose, a program called *Odie* is used in the MARS analysis chain. The parameter θ is defined as the angular distance between the expected source position and the reconstructed source position for each event. If the events come from the direction of the observed source, the θ^2 distribution should be peaked near zero and any event located at larger values of θ^2 are most probably originating from background (unless the source is extended or there is an additional source in the observational field of view). For each such event a signal region is defined by placing a cut on θ^2 (which is a circle of radius θ surrounding the source position). Events inside the signal region (or ON region) are chosen after they survive a set of cuts in hadronness, size, estimated energy. These cuts are optimized to have the best sensitivity for the Crab Nebula observations, which is considered a standard candle in VHE γ -ray astronomy due to the high intensity and stability of its flux. To evaluate the amount of background inside the ON region, one or more OFF regions are defined (see [Sec. 3.4.2](#)). The OFF region is a circle of the same radius θ as the ON region but centred in a position of the camera where no γ -ray signals are expected. For N_{ON} number of ON events and N_{OFF} number of OFF events distributed amongst $1/\alpha$ number of

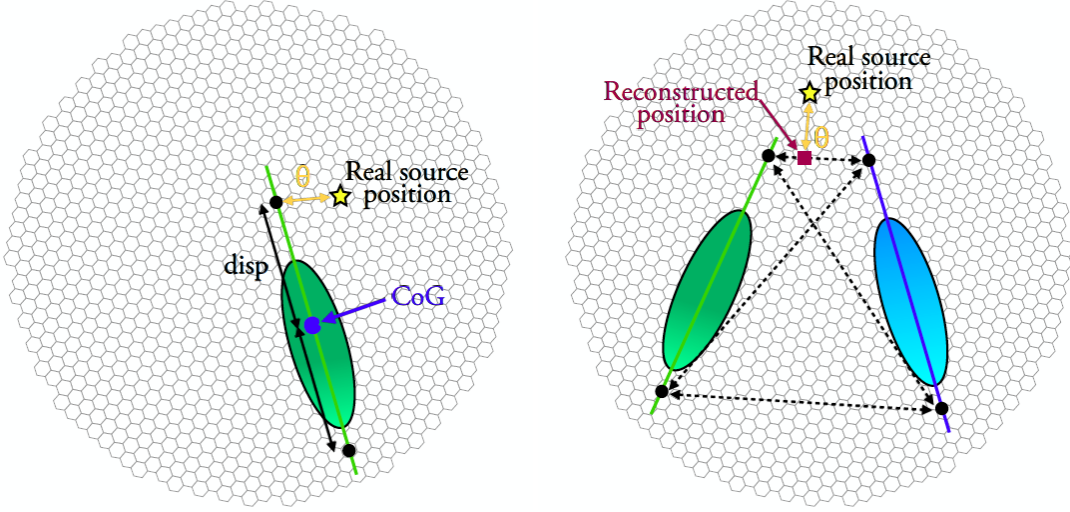


Figure 3.12: Left panel: The two possible reconstructed directions of a single telescope image estimated using the *disp* parameter. Right panel: All possible combinations of the distances between the different reconstructed source positions from images produced in both the telescopes. The closest distance is chosen and the reconstructed position is a weighted average of the two chosen positions. Figure taken from [Fernández Barral \(2017\)](#).

OFF positions, the excess is defined as

$$N_{ex} = N_{ON} - \alpha N_{OFF}$$

The significance of the signal is then evaluated using the formula given in Eq.17 of Li & Ma ([Li and Ma, 1983](#)). In Fig. 3.13, an example is shown for the θ^2 distribution of a sample of Crab Nebula data. The black shaded area represents the distribution of OFF events and the black points are the number of excess events. The defined signal region is shown by the black dotted line.

Effective collection area

Effective collection area is defined as the area of an equivalent instrument that could detect the same rate of γ rays as the real detector, with 100% efficiency. It is calculated using Monte Carlo simulations. Mathematically, for a total number of simulated γ rays N_{sim} falling within an area A_{coll} out of which N_{det} are detected, the effective collection area (energy-dependent) is defined as:

$$A_{eff}(E) = A_{coll} \times \frac{N_{det}}{N_{sim}}$$

The effective collection area is dependent on the energy of the incident Cherenkov light and the zenith angle of observations. The higher the energy of the primary particle, more the number of secondary particles it generates and hence higher the probability to get detected, thereby increasing the collection area. For a fixed energy above the threshold, the collection area increases with the zenith angle - showers are developed further from the telescopes and hence the Cherenkov light pool is larger. The effective collection area is also dependent on the azimuth angle, but the dependence is much less compared to the zenith angle or the energy of the γ rays (see the discussion in Sec. 5.2.1, Chapter 5).

Energy threshold

Energy threshold of an IACT is calculated from Monte Carlo-simulated γ rays. It is defined as the energy corresponding to the peak of the differential event rate. The differential event rate is obtained by multiplying the assumed source spectrum (usually assumed to be a power-law with spectral index 2.6) with the effective collection area as a function of energy. The threshold energy is obtained by fitting a Gaussian distribution around a narrow

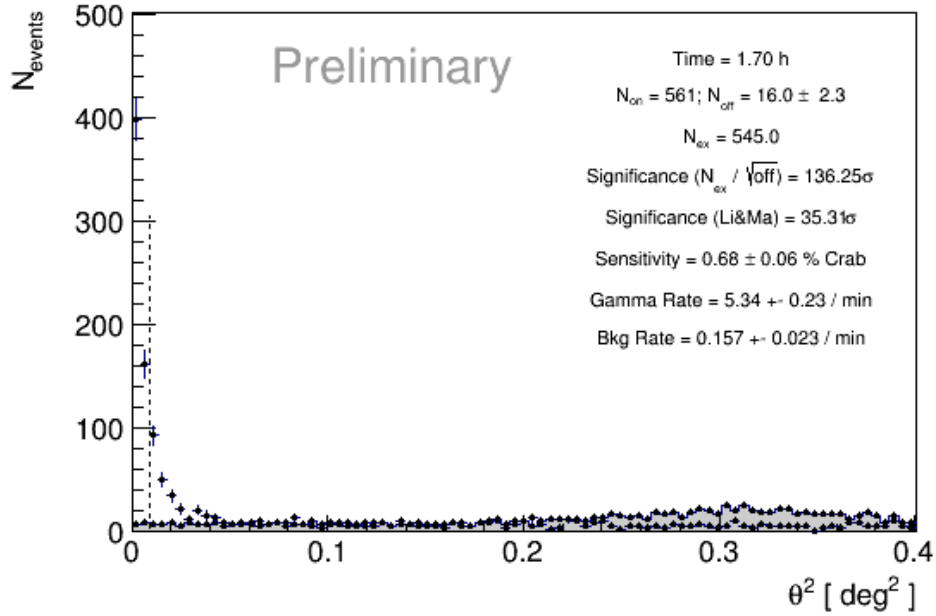


Figure 3.13: θ^2 distribution for a sample of Crab Nebula data amounting to effective observation time of 1.7 hours. The black points are the number of observed events and the gray shaded region show the expected background / OFF events, which are expected to be flat for different values of θ^2 . The region towards the left of the dotted horizontal line is defined as the signal region. The excess events are calculated from this signal region.

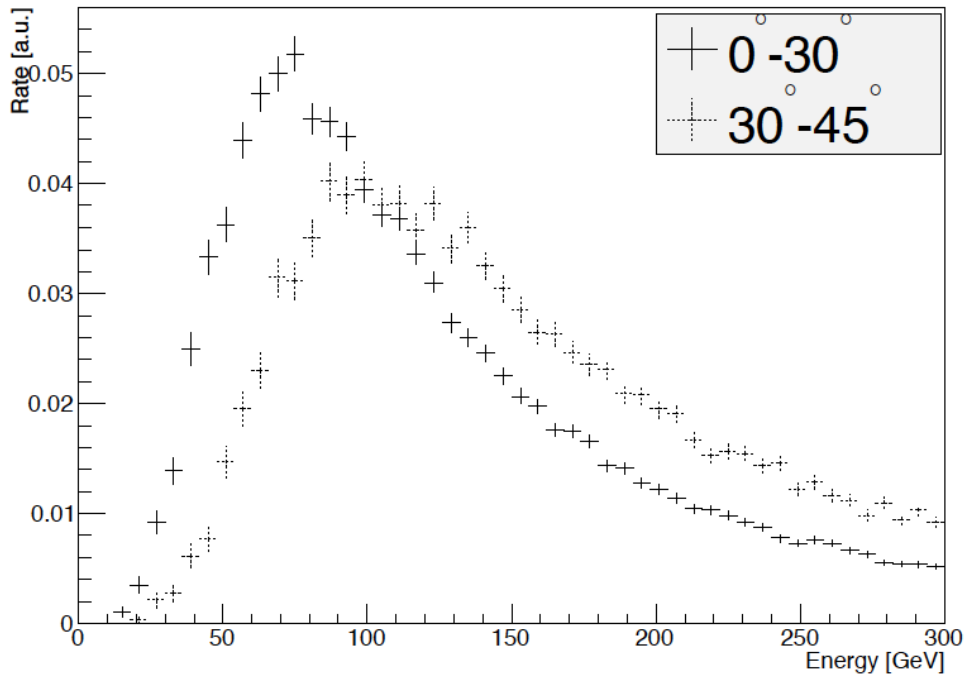


Figure 3.14: Dependence of the energy threshold (energy corresponding to the peak of the differential event rate) of MAGIC on the zenith angle of observations for a hypothetical source with spectral index -2.6 . Solid crosses: Zenith $0 - 30^\circ$. Dotted crosses: Zenith $30 - 45^\circ$. Image credit: [Aleksić et al. \(2016a\)](#).

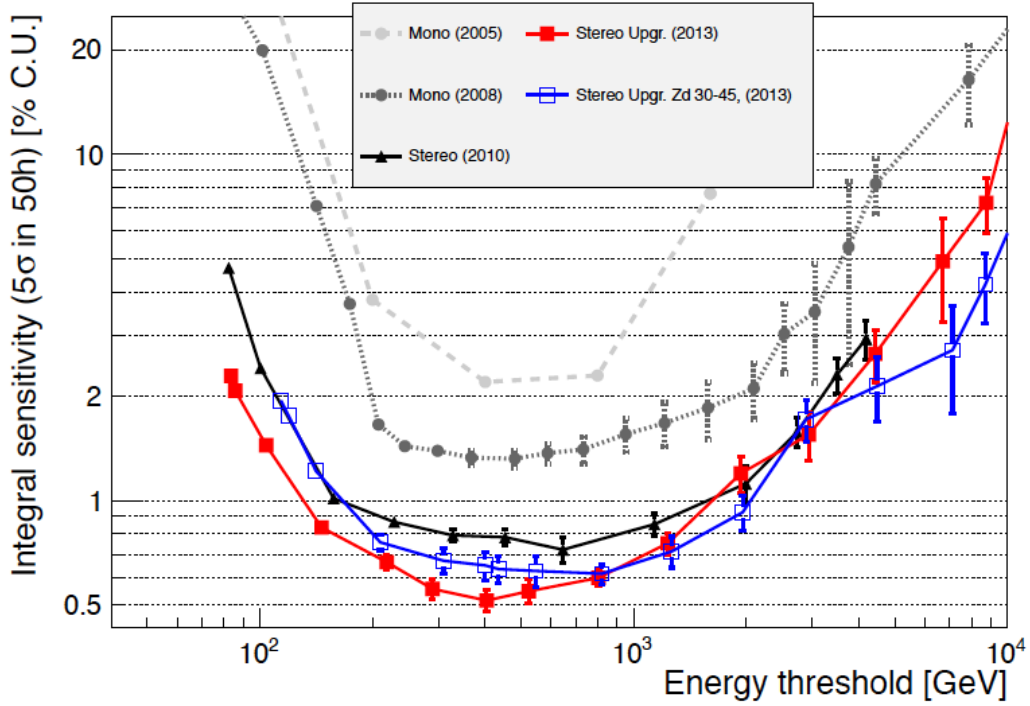


Figure 3.15: Sensitivity curves of MAGIC for low ($< 30^\circ$; red line) and medium ($30 - 45^\circ$; blue line) zenith angle. For comparison, the sensitivity of MAGIC before installation of the DRS4 readout (grey curve) and in single-telescope mode readouts (before 2009) are also shown. Image credit: [Aleksić et al. \(2016a\)](#)

energy range of the peak of the differential event rate. The energy threshold of an IACT increases with increasing zenith angle - at large zenith angles the low-energy photons are scattered or absorbed by the atmosphere enabling only the detection of comparatively higher energy photons. The dependence of the energy threshold on zenith can be seen from Fig. 3.14.

Energy threshold can be evaluated at different stages of the analysis- at the trigger level, or after the image cleaning and parametrization (reconstruction level) or after all the analysis cuts (analysis level). The lowest value is obviously obtained at the trigger level which can be as low as 50 GeV for MAGIC observations performed with the standard trigger configuration, under dark conditions for zenith angle below 30° . For observations using the Sum Trigger configuration, the energy threshold could be even lowered down to 30 GeV (for more details see [García et al. \(2014\)](#)).

Sensitivity

Sensitivity of the instrument is defined as the minimum flux that can be detected with a significance of 5σ in 50 hours of observation. For a certain observation, if the number of excess events is denoted by N_{ex} and the number of background events in the signal region obtained for a time t is denoted by N_{OFF} , then the significance for an observation time t_0 is defined as:

$$\sigma_{t_0} = \sqrt{\frac{t_0}{t}} \frac{N_{ex}}{\sqrt{N_{OFF}}}$$

Then the sensitivity can be evaluated in units of the Crab Nebula flux (C.U.) assuming the standard values of $t_0=50$ hours and $\sigma_{t_0}=5$ as:

$$S = \frac{5\sigma}{\sigma_{50}} \text{C.U.}$$

Two additional conditions are imposed: $N_{ex} > 10$ and $N_{ex} > 0.05N_{OFF}$. The first criterion ensure that one

can use a Gaussian approximation to the Poissonian event rate and the second condition is used to eliminate the possibility of mimicking a statistically significant signal if the residual background rate is large. The integral sensitivity is obtained by optimizing the analysis cuts that provide the best sensitivity above a certain energy threshold. The integral sensitivity curves of MAGIC for low ($< 30^\circ$) and medium zenith ($30 - 45^\circ$) angles, as function of energy are shown in Fig. 3.15.

The sensitivity at lower energies is higher for smaller zenith angles. At such energies the amount of Cherenkov light produced by the shower is low and hence the effect of atmospheric absorption starts becoming important. Showers developed at low zenith angles are less severely affected by atmospheric absorption compared to showers developed deeper into the atmosphere at high zenith angles. At higher energies the sensitivity increases for higher zenith angles mainly due to increase in the size of the Cherenkov light pool and hence increase in the effective collection area (see the section above).

Flux and spectrum

The gamma-ray differential energy spectrum per unit energy dE , per unit area dA , per unit time dt is defined as:

$$\frac{dF}{dE} = \frac{d^3N_\gamma}{dEdAdt}$$

where F denotes the γ ray flux and N_γ denotes the excess number of γ rays over the background for a given (estimated) energy bin after applying cuts in *hadronness* and θ^2 . The *hadronness* and θ^2 cuts are sometimes applied to achieve a desired efficiency of selecting Monte Carlo γ rays. First, the data are divided into certain number of small energy intervals and individual θ^2 distributions are built for each energy bin. The excess is calculated from the signal region of each θ^2 distribution and the background is estimated using one or more OFF positions (usually chosen three OFF regions), in the same way as described in Sec. 3.4.4. A program called *Flute* is used to calculate the spectrum.

A tentative spectrum of the Monte Carlo sample has to be assumed in *Flute* for the effective area calculation, which should be as close as possible to the original spectrum of the source. Since the intrinsic spectral shape of the source is not known a-priori, the program *Flute* has to be run multiple times until convergence is achieved. A better way to estimate the tentative source spectrum is to use another program called *Fold* (described below).

Another parameter required for the spectrum calculation is called effective on-time, which is defined as the total observation time minus the time for which the instrument was not ready to take data (dead time after each run during which the data acquisition system is busy and cannot accept any new events). Sometimes to get a better visual representation of spectral features like a cutoff or breaks, the spectral energy distribution (SED; $E^2 \times \frac{d\phi}{dE}$) is used instead of the differential spectrum.

Unfolding: In IACT observations, the observed events have an estimated energy but their true energy is not known. The number of γ rays are calculated in bins of estimated energy (E_{est}) but the effective area is calculated using Monte Carlo γ rays which are assigned a true energy (E_{true}). Most of the simulated γ rays do not even trigger the telescope and hence do not have an E_{est} . Hence if we divide the excess rates in bins of E_{est} by the collection area calculated in the corresponding bins of E_{true} , it would be affected by imperfect energy estimation. Events with E_{true} in the range $E_1 - E_2$ can have a reconstructed energy which lies outside $E_1 - E_2$. Similarly a reconstructed energy in the range $E_1 < E_{est} < E_2$ can have a corresponding true energy lying outside $E_1 - E_2$. This is known as "spillover" effect and hence unfolding is required for a proper energy estimation.

In MAGIC various unfolding methods are used as described in [Albert et al. \(2007c\)](#). For a proper transformation between the bins of E_{est} and E_{true} after taking into account the migration effects due to the limited acceptance and resolution of the detector, a *migration matrix* is calculated. Each element of the *migration matrix* M_{ij} thus maps a true energy in a true energy bin with a corresponding estimated energy in an estimated energy bin. The calculations are done by a chi-square minimization technique. The method usually gives unstable solutions, so a regularization is performed to smooth the solution. The strength of regularization needs to be controlled - too less regularization implies a solution that contains a lot of fluctuations while too much regularization smooths out essential features in the solution and the smoothed unfolded distribution can deviate from the data. At the end of the unfolding procedure a set of spectral points corresponding to the estimated energy bins are obtained.

Fold: The main purpose of the program *Fold* is to evaluate the spectral parameters of the source and their uncertainties. The spectral parameters obtained from *Fold* can be used as the tentative spectrum in *Flute* to calculate the effective collection area and obtain the integral flux of the source. The approach of *Fold* is different from the

unfolding which assumes Gaussian uncertainties for the excess events in bins of estimated energy. For bins with low statistics, the approximation of Gaussian uncertainties in the event excesses might not hold.

The inputs required by *Fold* are the ON and OFF histograms from *Flute*, effective time and the instrument response function of the telescope (effective collection area vs true energy for each estimated energy bin). For this method, a spectral model (for eg: power law, log parabola, power law with exponential cutoff etc.) with parameters $\theta = \theta_1, \theta_2, \dots, \theta_n$ has to be assumed. If a redshift is provided, the spectral shape is assumed to be intrinsic. For a given redshift and spectral function, *Fold* calculates the expected rate of gamma events in bins of estimated energy by using the instrument response. Then it converts the expected gamma rate into number of gammas by multiplying with the effective observation time. The obtained number of (expected) gammas vs estimated energy is then used to calculate the Poissonian likelihood of the assumed spectral model, given the ON and OFF events from the data. A minimizer samples the parameter space of the assumed spectral function to find the best fit spectral parameters and their uncertainties by maximizing the total likelihood.

Light curve

A light curve is defined as the plot of the integral flux in a certain energy range (say E_1 and E_2) as a function of time. It shows the flux variations over a period of time and can be very useful to detect fast variability of the source and high flux states (flaring states). For a given time interval $[T_1, T_2]$ the integral flux is defined as:

$$F = \int_{T_1}^{T_2} \int_{E_1}^{E_2} \frac{dN_{ex}(E)}{dEdAdt} dEdt$$

The number of excess events N_{ex} is calculated from a θ^2 distribution in the energy range $[E_1, E_2]$ for that time interval. For each time bin, the differential spectrum is computed for the excess events which is then integrated between a minimum and a maximum energy to build the light curve. The maximum energy is often set to $E_2 = \infty$. *Flute* is used to calculate the light curve for MAGIC observations. For time bins where no significant γ ray events were found, an upper limit (U.L.) is calculated following the method described in [Rolke et al. \(2006\)](#).

3.4.5 Moon-adapted analysis

During observations under moon light, the NSB level increases which introduces additional noise in the data. This causes a higher number of accidentally triggered pixels in the camera - the pixels triggered by background light effects. As a result, the trigger thresholds are changed to keep a reasonable trigger rate. Although not used in this thesis, for MAGIC observations under very intense moon conditions in general, the gain of the PMTs have to be reduced or a UV-pass filter must be applied. Thus due to different levels of noise fluctuations and different hardware settings, special moon-adapted analysis is required, which is described briefly in the section below. A measure of the NSB can be obtained indirectly from the mean DC of the cameras, which is directly proportional to the NSB level. Based on the NSB level, the data can be classified into different moon categories and a dedicated analysis has to be performed for each data set. All the data analyzed in this thesis has been taken with standard hardware settings i.e. by using nominal high voltage (HV). For more details about the analysis for reduced HV and UV-pass filter data, see [Ahnen et al. \(2017\)](#). The special steps and certain modifications in the analysis chain for the moon analysis, with respect to the standard analysis are stated below.

Signal extraction

As already mentioned before in Sec. 3.4.3, in absence of a signal the sliding window algorithm picks up the largest noise fluctuation. The main sources of backgrounds are the NSB fluctuations, the PMT afterpulses and electronic noise. The noise due to the NSB increases with the background light fluctuations. The PMT afterpulses are proportional to the PMT current which increases linearly with the NSB. Under nominal HV, the electronic noise is equal to the NSB fluctuations for observation of a dark extragalactic FoV with no bright stars. For dark Crab Nebula observations, the NSB level (abbreviated as NSB_{dark}) is already 60% higher than a dark extragalactic FoV and thus the NSB-induced noise already dominates over the electronic noise.

During moon light observations with nominal HV settings, the noise due to NSB increases while the electronic noise remains the same. Hence NSB is the most dominant source of noise. The pedestal charge distribution for randomly triggered events without signal can be used to measure the mean noise and its RMS. The pedestal

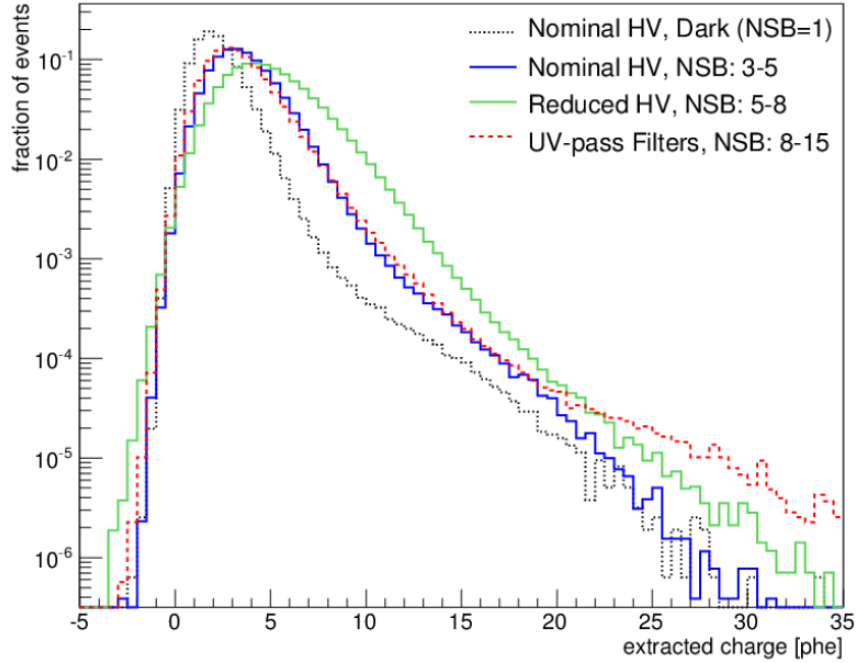


Figure 3.16: Distribution of the pedestal events for dark (black histogram) and different moon (colored histograms) levels. During moon observation, the NSB increases and as a result the pedestal mean and RMS also increases. The PMT after-pulse tail is also enlarged for large charge values. Credit: [Ahnen et al. \(2017\)](#).

Table 3.1: Typical NSB levels during MAGIC observations under different sky brightness and the adopted cleaning levels. Reference: [Ahnen et al. \(2017\)](#).

Sky brightness ($\times \text{NSB}_{\text{dark}}$)	Hardware settings	Pedestal dist. mean / rms (phe)	Cleaning levels Q_c / Q_b (phe)	Size cut (phe)
1 (Dark)	nominal HV	2.0 / 1.0	6.0 / 3.5	50
1-2	nominal HV	2.5 / 1.2	6.0 / 3.5	60
2-3	nominal HV	3.0 / 1.3	7.0 / 4.5	80
3-5	nominal HV	3.6 / 1.5	8.0 / 5.0	110

distribution is asymmetric with a tail at large charge values that is produced by the PMT after pulses. Compared to the observations under dark conditions, the moon level increases the mean noise and its RMS in the pedestal charge distribution with increasing sky brightness. Also the after-pulse tail gets enlarged with increasing NSB. This effect is shown in Fig. 3.16, where the black histogram denotes the pedestal distribution during dark observations and the coloured ones during moon observations.

The typical pedestal distribution mean and RMS for different NSB contributions (under nominal HV settings) are summarized in Table 3.1. A broad pedestal charge distribution affects the real Cherenkov signal. If the signal is weak, the noise fluctuations can be larger than the Cherenkov signal and the sliding window can select the wrong slice. The pulse arrival time is then random and the signal is lost. In case of strong signals, the sliding window can pick up the correct slice, but the signal arrival time and signal amplitude might be less precise.

Image cleaning

During moon light observations, the background fluctuations are higher than under dark conditions. Hence the image cleaning thresholds at the *Star* level has to be increased compared to the analysis of data taken under a dark night sky. The higher cleaning thresholds used for different NSB levels are shown in Table 3.1. For more details

regarding the required cleaning levels and pedestal distribution for different hardware configurations, please see [Ahnen et al. \(2017\)](#).

The cleaning levels of the Monte Carlo and OFF samples has to be the same as the data. During moon light observations, the NSB level changes continuously and it is practically impossible to fine-tune the cleaning levels for every NSB fluctuation. Hence broad NSB bins are defined where the fluctuations are considered to produce the same effect. The process of adapting the Monte Carlo and OFF data for moon light observations is described in the next subsection.

Adapting the Monte Carlo and OFF data

The Monte Carlo simulations are produced for dark observations. The OFF data is generally chosen by the analyzer once at the beginning of the observation period and the data are mostly taken under dark conditions. During moon observations the simulations and the OFF event sample have to be adapted to match the moon level of the data. During high sky brightness for moon observations, the accidental trigger rates increase and the IPRC constantly react by changing the DTs to keep a reasonable value of the trigger rates. Hence the main effects of moon observations on the Monte Carlo and the dark OFF data are the change in the DT by the IPRC and change in the noise level compared to dark conditions

The noise level of the data (mean and RMS) can be computed from the interleaved pedestal events randomly triggered between the observations (see [Sec.3.4.2](#)). Using these values, artificial noise is added to the simulations to mimic the effect of increased NSB for each of the NSB bins described in [Table 3.1](#). The noise is added after the calibration, at the pixel level before image cleaning. The same is done for the OFF data. As an alternative one can search for OFF data taken under the same sky brightness as the data. But due to constantly changing NSB level and in order to achieve a good event statistics in the OFF sample this method is often practically unfeasible and adding artificial noise provides an easier and efficient solution. After adding noise, an image cleaning is performed with the same cleaning thresholds as the data.

The effect of the changing trigger threshold due to the changing DTs controlled by the IPRC are not simulated. Instead, the simulations and OFF data produced with dark DTs are used and a cut in the image size is made after the image cleaning, which acts as a software trigger. The cut is optimized bin-wise as the minimal size to ensure data-Monte Carlo matching. The cuts in size for each moon level (under nominal HV hardware configuration) are described in [Table 3.1](#). Even in absence of moon light a cut in the image size is made, since images with too small size are either difficult to reconstruct or difficult to separate from the hadronic background.

3.4.6 Systematic uncertainties

IACT observations are affected by various systematic uncertainties which can influence the calculation of the energy spectra and light curves. The main sources of systematic uncertainties that can affect the MAGIC data analyzed in this thesis are discussed below. For more details, the reader is referred to [Aleksić et al. \(2012a\)](#).

- **Effect of the atmospheric variations:** The Monte Carlo simulations used for the MAGIC analysis uses the *MagicWinter* atmospheric model, which does not take into account the nightly and season-wise variations of temperature, humidity and atmospheric transmission. This causes a systematic error in the estimation of γ -ray energy of $\leq 10\%$.
- **Night sky background:** The higher NSB levels during an observation (for e.g.: during moon time) can produce a systematic error of $< 4\%$ on the γ -ray collection efficiency at low energies (~ 100 GeV). This is caused by decrease in the precision of the Hillas parameter estimation due to larger induced signal fluctuations. At higher energies above 300 GeV, the systematic effect is negligible ($< 1\%$).
- **PMT performance and flat-fielding:** The PMTs can introduce additional systematic errors to the energy scale due to uncertainties in the light collection efficiency of the Winston cone ($\sim 4\%$), electron collection efficiency of the first PMT dynode ($\sim 5\%$), quantum efficiency of the PMTs ($\sim 4\%$) and the F-factor values used to convert photons into number of photo-electrons ($\sim 10\%$). Muon calibration ([Pühlhofer et al., 2003](#)) and inter-telescope cross-calibration methods are used to eliminate most of the errors related to photon to photo-electron conversion. The PMT gains are temperature-dependent which introduces an additional 2% systematic uncertainty. The flat-fielding procedure applied in order to make the PMT gains uniform is done

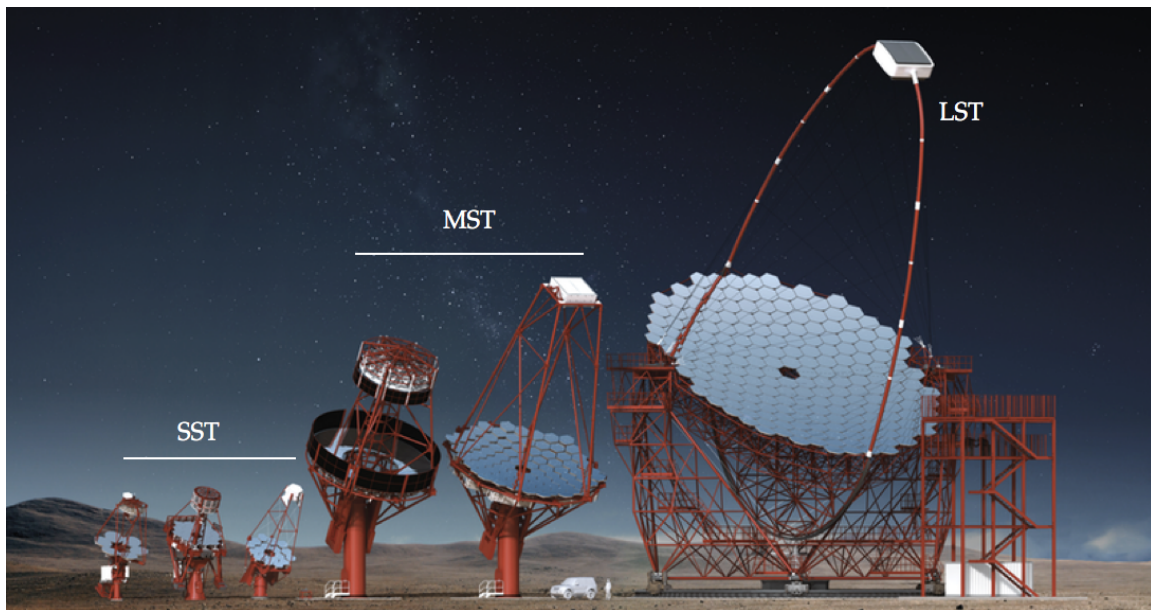


Figure 3.17: Design of the three prototype telescopes of CTA. From left to right: the SSTs, the MSTs and the LST. Image adapted from <https://www.cta-observatory.org/>.

using only one wavelength of the calibration pulser and it is temperature-dependent as well. This produces a $\sim 6 - 8\%$ error to the energy scale at lower energies ($E \sim 100$ GeV) and $\leq 2\%$ error at energies above 300 GeV.

- **Monte Carlo-data mismatch:** Differences in the simulated Monte Carlo γ rays and the real data can lead to an uncertainty in the γ -hadron separation. The Monte Carlo-data mismatch can produce a systematic error on the estimated flux level up to 10 – 15%.
- **Mirror reflectivity:** Due to deposition of dust on the mirror surface or due to misaligned mirrors at the beginning of the observations (mirror alignment is done by the observers on duty at the MAGIC site before every observation night), the amount of light focused by the mirrors can vary between different observation periods. This introduces a systematic error in the estimated γ -ray energy of $\sim 8\%$.
- **Telescope mispointing:** If the two MAGIC telescopes are pointed in slightly different sky positions, the reconstructed stereo image parameters loose precision. The typical mispointing of individual telescopes is $\leq 0.02^\circ$, which leads to a systematic error in the γ -ray efficiency of $\sim 4\%$.
- **Total systematic uncertainty:** Taking into account all the systematic uncertainties related to γ -ray measurements with the MAGIC telescopes, the total uncertainty can be estimated for low ($E \leq 100$ GeV) and medium ($E \geq 300$ GeV) energies. The systematic error in the energy scale for low energies is about 17% and for medium energies is about 15%. The slope of the energy spectra has a systematic uncertainty of about 0.15. The flux normalization can be estimated with a precision of about 19% for low energies and 11% for medium energies.

3.5 Cherenkov Telescope Array

CTA is the future generation ground-based IACT system designed to observe γ rays at very high energies. It will consist of more than 100 telescopes with a large collection area distributed in the northern hemisphere (known as the CTA North array, located in El Roque de los Muchachos, La Palma) and southern hemisphere (known as CTA South array, located in the Paranal Observatory, Chile). The northern and southern sites will together

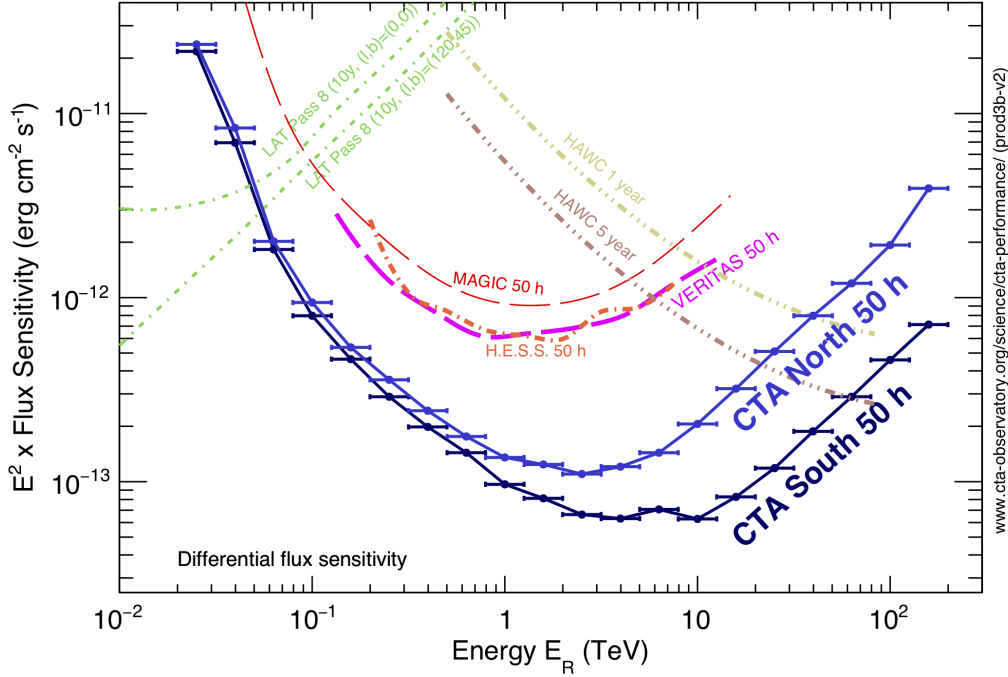


Figure 3.18: Differential flux sensitivity of CTA North (blue line) and CTA South (black line) for 50 hours of observation in comparison with the current generation of γ -ray instruments. Image taken from <https://www.cta-observatory.org/>.

constitute the CTA Observatory (CTAO). Three types of IACTs of different sizes will be used for the array: Large Size Telescopes (LSTs), Medium Size Telescopes (MSTs) and Small Size Telescopes (SSTs) (descriptions given below). The prototype designs of the three telescope types are shown in Fig. 3.17. CTA will be the world's largest and most sensitive open γ -ray observatory that will offer a substantial improvement in performance compared to the current generation of IACTs. It will cover a wide energy range from 20 GeV up to 300 TeV. The angular resolution of CTA is expected to reach $< 0.1^\circ$ for most energies, with an energy resolution of $\sim 10\%$. The sensitivity to detect VHE γ rays will improve by about one order of magnitude compared to the current generation of instruments (see Fig. 3.18). For more details, the reader is referred to <https://www.cta-observatory.org/>.

3.5.1 Types of IACTs in the CTA array

A brief description of the three types of IACTs that will constitute the CTA are described below.

- **LST:** The LSTs will have large parabolic reflectors with a diameter of 23 m and focal length of 28 m. The LST camera will provide a total FoV of 4.3° . They are designed to achieve the lowest energy threshold, down to 20 GeV. The telescope structure will be light-weight made of carbon fiber, designed to achieve fast movement in order to study γ -ray transients such as GRBs, AGN flares and galactic transients. The CTA baseline design includes 4 LSTs in each hemisphere. The first prototype LST telescope was inaugurated in the northern array site on 10 October, 2018 (press release information: https://www.cta-observatory.org/lst-1_inauguration/).
- **MST:** There are currently two MST prototype designs: one with a modified Davies-Cotton reflector having a diameter of 11.5 m and focal length of 16 m and another one with a dual mirror optical system called Schwarzschild-Couder Telescope with primary reflector diameter of 9.7 m and secondary reflector diameter of 5.4 m. A prototype Schwarzschild-Couder Telescope (pSCT), first of its kind in the history of γ -ray Cherenkov telescopes was inaugurated on 17th January, 2019 in the Whipple Observatory, Arizona. Three

different pixelized cameras are designed for the MSTs: FlashCam, NectarCam, SCT and each have a FoV of about 7.6° . The CTA baseline design have 15 MSTs in the northern site and 25 MSTs in the southern site. The MSTs will offer best sensitivity in the energy range 150 GeV to 5 TeV.

- **SST:** The SSTs will be located in the outer parts of the array and their main purpose would be to increase the sensitivity of CTA to the highest energies from about 5 TeV up to 300 TeV. A total of 70 SSTs will be installed in the southern array according to the planned baseline. Three different prototypes were tested: one single mirror telescope (SST-1M) and two dual mirror systems (SST-2M ASTRI and SST-2M GCT). Each of them have a primary reflector diameter of about 4 m and FoV of about $8.3\text{--}10^\circ$. Currently there are efforts to unify the design.

3.5.2 The CTA Key Science Projects

The core science programs of the CTA are known as the Key Science Projects (KSPs). The KSPs are developed by the members of the CTA Consortium along with substantial inputs from various external scientists and the programs will be updated as the observatory moves closer to its operational phase. A brief description of some of the proposed CTA KSPs is given below and for more details, the reader is referred to [CTA Consortium et al. \(2019\)](#).

- **Galactic Plane Survey and cosmic PeVatron search:** One of the long-standing questions in the field of Astroparticle Physics is to identify the sources of high-energy cosmic rays accelerated to PeV energies (PeVatron sources). SNRs are considered to be good cosmic PeVatron candidates. However their energy spectra extend up to 10 TeV and no convincing evidence of a cosmic PeVatron candidate has been found yet. The CTA will survey the entire Galactic plane with high sensitivity and angular resolution to identify bright sources whose spectra extend up to 100 TeV. The observatory will then perform deep observations of the detected objects in order to identify a cosmic-ray PeVatron.
- **Extragalactic Survey:** The CTA will observe a large portion of the extragalactic γ -ray sky with a high sensitivity (0.6% of the Crab Nebula flux, our standard candle) in order to get a better understanding of AGNs, determine their luminosity function, discover VHE γ -ray emission from as yet unidentified extragalactic objects and detect transient objects such as GRBs, flares from AGNs, high-energy neutrino sources following prompt alerts etc. There is also a separate Transient KSP for CTA (see [CTA Consortium et al. \(2019\)](#) for more details). Both the northern and southern observatories will take part in the extragalactic survey.
- **Indirect search for Dark Matter:** CTA will search for indirect signatures of dark matter through annihilation or decay of Weakly Interacting Massive Particles (WIMPs) from various plausible astrophysical targets, such as the Galactic center, dwarf spheroidal galaxies, galaxy clusters etc. This will shed light on the nature of dark matter and their distribution. With a deep observation campaign of almost 500 hours, CTA will achieve a better sensitivity compared to the current benchmark limits for dark matter annihilation from various astrophysical objects.

Chapter 4

Active galactic nuclei and blazars

In this chapter the principle features of AGNs and blazars will be reviewed. Sec. 4.1 will give a brief description of the morphology AGNs, its classification and the current unification model. The main focus of this thesis is devoted to a sub-class of AGNs, known as blazars. In Chapter 5, the VHE γ -ray and multi-wavelength emission of the blazar 1ES 1959+650 will be discussed along with characterization of its broadband spectrum. In Chapter 7 another blazar named TXS 0506+056 will be discussed in the context of its multi-messenger association with a high-energy neutrino event. Sec. 4.2 will give a short introduction to the blazar class, the different sub-categories of blazars and the so-called "blazar sequence", that the spectral shape of all blazars are believed to follow.

4.1 Active galactic nuclei

With the term AGN we refer to any kind of galactic nucleus showing activity due to accretion of matter onto a supermassive black hole (see for eg: [Schneider 2006](#)). Modern surveys show that almost every galaxy, including ours hosts a supermassive black hole at the center. The accretion flow into the central black hole produces extremely powerful non-thermal radiation that outshines the thermal radiation from other components of the AGN by several orders of magnitude. Surrounding the central black hole there is an accretion disk and a dusty torus and two relativistic collimated plasma outflows (mostly for radio-loud AGNs) perpendicular to the accretion disk, known as jets. The AGN jets are often the dominant source of its non-thermal radiation. Although the theoretical understanding of the origin of the AGN jets is still not clear, the observational evidences suggest that these jets are magnetically collimated and can reach large lengths of millions of light years. Accelerated charged particles move along the jet at ultra-relativistic velocities and emit a wide variety of non-thermal emission. For a review of AGN jets, the reader is referred to [Ghisellini \(2011\)](#). The dusty torus supplies matter to the accretion disk and also obscures the central nucleus depending on the viewing angle. A detailed review of AGNs can be found in the following references: [Robson \(1999\)](#) and [Longair \(2011\)](#). The class of AGNs is not homogeneous and consists of a wide variety of objects differing in luminosity, spectral features and temporal variability which can be understood in terms an unification scenario, that will be discussed later in this section. Fig. 4.1 shows the different components of an AGN. Their morphology will be introduced in the next section, followed by a discussion on the different types of AGNs and the unification scenario.

4.1.1 Morphology of AGNs

Supermassive black hole

As mentioned in the introduction, an AGN hosts a supermassive black hole at the center which is believed to be rotating ([Reis et al., 2014](#)) and accretes matter from the surroundings. The mass of the black hole can be measured from the motion of the nearby star and gas clouds by measuring the velocity dispersion of the host galaxy ([Gültekin et al., 2009](#)) or by measuring the time delays between the brightness variations of the broad emission lines, a method known as reverberation mapping ([Gebhardt et al., 2000](#)). AGNs are believed to host supermassive black holes with mass (M_{BH}) ranging from $10^6 - 10^{10}$ solar masses. The event horizon of a non-rotating black hole is found from its Schwarzschild radius and for a maximally rotating black it is equal to the gravitational radius: $R_S = 2R_G = \frac{2GM_{BH}}{c^2}$

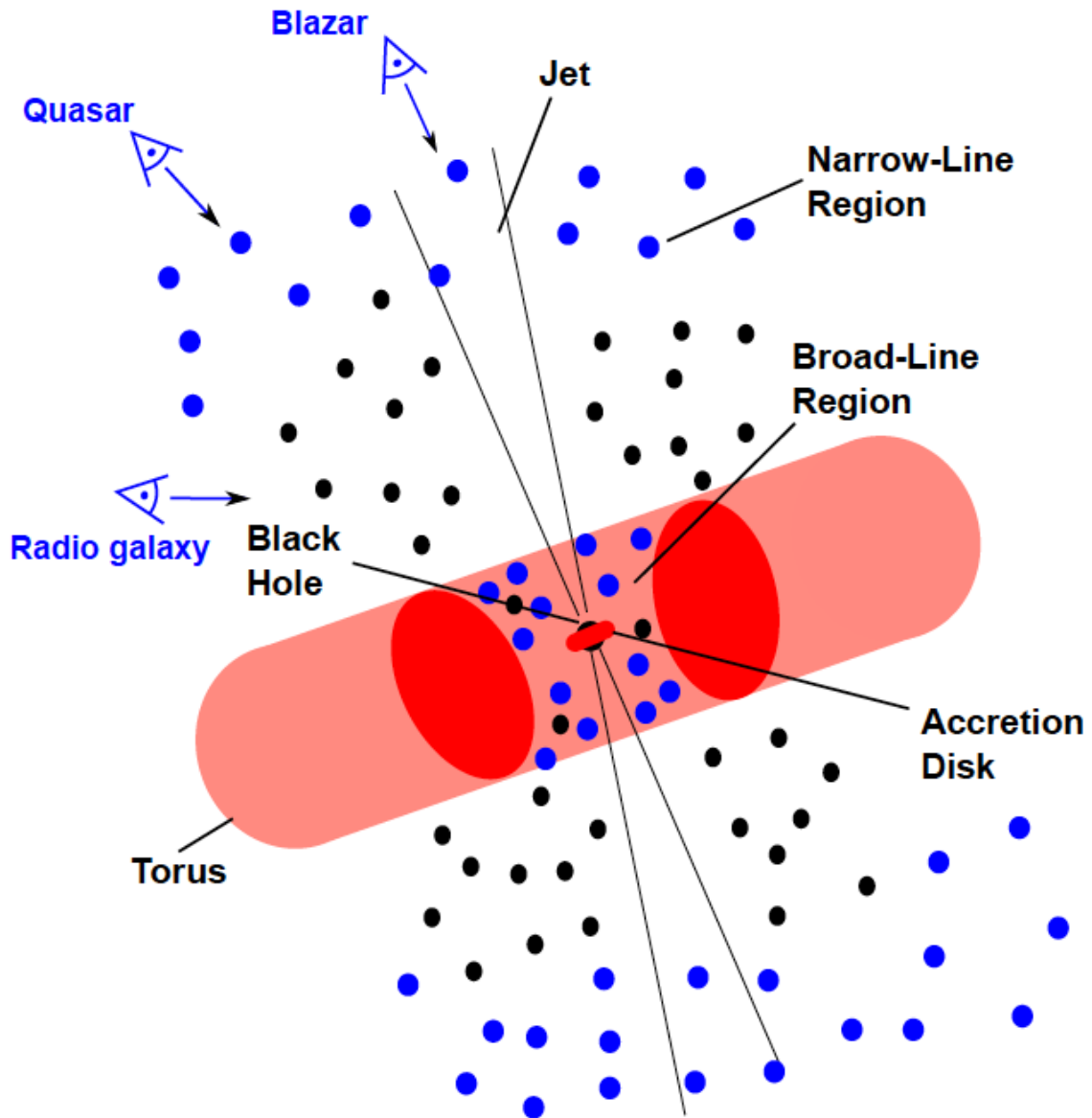


Figure 4.1: Schematic representation of an AGN. The central region consist of a supermassive black hole. It is surrounded by an accretion disk (in red) and a dusty torus (in pink). The black and blue dots represent the gas clouds present in the broad line and the narrow line region. The position of the eyes shows the unification scheme of AGNs based on the viewing angle by an observer on Earth. Figure adapted from [Urry and Padovani \(1995\)](#).

Accretion disk

Surrounding the supermassive black hole, a disk is formed due to accretion of matter onto the center, known as accretion disk. A standard accretion disk mainly emits photons by thermal mechanisms, i.e. its spectrum can be described by a superposition of Planckian distributions of different temperatures. In some AGNs, the thermal radiation from the disk can become visible in the optical-UV wavelengths. However, the properties of accretion flow are governed by the mass accretion rate \dot{m} (in Eddington units¹). If $\dot{m} > 10^{-2}$, it forms a standard accretion disk (Shakura and Sunyaev, 1973) that is geometrically thin, optically thick and emits predominantly thermal optical-UV photons. However, if $\dot{m} < 10^{-2}$, the accretion flow becomes geometrically thick, optically thin and emits a broadband spectrum (by non-thermal and Bremsstrahlung mechanisms) spanning from radio to soft X-ray regime. Such a disk is governed by the advection dominated accretion flow (Narayan and Yi, 1994) and the luminosity of the accretion disk is expected to be low.

Broad line and narrow line region

Surrounding the central core and accretion disk in AGNs, there are regions composed of mainly gas clouds, which are known as broad and narrow line regions. The broad line region is at a closer proximity to the central black hole having dimension of 0.01-1 parsec while the narrow line region is more extended at larger distances from the nucleus (> 300 parsec). The name is attributed to the width of the spectral lines in the optical emission that is produced in these regions. The emission lines are produced by atomic transitions when the gas clouds are illuminated by the thermal radiation from the accretion disk. The lines in the emission spectra are then broadened by Doppler effect, which depends on the speed of the clouds. The two regions are composed of both fast and slow moving clouds. The clouds in the broad line region have typical speeds of the order of $10^3 - 10^4$ km / s and high gas density ($n_e > 10^9 \text{cm}^{-3}$), that gives rise to the broad lines. In the narrow line region, the clouds are expected to have lesser speeds of the order of $10^2 - 10^3$ km / s, thus producing narrow line features. The narrow lines arise from gas of fairly low density ($n_e \sim 10^3 \text{cm}^{-3}$) that is spatially extended.

Torus

Surrounding the central region of an AGN, a dusty toroidal structure is formed with dimension of tens to hundreds of parsec from the central nucleus. This dusty torus causes anisotropic obscuration of the central region, depending on the viewing angle of an observer. Krolik and Begelman (1988) (see also Nenkova et al. (2008)) claimed that the torus is composed of a number of optically thick dusty clouds, instead of a smooth density distribution that was previously used to describe the torus (see for e.g.: Pier and Krolik (1992)). The main difference between a clumpy structure and a smooth density distribution is that the radiation can propagate freely between different regions of a clumpy medium, but not otherwise. The radiation from the torus is mainly emitted in the infrared band.

Jets

Perpendicular to the plane of the accretion disk and the dusty torus, two relativistic plasma outflows known as jets are originated in some AGNs (mainly the ones which are radio-loud). The relativistic extragalactic AGN jets are able to carry huge amount of power to large distances, not only in the form of radiation, but also in the form of kinetic energy of matter and fields (Ghisellini, 2011). In some cases the jets have dimensions much larger than the host galaxy, extending up to megaparsec scales. The AGN jets are believed to be one of the most powerful particle accelerators of the universe. The jets emit non-thermal radiation across a wide range of energies from radio to γ rays. Jetted AGNs, in particular blazars with their relativistic jet closely aligned to the line of sight of an observer are considered to be good candidates for neutrino emission. This is because, due to the favourable geometry of blazar jets, the intrinsic emission component appear highly boosted in the frame of the observer owing to relativistic Doppler effect. Due to the same reason, blazars are highly variable, powerful and the most dominant population in the extragalactic γ -ray sky. The models that try to explain the mechanisms giving rise to the non-thermal emission, typically assumes a homogeneous emission region containing a tangled magnetic field of strength B , moving down the jet with a bulk Lorentz factor Γ . The typical values of B and Γ as function of distance z from the central black hole was inferred by Barkov et al. (2012), as shown in Fig. 4.2. γ -ray observations in the HE band by the *Fermi*

¹ $\dot{m} = \dot{M}/M_{\text{Edd}}$ where $M_{\text{Edd}} = L_{\text{Edd}}/\eta_a c^2$, $L_{\text{Edd}} = 4\pi GM_{\text{BH}}m_p c/\sigma_T$, $\eta_a = 0.1$ (accretion efficiency)

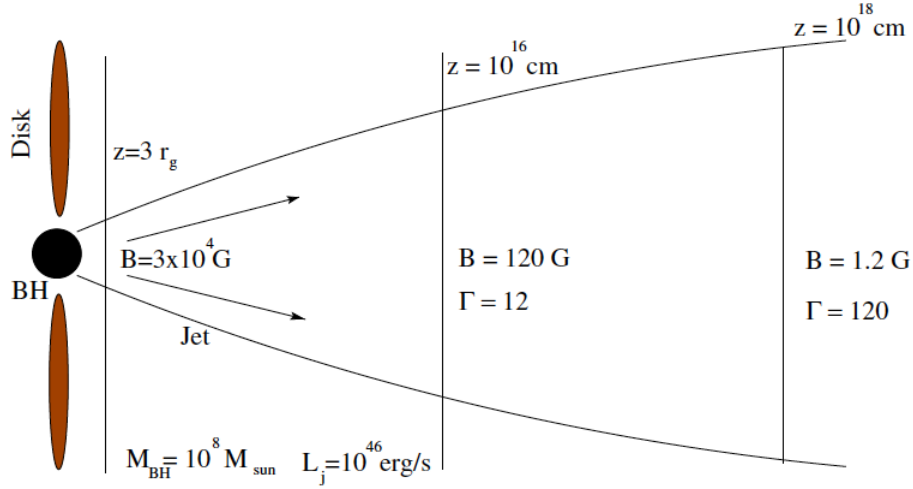


Figure 4.2: Schematic representation of an AGN jet showing the characteristic magnetic field strength B and bulk Lorentz factor Γ as a function of distance from the central black hole ($M_{BH} = 10^8$ solar mass). Image adapted from [Barkov et al. \(2012\)](#).

satellite and in the VHE band by the ground-based IACTs such as MAGIC can play a crucial role in understanding the properties of AGN jets, which emit most of their electromagnetic output in the γ -ray band (depending on the AGN class). High spatial-resolution radio images have shown that sometimes the jets consist of finer-scale substructures called *knots*. For example, in one of the highest resolution images of the jet of Centaurus A ([Abdo et al., 2010a](#)) obtained by the *Very Long Baseline Interferometry* technique ([Müller et al., 2011](#)), the presence of knots could be seen.

4.1.2 The different kinds of AGNs

The characteristics of AGNs show a wide range of variations in their morphology and properties such as temporal variability, broadband emission spectra, strength of the emission lines in their spectra and so on. Hence at first glance, the task of classification of AGNs seem difficult. Properties like the strength of the emission spectra were used to classify AGNs in the past ([Baldwin et al. \(1981\)](#), [Veilleux and Osterbrock \(1987\)](#)). Moreover a single sub-class of AGNs show a wide range of inhomogeneity - the class of blazars for example, which will be the main focus of this thesis, is not a homogeneous group and consists of highly luminous quasars and BL Lacartae (BL Lac) objects. Hence a review of the historical evolution of AGN studies and their classification will be discussed in the following.

AGN classification can be broadly done based on their radio and optical/UV emission properties. Depending on the ratio between the radio and the optical flux ([Kellermann et al., 1989](#)), AGNs can be divided into the following two categories: radio-loud, if the radio emission at 5 GHz is greater than the optical emission and radio-quiet, if the radio emission is weaker than the optical emission. On the other hand, if an AGN exhibit broad optical emission lines it is classified as Type 1 and if the optical emission lines are narrow or weak, the AGN is classified as Type 2.

Radio-quiet AGNs are further sub-divided depending on their optical emission features. Majority of radio-quiet AGNs are consisted of Seyfert galaxies ([Seyfert, 1943](#)). The Seyfert galaxies that exhibit thick optical emission lines (of the order of thousands km s^{-1}), are known as Seyfert type-1 galaxies and those that show narrow line features (of the order of hundreds km s^{-1}), are called Seyfert type-2 galaxies. In some cases, the spectrum shows both broad and narrow emission lines, which are classified as an intermediate type between Seyfert 1 and Seyfert 2 - known as Seyfert 1.5. However there exists a class of Seyfert galaxies which do not follow this scheme and are known as *narrow-line Seyfert galaxy* (NLS1, [Osterbrock and Pogge 1985](#)). They exhibit a spectrum like the Seyfert 1 galaxies but at the same time, show unusually narrow emission lines.

Amongst the radio-loud population, the AGNs which have a resolved host galaxy as an optical counterpart, are known as radio galaxies, while if the host galaxy cannot be resolved it is known as a radio quasar.

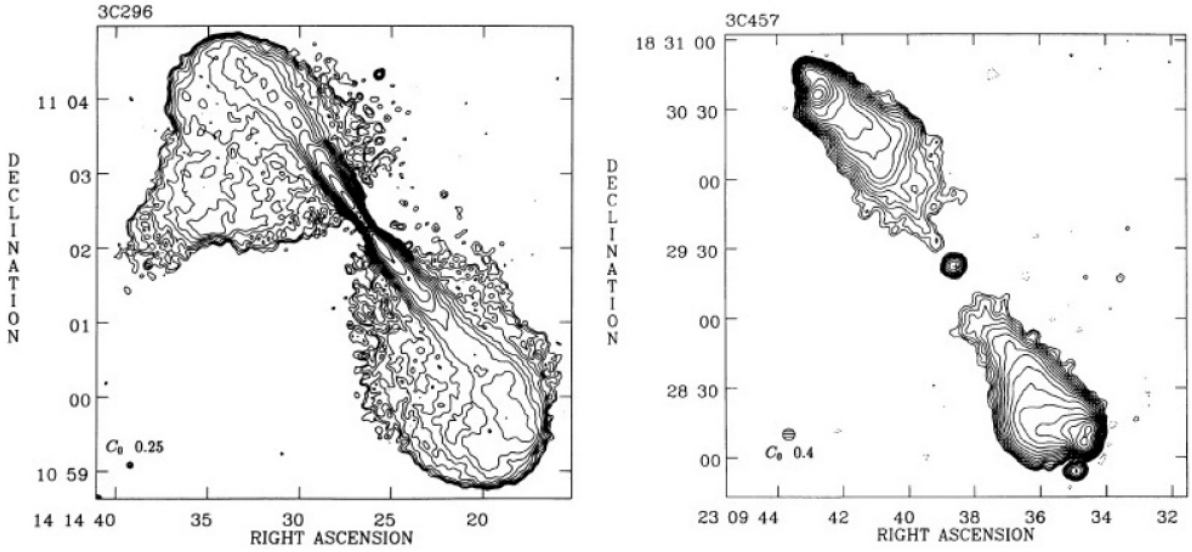


Figure 4.3: Morphology of radio galaxies. Left panel: Image of the FR I radio galaxy 3C 296. Right panel: Image of the FR II radio galaxy 3C 457. Image taken from Leahy and Perley (1991)

The radio-loud galaxies showing narrow line features (i.e. of Type 2) are further classified into two sub-categories based on their radio luminosity: Fanaroff-Riley (FR) type I, which show a low intrinsic radio luminosity ($\leq 10^{43}$ erg/s) and FR type II, which have a much higher intrinsic radio luminosity ($10^{43} - 10^{47}$ erg/s). The emission from FR I radio galaxies mainly originates from the central core while in case of the FR II radio galaxies, it comes from distant hotspots (bright regions in the jet) or lobes. The morphology of FR I and FR II radio galaxies is shown in Fig. 4.3. The radio-loud galaxies having broad optical emission lines (i.e. of Type 1) can similarly be sub-divided into different sub-classes based on the luminosity: Broad Line Radio Galaxies (BLRG) having low luminosity and radio-loud quasars at higher luminosity (Flat Spectrum Radio Quasar (FSRQ) if the spectral index in the radio band $\alpha_r < 0.5$ and Steep Spectrum Radio Quasar (SSRQ) if $\alpha_r > 0.5$).

Some radio-loud AGNs show unusual spectral features. In such objects, the optical spectra consist of a non-thermal continuum instead of emission or absorption lines. These objects are known as BL Lacs. The threshold to classify an object in this category is that the equivalent width of the lines in the spectrum has to be lower than 5 \AA (Angel and Stockman 1980).

The term blazar is coined for radio-loud AGNs, which have an ultra-relativistic jet pointed towards an observer on Earth. Blazars show a great deal of flux variability, sometimes on short timescales (down to few minutes). It is nowadays established that both BL Lacs and FSRQs fall under the same category: blazars, the only difference being in their optical emission spectra and luminosity.

4.1.3 The unification model

The unification model tries to explain the multitude at different AGN classes within a single framework. It was introduced by Urry and Padovani (1995) to explain the AGN classification due to a simple orientation effect as shown in Fig. 4.1. The AGN morphology considered in the unified scenario is a central supermassive black hole accreting matter, surrounded by an accretion disk from which part of the accreting matter is expelled out in the form of relativistic plasma outflows. However the exact production mechanism of jets still remains unclear. Some authors link the presence of absence of jets to the spin of the black hole (Tchekhovskoy et al., 2010), but this hypothesis has not been confirmed yet.

The presence/absence of jets is considered to solve the dichotomy in the brightness of the radio flux in AGNs. The radio-loud AGNs are the ones which possess ultra-relativistic jets, while the AGNs where no jets are observed can be classified as radio-quiet. In radio loud AGNs, the dichotomy between radio galaxies and blazars can be explained by the effect of the viewing angle of the jet as observed from Earth - the objects whose jets subtend a

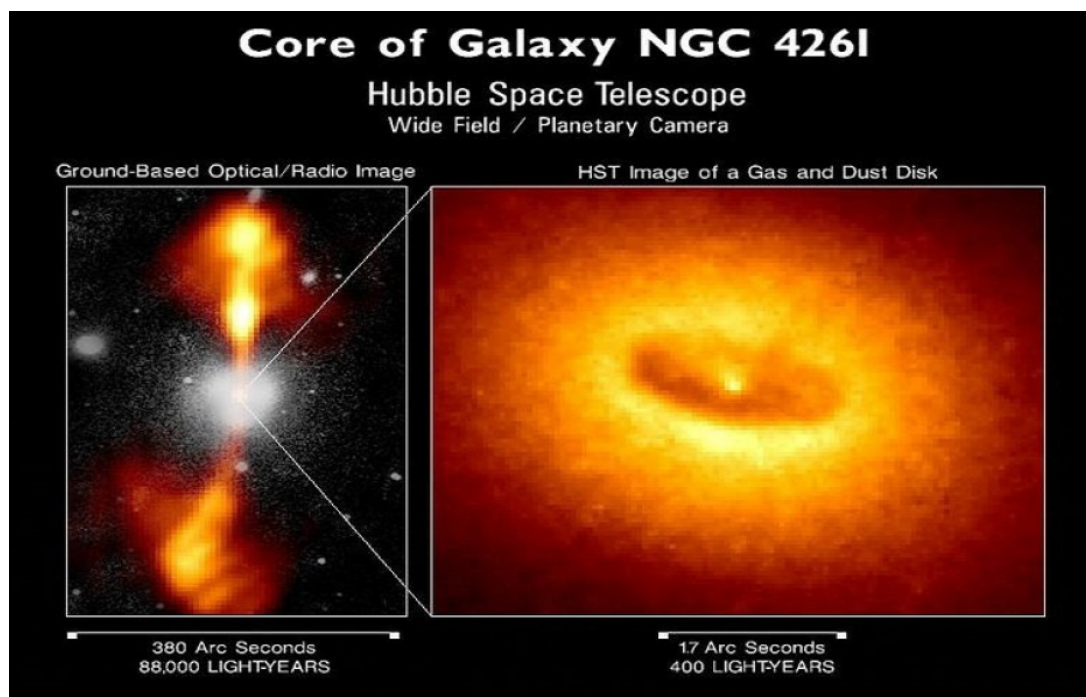


Figure 4.4: The active galactic nucleus of the AGN NGC 4261. Left: optical image of the galaxy with the relativistic jets observed in radio. Right: A zoomed plot of the central region showing the dusty torus obscuring the central engine of the active galactic nucleus. Credits: HST/NASA/ESA, adapted from [Jaffe et al. \(1993\)](#)

very small viewing angle to the line of sight of an observer on Earth are known as blazars, whereas objects having jets at larger viewing angle are known as radio galaxies i.e. misaligned counterparts of blazars.

The presence of the dusty torus and its orientation also plays a major role in the unification scenario. The dusty torus is believed to lie in the same plane as the accretion disk. Hence if a jet is viewed edge-on i.e. from a region co-planar with the dusty torus, then it obscures the central engine of the AGN. On the other hand if the AGN is observed from a location that is not co-planar with the torus (i.e. observed face-on), then the accretion disk is directly visible.

The difference of the thickness in the optical emission lines in the Seyfert galaxies as well as radio-loud AGNs, can be attributed to the location from which the emission originates. As mentioned earlier, the thickness of the emission lines depends on the amount of Doppler broadening, which is dependent on the distance of the gas clouds from the center of the gravitational potential. If the clouds are located very far away from the center, i.e. in the farthest emission regions (the so-called narrow line region), the Doppler broadening is weak giving rise to narrow emission lines. On the other hand if the gas clouds are located in the comparatively nearer broad line region, the Doppler broadening is larger giving rise to broader emission lines. In the unification scenario, it is proposed that the orientation of the Seyfert 2 galaxies is such that the broad line region is obscured, thus leading to observation of only the narrow line features. The classification based on this simple orientation effect, naturally takes into account the intermediate objects as well. This explains the dichotomy between Seyfert 1 and Seyfert 2 galaxies besides the differences between the broad-line and the narrow-line radio-loud AGNs.

The first observational proof of the unification scheme is the observation of broad lines from Seyfert 2 galaxies when observed in polarized light ([Heisler et al., 1997](#)). The observations are interpreted as the emission coming from the broad line region, which is scattered towards the direction of the observer on Earth. The other observational proof is the direct detection of a dusty torus obscuring the central engine in the case of the nearby AGN NGC 4261 as shown in Fig. 4.4 ([Jaffe et al., 1993](#)).

The main feature of AGNs proposed in the unification model, is the presence of a central supermassive black hole that shows activity due to accretion of matter. There are examples of non-active galaxies that can host supermassive black holes but are silent i.e. do not show activity since the black hole is not accreting matter. One

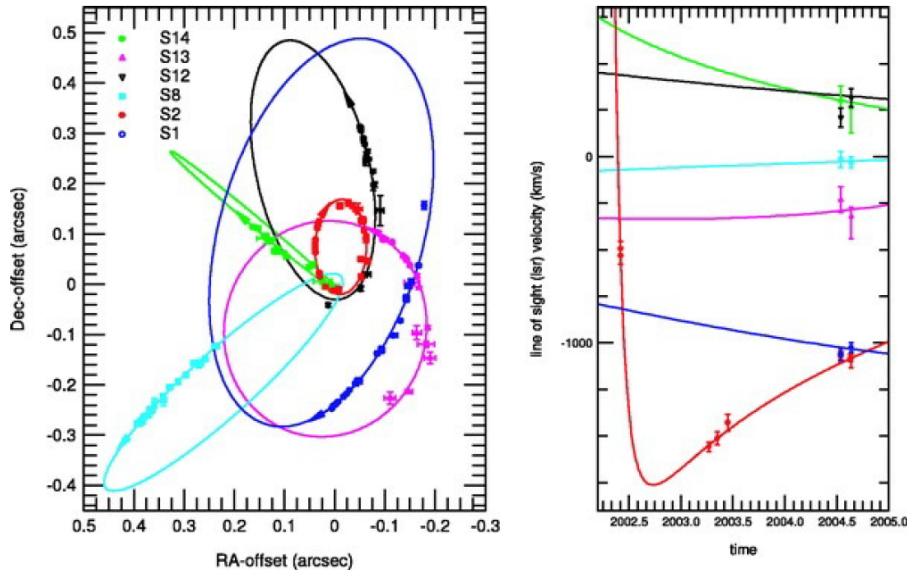


Figure 4.5: Left: Orbital motion of stars around $SgrA^*$. Right: Radial velocity of the six stars shown in the left panel. Image taken from Eisenhauer et al. (2005).

such non-active supermassive black hole resides at the center of our own galaxy (known as $SgrA^*$). It has a mass of $10^6 M_{\odot}$ and its presence can be detected from the orbital motion of stars in its gravitational potential. Fig. 4.5 (Eisenhauer et al., 2005) shows the orbital motion of six stars around $SgrA^*$ along with measurement of their radial velocity. This represents one of the most important validations of the unification model.

Moreover, recently the *Fermi*-LAT telescope observed two giant γ -ray lobes in our galaxy (Su et al., 2010), known as *Fermi* bubbles (shown in Fig. 4.6). One possibility could be that the lobes originate due to a past activity of our galaxy, which might imply that the activity of AGNs could be switched on and off depending on the activity of the central black hole, which would be another important confirmation of the unified model.

4.2 Blazars

Most of the known extragalactic γ -ray emitters are AGNs and amongst them, the largest sub-class is composed of blazars. Blazars are the most luminous and energetic objects known in the universe and are one of the most powerful natural particle accelerators. The interactions of the accelerated particles generates secondary by-products such as photons and neutrinos that can be used to probe the innermost regions of their jets. The emitted electromagnetic spectra show a double-peaked structure (often called the spectral energy distribution (SED)) spanning a wide range of frequencies including radio, optical, X-rays up to VHE γ rays. One of the key characteristics observed in blazars are very short timescale flux variability in the highest energy bands with time of variation as low as a few minutes (e.g.: PKS 2155-304: Aharonian et al. (2007), Mrk 501: Albert et al. (2007b)). The observation of fast flux variability in blazars can help us to probe the location of the high-energy emitting region within the jet (Vovk and Neronov, 2013). Blazars are also not uniform and can be classified into different sub-branches. This section will give a brief description of the classification of blazars, their broadband emission spectra, non-thermal radiation mechanisms and the so-called sequence which all blazars are believed to follow. Chapter 5 and Chapter 7 will be focused on the multi-wavelength emission properties from two particular blazars, namely 1ES 1959+650 and TXS 0506+056 (with a special emphasis on the VHE γ -ray and neutrino emission), along with interpretation of their broadband spectral and temporal characteristics.

4.2.1 Classification of blazars

As mentioned in the introduction, the emission spectra of blazars consist of two peaks or humps. The frequency of the peaks and their luminosity can vary among different class of blazars. The most luminous blazars are believed

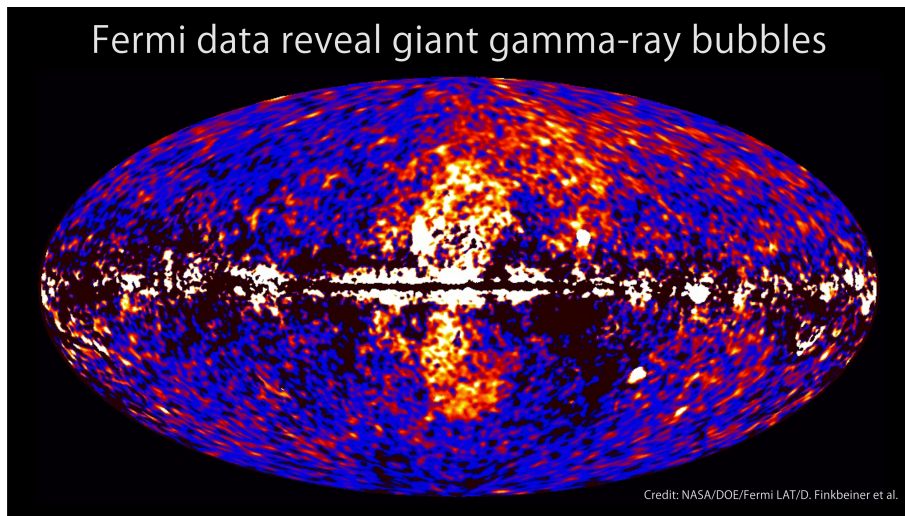


Figure 4.6: An image of the *Fermi* bubble in the Milky way. The image represents the sky in galactic coordinates. Image: <https://apod.nasa.gov/apod/ap101110.html>

to be redder, although this statement does not take into account the flaring states of the sources i.e. periods of enhanced activity. Blazars are classified into FSRQs and BL Lacs (based on the presence/absence or thickness of the emission lines in their optical spectra) as described in Sec. 4.1.3. A difference between the optical spectrum of FSRQs and BL Lacs can be seen in the Fig. 4.7. However during flaring states the emission lines can be hidden under the intense non-thermal continuum which can lead to misclassification - for example see the case of BL Lac (Vermeulen et al., 1995). FSRQs are the most luminous blazars, having luminosity much greater than the BL Lacs. The first lower energy peak of the non-thermal continuum of FSRQs lies at optical-infrared frequencies. Sometimes FSRQs show a big blue bump in their emission spectra peaking at optical and UV frequencies. It is believed to originate due to the accretion disk emission. In such objects, the black hole mass and the mass accretion rate can be measured.

The BL Lacs are again classified into three categories based on the position of their lower energy SED peak - low-frequency-peaked BL Lac (LBL), intermediate-frequency-peaked BL Lac (IBL) and high-frequency-peaked BL Lac (HBL). The LBLs and IBLs usually have their first SED peak located at optical-infrared frequencies. On the other hand, the HBLs usually have their low-energy peak at the soft X-ray frequencies. There exists an extreme class of BL Lacs known as extreme-HBL (EHBL) which usually have their low-energy SED peaking in the hard X-ray band and show very hard γ -ray spectra (Costamante et al., 2001). HBLs are the most easily detectable objects by ground-based Cherenkov telescopes because their second SED peak usually lies at few hundreds of GeV, the region where ground-based γ -ray Cherenkov telescopes are most sensitive.

In the unification model, bright FSRQs are considered as counterparts of the FR II radio galaxies observed close to the direction of the jet and BL Lacs are considered as the fainter counterpart of FR I radio galaxies (Urry and Padovani, 1995). Apart from the differences in luminosity and peak frequencies, BL Lacs and FSRQs also exhibit a difference in their redshift distribution. While the FSRQs distribution peak at redshift $z = 1.0$ the BL Lacs usually are located much closer at redshifts $z < 0.6$ (Massaro et al., 2009). However this difference can be a consequence of an incomplete sample of BL Lacs due to the absence of emission lines in their optical spectra that prevents redshift measurements.

4.2.2 Emission models

Various emission models have been proposed to explain the double-humped structure in the blazar non-thermal emission. While the existing models can explain the peculiar shape of the SED reasonably well, the debate whether leptons or protons are giving rise to the electromagnetic emission is still ongoing. The emission models can be broadly classified into two categories based on the nature of the parent particles responsible for the emission - leptonic and hadronic models. In the following two subsections, a brief introduction will be given for both types

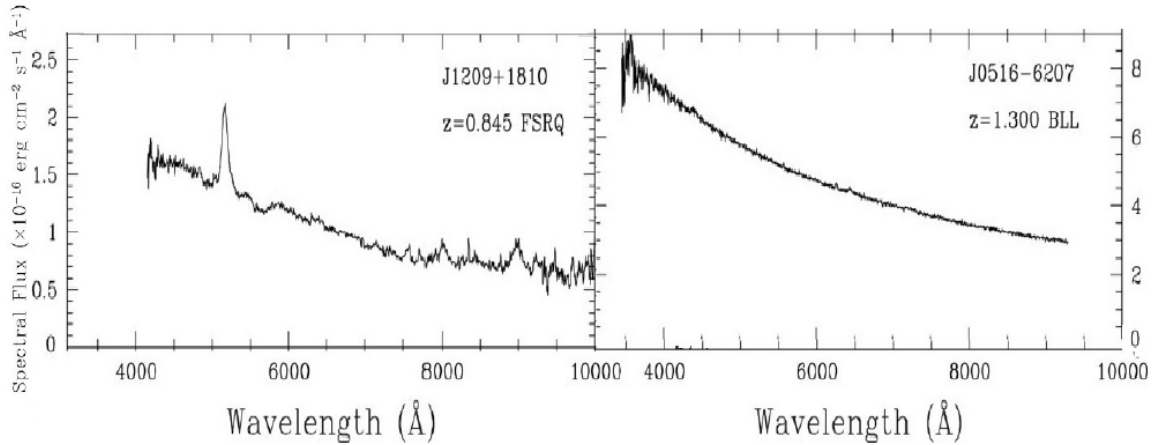


Figure 4.7: Example of the optical spectrum of blazars. Left panel: spectrum of the FSRQ 1FGL J1209.7+1806. Right panel: Spectrum of the BL Lac PKS 0516-621 (1FGL J0516.7-6207). Images taken from [Shaw et al. \(2013\)](#).

of models. During the course of this thesis, a leptonic modelling code is developed by the author for the interpretation of the non-thermal emission from AGNs. The implementation of the code will be discussed in Chapter 6 and its applications in the context of two blazars, 1ES 1959+650 and TXS 0506+056 will be discussed in Chapters 5 and 7.

Leptonic models

In leptonic models the widely used primary assumption is of a homogeneous spherical medium or blob containing a randomly-oriented magnetic field and moving down the jet towards the observer with a Lorentz factor Γ . The radiation in the jet frame is boosted in the observers' frame due to the relativistic Doppler effect. The blob is assumed to be filled with a homogeneous distribution of relativistic electrons (which usually are injected as a power-law). One key feature of leptonic emission models is that they can explain the fast variability observed in some blazars reasonably well due to fast cooling time of the leptons. The main advantage of the leptonic models is that the number of free model parameters describing the emission region and the leptonic particle distribution, are quite small.

The lower energy SED peak is ascribed to the synchrotron radiation by the relativistic electrons in presence of the tangled magnetic field inside the blob. The electron distribution suffers a break in their spectrum due to the radiative cooling. If the break in the electron spectrum is indeed due to synchrotron cooling, then a typical change of the spectral index by 1 is expected. However often the observations require a much more drastic break ([Tavecchio et al., 2010a](#)) and the mechanism of such a break is still not clear. It might indicate the presence of additional injection and cooling terms describing the continuity equation of the electrons.

The radio emission cannot be explained by the synchrotron radiation of the electrons that give rise to the optical photons. The radio photons are believed to originate from a different zone in much more extended regions of the jet which are further out. This is also in agreement with the apparent observational inconsistency that the Doppler factor measured from radio observations are much lower than that required to model the optical - X-ray emission ([Lyutikov and Lister, 2010](#)).

The higher energy peak of the SED can be explained mainly by Inverse Compton scattering of the low-energy radiation field by the high-energy electrons present within the jet. In case of BL Lacs, the low-energy target radiation field is provided by the synchrotron photons that gives rise to the lower energy hump itself (the so-called Synchrotron self-Compton (SSC) scenario) (see for eg: [Konigl 1981](#), [Maraschi et al. 1992](#)). SSC models are able to successfully explain the broadband SED of most HBLs - Fig. 4.8 shows an example of an SSC model successfully describing the data of the HBL Mrk 421. But they have difficulties to explain the SEDs of LBLs and FSRQs, as discussed for example in [Ghisellini et al. 2011](#).

On the other hand for the FSRQs, the low-energy radiation field can originate external to the jet. The most probable targets are the broad emission lines observed in their optical spectra or the photons from the accretion

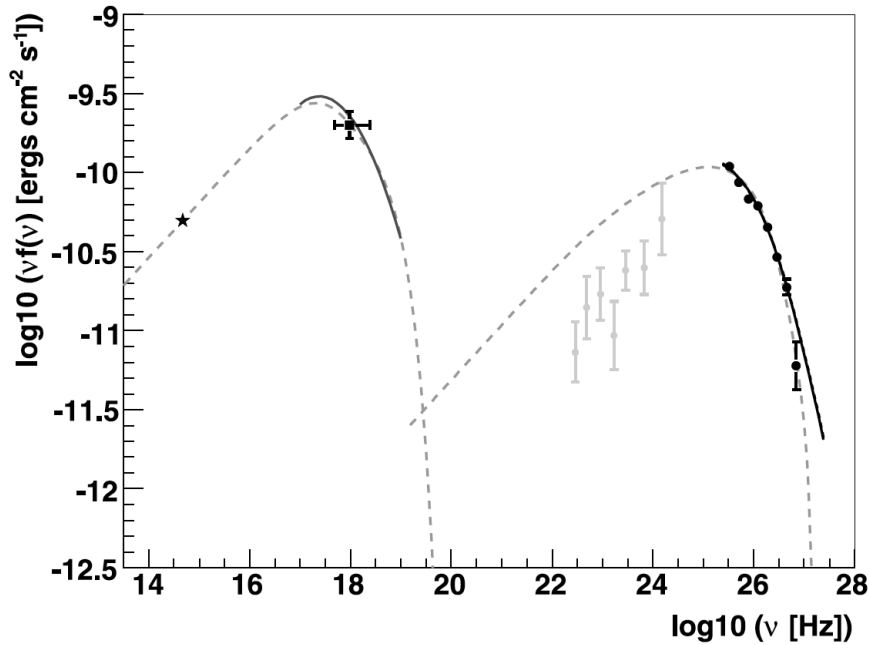


Figure 4.8: An SSC model successfully explaining the data from the HBL Mrk 421. The grey dashed line shows the SSC model fitted to the observational data. The lower energy hump in the SED arises from synchrotron radiation of relativistic electrons within the jet in presence of a magnetic field. The high-energy peak is attributed to inverse Compton upscattering of the synchrotron photons by the same population of electrons. For more details, see [Albert et al. \(2007a\)](#).

disk, the dusty torus or cosmic microwave background (the so-called external Compton scenario) (see for eg: [Ghisellini et al. 1998](#), [Madejski and Sikora 2016](#), [Arbeiter et al. \(2002\)](#), [Harris and Krawczynski \(2002\)](#)).

Hadronic models

Hadronic models are discussed only in the context of the higher energy peak of the SED - the lower energy peak is always unanimously attributed to synchrotron radiation by the primary relativistic electrons (sometimes in case of FSRQs, the host galaxy contribution is visible in the optical data). In the hadronic models an additional population of relativistic protons is assumed along with the electrons present inside the emission region. Hence the hadronic emission models almost double the number of free model parameters related to the primary particle distribution, compared to a conventional leptonic model.

In general, hadronic models require larger magnetic field strength inside the emission region compared to the leptonic scenarios ([Mücke et al., 2003](#)). If the magnetic field in the emission region is large, of the order of few tens to few hundreds of Gauss, then the ultra-relativistic protons in the jet can also emit synchrotron radiation analogous to that of the ultra-relativistic electrons ([Aharonian, 2000](#)). The proton synchrotron radiation in such cases can give a dominant contribution to the SED in the X-ray to VHE γ -ray band. Apart from the direct synchrotron radiation, in case of BL Lacs the relativistic protons also interact with the low-energy photon field provided by the synchrotron photons via photo-meson interactions ([Mannheim 1993](#), [Mücke et al. 2003](#)) and generate γ -ray photons by neutral pion decay or via pair cascades. In a photo-meson interaction both charged and neutral pions are created as secondaries. The secondary γ rays from neutral pion decay can further produce e^+/e^- pairs. Moreover, the charged pions decay to eventually create further e^+/e^- pairs which emit synchrotron photons that can again pair produce, thereby triggering an electromagnetic cascade. The cascade development stops when the internal optical depth allows the γ -ray photons to escape without further interaction. The escaping photons can be detected by the γ -ray satellites in space or ground-based IACTS such as H.E.S.S., MAGIC and VERITAS. This interaction channel is termed as p- γ scenario in this thesis. An example of a hadronic model applied to the data set of the IBL BL Lacertae is shown in Fig. 4.9. Like the external Compton scenario in leptonic models, in the hadronic models also

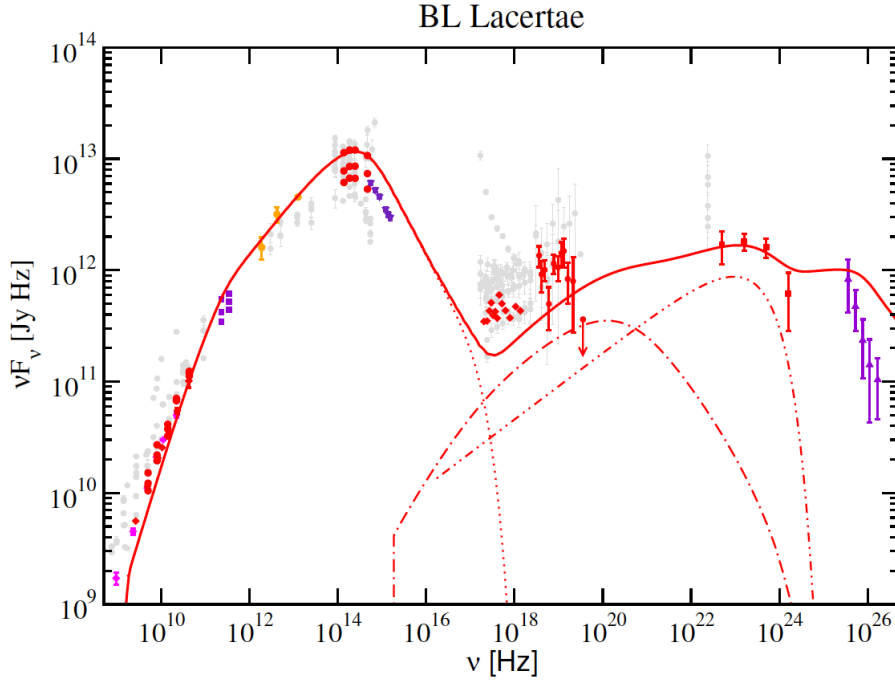


Figure 4.9: A hadronic model fitting the data for the IBL BL Lacertae. The lower energy hump is attributed to synchrotron radiation of the relativistic electrons. The high-energy part is attributed to contributions from the proton synchrotron, photo-meson cascade and SSC radiation components. For more details, see [Böttcher et al. 2013](#).

we can consider the interaction of proton with an external photon field (see for eg: [Atoyan and Dermer \(2001\)](#)).

Generally in blazar the density of the low-energy photon fields exceed the density of particles in the jets and thus the proton-proton interactions (p-p interactions) are generally disfavoured. However an interesting possibility worth mentioning is the interaction of a cloud or star with the jet as described in [Barkov et al. \(2012\)](#). In this scenario the p-p interactions can explain the ultra-fast variability in blazars via hadronic emission scenarios.

One key feature of hadronic models is their predictive power of high-energy neutrino emission based on the modelling of the blazar electromagnetic SEDs. Detection of a neutrino in coincidence with a blazar would thus be a smoking gun signature of hadronic particle acceleration inside the source. More on this topic will be discussed in Chapter 7.

4.2.3 The cosmic gamma-ray horizon

The transparency of our universe to VHE γ rays is limited by the interaction of the γ -ray photons with the EBL. EBL is the radiation formed during star formation process and is mainly composed of star light as well as star light absorbed/re-processed by dust. While propagating towards the Earth, a flux attenuation of VHE γ rays occur due to γ - γ pair production with the low-energy photon field of the EBL. With increase of the distance from the Earth and the energy of the primary photon, the probability of interaction with the EBL photons increases and subsequently, the attenuation increases. Thus very high energy photons (say > 1 TeV) from far away objects gets completely absorbed before reaching the Earth. If the source is at extremely large distance, even photons below 1 TeV can get significantly attenuated due EBL-absorption. The most distant γ -ray source detected by the *Fermi*-LAT satellite is the γ -ray transient B3 1428+422, having redshift $z=4.72$ ([Liao et al., 2018](#)). The next farthest source detected by *Fermi*-LAT is the GRB 080916C at a redshift of 4.35 ([Greiner et al., 2009](#)). VHE γ -ray emission was first detected from the source PKS 1441+25 located at a redshift of ~ 0.939 by VERITAS and MAGIC ([Abeysekara et al. \(2015\); Ahnen et al. \(2015\)](#)). In 2016, the MAGIC telescopes observed VHE γ -rays from the gravitationally-lensed blazar QSO B0218+357 ([Ahnen et al., 2016](#)). This is the farthest VHE γ -ray source observed till date.

A measure of the transparency of the universe to VHE γ rays can be given in terms of the optical depth. The

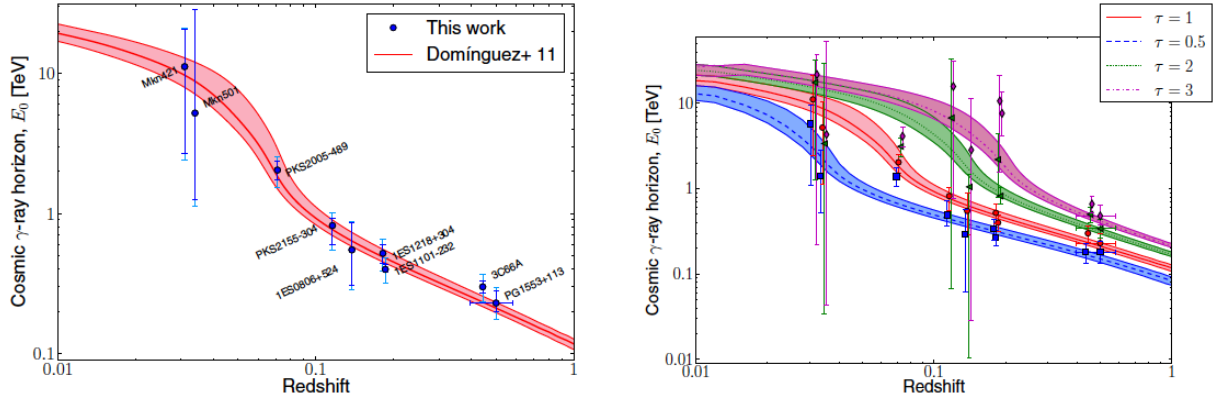


Figure 4.10: The CGRH obtained by comparison of the intrinsic/unattenuated spectrum from the SSC modelling of a sample of blazars and the observations from IACTs. The sample of blazars used in the modelling is shown in the left panel. For comparison (left panel) the CGRH predicted from the EBL model of D11 is also shown by the red shaded region. The results from the comparison of SED models and observational data, are in agreement with the prediction from D11 within the uncertainties. Right panel: The CGRH for the sample of blazars in left panel calculated for different values of the optical depth (indicated in the legend).

cosmic gamma ray horizon (CGRH) is defined as the energy, E_0 at which the optical depth τ for the photon-photon pair production becomes equal to unity (Dominguez et al., 2013). The attenuation factor for the VHE flux is given by $e^{-\tau}$. Due to this exponential nature of the flux attenuation, an alternative definition of the CGRH is the energy at which the intrinsic spectrum is attenuated by a factor of $1/e$ due to the EBL (see for eg: Aharonian (2004)).

Direct measurement of the EBL is difficult because of the zodiacal light contamination. If the EBL shape and spectral strength are known, then the intrinsic spectrum of the γ -ray source can be reconstructed. An efficient way to calculate the spectrum of the EBL based on observations is discussed in Dominguez et al. (2011) (henceforward D11). However there are several other measurements of the EBL as well (Franceschini et al. (2008), Kneiske and Dole (2010), Finke et al. (2010), Gilmore et al. (2012), Stecker et al. (2012)), all of which are in agreement within uncertainties to the model of D11. In this thesis the EBL model of D11 is used for the intrinsic spectrum calculation.

There are various methods to calculate the CGRH which are EBL-model-based lower limits obtained from the VHE γ -ray observations (Albert et al., 2008), lower limits based on the Fermi-LAT observations (Abdo et al., 2010b), or those based on the current EBL models mentioned above. Another approach to measure the CGRH which is independent of any EBL model is given in Dominguez et al. (2013). In this method, the intrinsic/unattenuated VHE fluxes of a large sample of blazars is predicted by simple SSC models and the predictions are compared with the observations from IACTs to find an estimate of the optical depth due to the EBL. The results obtained from this method are shown in Fig. 4.10.

The VHE photons should also interact with the cosmic microwave background (CMB) while travelling towards the Earth and produce pairs. These pairs can up-scatter the CMB photons up to γ -ray energies which can again pair-produce thus creating an intergalactic cascade. These cascades could give rise to a secondary component in γ -ray band of the blazar SEDs. However the development of intergalactic cascades are affected by the intergalactic magnetic field which deflects the secondary charged particles thereby broadening the cascade and thus decreasing its intensity along the line of sight. This would also imply that the emission from blazars is not point-like but extended in the form of pair halos (Aharonian et al., 1993). However no evidence of pair halos has been detected so far. In this work the contribution from the intergalactic cascades will be considered negligible.

4.2.4 The blazar sequence

The broadband emission spectra of all blazars (BL Lacs and FSRQs) are believed to form a sequence, known as the blazar sequence. The blazar sequence was originally proposed by Fossati et al. (1998) including a sample of 126 blazars (at that time the largest available flux limited sample) and later modified by Donato et al. (2001). To

construct the blazar sequence, the sample of all the 126 blazars were divided into 5 GHz radio luminosity bins (which was used as a tracer of the bolometric luminosity) and their average SEDs were constructed for each bin. The main inferences of the original blazar sequence were that with increasing bolometric luminosity, the blazars become "redder" (i.e. the peak frequencies of the two SED humps decreases) and their "Compton dominance" (defined as the luminosity ratio between the high-energy hump and the low-energy hump of the SED) increases. These conclusions were explained by Ghisellini et al. (1998) by different amounts of radiative cooling in different sources. The less powerful blazars could have less amount of radiative cooling (could be due to weaker magnetic fields) thus leading to a more energetic population of electrons. These highly energetic electrons can emit photons at higher energies, thus leading to an increase in the SED peak frequencies. On the other hand in more powerful blazars the radiative cooling could be more severe (due to presence of higher magnetic field strengths), due to which electrons can no longer attain higher energies. Thus the peak frequencies in the powerful blazars shift towards lower values. Moreover in FSRQs larger fraction of external radiation fields exist (due to the re-isotropized radiation fields from the disk and the dusty torus) compared to BL Lacs. Hence the inverse Compton luminosity of FSRQs is larger compared to BL Lacs due to presence of higher target photon fields.

Although the blazar sequence can explain the observed SED of blazars within a simple theoretically-motivated framework, its existence has been challenged by several works (Giommi et al. (1999), Perlman et al. (2000), Caccianiga and Marcha (2004), Giommi et al. (2005)). Giommi et al. (2012) proposed an alternative scheme known as the "simplified blazar scenario", where the blazar sequence was argued to be arising as a consequence of selection effects in the sample. Using two Monte Carlo simulated samples of radio flux density limited survey and X-ray flux limited survey, they showed that FSRQs are more prevalent in the radio-selected samples than BL Lacs and vice versa in the X-ray selected samples. Moreover, they showed that in both the surveys, the synchrotron peak frequency ν_s^{peak} (assumed independent of the bolometric luminosity in their simulations) of BL Lacs are higher compared to FSRQs. The plot of $\log \nu_s^{peak} - \log \nu L_\nu$ (at 5 GHz) from Giommi et al. (2012) is shown in Fig. 4.11. The radio-selected sources (dominated by FSRQs having low ν_s^{peak}) populate the top-left corner of the plot while the X-ray selected BL Lacs (which have intrinsically high ν_s^{peak}) fill the lower right corner of the plot, thus causing a selection effect. The "simplified blazar scenario" also predicts high- ν_s^{peak} -high-luminosity sources (red and green filled points in the top right part of Fig. 4.11), which are forbidden in the original blazar sequence. Those sources would not have a redshift estimate in a real survey and hence their luminosity would be undetermined, leading to their absence in the sequence of Fossati et al. (1998).

Giommi et al. (2012) claims that the optical spectrum of blazars is affected by three components: the non-thermal emission from the jet, the thermal emission from the accretion disk and broad line region and the contribution from the host galaxy. Hence according to their scheme, the objects classified as BL Lac based on the weakness/absence of optical emission lines, actually belong to two different classes - the ones with strong emission lines diluted by the non-thermal jet component (mostly arise from radio-selected samples) and intrinsically weak-lined objects with a strong non-thermal jet component (mostly arise from the ones selected in X-ray band).

Recently the blazar sequence have been updated (Ghisellini et al., 2017) by extending the sample of blazars used for its construction in the era of highly sensitive instruments like *Fermi*-LAT. For constructing the new blazar sequence, a complete flux limited sample of blazars with known redshift detected by *Fermi*-LAT in its 4-years of operation (the 3Lac sample; Ackermann et al. (2015)) has been used. All the blazars were divided into five γ -ray luminosity bins and the average SEDs in all the luminosity bins were described by phenomenological functions comprised of two broken power law functions, describing the low-energy and the high-energy SED hump, connected with a power law function describing the radio observations.

The general trends of all blazars combined and individually for the population of BL Lacs and FSRQs are shown in Fig. 4.12 and described in Ghisellini et al. (2017). The main conclusions are

- With an increase of the luminosity, in FSRQs the relative importance of the high-energy peak increases.
- The FSRQs do not exhibit a shift in the peak frequencies with the changing luminosity i.e. the FSRQs alone do not follow the original blazar sequence.
- Due to increasing importance of the second SED peak in FSRQs with increase of luminosity, the X-ray spectrum becomes harder with increasing luminosity.
- For BL Lacs, as the luminosity increases, both the SED peaks becomes redder i.e. shifts towards lower frequencies, which is agreement with the original blazar sequence.

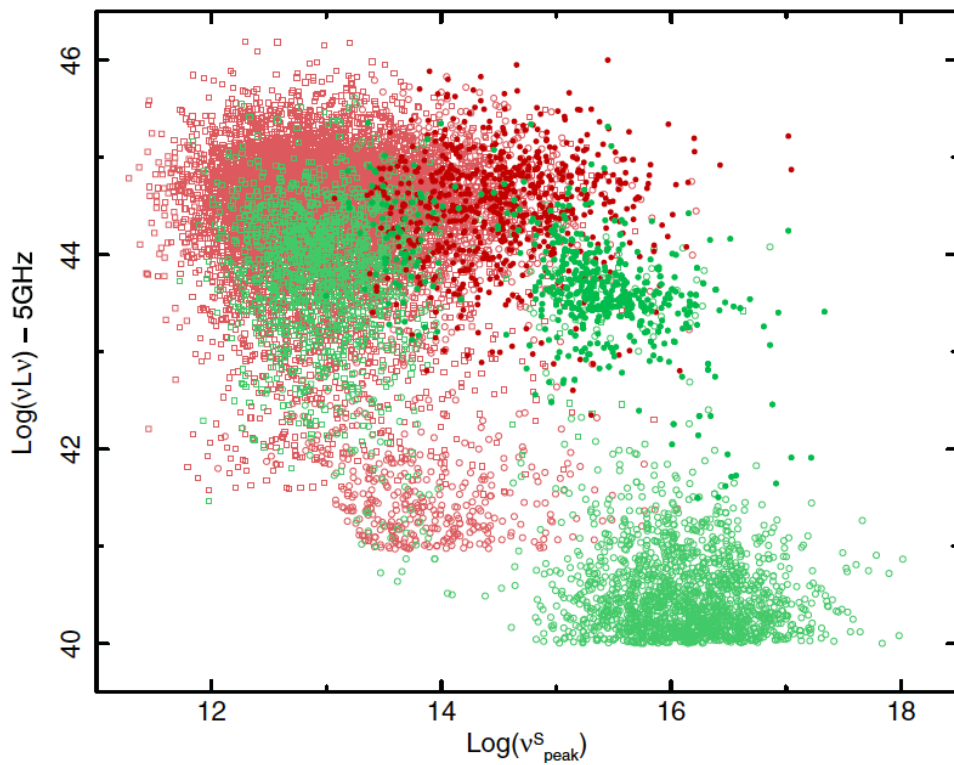


Figure 4.11: FSRQs (open squares) and BL Lacs (open circles) selected from the simulated radio flux density limited sample (red) and the X-ray flux limited sample (green) of [Giommi et al. \(2012\)](#). The filled circles represent BL Lacs with very weak emission lines or featureless spectra, that in a real survey would most likely not have a redshift estimate and hence would not have a luminosity value.

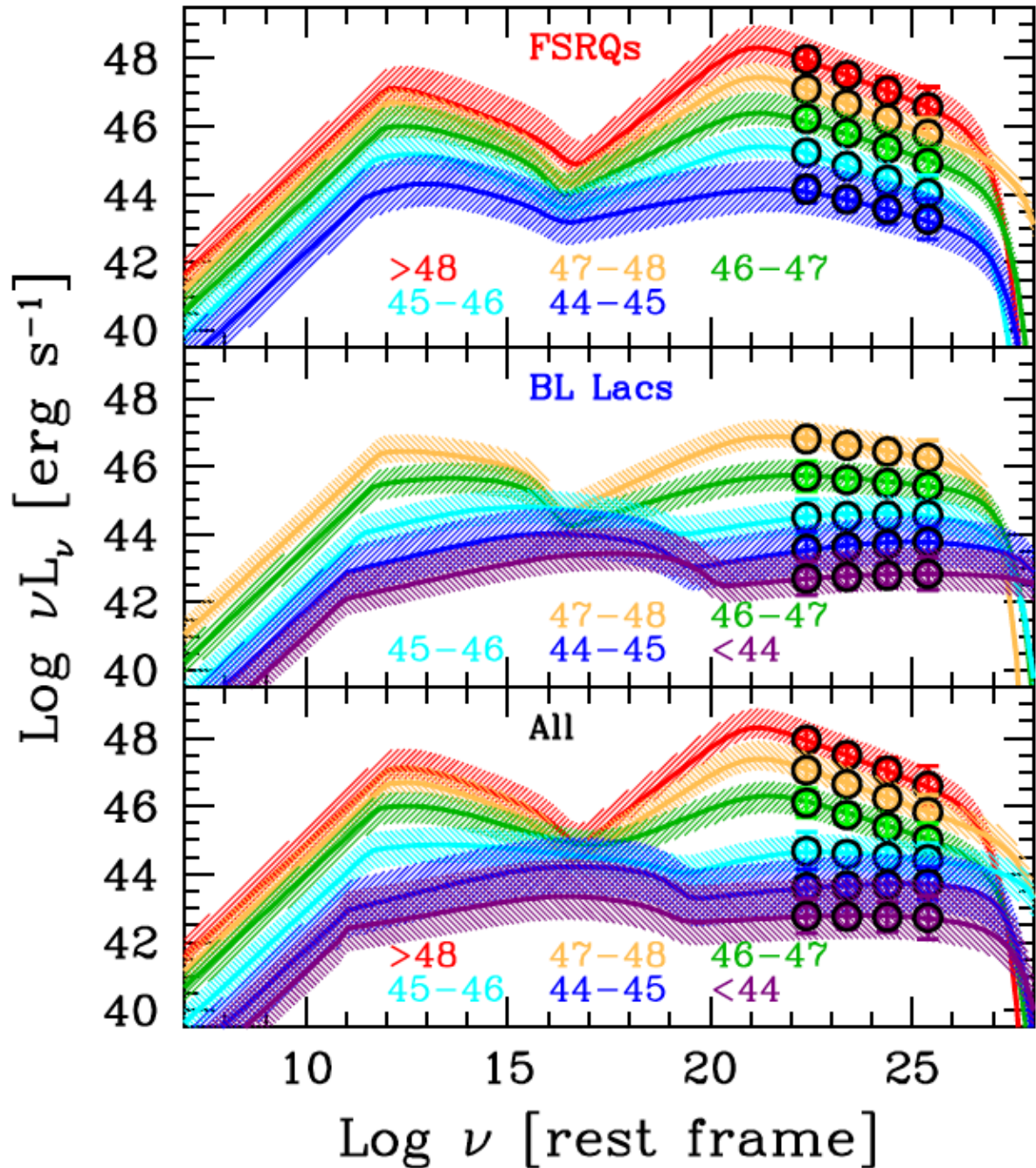


Figure 4.12: The new blazar sequence for different γ -ray luminosity bins (indicated by the respective labels) for different sources - FSRQs (top), BL Lacs (middle), BL Lac and FSRQs combined (bottom). With increasing bolometric luminosity, the peak position in the SEDs of the FSRQs does not change much (unlike the original sequence), but the "Compton dominance" increases and the X-ray spectrum becomes harder. In BL Lacs a clear trend exists as in the original blazar sequence i.e. with increasing bolometric luminosity, the peak frequencies of the synchrotron and inverse Compton bump becomes smaller (and the Compton dominance increases). The blazar sequence can be clearly seen by merging BL Lacs and FSRQs, with FSRQs occupying the highest luminosity bins and the BL Lacs occupying the lowest luminosity bins. Image credit: Ghisellini et al. (2017).

- The γ -ray spectrum becomes softer with increasing luminosity.
- For all blazars (FSRQs + BL Lacs) the trends become clearer with the FSRQs occupying the highest luminosity bins and the BL Lacs occupying the lowest luminosity bins. This is in agreement with the original blazar sequence.
- At large luminosities, a large fraction of FSRQs show the contribution from the accretion disk in their optical - UV spectrum.

The main assumption in the new sequence is that the cooling occurs inside the BLR and/or the dusty torus and the inverse Compton cooling dominates over the synchrotron cooling. Since the energy densities of the external radiation fields (coming from the disk and the torus) are more or less constant in all the FSRQs, the cooling rate only depends on square of the bulk Lorentz factor (Γ^2) of the emission volume. If the value of Γ is more or less constant amongst different sources, then their cooling rates are also quite similar, which causes the same value of the peak frequencies in the different luminosity bins of FSRQs. On the other hand for BL Lacs, the cooling depends on the synchrotron photon density which is not constant amongst different sources. In more luminous sources where the synchrotron photon density is more, the cooling is more severe, thus limiting the maximum energy of the electron to lower values.

The blazar sequence have some important caveats: i) It does not consider high activity states of blazars, which are rapidly variable objects, especially in the γ -ray band, ii) the apparent luminosity depends on the level of Doppler boosting and hence on the viewing angle of the jet, iii) the jet luminosity depend on the black hole mass ([Ghisellini and Tavecchio, 2008](#)). Future observations will increase the sample of γ -ray emitters and offer a wider distribution of spectral properties, that can be used to validate the predictions from the blazar sequence.

TeV BL Lacs: At the low luminosity end of the blazar sequence, there exists BL Lac objects which have a synchrotron peak frequency in the UV or X-ray band (sometimes even in hard X-rays). These objects sometimes exhibit TeV γ -ray emission. One of the interesting features of such TeV BL Lac objects is their ultra-fast variability (for e.g.: Mrk 501 [Albert et al. \(2007b\)](#); PKS 2155-304 [Aharonian et al. \(2007\)](#)), which can help to constrain the size of the emission region. One such TeV BL Lac object located nearby is 1ES 1959+650, which will be discussed in detail in Chapter 5 in the context of its TeV emission, rapid flux variability and broadband emission properties. From the interpretation of its broadband spectral characteristics, implications will be drawn for cosmic-ray and neutrino emission.

Chapter 5

Broadband characterization of the blazar 1ES 1959+650

In this chapter, the results will be presented from the VHE γ -ray and multi-wavelength monitoring campaign of the blazar 1ES 1959+650 led by MAGIC in 2016-2017, in association with other telescopes such as *Fermi*-LAT and the instruments on-board the *Swift* satellite. First, the basic properties of the source and its observation history will be discussed. Then the description of the data set used for the analysis and the principle analysis considerations will be briefly presented. The results from the long-term monitoring of the source during 2016 will be discussed followed by a more detailed description of some selected observation nights. On those nights, the source exhibited remarkable flaring activity in the VHE γ -ray band. These observations will be investigated in details in terms of their flux variability, spectra and broadband emission properties.

5.1 The blazar 1ES 1959+650

5.1.1 The discovery and basic properties

1ES 1959+650 is a bright and well-known blazar observed across the entire electromagnetic spectrum by several multi-wavelength instruments since a long time. 1ES 1959+650 was classified as a BL Lac object in 1993 by using a combined radio/optical/X-ray technique (Schachter et al., 1993). These measurements provided the optical spectrum of the source, that showed a flat and featureless nature with no emission lines (see also Marcha et al., 1996) and only a few absorption lines. From these absorption lines the redshift of the source could be derived as $z = 0.047$ (Schachter et al., 1993). The optical spectrum of the source was also obtained from the *Einstein* Slew Survey in 1993 (shown in Fig. 5.1). In 1996 new spectroscopic measurements including the whole *Einstein* Slew Survey for the BL Lac objects were presented yielding a higher signal-to-noise ratio which revised the redshift estimate of the source to $z = 0.048$ (Perlman et al., 1996).

In 1999, Scarpa et al. (1999) reported that 1ES 1959+650 is hosted by a gas-rich elliptical galaxy containing a prominent dust lane. Later from the high resolution optical imaging of selected BL Lac objects from the *Einstein* Slew Survey, it was confirmed that 1ES 1959+650 is embedded in a bright elliptical galaxy with an average absolute magnitude of $M_R = 23.1$ (Heidt et al., 1998).

For the estimation of the mass of the black hole of a BL Lac, various methods have been used - relating the mass of the black hole to the observed variability timescale (Ma et al., 2010) or from the stellar velocity dispersion σ from the measurements of the optical spectra of the host galaxy (Falomo et al. (2002), Falomo et al. (2003)). The mass of the central black hole for 1ES 1959+650 was measured to be few times $10^8 M_\odot$ (solar masses). An upper limit to the black hole mass of $\sim 4 \times 10^8 M_\odot$ was obtained by Ma et al. (2010) considering the fastest variability timescale of 7 hours obtained from the VHE γ -ray observations.

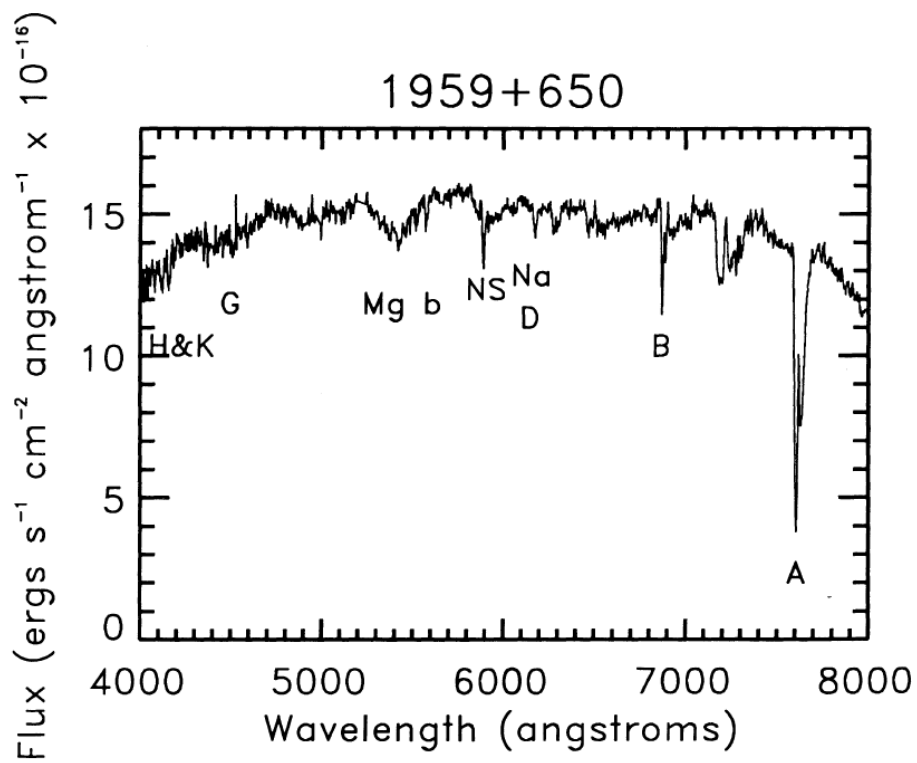


Figure 5.1: The optical spectrum of 1ES 1959+650 obtained from the *Einstein* Slew Survey during 1993. The spectra is featureless with no emission lines and only a few absorption lines. Image taken from [Schachter et al. \(1993\)](#)

5.1.2 The observational history

1ES 1959+650 was first observed in the radio band by the 91 m Green Bank Telescope (Gregory and Condon, 1991). It was first detected as an X-ray source in the *Einstein* Slew Survey of 1992 (Elvis et al., 1992) with the Imaging Proportional Counter (IPC; Gorenstein et al. 1981). The Utah Seven Telescope Array detector observed the source for 56.6 hours in total from May 1998 to August 1998 which led to the first detection of the source in the VHE γ -ray band (Nishiyama, 1999). The authors also reported the detection of VHE γ -ray variability from the source. The source has also been detected in the HE γ -ray regime by the *Fermi*-LAT satellite (Acero et al., 2015).

1ES 1959+650 was in a period of extreme activity across several wavebands during 2001-2002. The observations of the source with the HEGRA stereoscopic system during 2000-2002 (Aharonian et al., 2003), led to the detection of TeV γ rays from the source and a strong outburst with flux levels up to ~ 2.2 times the Crab Nebula flux, making it one of the brightest VHE γ -ray source along with Mrk 421 and Mrk 501. Tagliaferri et al. (2003) report a high X-ray state of the source during 2001 from their optical-X-ray joint observation campaign. During May 16 and 17 2002, the observations with the Whipple 10 m telescope revealed an extremely bright flare from the source with magnitude of 5 times the Crab Nebula flux and flux variability within short timescales of 7 hours (Holder et al., 2002). This is the highest historical VHE flux observed from this source till date.

The orphan TeV flaring activity

Following the detection of the extremely bright outburst detected by Whipple in the summer of 2002, a multi-wavelength campaign was initiated between May 18 and August 14, 2002 by the Whipple and HEGRA VHE γ -ray telescopes and the X-ray telescope *Rossi X-ray Timing Explorer* (RXTE), along with the optical Boltwood and Abastumani observatories and the Michigan Radio Astronomy Observatory (UMRAO). Several high X-ray and γ -ray flares were reported in this campaign, the most interesting one being an "orphan" TeV flare¹ with a flux magnitude of ~ 4 C.U. on 4th June 2002 detected by Whipple.

Fig. 5.2 shows the light curves in different energy bands during the multi-wavelength campaign of 2002 and Fig. 5.3 shows a zoomed plot of the orphan flaring activity in the TeV band.

Apart from the detected orphan flare, the authors reported that the X-ray and VHE γ -ray flux to be correlated in general. Correlated variability in these two energy bands can generally be explained in the framework of the standard single-zone leptonic models (Synchrotron Self-Compton or SSC models), whereas a lack of such a correlation challenges the SSC interpretation of the VHE γ -ray flux. The origin of the orphan TeV flare was explained by Böttcher (2005) with the help of a hadronic synchrotron mirror model. In this model it was assumed that an ultra-relativistic proton population that is present within the jet, interacts with the synchrotron photons reflected from a dilute reflector. These photons will not produce any observable effect by interacting with the ultra-relativistic electrons in the jet, but they can produce a γ -ray flare through the decay of neutral pions produced in p- γ interactions, after colliding with the relativistic protons.

Another strong VHE flare was reported in the multi-wavelength campaign during 2012 by Aliu et al. (2014) with the highest VHE flux measured by VERITAS reaching 66% of the Crab Nebula flux. An uncorrelated variability was observed during this period between the VHE, X-ray and UV bands, which could also be explained by the reflected emission scenario similar to Böttcher (2005).

Low VHE flux states

1ES 1959+650 was also observed by various instruments during a low VHE flux state. The source was observed for 6 hours in 2004 by the MAGIC telescopes during a low activity period in both optical and X-rays. The observations reported in Albert et al. (2006) gives an integral VHE flux level of 20% of the Crab Nebula flux above 180 GeV and reports no sign of flux variability. Low VHE flux state of the source was also measured by the VERITAS observations during 2007-2011 (Aliu et al., 2013). In 2006, Tagliaferri et al. (2008) observed an integral VHE flux above 300 GeV of $\sim 10\%$ of the Crab Nebula flux. During the low VHE state in 2006, the optical and X-ray flux was found to be more variable compared to the VHE γ -ray flux, with the 2-10 keV X-ray varying by a factor of ~ 2 . Moreover, the authors reported that the X-ray flux at energies above the lower energy SED peak varied more rapidly compared to the X-ray flux at lower energies. Considering the rise and decaying times of the X-ray flare on a timescale of ~ 10 days the authors postulated that the emission cannot be produced by a single emission region,

¹a standalone increase in the TeV flux without a simultaneous increase in the other wavebands

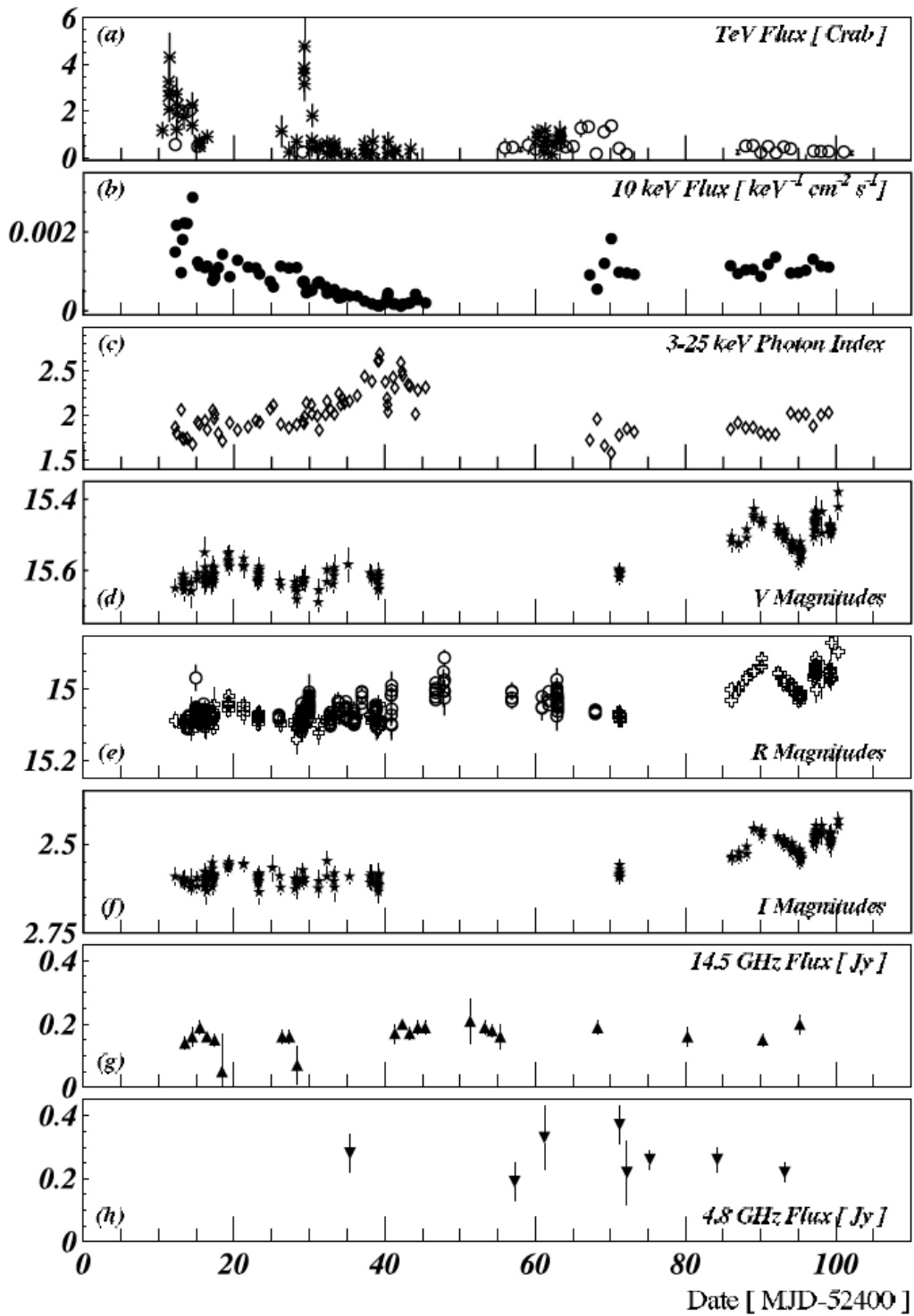


Figure 5.2: Light curves obtained from the 2002 multi-wavelength campaign (May 16 - August 14 2002). (a) The Whipple (star) and HEGRA (open circles) integrated TeV flux above 600 GeV and 2 TeV respectively. The Whipple data is binned with 20 mins while the HEGRA data is in daily bins. (b) RXTE X-ray flux at 10 keV. (c) RXTE photon index between 3-25 keV. (d) Absolute V-band magnitudes from Boltwood. (e) Absolute R-band magnitudes from Boltwood (crosses) and Abastumani (circles). (f) Relative I-band magnitude (Boltwood). (g) 14.5 GHz flux density from UMRAO. (h) 4.8 GHz flux density from UMRAO. Image taken from [Krawczynski et al. \(2004\)](#).

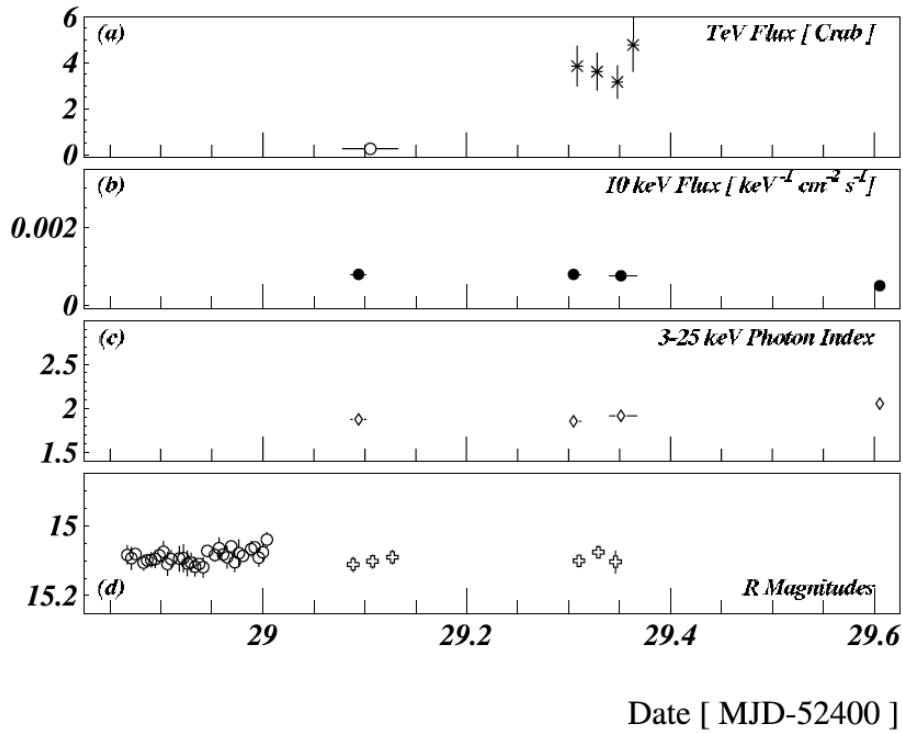


Figure 5.3: Zoomed image of the TeV orphan flare observed by Whipple on 4th June 2002. The meaning of the symbols are same as in Fig. 5.2. Image taken from [Krawczynski et al. \(2004\)](#).

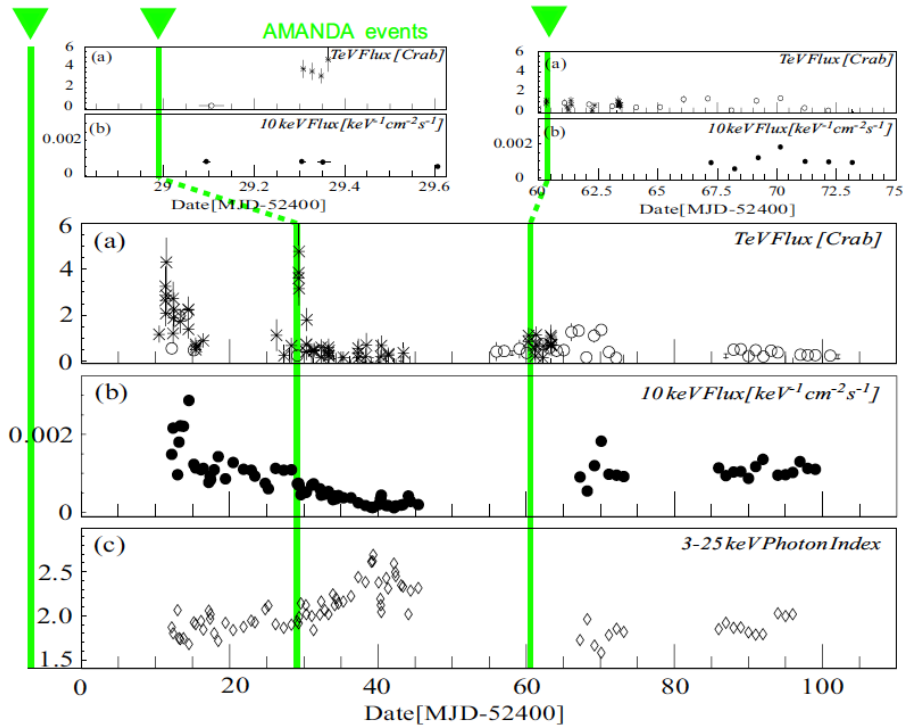


Figure 5.4: The arrival times of the neutrino events coming from the direction of 1ES 1959+650 (green lines) detected by AMANDA-II, superimposed on the multi-wavelength light curve after Modified Julian Date (MJD) 52410. Image taken from [Ackermann \(2006\)](#).

since within the timescale of the flare the emitting blob would expand and lose energy due to adiabatic processes. They instead proposed a "standing shock" scenario to explain the X-ray flaring behaviour.

Search for neutrino emission

In 2005, the AMANDA-II neutrino telescopes had reported the detection of 5 neutrino events within a distance of 2.25° from the direction of the source. 3 out of 5 of these events arrived within a span of 66 days between May 2002 and July 2002 (Halzen and Hooper (2005), Bernardini et al. (2005), Ackermann (2006)). The first event detected at Modified Julian Date (MJD) 52394 arrived just a few days before the multi-wavelength campaign of 2002. The second event arrived only a few hours before the "orphan" TeV flare on MJD 52429 and the third event was detected in coincidence with a smaller flare observed by Whipple on MJD 52460.3. The arrival time of the three neutrino events are shown in Fig. 5.4, superimposed on the multi-wavelength light curve during 2002. Although the coincidence of the neutrino and the blazar was not statistically significant, the arrival of the neutrino was considered as a possible hint of hadronic particle acceleration which triggered many theoretical interpretations (Halzen and Hooper (2005), Reimer et al. (2005)) and also led to search for time-clustered neutrino events from predefined sources in IceCube (Satalecka et al., 2007). Since then the source has been considered as a promising accelerator of high-energy cosmic-rays.

In 2006, the HiRes collaboration stated two cosmic-ray events at the location of 1ES 1959+650 in excess above the expected background, which was only found in 0.8% of the isotropic Monte Carlo sets (Abbasi et al., 2006). From the analysis done by IceCube in 2017, the source was found to represent one of the largest over-fluctuation of neutrino events in the northern sky from 7 years of IceCube data with a p-value of $\sim 2\%$ (Aartsen et al., 2017a). However, the most recent IceCube analysis, spanning 8 years of data, results in the local p-value at the position of 1ES 1959+650 of $\sim 25\%$ (Aartsen et al., 2018), which is consistent with the background-only hypothesis.

5.2 Observation and data analysis for 2016

During 2015 and 2016 the source again entered into an active state across several energy bands, most notably in optical (Baliyan et al., 2016), X-rays (Kapanadze 2015; Kapanadze et al. 2016) and also γ rays as reported by the Astronomers' Telegram (ATels) from the MAGIC, Fermi-LAT, FACT and VERITAS collaborations (e.g. Buson et al. 2016, Biland et al. 2016, Biland and Mirzoyan 2016). MAGIC started observing the source in 29th April 2016 following a high activity state as reported in Buson et al. (2016). After that it continued observing the source throughout 2016 in monitoring mode as well as follow-up observation mode, after receiving high activity alerts from the other multi-wavelength instruments (in X-rays, HE and VHE γ rays).

In this section, the MAGIC observation and data analysis for the 2016 dataset will be discussed along with a short description of the collected multi-wavelength data. During 2016 MAGIC detected three extremely bright VHE flux states of the source. A special analysis dedicated to these VHE flaring states was performed along with the long-term analysis. Results from the high-activity states of 2016 will be discussed in Sec. 5.4. Broadband interpretation of the multi-wavelength data collected during this period will also be demonstrated in the framework of different blazar emission models.

5.2.1 MAGIC observations and data analysis

MAGIC observed 1ES 1959+650 between 29th April (MJD 57507) to 29th November (MJD 57721) 2016 covering a zenith range of $35 - 50^\circ$. The data were taken in wobble mode with the standard wobble offset of 0.4° from the center of the source. The effective observation time reached ~ 72 hours for 67 nights including different VHE flux states.

To analyze the VHE γ -ray data measured by MAGIC, the standard analysis software MARS was used (see Chapter 3). The signal extraction, calibration and image parametrization was done following the prescriptions given in the mentioned chapter. The observations were performed under different brightness levels of the night sky - from dark to moderate moon conditions. As stated earlier, the NSB noise contribution increases during high sky brightness conditions (as during moon light observations), which is indirectly measured in terms of the mean DC of the MAGIC cameras. Fig. 5.5 shows the different moon levels during the individual observation nights, measured in terms of the mean DC of the MAGIC I camera. The green horizontal line shows the reference DC value during

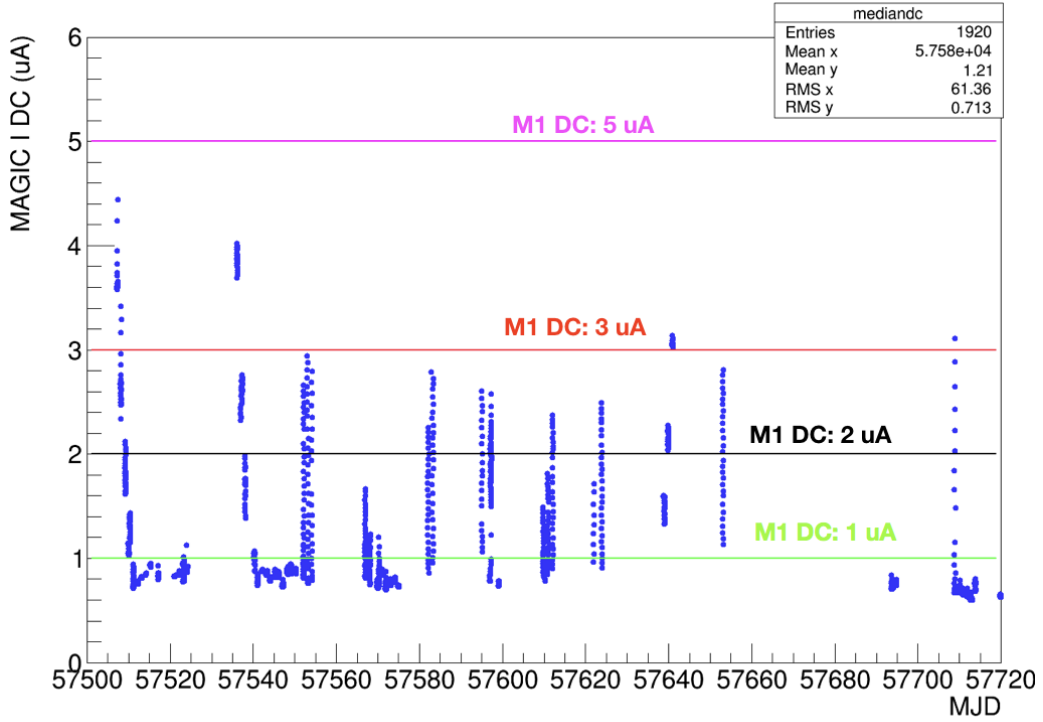


Figure 5.5: The distribution of median DC of the MAGIC I camera as a function of Modified Julian Date (MJD) for the 1ES 1959+650 2016 MAGIC data set. The horizontal lines indicate the DC categories (according to the label) in which the data set is divided.

dark conditions and the rest of the horizontal lines (black, red, magenta) show the different DC categories used for binning the data according to the NSB levels. For the dark observations, the standard cleaning levels of 6-3.5 were used. For the moon observations binned into DC categories, the cleaning levels of the data were tuned as described in Table. 3.1 of Chapter 3.

For the analysis of a VHE γ -ray dataset, a sample of OFF and Monte Carlo data are required as described in Chapter 3. The data from RBS 0970, 3C 271, Triangulum II and M87 were used as OFF sources, when no significant γ rays could be observed by MAGIC (see Appendix A for details regarding the observation dates). In order to train the Random Forests and estimate the lookup tables for analyzing the moon data, the OFF data and the Monte Carlo simulations were specially tuned by adding artificial noise to mimic the high NSB conditions. Then the same image cleaning thresholds as the original data were applied. The added noise (i.e. the pedestal events mean and RMS) for each NSB bin represents the typical noise level for that particular bin (see Table. 3.1, Chapter 3). After generating the proper Random Forests and lookup tables, γ -hadron separation, energy estimation and direction reconstruction were performed with the standard analysis chain of MARS. For reconstruction of the spectra and light curves of the source, a test Monte Carlo sample is required to calculate the instrument response functions. Similar to the training samples, the test Monte Carlo samples used for the moon data analysis were prepared by adding artificial noise to them and then applying the same image cleaning threshold as the data.

Data quality cuts

In this subsection we describe the data quality cuts used for the 1ES 1959+650 analysis. Cuts on the data are placed based on the mean DC level (in order to suppress NSB noise), zenith angle (to keep a reasonable energy threshold), and the atmospheric transmission parameters (atmospheric transmission based on the LIDAR data, or the number of visible stars as observed by the Starguider camera). The number of stars is used to assess the atmospheric transmission along with the cloudiness parameter measured by Pyrometer, only for the nights where the LIDAR

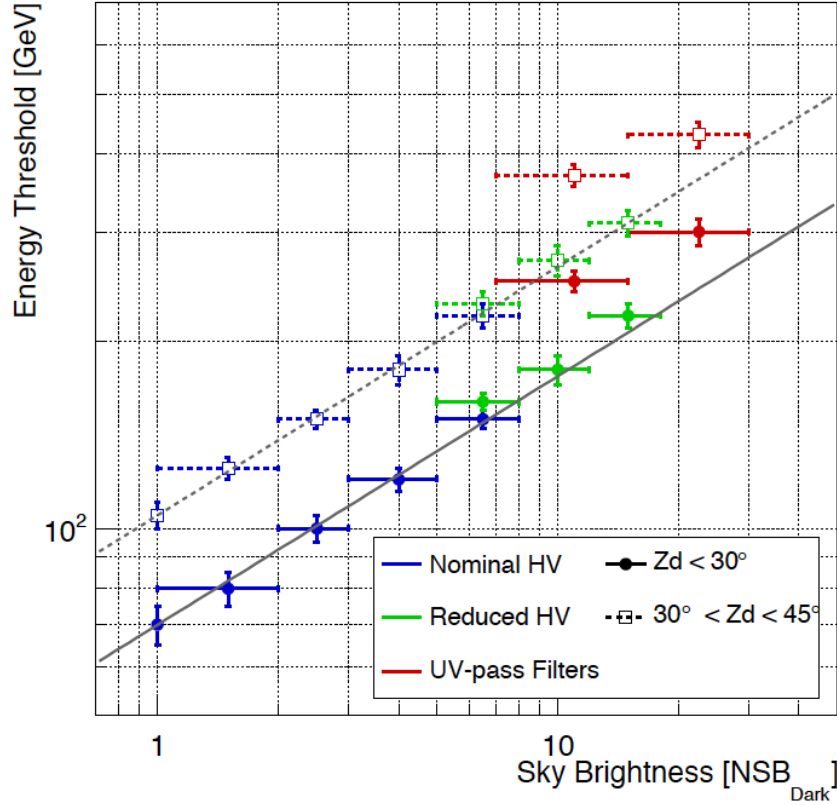


Figure 5.6: Dependence of the energy threshold at the reconstruction level as a function of the sky brightness (in units of NSB_{Dark}). Blue points: nominal HV, green points: Reduced HV, red points: UV-pass filter. Dotted and solid gray lines: Analytic approximations given by Eqn. 5.1 for zenith angle below 30° and $30 - 45^\circ$ respectively. Image credit: Ahnen et al. (2017).

data are not available due to technical problems. The distributions of the data quality parameters for the entire observation period and the cut value used in the analysis are shown in Fig. 5.7.

After the data quality cuts, 62 hours of data over 61 nights survive.

- **Cut on the mean DC:** The reconstruction energy threshold depends on the NSB level (measured in terms of the mean DC of the MAGIC-I camera) during observations (as shown in Fig. 5.6). The dependence of the energy threshold on the NSB can be approximated with the following formula (Ahnen et al., 2017):

$$E_{th}(NSB) = E_{th,dark} \frac{NSB}{NSB_{Dark}} \quad (5.1)$$

where $E_{th,dark}$ represents the energy threshold for dark Crab Nebula observations and $NSB_{dark} \sim 1.2 \mu A$ represents the NSB level of a dark Crab Nebula FoV under good weather conditions. The cut on the mean DC of M1 is placed at $4.5 \mu A$ ($\sim 3.8 \times NSB_{dark}$). Data with higher mean DC gives a negligible contribution to the effective observation time.

- **Cut of the zenith angle:** The data with zenith angle in the range $35 - 45^\circ$ is used in the analysis in agreement with the Ahnen et al. (2017). The reconstruction energy threshold depends on the zenith angle along with the NSB level. The zenith and mean DC cuts are so chosen as to keep the energy threshold close to 100 GeV during dark observations and below 200 GeV for observations under moderate moon light.
- **Cut based on atmospheric transmission:** With decrease in the transparency of the Earth's atmosphere, the γ -ray event rate starts decreasing due to scattering and absorption by the dust and clouds. MAGIC uses the

LIDAR and the Pyrometer instruments to measure the atmospheric transmission and cloudiness. In order to keep only the data taken under good weather conditions, a cut is placed on the transmission at 9 km above the ground-level of MAGIC, at 0.75 and the maximum cloudiness is set to 45.

- **Cut based on the number of stars:** In some of the observation nights of 2016 the LIDAR data were not available due to technical problems. In such situations, the number of stars detected in the MAGIC FoV by a CCD camera called the Starguider camera was used as an additional indicator to measure the atmospheric transparency. The number of stars in the FoV can vary between different source pointings and different weather conditions (e.g.: in presence of clouds, the detected number of stars are considerably less compared to good weather nights. The number can vary from zero to a few). In order to determine a cut value, all the dark observations of 1ES 1959+650 during 2016 were assembled and the distribution of the detected number of stars by the Starguider camera was measured (shown in Fig. 5.7, bottom-right panel). The distribution has a mean of ~ 56.02 and an RMS of ~ 9.67 . Hence a conservative cut on the number of stars is placed at 40 i.e. observations with detected number of stars in the FoV less than 40 are rejected.

Another indicator for the stability of the weather conditions can be the event rates. However it cannot be considered as a global indicator of the data quality for all observations since the event rates can vary night by night depending on the atmospheric transmission as well as change in the DTs, external disturbances (like a flash of artificial light on the cameras) or hardware problems.

Spectral and temporal analysis

At the reconstruction level for generating spectra and light curves, special analysis cuts were used in *Flute* as discussed in this section. For the observations under moon light conditions, a cut on the size parameter of the shower image was made as described in Table 3.1, Chapter 3. For dark observations a lower size cut of 50 was used.

As mentioned earlier, the effective area calculated by using Monte Carlo simulations has a weak dependence on the azimuth angle along with the zenith-dependence. The projected distance between the two telescopes changes with azimuth and the geomagnetic field affects the data differently at different values of azimuths. Hence binning the Monte Carlo data in different azimuth bins is necessary to reduce the systematic uncertainties. However binning in azimuth also decreases the Monte Carlo statistics and the relative error in A_{eff} starts increasing. Hence one needs to find a trade-off between the systematic uncertainty due to azimuth-dependence of A_{eff} and the available Monte Carlo statistics. With sufficient Monte Carlo statistics, the relative error in the A_{eff} should be much less compared to the statistical error of the excess events, but under no condition the Monte Carlo statistical error in A_{eff} should dominate over the statistical error of the data. Fig. 5.8 shows the comparison of the two errors for 1 and 12 azimuth bins respectively for two test cases of the data from 14th June and 1st July 2016. It is evident that with 12 azimuth bins, the relative errors in A_{eff} is either lower or comparable to the statistical errors in the excess. Using a lower number of azimuth bins suppresses the A_{eff} errors by less than 20%. Hence 12 azimuth bins were used as optimal binning in our analysis.

The long-term light curves are generated by averaging the flux from individual observation nights. For the nights with the highest flux levels, finer-binned light curves were produced with a fixed time-binning of 10 minutes. A shorter time binning was not sufficient to resolve finer sub-structures in the light curves, at the cost of decreased statistics. The energy threshold of both the light curves was kept fixed at 300 GeV.

As mentioned earlier, three major VHE flares were observed by MAGIC in 2016 (13th June, 14th June, 1st July). We performed detailed analysis of the data during these highest flux nights. We unfolded the observed VHE spectra by the instrument response function and energy dispersion of MAGIC, corrected for the EBL absorption using the model of Dominguez et al. (2011) and fitted the obtained intrinsic spectra by several mathematical functions as given below:

- A simple power law (PL):

$$\frac{dF}{dE} = F_0 \left(\frac{E}{E_0} \right)^{-\Gamma}, \quad (5.2)$$

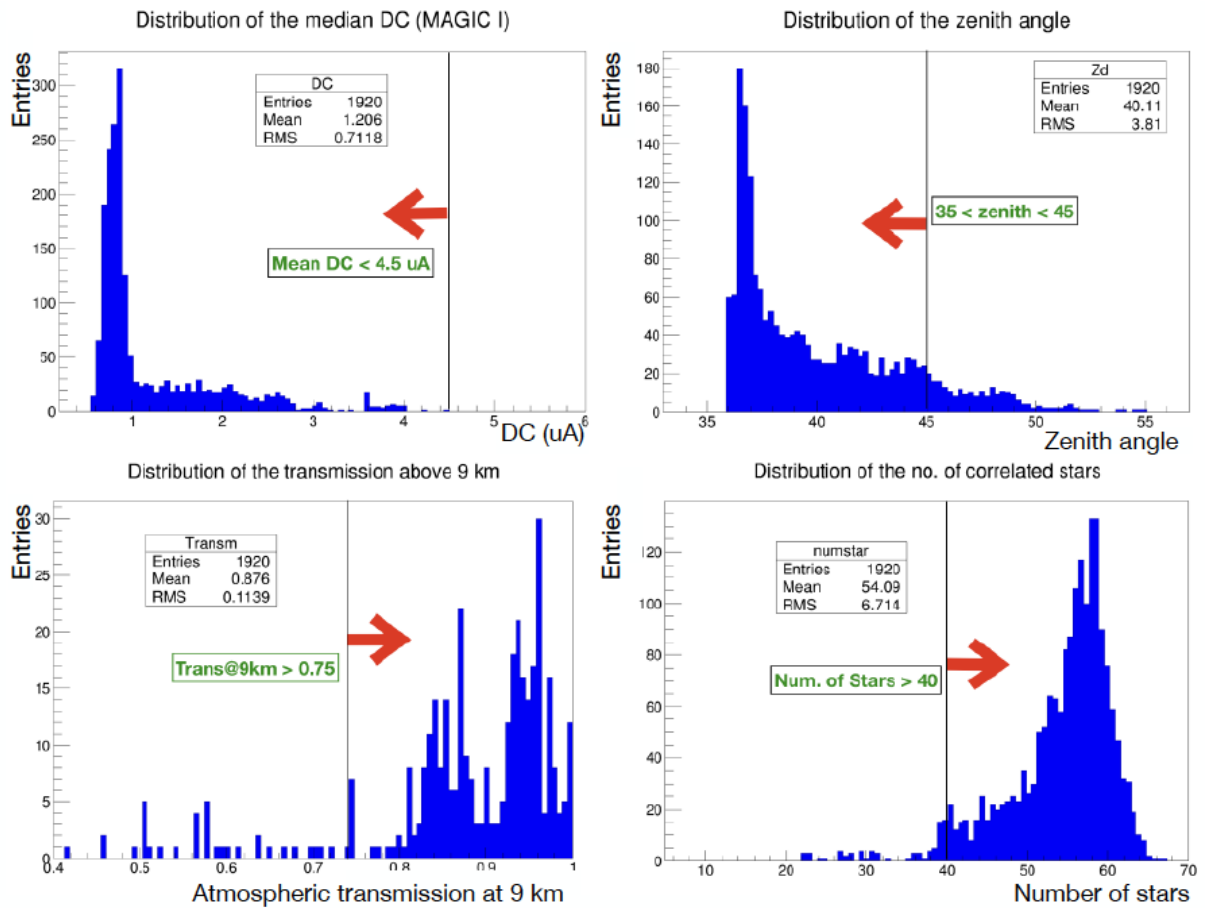


Figure 5.7: Distribution of the data quality parameters to assess the data quality cut for 1ES 1959+650 2016 MAGIC data analysis. Top left: Cut on mean DC of MAGIC I camera ($< 4.5\mu\text{A}$), top right: cut on zenith angle from $35 - 45^\circ$, bottom left: cut on the atmospheric transmission at 9 km above the ground-level of MAGIC at 0.75, bottom right: cut based on the average number of stars > 40 .

- A PL with an exponential cutoff:

$$\frac{dF}{dE} = F_0 \left(\frac{E}{E_0} \right)^{-\Gamma} \exp \left(-\frac{E}{E_{cut}} \right), \quad (5.3)$$

- A log-parabola (LogP):

$$\frac{dF}{dE} = F_0 \left(\frac{E}{E_0} \right)^{-\alpha - \beta [\log_{10}(E/E_0)]}, \quad (5.4)$$

- A LogP with an exponential cutoff:

$$\frac{dF}{dE} = F_0 \left(\frac{E}{E_0} \right)^{-\alpha - \beta [\log_{10}(E/E_0)]} \exp \left(-\frac{E}{E_{cut}} \right), \quad (5.5)$$

where F is the integral γ -ray flux and E is the γ -ray energy. The value of the normalization energy E_0 was fixed to 300 GeV. For the spectral analyses of these three brightest nights, we discarded the time windows with relatively bright moon levels in order to reduce systematic uncertainties.

5.2.2 Multi-wavelength observations

Multi-wavelength data from instruments spanning the optical to HE γ rays have been collected during 2016 along with the VHE γ -ray data from the MAGIC observations. The multi-wavelength data were used to generate a long-term light curve as well as broadband spectra for some of the selected observation nights with the highest VHE flux levels. The multi-wavelength data used in this thesis include publicly available optical and X-ray data from the instruments on board the *Neil Gehrels Swift* observatory and the HE γ -ray data from the *Fermi*-LAT instrument. The multi-wavelength data analysis have been done by Mitsunari Takahashi (Institute for Cosmic Ray Research, University of Tokyo) and Masaaki Hayashida (Department of Physics, Konan University, Japan). The MAGIC data has been analyzed by the author himself. The results of the MAGIC and multi-wavelength analysis and interpretation of 1ES 1959+650 has been submitted to the journal *Astronomy and Astrophysics* and currently under review.

The HE γ -ray data

The *Fermi*-LAT data from 28th April to 24th November 2016 was analyzed by the standard binned likelihood method with a binning of 3 days. The data from 12th June 21:00 to 14th June 9:00 was analyzed (with a binning of 1.5 days) separately. This time window covers the MAGIC observations on 13th and 14th June 2016. In order to suppress the contamination from the Galactic diffuse emission and contribution from nearby sources to 1ES 1959+650, the lower energy threshold of the analysis was set to 300 MeV and only three of the P8R2_SOURCE_V6 data types with better PSF were used, namely, the event type PSF1, PSF2, and PSF3. The entire analysis energy range is consisted of 300 MeV - 300 GeV.

The X-ray data

The publicly available data from the *X-ray Telescope* (XRT) on-board the *Swift* instrument was used covering the entire MAGIC analysis period from 28th April to 22nd November 2016. For the long-term analysis the energy-flux light curve was produced in the energy range 0.5 to 5 keV. During the brightest VHE flux nights of 13th and 14th June 2016, two XRT observations from 02:44 to 04:00, 13th (ID: 35025243) and from 02:16 to 03:20, 14th (ID: 35025245) June 2016 were found with exposure times 972 s and 865 s, respectively. These observations were considered to be quasi-simultaneous with MAGIC and *Fermi*-LAT. The differential energy-flux in the range 0.6 keV to 7.5 keV was derived for these observations.

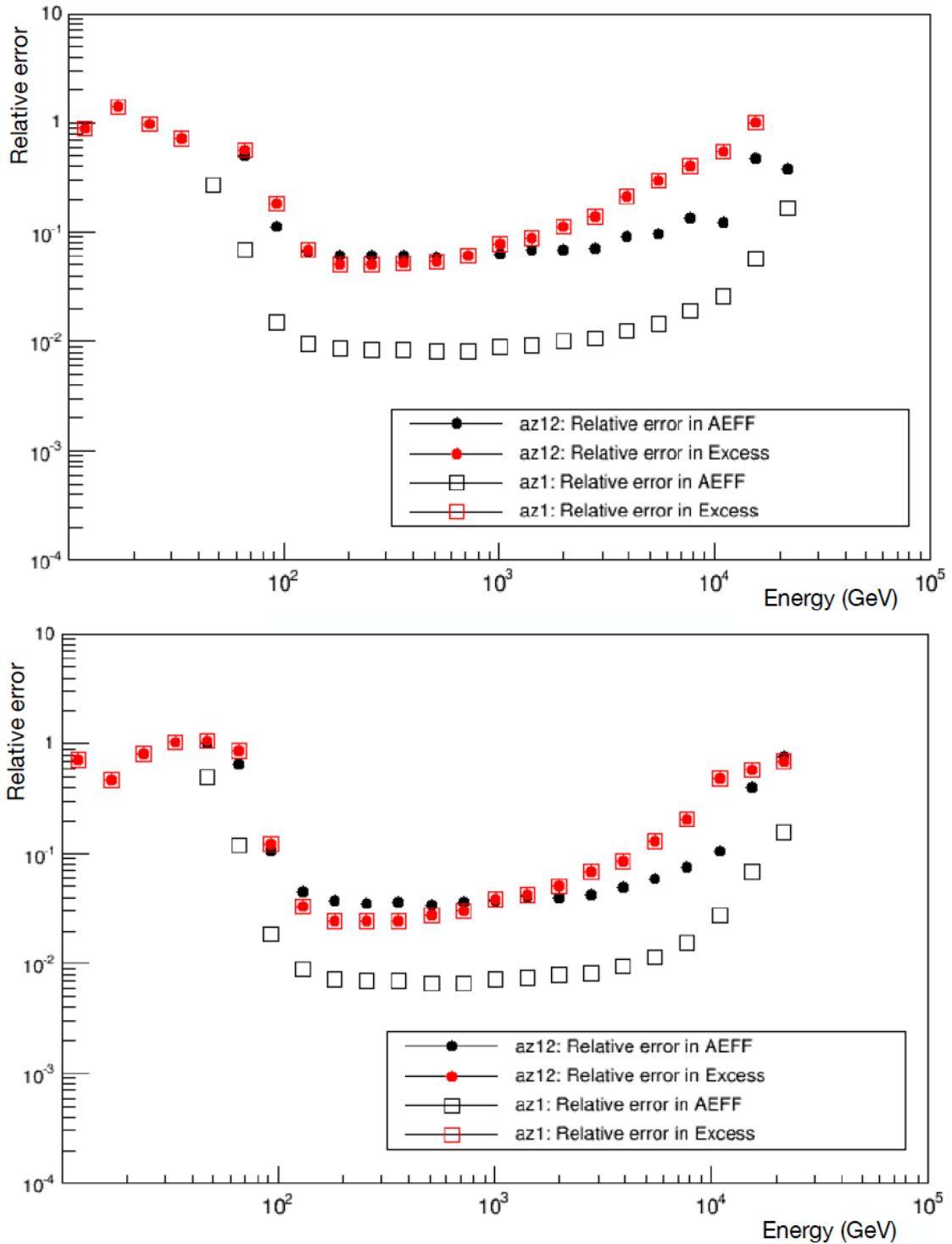


Figure 5.8: Relative error in A_{eff} due to azimuth-binning vs statistical error in the γ -ray excess for 14th June and 1st July 2016 (as an example). The black circles and black open squares represent the relative error in A_{eff} due to 12 and 1 azimuth bins respectively and the red circles and red open squares represent the errors in the excess (independent of azimuth). The errors in A_{eff} are always below (or comparable to) the statistical errors up to 12 azimuth bins. Hence 12 azimuth bins have been used in our work as a compromise between keeping sufficient Monte Carlo statistics and decreasing the systematics due to azimuth-dependence of A_{eff} .

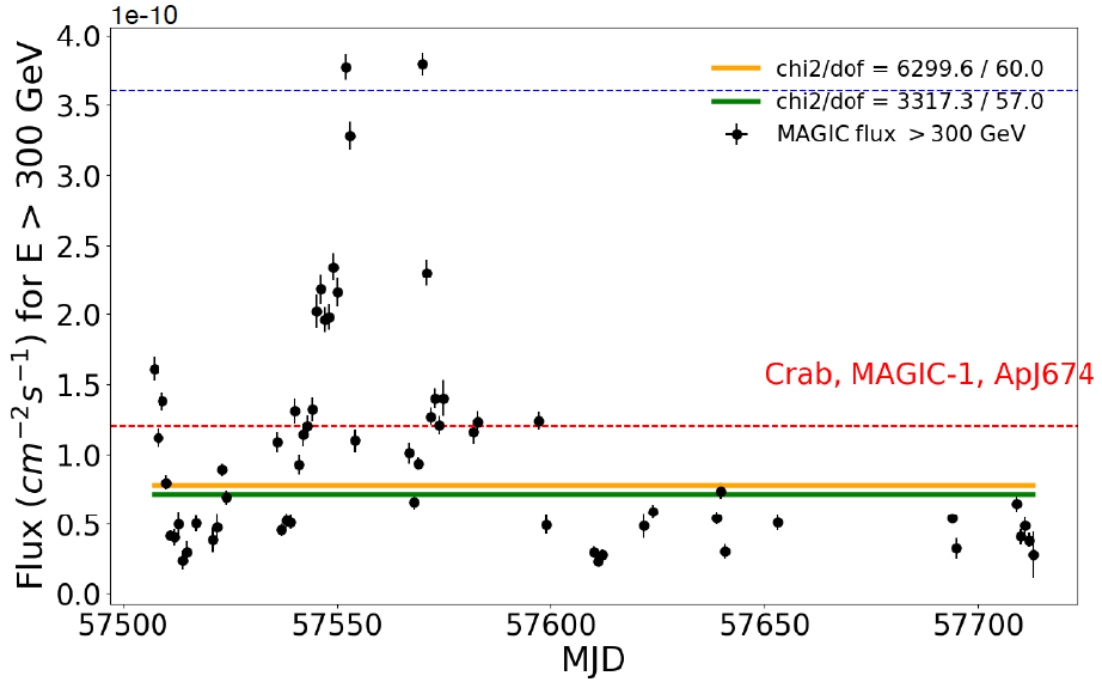


Figure 5.9: The daily-binned VHE light curve of 1ES 1959+650 above 300 GeV from 29th April (MJD 57507) to 21st November (MJD 57713) 2016. The red-dashed and the blue-dashed lines show the integral flux and three times the integral flux of Crab Nebula above 300 GeV respectively. Fits with constant functions and their respective $\chi^2/\text{d.o.f}$ are shown with the orange (including all points) and green (excluding the three brightest flares) solid lines.

The UV/optical data

The UV/optical data in the range 28th April - 21st November 2016 covering the entire MAGIC analysis epoch was obtained from the *Swift Ultraviolet/Optical Telescope* (UVOT). Among the six filters of UVOT which have a narrow effective waveband ranging from 170 nm to 600 nm (Roming et al., 2005; Poole et al., 2007), the data of the filter W1 centered at 260 nm was used for the long-term analysis since this was the most frequently used filter amongst others. Quasi-simultaneous multi-wavelength analysis for the VHE flares on 13th and 14th June 2016, was performed with the data from the filters [W1, W2: centered at 192.8 nm] and [W1, M1: centered at 224.6 nm, W2] respectively.

5.3 Long-term analysis results

5.3.1 The MAGIC light curve

To generate a light curve, an assumption on the shape of the differential spectra is required for calculation of the integral flux. For this purpose, the spectra from each individual night was fitted with various spectral functions as described in Eqn. 5.2-5.5 using the program *Fold*. The obtained best-fit spectrum (the one with lowest value of the reduced- χ^2) was used as the input spectrum for integral flux calculation. The resulting light curve computed above 300 GeV for the period 29th April 2016 (MJD 57507) to 21st November 2016 (MJD 57713) is shown in Fig. 5.9. For comparison the integral flux of the Crab Nebula above the same energy threshold is plotted as the red-dashed line. The blue-dashed line indicates three times the Crab Nebula flux.

As can be seen from the daily-binned light curve, there are three nights in 2016 with the highest flux level up to 2.5-3 times the Crab Nebula flux - the nights of 13th June (MJD 57552.0), 14th June (MJD 57553.0) and 1st July (MJD 57570.0). These represents remarkably bright states of 1ES 1959+650 and is the highest flux measured from this source in the VHE band since 2002. The lowest average flux level above 300 GeV during 2016 is equivalent to

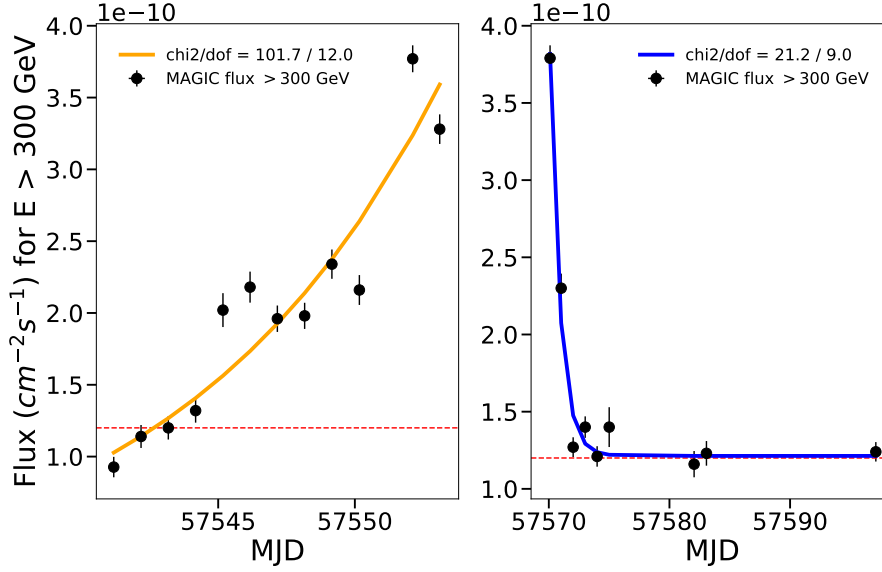


Figure 5.10: Zoomed light curves for 2nd June-14th June 2016 (left panel) and 1st July-28th July 2016 (right panel). The flux doubling timescales for the rising and falling parts obtained by fitting Eqns. 5.6 and 5.7 are of the order of ~ 6 -7 days and ~ 0.5 -1 day respectively.

$\sim 20\%$ of the Crab Nebula flux, which is comparable (slightly higher) to the low flux states measured by MAGIC in the past (Tagliaferri et al., 2008).

In long-term, the light curve shows a wide range of flux variability in different timescales by more than one decade. A fit with a constant function including all the light curve points yields a $\chi^2/\text{d.o.f} \sim 6300/60$ (shown with the orange solid line in Fig. 5.9) and a constant fit excluding the three highest flux nights mentioned above, gives a $\chi^2/\text{d.o.f} \sim 3317/57$ (shown with the green solid line in Fig. 5.9). Both of these have a fit probability equivalent to 0%. However, note that the constant fits do not represent the low emission state of the source since the fits are strongly biased by the higher flux measurements. Such erratic trends in the light curve are a common feature of HBLs.

The period of brightest activity is from the beginning of June to end of July 2016 (MJD 57541.18-57597.11). During most of this period the integral flux above 300 GeV was comparable to or greater than the Crab Nebula flux (except for 3 nights on 28th June, 29th June and 30th June 2016). Apart from the three brightest flares on 13th June, 14th June and 1st July of magnitude ~ 3 C.U., there were several other mini-flares with varying flux levels (for e.g.: several flares comparable to ~ 2 C.U. between MJD 57545-57550 and near MJD 57570). There was a gap of 14 days in the MAGIC observation window from 14th June - 28th June, hence the behaviour of the source cannot be quantified during this span of the brightest activity period. In order to get a quantitative estimate of the long-term variability, the data within the most variable period is divided into two parts - from 2nd June - 14th June where a rising trend is observed in the light curve (Fig. 5.10, left panel) and from 1st July - 28th July where a falling trend is observed (Fig. 5.10, right panel). In order to get a rough estimate of the flux doubling time, the rising and falling parts were fitted with the functions given in Eqn. 5.6 and 5.7 respectively.

$$F(t) = A_0 e^{-|t-t_0|/t_r} \quad (5.6)$$

$$F(t) = F_0 + A_0 e^{-|t-t_0|/t_f} \quad (5.7)$$

Here A_0 and t_0 represents the maximum flux amplitude and time corresponding to the maximum flux amplitude respectively, F_0 represents the constant part of the function and t_r and t_f are the rising and falling times respectively. All of these parameters are left as free while fitting and the flux doubling time is denoted by $t_{\text{dbl}} = t_r \times \ln(2)$ or $t_{\text{dbl}} = t_f \times \ln(2)$.

The exponential fit (Eqn. 5.6) to the rising part of the nightly-binned light curve gives a flux doubling time of $t_{dbl} = 6.6 \pm 0.8$ days with a reduced chi-squared $\chi^2/d.o.f \sim 101/12$. The Eqn. 5.7 fitted to the falling edge of the light curve gives a doubling timescale of $t_{dbl} = 0.6 \pm 0.32$ days with a reduced chi-squared value of $\chi^2/d.o.f \sim 22/9$. The results of the fit are shown with the orange and blue curves in Fig. 5.10. However, it is to be noted that the obtained timescales can be considered as somewhat rough estimate of the variability since the erratic trends in the light curve are difficult to be exactly reproduced by fitting with simple exponential functions.

5.3.2 The multi-wavelength light curve

Fig. 5.11 shows the multi-wavelength light curve of 1ES 1959+650 for the period of 28th April to 24th November 2016. The topmost panel corresponds to the MAGIC photon flux (above 300 GeV), followed by the *Fermi-LAT* flux in the range 0.3–300 GeV, XRT energy flux in the range 0.5–5 keV and the UVOT energy flux. From the light curve it is evident that the VHE band and the XRT band are the most variable energy bands for the source. The optical flux shows less activity compared to the other bands.

The X-ray to VHE correlation For 1ES 1959+650, it is anticipated that the lower-energy and higher-energy peaks of the SED lies in the X-ray and VHE bands respectively. Thus a correlation study between these two energy bands can provide important information regarding the underlying emission mechanisms giving rise to the two SED peaks - whether the two peaks share commonalities in their origin in terms of the emission zone or nature of the emitting particles. These considerations are very important for modelling the broadband electromagnetic SED.

To quantify an overall general trend between the X-ray and VHE energy bands, quasi-simultaneous X-ray and VHE data within 18 hours were chosen. The quasi-simultaneous X-ray and VHE flux considered in our studies is shown in the top panel of Fig. 5.12. The fluxes are normalized to the highest flux level in the respective energy bands. About 27 observations were found where the two fluxes can be considered quasi-simultaneous. The bottom panel of Fig. 5.12 shows the correlation plot of the two energy bands. From the limited data sample used in this work, there appears to be a hint of increase in the XRT flux with an increase of the MAGIC flux.

A linear correlation between two data sets can be quantified in terms of the Pearson's correlation coefficient which is defined in the following manner for two random variables X and Y:

$$corr_{xy} = \frac{cov_{xy}}{\sqrt{cov_{xx} cov_{yy}}} \quad (5.8)$$

where cov_{xy} , represents the covariance among X and Y and cov_{xx} , cov_{yy} represents the variance in the variables X and Y respectively. The correlation coefficient can take any value between -1, 0, 1. A positive value hints towards a positive linear correlation and a negative value indicates a negative linear correlation while zero indicates no linear correlation. Since the random variables in consideration here (the fluxes in the X-ray and VHE γ -ray bands) also have errors, a weighted correlation should be calculated to get a more precise estimate. In the following calculations the errors of the respective observations has been used as the weight w_i for each energy band. With these considerations the weighted flux mean, covariance and correlation can be defined respectively for two energy bands having fluxes a_i and b_j as:

$$\begin{aligned} \bar{a} &= \frac{\sum a_i w_i}{\sum w_i} \\ C_{ij} &= \frac{\sum w_{ij} (a_i - \bar{a}_i) (b_j - \bar{b}_j)}{\sum w_{ij}} \\ R_{ij} &= \frac{C_{ij}}{\sqrt{C_{ii} C_{jj}}} \end{aligned} \quad (5.9)$$

The weighted Pearson's correlation coefficient R_{ij} between the X-ray and VHE bands was calculated to be 0.35 (the unweighted correlation coefficient calculated using the Python functions in the *numpy* library provides a value for the correlation coefficient to be 0.43). This only hints towards a marginal positive correlation between the two energy bands.

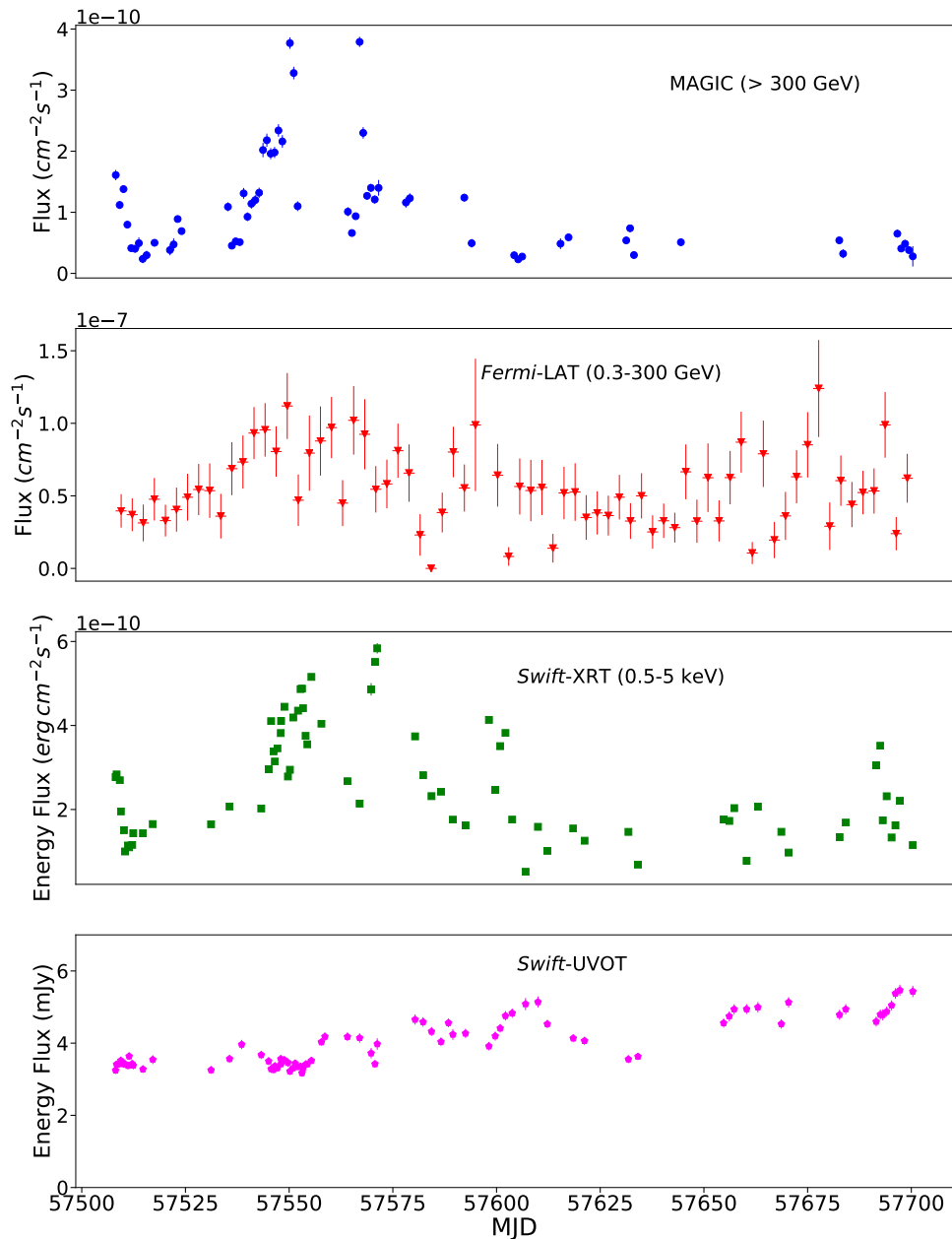


Figure 5.11: The multi-wavelength light curve of 1ES 1959+650 for the period 28th April–24th November 2016. Topmost panel: the VHE flux above 300 GeV measured by MAGIC. Second panel: The HE γ -ray photon flux from *Fermi*-LAT in the energy range 0.3–300 GeV. Third panel: X-ray energy flux from *Swift*-XRT in the energy range 0.5–5 keV. Bottom panel: UV/Optical energy flux from the *Swift*-UVOT instrument.

A better method to quantify the correlation between two discrete time series is the Discrete Correlation Function (DCF; (Edelson and Krolik, 1988)). For two discrete data trains, a_i and b_j , the unbinned discrete correlation is defined as:

$$UDCF_{ij} = \frac{(a_i - \bar{a})(b_j - \bar{b})}{\sqrt{(\sigma_a^2 - e_a^2)(\sigma_b^2 - e_b^2)}} \quad (5.10)$$

where σ_a, σ_b represents the standard deviations of the two data trains and e_a, e_b are the measurement errors associated with them. The DCF is obtained by averaging over M points having pairwise lag $\Delta_{ij} = t_i - t_j$ is the range of time-lag $\tau + d\tau/2 < \Delta_{ij} < \tau - d\tau/2$:

$$DCF(\tau) = \frac{1}{M} \sum UDCF_{ij} \quad (5.11)$$

Fig. 5.13 shows the DCF as a function of time-lag for the VHE γ rays and X-rays from the 1ES 1959+650 2016 monitoring campaign. The time-lag is calculated within $[-100, 100]$ days with a bin-size of 2.5 days. A hint of positive long-term correlation with zero lag can be seen between the two wavebands from the correlation plot shown in Fig. 5.13.

However, it is to be noted that providing a general trend for the entire light curve is a simplified approach. In general the cross-correlation behaviour can be quite complex with different trends between different observation epochs. A detailed statistical cross-correlation study requires a denser multi-year multi-band temporal coverage and should involve dividing the data into multiple epochs under varying source conditions to investigate its broadband variability, acceleration and emission mechanisms. Also the correlation patterns can differ by sub-dividing the X-ray and VHE band into sub-bands and cross-correlating them (Ahnen et al., 2018).

5.3.3 Spectral index vs flux correlation in VHE γ -ray and X-rays

As mentioned, the X-rays and VHE γ rays represent the most variable energy bands in 1ES 1959+650. The transition between the different flux states of the source are mostly reflected at these two energies.

In order to understand the trends in the spectral slopes as a function of the source flux, each observation night in MAGIC was fitted with a log-parabola-type spectrum (Eqn. 5.4) where the energy-dependent photon index is defined as $\Gamma(E) = \alpha + 2\beta \log_{10}(E/E_0)$ (Massaro et al. 2004) (a similar task was performed for the *Swift*-XRT dataset; analysis performed by Masaaki Hayashida). For the MAGIC analysis, the energy range of the fitting was fixed to 150 GeV - 1 TeV in order to avoid a possible high-energy cutoff and the normalization energy was fixed to 300 GeV (for XRT it was fixed to 1 keV). For each fit, the value of χ^2 was calculated and if the LogP function deviated from the observed spectra having a fit probability smaller than 5%, the observation night was discarded. For the surviving number of points, the value of the spectral index α was adopted as a measure of the local spectral index at the normalization energy E_0 .

Fig. 5.14 shows the plot of the MAGIC photon index vs flux on the left panel and the corresponding plot for XRT in the right panel. The index variation in X-rays clearly deviates from a fit with a constant function and shows a harder spectral index with increasing flux ("harder when brighter" behaviour) confirming the past trends (Krawczynski et al., 2004). A hint of a similar behaviour is also seen in the VHE band, but quantifying the exact trend might require a richer data set. Typicality of the "harder when brighter" trend in the VHE band will be further investigated by the author with a larger data set.

5.4 The remarkably bright VHE flares

The light curve above 300 GeV measured by MAGIC (Fig. 5.9), shows three very intense VHE flares on the nights of 13th June, 14th June and 1st July 2016, as discussed earlier. The average integral VHE flux in these nights reached $\sim 2.5 - 3$ times the Crab Nebula flux. In the following subsections a detailed study of these exceptional bright nights will be presented. The MAGIC data analysis and interpretation of the multi-wavelength data has been performed by the author himself.

5.4.1 The spectra during the highest flux nights

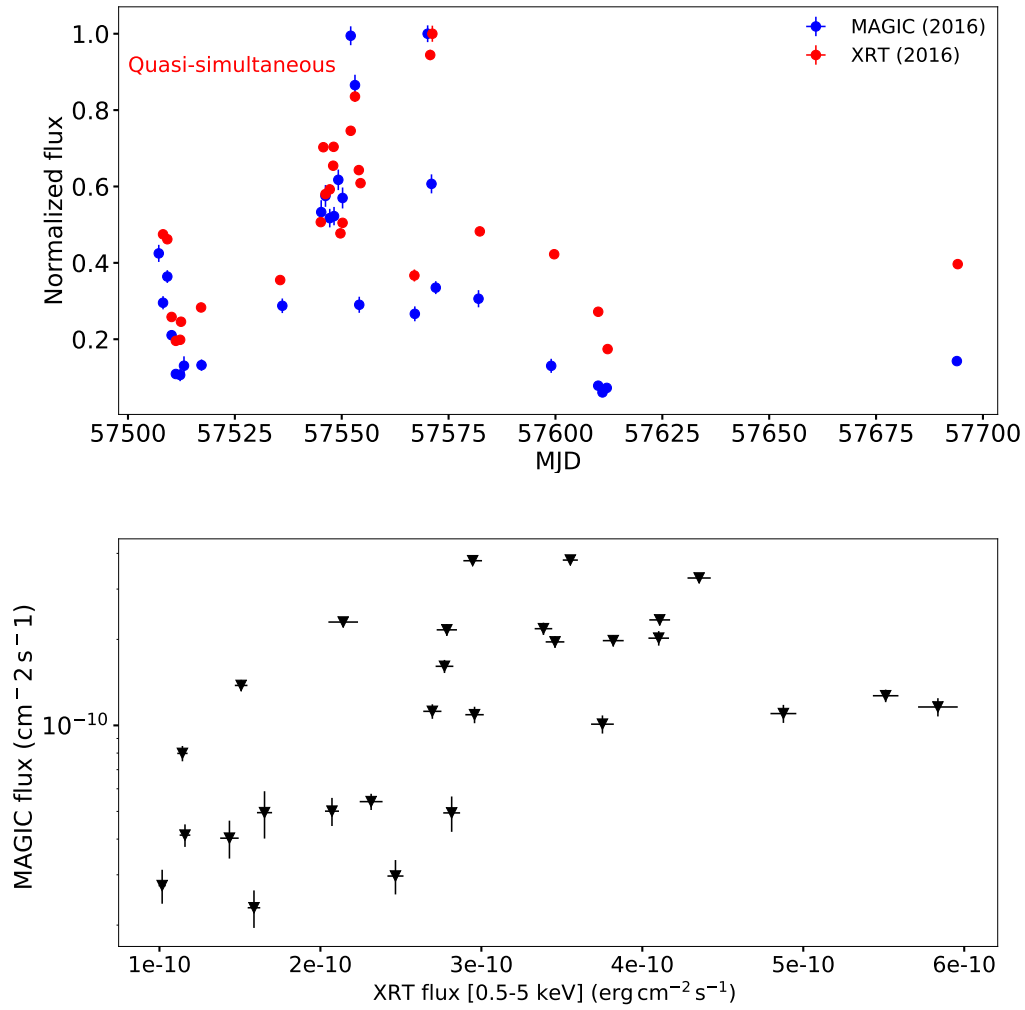


Figure 5.12: Long-term X-ray to VHE γ -ray correlation study. Top panel: Quasi-simultaneous X-ray and VHE flux (normalized to the highest flux in the respective energy band) vs MJD. Bottom panel: Correlation plot for the fluxes measured in the two energy bands.

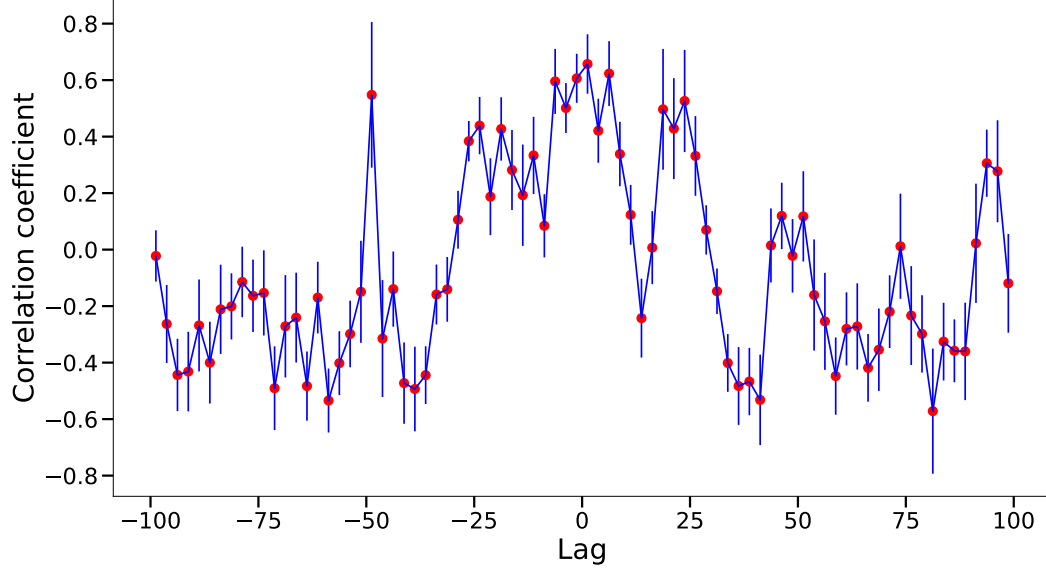


Figure 5.13: Discrete Correlation Function (DCF) plotted a function of time-lag in the range $[-100, 100]$ days for the VHE γ -ray and X-ray light curves of 1ES 1959+650 during 2016 monitoring campaign. The VHE γ rays show a hint of long-term correlation with the X-rays with zero time lag.

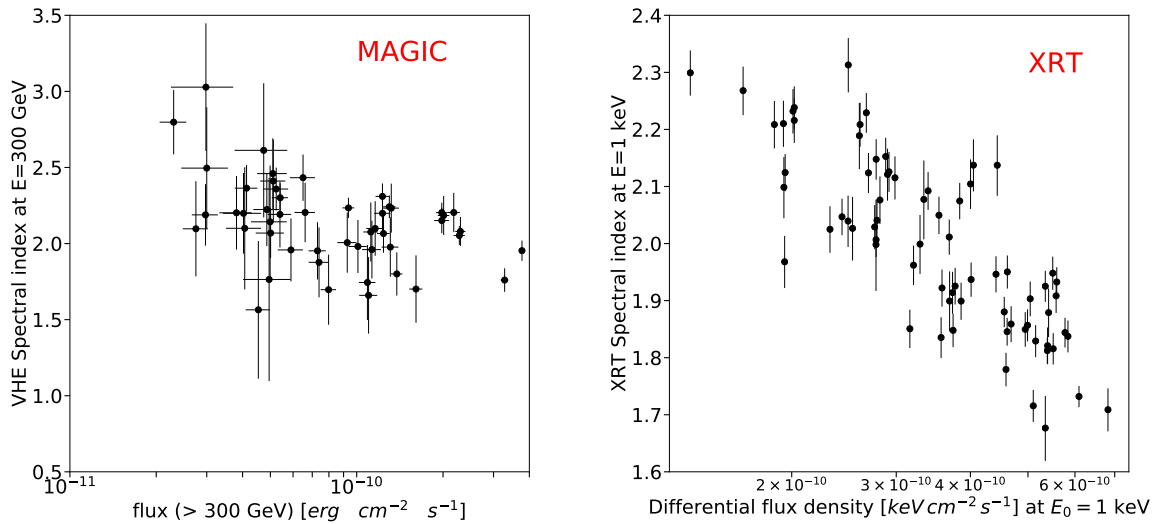


Figure 5.14: The α index of a LogP spectrum as a function of the MAGIC flux (left panel) and the XRT flux (right panel). The normalization energy was set to $E_0 = 300$ GeV for MAGIC and 1 keV for *Swift*-XRT. α gives a measure of the local spectral index at E_0 .

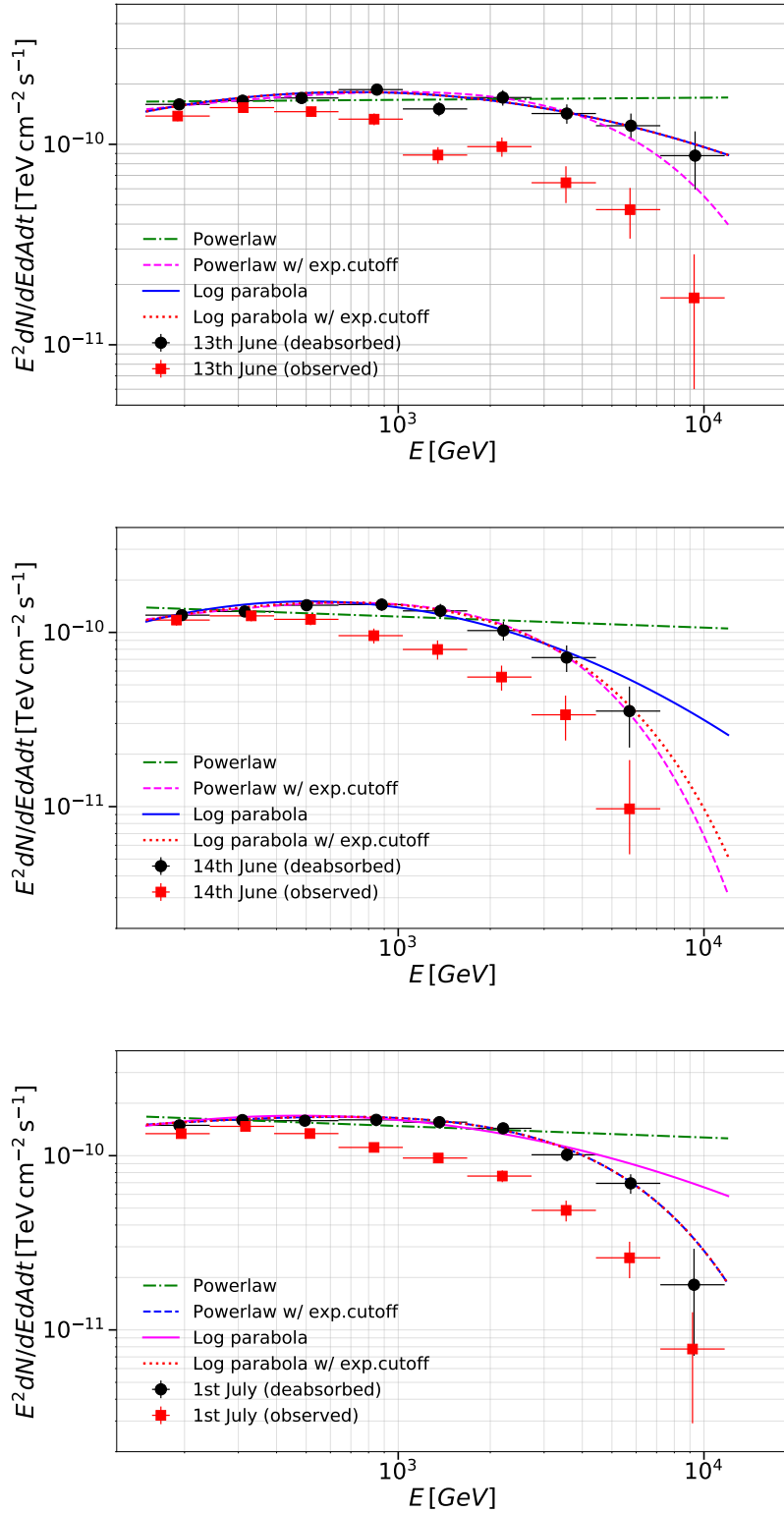


Figure 5.15: The SEDs from 13th June, 14th June, 1st July 2016 (top to bottom) obtained from MAGIC observations. The black points are the EBL-deabsorbed SEDs (with the model of Dominguez et al. (2011)) and the red points are the observed SEDs. The differential spectral functions fitted to the SEDs are shown with the solid, dashed, dotted and dot-dashed lines (see figure legend).

The VHE γ -ray spectra: The measurement of the VHE γ -ray spectra for 1ES 1959+650 is especially important for this study since the peak of the second SED hump lies in the VHE domain and is used to constrain the emission mechanisms and nature of the emitting particles.

Fig. 5.15 shows the SEDs for the nights of 13th June, 14th June and 1st July (top to bottom). The SEDs are unfolded with the instrument response functions of MAGIC. They are quite flat and extend up to several TeVs. The SEDs are fitted with four types of functions as given in Eqn. 5.2-5.5. The results are documented in Table 5.1. In all cases, the EBL-deabsorbed VHE spectra corrected with the EBL model of Dominguez et al. (2011) deviate from a pure power law behaviour and show a hint of curvature. However, no decisive preference is found between the fits with Eqns. 5.3-5.5. In most of the cases of the curved functions, the spectral index around 300 GeV is harder than 2.0. The bright flares allowed determination of the spectral cutoff energy with a statistical uncertainty of $\sim 30\%$. The spectra show a cutoff at few TeV energies when fitted with Eqn. 5.3 (see Table 5.1).

In order to perform unfolding of the EBL-deabsorbed spectra, a spectral function has to be assumed. For 13th June, a log-parabola-type spectrum is assumed for this purpose as the best-fitted function although the preference over a power law with exponential-cutoff-type function is very marginal (21% and 15% fit probability respectively). For the night of 14th June as well no decisive preference was found between the log parabola and power law with exponential cutoff-type spectral functions (fit probability 92% and 97% respectively). For 1st July the unfolding is performed by assuming a power law with exponential-cutoff spectral function (fit probability $\sim 20\%$). In all cases for the above three nights, the Likelihood Ratio Test shows only a marginal preference for a LogP with cut-off over a pure LogP (Eqn. 5.4) or PL with cutoff (Eqn. 5.3).

Constraining the second SED peak: The MAGIC observations plays a very important role to constrain the second peak of the broadband SED which lies in the VHE domain. The high flux states of the source enabled us to measure the peak of the second SED from the VHE γ -ray observations with a statistical uncertainty of less than 20%. To obtain the peak location, the SEDs are fitted with two additional functions apart from Eqns. 5.2-5.5 which are defined as:

$$\frac{dF}{dE} = F_0 \left(\frac{E}{E_{peak}} \right)^{-2} 10^{-\beta[\log(E/E_{peak})]^2} \quad (5.12)$$

and

$$\frac{dF}{dE} = F_0 \left(\frac{E}{E_{peak}} \right)^{-2} 10^{-\beta[\log_{10}(E/E_{peak})]^2} \exp\left(-\frac{E}{E_{cut}}\right). \quad (5.13)$$

At $E = E_{peak}$, the first derivative (with respect to energy) of the functions defined in Eqns. 5.12 and 5.13 multiplied by E^2 becomes zero, which enables us to measure the spectral peak position from the MAGIC SED. The peak location could be determined for the brightest flux nights to lie within 400 – 700 GeV, well constrained by the MAGIC observations. The obtained peak energies are similar to that of Mrk 501 SED observed in April 1997, June and July 2005 (Djannati-Atai et al., 1999; Albert et al., 2007b). Compared to the peak energy of Mrk 501 SEDs observed at some nights in 2012 (Ahnen et al., 2018), those peaks lie at slightly lower energies.

The multi-wavelength spectra: The analysis of the multi-wavelength spectra using the data from *Swift*-XRT, UVOT and *Fermi*-LAT instruments were performed for the purpose of broadband SED modeling of the flares. The data analysis was done for 13th June and 14th June. 1st July was discarded from the SED modelling due to lack of simultaneous X-ray and optical data. The multi-wavelength spectra in the optical/UV, X-ray and HE γ -ray bands are shown in the SED plots Fig. 5.20-5.23 (broadband SED modelling discussed in Sec. 5.4.4). The spectral data from the *Swift* and *Fermi*-LAT, along with the VHE γ -ray data are given in Appendix A.

The spectral index of the HE γ -ray spectra measured by *Fermi*-LAT with a binning of 1.5 days is 1.57 ± 0.20 . The measured index is harder than the value reported in the 3FGL catalogue, 1.88 ± 0.02 by more than 1σ (Acero et al., 2015) although the analysis energy range was different. The X-ray spectra are compatible with fitting by a power law function with indices 1.81 ± 0.01 on 13th June and 1.82 ± 0.01 on 14th June. These values of the spectral indices are harder than measurements from Tagliaferri et al. (2008) using the data from *Suzaku*-XIS in 0.7–10 keV, when the source was in a VHE-low state. The reason of increased hardness in the X-ray spectra during the 2016 flares may be attributed to the higher brightness of the source in the X-ray band in 2016: since in long-term 1ES 1959+650 typically showed a "harder when brighter" behaviour in the X-ray band, as shown in Sec. 5.3.3.

Table 5.1: VHE fit parameters for the nights of 13th June, 14th June, 1st July 2016.

Time	Flux > 300 GeV ($\text{cm}^{-2} \cdot \text{s}^{-1}$)	Fit model	F_0 ($\text{TeV}^{-1} \cdot \text{cm}^{-2} \cdot \text{s}^{-1}$)	Γ or α	E_{cut} (TeV)	β	E_{peak} (TeV)	$\chi^2/d.o.f$	
13th June 02:15–04:37 (MJD 57552.094 –57552.192)	$(3.77 \pm 0.09) \times 10^{-10}$	(5.2) PL	$(1.82^{+0.05}_{-0.05}) \times 10^{-9}$	$2.01^{+0.02}_{-0.02}$	24.68/10	
		(5.3) PL w/ cutoff	$(1.94^{+0.06}_{-0.06}) \times 10^{-9}$	$1.84^{+0.05}_{-0.05}$	$7.01^{+2.5}_{-1.5}$	13.2/9
		(5.4) LogP	$(1.89^{+0.05}_{-0.05}) \times 10^{-9}$	$1.84^{+0.04}_{-0.04}$...	$0.21^{+0.05}_{-0.05}$...	$0.72^{+0.11}_{-0.09}$	12.05/9
		(5.5) LogP w/ cutoff	$(1.89^{+0.05}_{-0.05}) \times 10^{-9}$	$1.83^{+0.05}_{-0.05}$	$+\infty$	$0.16^{+0.05}_{-0.05}$...	$0.7^{+0.02}_{-0.03}$	13.34/10
		(5.2) PL	$(1.48^{+0.05}_{-0.05}) \times 10^{-9}$	$2.08^{+0.02}_{-0.02}$	33.3/10
14th June 02:07–03:35 (MJD 57553.088 –57553.149)	$(3.28 \pm 0.02) \times 10^{-10}$	(5.3) PL w/ cutoff	$(1.72^{+0.07}_{-0.07}) \times 10^{-9}$	$1.77^{+0.07}_{-0.07}$	$3.01^{+0.9}_{-0.6}$	2.5/9	
		(5.4) LogP	$(1.59^{+0.06}_{-0.06}) \times 10^{-9}$	$1.81^{+0.05}_{-0.05}$...	$0.38^{+0.07}_{-0.07}$...	$0.51^{+0.05}_{-0.06}$	3.8/9
		(5.5) LogP w/ cutoff	$(1.68^{+0.09}_{-0.09}) \times 10^{-9}$	$1.81^{+0.06}_{-0.06}$	$+\infty$	$0.36^{+0.05}_{-0.18}$...	$1.0^{+1.8}_{-1.8}$	2.35/8
		(5.2) PL	$(1.77^{+0.03}_{-0.03}) \times 10^{-9}$	$2.1^{+0.02}_{-0.02}$	54.4/10
		(5.3) PL w/ cutoff	$(1.92^{+0.04}_{-0.04}) \times 10^{-9}$	$1.83^{+0.03}_{-0.03}$	$4^{+0.5}_{-0.4}$	12.6/9
23:59 30th June –04:58 1st July (MJD 57569.999 –57570.207)	$(3.79 \pm 0.08) \times 10^{-10}$	(5.4) LogP	$(1.84^{+0.04}_{-0.04}) \times 10^{-9}$	$1.88^{+0.03}_{-0.03}$...	$0.29^{+0.03}_{-0.03}$	$0.47^{+0.04}_{-0.04}$	18.5/9	
		(5.5) LogP w/ cutoff	$(1.92^{+0.04}_{-0.04}) \times 10^{-9}$	$1.82^{+0.04}_{-0.04}$	$3^{+1.03}_{-0.6}$	$0.1^{+0.1}_{-0.1}$	$+\infty$	$+\infty$	12.9/10

fitting functions are defined in Eqns. 5.2–5.5. Normalization energy $E_0 = 300$ GeV. The EBL model of Dominguez et al. (2011) has been used to calculate the deabsorbed spectra. The peak energy E_{peak} is determined by fitting the spectra with the functions defined in Eqns. 5.12–5.13. $+\infty$ means that the obtained energy is higher than the fitting range.

5.4.2 Intra-night variability

The investigation of the intra-night variability behaviour during bright VHE flaring states of blazars is not only important to constrain the size of the emission region giving rise to the high-state emission, but also essential to replicate the physical conditions inside the source contributing to the origin of the second SED hump.

During 2016, 1ES 1959+650 showed evidences of rapid flux variation within short timescales in the VHE γ -ray band observed by MAGIC, especially during the nights of the brightest flares. Typically, a MAGIC observation data run had a duration of 20 minutes. In order to investigate finer-scale flux variations of the source, the author analyzed the VHE light curve above 300 GeV with a fixed time-binning of 10 minutes. A finer time binning did not help to resolve finer substructures in the light curve and increased the statistical uncertainties of individual measurements.

The VHE light curves above 300 GeV with a fixed time binning of 10 minutes for the highest flux nights of 13th June, 14th June and 1st July 2016 are shown in Figs. 5.16-5.18. The flux level above the same energy threshold of our standard candle, the Crab Nebula is shown as well with a red dotted line for comparison purpose. As evident from the figures, on the nights of 13th June and 1st July, the source exhibited significant intra-night variability within short timescales. The night of 14th June did not show any significant short-term flux variations although the flux level was comparable to the other two nights. The probability of a constant flux on 14th June, as obtained by fitting the light curve with a constant function is $\sim 78\%$ as shown in the Fig. 5.18.

Fractional variability: The mean variability of the source can be measured in terms of its fractional variability amplitude (Vaughan et al., 2003). The fractional variability amplitude F_{var} is defined for a set of N flux points x_i having mean flux x_{mean} and error $\sigma_{i,err}^2$, in the following manner:

$$F_{var} = \sqrt{\frac{S^2 - \sigma_{mean,err}^2}{x_{mean}^2}} \quad (5.14)$$

where S^2 denotes the sample variance defined as :

$$S^2 = \frac{1}{N-1} \sum (x_i - x_{mean})^2 \quad (5.15)$$

and $\sigma_{mean,err}$ denotes the mean squared error defined as:

$$\sigma_{mean,err} = \frac{1}{N} \sum \sigma_{i,err}^2. \quad (5.16)$$

The error in F_{var} can be obtained following Eqn. B2 in Vaughan et al. (2003) which is defined as:

$$err(F_{var}) = \sqrt{\left(\sqrt{\frac{1}{2N} \frac{\sigma_{mean,err}}{x_{mean}^2 F_{var}}}\right)^2 + \left(\sqrt{\frac{\sigma_{mean,err}}{N} \frac{1}{x_{mean}}}\right)^2} \quad (5.17)$$

The fractional variability amplitude for 13th June, 14th June and 1st July are $F_{var} = 0.20 \pm 0.02, 0.06 \pm 0.05$ and 0.16 ± 0.02 respectively. The results shows that the activity levels of 13th June and 1st July are comparable, while no significant VHE activity can be detected on the night of 14th June.

Power spectral density: An alternative quantitative approach to measure the variability of a source is to calculate the power of variability as a function of the temporal frequency from the power spectral density (PSD) (Vaughan et al., 2003). The power spectrum can be defined as the modulus value of the discrete Fourier transform (DFT). For a fixed time-binned light curve having a discrete set of points at times t_i (where $i= 1, 2, \dots, N$), the power can be calculated from the following relation:

$$Pow(f_i) = A_0 \times |DFT(f_i)|^2 \quad (5.18)$$

where

$$|DFT(f_i)|^2 = [\sum x_i \cos(2it_i)]^2 + [\sum x_i \sin(2it_i)]^2 \quad (5.19)$$

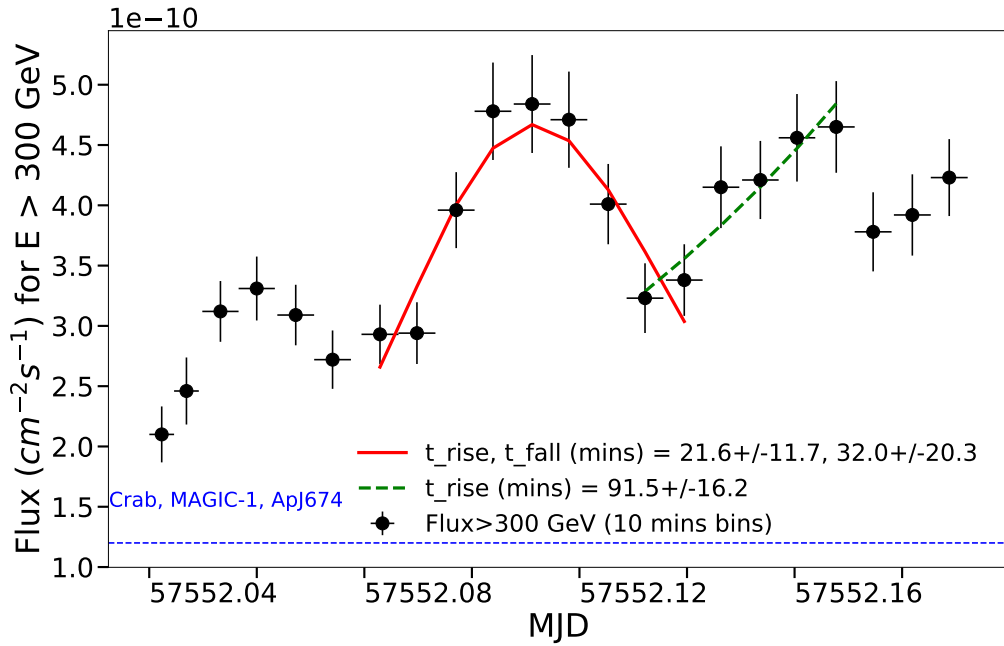


Figure 5.16: Intra-night variability observed in the VHE band on 13th June 2016. Solid-red curve: fit with the function given in Eqn. 5.21; green-dashed curve: fit with the function given in Eqn. 5.6. Rise and decay times of the individual substructures in the light curve are indicated in the legend.

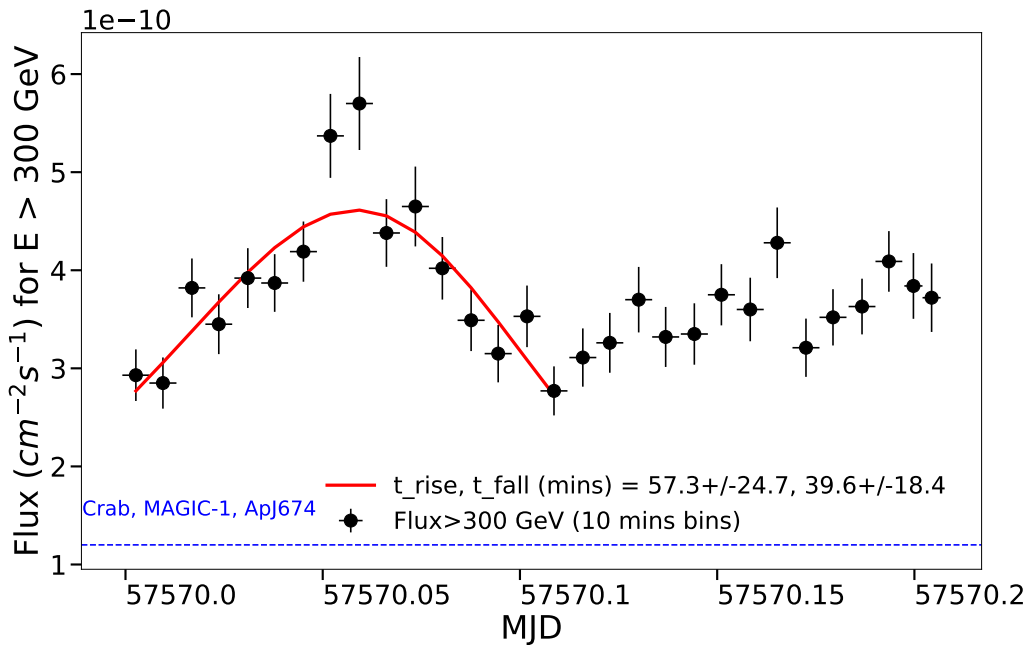


Figure 5.17: Intra-night variability observed in the VHE band on 1st July 2016. Solid-red curve: fit with the function given in Eqn. 5.21. Rise and decay times of the individual substructures in the light curve are indicated in the legend.

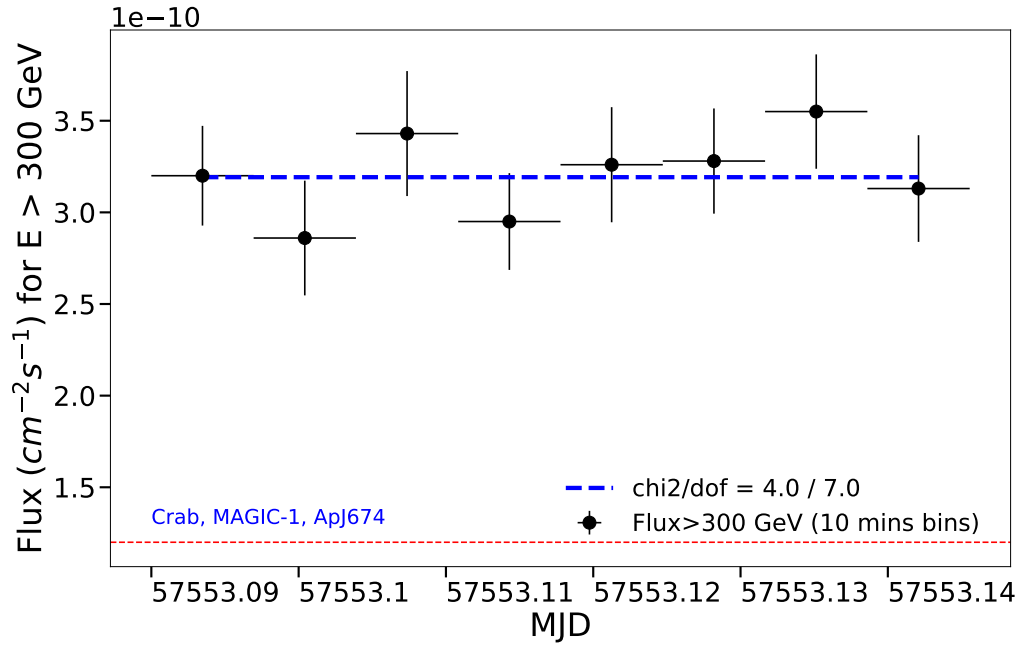


Figure 5.18: The fixed time-binned light curve above 300 GeV on 14th June 2016. The flux of 14th June was more or less a constant. blue-dashed curve: constant fit.

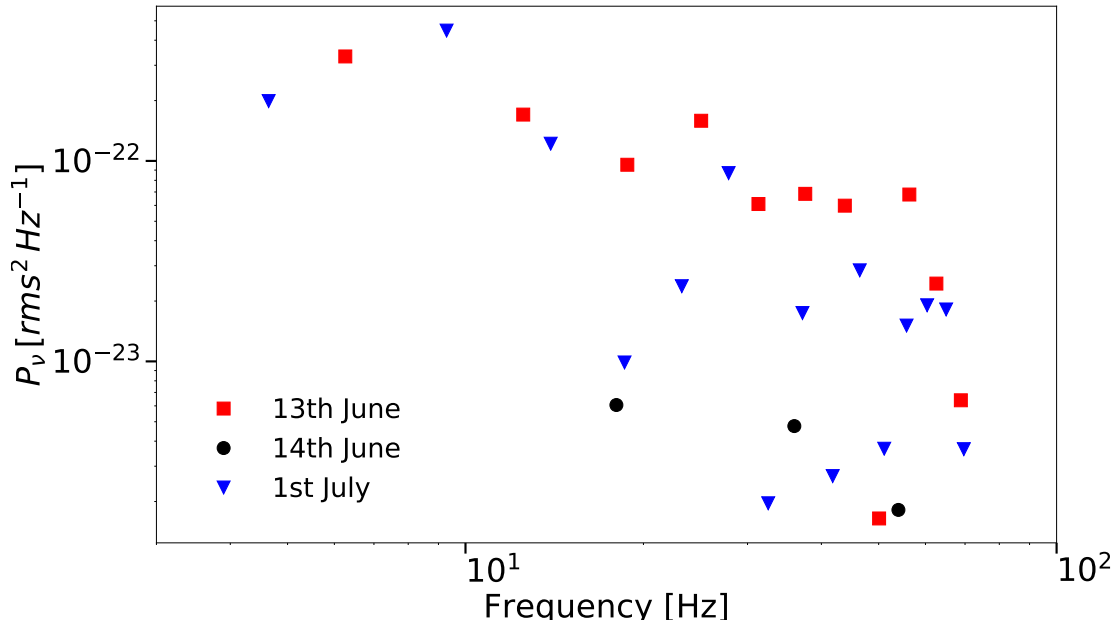


Figure 5.19: The power spectrum of the 2016 flares of 1ES 1959+650. Red squares: power spectrum of 13th June 2016; black circles: that of 14th June 2016; blue triangles: that of 1st July 2016.

Table 5.2: Results from fitting the individual substructures in the intra-night light curve of 13th June and 1st July with the functional forms given in Eqn. 7 and 8. $t_{rise} = t_r \times \log(2)$ and $t_{fall} = t_f \times \log(2)$

		13th June		
Func.	$\chi^2/d.o.f.$	t_{rise} (mins)	t_{fall} (mins)	
Eqn. 5.6	1.6/3	91 ± 16	-	
Eqn. 5.21	7.75/5	22 ± 12	32 ± 20	
		1st July		
Eqn. 5.21	19.1/12	57 ± 25	40 ± 19	

and the frequencies are defined as $f_i = \frac{j}{N}$ with $j=1,2,\dots,N/2$. A_0 represents the normalization factor of the power spectrum, defined as $A_0 = \frac{2}{N}$ according to [Vaughan et al. \(2003\)](#).

The results obtained from the PSD analysis are shown in Fig. 5.19. The index obtained from a power law fit to the PSD gives a measure of the variability power. The analysis of our data points shows that the power law index obtained from a fit to the PSD has the hardest value for 13th June, followed by 1st July (1.14 ± 0.12 and 1.36 ± 0.19 respectively). 14th June has the softest index (2.09 ± 0.28) amongst all 3 nights. Thus the nights of 13th June and 1st July shows more power in short-timescale variability compared to the night of 14th June. These results can be considered to be in agreement with the obtained fractional variability amplitudes. However, due to the small number of data points in our analysis, the slope determination of the PSD is not robust. Hence the fractional variability amplitude gives a more reliable measure of the flux variations.

The fastest variability timescale: The fastest variability can be estimated from the flux doubling timescale which is defined according to [Zhang et al. \(1999\)](#) as:

$$t_{var} = \frac{F_i + F_{i+1}}{2} \frac{t_{i+1} - t_i}{|F_{i+1} - F_i|} \quad (5.20)$$

F_i , F_{i+1} and t_i , t_{i+1} denote the fluxes and the corresponding observation times for two consecutive data points in the light curve respectively. The errors in the flux doubling timescale can be propagated through the errors of the individual flux points. The pair-wise shortest variability timescale for the night of 13th June 2016 was obtained between the 8th and the 9th points in the light curve shown in Fig. 5.16, having a value of $t_{var} = 36 \pm 14$ mins. The minimum value of the same quantity calculated for the night of 1st July 2016 was found to lie between the 2nd and the 3rd data points in the light curve with a flux doubling time of $t_{var} = 36 \pm 15$ mins.

The fastest variability timescale can be obtained with an alternative approach: by investigating the rising and decaying trends in the individual sub-structures in the light curves. The rising and decaying time of the individual sub-structures can be obtained by fitting them with an exponential function as defined in Eqn. 5.6 or sum of two exponential functions represented by the following formulae:

$$F(t) = A_0 / (e^{\frac{t_0-t}{t_r}} + e^{\frac{t-t_0}{t_f}}) \quad (5.21)$$

where A_0 represents two times the flux at time t_0 , t_r , t_f are the rise and decay times of the substructure. All these quantities are left as free parameters in the fitting process. The flux doubling time is defined as $t_{rise/fall} = t_{r/f} \times \log(2)$. For 13th June and 1st July, the results of the double-exponential fit are shown with the solid red curves in Figs. 5.16 and 5.17. The result of the single-exponential fit is shown with the green dashed curve in Fig. 5.16. The flux doubling times (t_{rise} and t_{fall}) obtained from the fitting procedure are tabulated in Table 5.2.

The fastest doubling times obtained from this procedure can be considered compatible with the results obtained from the [Zhang et al. \(1999\)](#) formulation. However, the results from the fitting technique are mildly dependent on the range of the fit. For the purpose of the theoretical discussions in the next section, the fastest timescales obtained from the [Zhang et al. \(1999\)](#) formulation have been used.

5.4.3 Size of the emission region

The size of the emission region can be constrained from the observed variability timescale of blazars. This step is fundamental to characterize the broadband emission properties of the source. In the broadband SED modelling discussed in the next section, the emission volume is assumed to be a uniform sphere of radius R . The variability timescales t_{var} can be used to derive an upper limit (UL) to the size of the radiating blob in the co-moving frame of the jet using the following relation (Tavecchio et al., 2010b):

$$R \leq \frac{ct_{var}\delta}{1+z}. \quad (5.22)$$

δ represents the Doppler factor of the emitting blob and z represents the redshift of the source. The fastest flux doubling time in the VHE γ -ray band obtained from the MAGIC observations (see Sec. 5.4.2) is used to calculate the UL on R . By assuming the value of the Doppler factor to lie between $\delta = 20 - 60$, the UL to R is estimated in the range $10^{15} - 3 \times 10^{15}$ cm. However, it is to be noted that the VHE spectra used in the broadband SED modelling of 13th June and 14th June, are representatives of an average emission state of the source for the whole observation night. It is thus not a true representative of the finer scale flux variations as shown in, for example, the 10 minutes-binned light curve of 13th June (Fig. 5.16). Hence our derived ULs are conservative estimates. In the calculations, a variability timescale of $t_{var} \sim 35$ minutes has been assumed (from Zhang et al. (1999) formulation; Sec. 5.4.2).

In the case of the hadronic emission models, where the presence of an ultra-relativistic proton population is assumed inside the emission region, an additional constraint to the size of the emission region is obtained by the following condition: size of the emission region should be always greater than the gyro-radius of the highest energy protons. This is known as the so-called Hillas criterion which can be represented by the following mathematical formula

$$B(\text{G}) \geq 30 \frac{E_{p,max}}{10^{19}(\text{eV})} \frac{R}{10^{15}(\text{cm})} \quad (5.23)$$

where $E_{p,max}$ represents the maximum energy of the protons and B represents the magnetic field strength inside the radiation zone. This condition is always respected in our broadband SED models.

5.4.4 Broadband emission modeling

In this section, the broadband SED modelling during the brightest flaring nights of 13th June and 14th June 2016 will be discussed (1st July is not included due to lack of simultaneous optical/UV and X-ray data). For the interpretation of the broadband SEDs, single emission zone models/one-zone models are considered, i.e. it is assumed that the multi-wavelength electromagnetic data spanning optical/UV up to VHE γ -rays originate from the same region of the blazar jet. The theoretical interpretation is discussed in the framework of three different emission scenarios - one-zone leptonic, hadronic and lepto-hadronic models. The code used for the broadband SED modelling is discussed in Chapter 6, where a more detailed description about the implementation of the individual non-thermal radiative processes can be found. The emission region is assumed to be a uniform spherical blob having a radius R and containing a randomly-oriented magnetic field of strength B . The spherical blob is moving down the jet with a bulk Lorentz factor denoted by Γ_{bulk} . The radiated photons in the co-moving frame of the jet are assumed to subtend an angle θ with respect to an observer on Earth. The outputs from the different non-thermal radiative processes at work inside the source are calculated in the frame of the jet and then transformed to the frame of the observer on Earth using the Doppler transformations (see Sec. 6.1.2). The Doppler factor is defined as $\delta = [\Gamma_{bulk}(1 - \beta \cos(\theta))]^{-1}$.

The total jet power is evaluated as:

$$L_j = \pi R^2 c \Gamma_{bulk}^2 (u_p + u_B + u_e) \quad (5.24)$$

where u_p, u_B, u_e represent the energy densities carried by the protons, magnetic field and electrons respectively, in the co-moving frame of the jet.

The different emission scenarios for the 1ES 1959+650 2016 flares are discussed below.

Leptonic emission model

First, a one-zone SSC model has been investigated for the SEDs of 1ES 1959+650. It was assumed that a stationary population of ultra-relativistic electrons is present within the jet. The stationary state of the primary electron distribution is assumed to follow a broken power law described with the following functional form:

$$f(\gamma) = e^{-\frac{\gamma}{\gamma_{e,max}}} \begin{cases} F_0 \left(\frac{\gamma}{\gamma_0}\right)^{-\alpha} & : \gamma < \gamma_{e,brk} \\ F_0 (\gamma_{e,brk}/\gamma_0)^{n_2-n_1} (\gamma/\gamma_0)^{-n_2} & \gamma > \gamma_{e,brk} \end{cases} \quad (5.25)$$

Here $\gamma = E_e/m_e c^2$ represents the Lorentz factor of the electrons (m_e is the electron rest mass), F_0 is the electron spectrum normalization, n_1 , n_2 are the two slopes before and after break, $\gamma_{e,brk}$ denotes the break Lorentz factor and $\gamma_{e,min}$, $\gamma_{e,max}$ denotes the minimum and maximum Lorentz factors respectively. γ_0 is the normalization factor which is fixed to the Lorentz factor equivalent to the rest mass energy of an electron i.e. 1.

In the formalism adopted for this work, the break energy is calculated assuming a balance between the synchrotron cooling timescale and the electron escape timescale. This can be formulated using the following relation:

$$t_{e,sync} = \frac{7.75 \times 10^8}{B^2 \times \gamma_{e,brk}} = \frac{R}{c} \quad (5.26)$$

Here $t_{e,sync}$ represents the synchrotron cooling timescale of the electrons and R/c parametrizes the energy-independent escape timescale of the electrons.

From the results of the leptonic modelling, values of n_1 between 2.25–2.3 were found to provide satisfactory description to the low energy data from *Swift*-XRT and UVOT instruments. Since it has been assumed in this work that the break in the stationary electron spectrum (injected as a power law) arises due to radiative cooling, the spectral index after the break is constrained as $n_2 = n_1 + 1$. However, it is to be noted that the assumption of cooling break ($\Delta N = n_2 - n_1 = 1$) comes from the simplest expectations and in reality the acceleration and cooling processes can be much more complex leading to a different spectral behaviour (see for e.g. [Tavecchio et al. 2010a](#)).

The minimum Lorentz factor is treated as a free parameter and chosen so as to obtain a satisfactory description of the HE γ -ray data. The data could be satisfactorily fit with $\gamma_{e,min} \sim 3 \times 10^2 - 10^3$, which are reasonable values broadly used in the literature (e.g.: [Ahnen et al. \(2018\)](#), [Abdo et al. \(2011\)](#)). The peak position of the first SED hump is used to constrain the magnetic field strength (although the first SED peak is not well-constrained due to lack of simultaneous hard X-ray data, it gives a rough estimate of the peak position). The magnetic field strength can be used to estimate the break Lorentz factor $\gamma_{e,brk}$ for a given value of R (from the Eqn. 5.26).

The EBL-corrected VHE spectra obtained from the MAGIC observations are quite flat and extend up to several TeV, especially for the 13th June flare. However, due to the fast radiative cooling of the ultra-relativistic electrons in the presence of the magnetic field and the Klein-Nishina effect that tries to steepen the spectra at the highest energies, the inverse Compton emission component is generally suppressed. Therefore, it is difficult to explain the flat photon spectrum observed up to TeV energies. In order to overcome this constraint, high values of the Doppler factor and low values of the magnetic field strength are adopted in this model to reproduce the VHE spectra observed by MAGIC up to multi-TeV energies.

The results from the SSC modelling are shown in Fig. 5.20. The multi-wavelength SED of 13th June can be satisfactorily explained with $\delta \geq 45-50$. The broadband SED of 14th June requires comparatively smaller values of the Doppler factor, $\delta \geq 30$. The difference in the values of the estimated Doppler factor mainly arises due to the differences in spectral cutoff/hardness in the VHE data measured by MAGIC for the nights of 13th June and 14th June. The parameter estimates obtained from the SSC modelling are tabulated in Table. 5.3.

The jet power is largely dependent on the value of $\gamma_{e,min}$, especially for soft electron spectra as in our case. For the relatively large values of $\gamma_{e,min}$ for the SSC solutions, the electron energy density u_e dominates over the magnetic energy u_B by ~ 2 orders of magnitude giving the dominating contribution to the overall jet power.

Hadronic model

In the hadronic model, it is assumed that an additional population of ultra-relativistic protons is injected into the emission region along with the primary electron distribution as described above. The proton distribution is

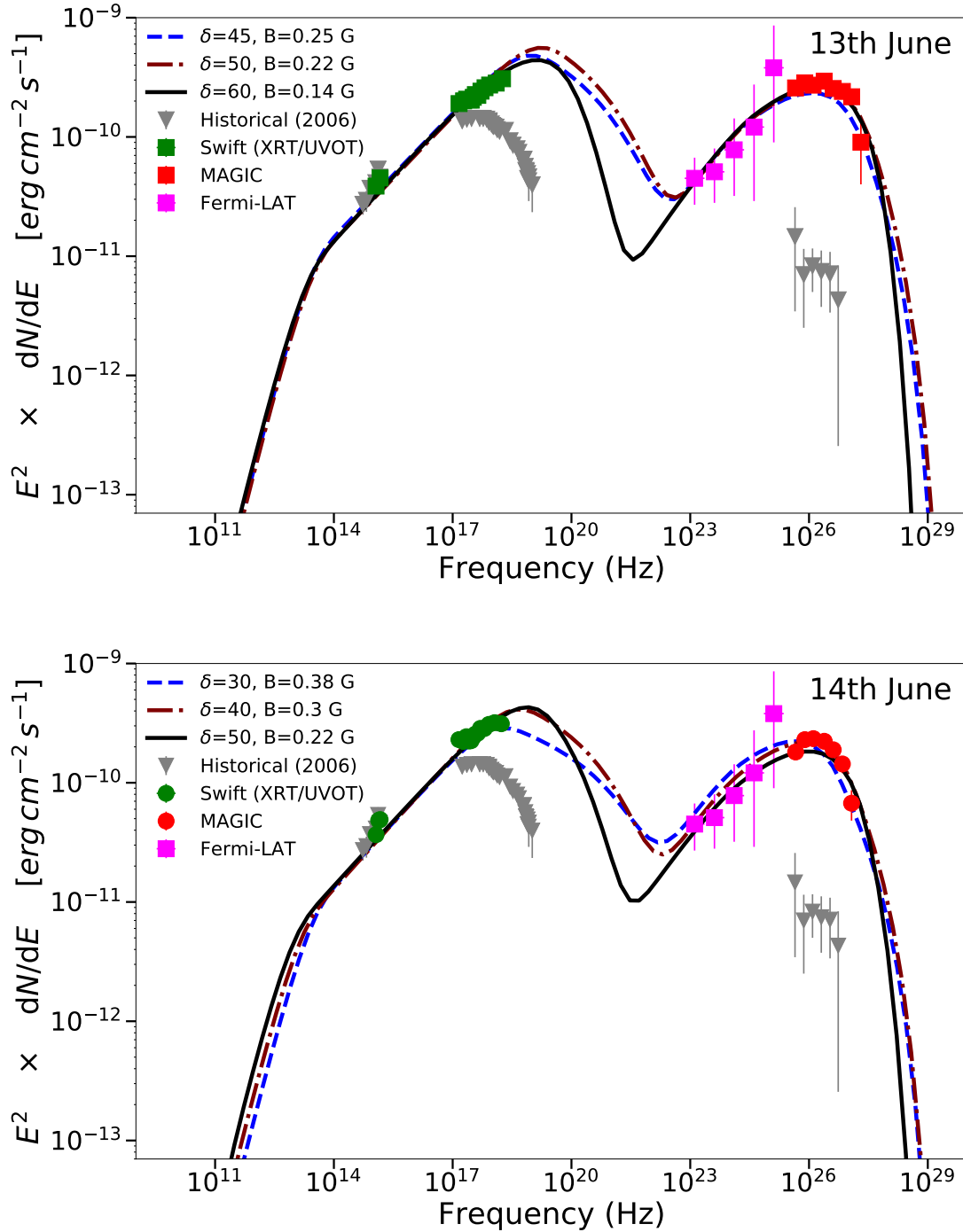


Figure 5.20: SSC model fits to the broadband SEDs of 13th June (top panel) and 14th June (bottom panel) 2016. The data from different instruments are indicated in the legend. The historical data taken from [Tagliaferri et al. \(2008\)](#) is shown in grey. The dashed blue, dot-dashed brown and black solid curves represent the summed SED model in increasing order of Doppler factor δ . The multi-wavelength data from 13th June requires high values of $\delta > 45$. The SED from 14th June could be explained with comparatively moderate values, $\delta \sim 30$ -50. The model parameters are given in Table 5.3.

Table 5.3: Parameters for the SSC, hadronic and lepto-hadronic modelling of the 13th and 14th June flares of 1ES 1959+650.

Parameters	13th June			14th June	
	SSC	Hadronic	Lepto-hadronic	SSC	Hadronic
δ	40–60	25	45	30–50	25
B (G)	0.1–0.25	150	0.6	0.2–0.4	150
R (cm)	7×10^{14} – 10^{15}	2.1×10^{14}	4×10^{14}	8×10^{14} – 10^{15}	2.1×10^{14}
n_1	2.2–2.3	2.3	2.3	2.2–2.3	2.28
n_2	3.2–3.3	...	3.3	3.2–3.3	...
$\gamma_{e,min}$	7×10^2	5	8×10^2	$3\text{--}7 \times 10^2$	5
$\gamma_{e,max}$	10^6 – 7×10^6	5×10^4	7×10^6	10^6 – 7×10^6	5×10^4
$\gamma_{e,brk}$	4×10^5 – 10^6	...	2×10^5	10^5 – 5×10^5	...
n_p	...	2.23	2.2	...	2.23
$\gamma_{p,min}$...	1	1	...	1
$\gamma_{p,max}$...	7×10^9	6×10^7	...	5×10^9
L_j (erg/s)	10^{43} – 5×10^{43}	1.5×10^{46}	8×10^{48}	10^{43} – 3×10^{43}	10^{46}

described with a power law with exponential cutoff function having the following parametric form:

$$f(\gamma) = F_0 \left(\frac{\gamma_p}{\gamma_{p0}} \right)^{-\alpha} e^{-\frac{\gamma_p}{\gamma_{p,max}}} \quad (5.27)$$

Here $\gamma_p = E_p/m_p c^2$ represents the Lorentz factor of the protons (m_p represents the rest mass of a proton). F_0 represents the proton spectrum normalization, the proton spectral index is denoted by n_p and the exponential cutoff Lorentz factor is denoted by $\gamma_{p,max}$. The minimum proton Lorentz factor was set to $\gamma_{p,min}=1$ in order to get a conservative estimate of the proton luminosity budget, which usually dominates the overall jet power in the hadronic solutions. The maximum proton energy in the co-moving frame is constrained by physical considerations on the acceleration and the different cooling timescales. $\gamma_{p,max}$ is determined from the following condition (Cerruti et al., 2015):

$$t_{acc} = \text{minimum}[t_{esc}, t_{psync}, t_{p-\gamma}] \quad (5.28)$$

Here $t_{acc} = 10\eta_{acc}E_p/eBc$ denotes the acceleration timescale where the dimensionless parameter η_{acc} denotes the acceleration efficiency; $\eta_{acc} = 1$ for the most efficient acceleration. t_{esc} denotes the particle escape timescale defined as $t_{esc} = \eta_{esc}R/c$ (Aliu et al., 2014), where η_{esc} denotes the efficiency of escape. $t_{psync}, t_{p-\gamma}$ represents the proton-synchrotron cooling and photo-meson cooling timescales respectively which are defined as:

$$t_{psync} = 4.5 \times 10^4 B_{100}^{-2} E_{19}^{-1} \quad (5.29)$$

where $B_{100} = B/100$ G and $E_{19} = E_p/10^{19}$ eV (Aharonian, 2000) and

$$t_{p-\gamma} = \frac{1}{c \langle \sigma_{pff} \rangle n_{ph}(\epsilon)} \quad (5.30)$$

where the inelasticity-weighted p- γ interaction cross-section $\langle \sigma_{pff} \rangle = 10^{-28} \text{cm}^2$ and $n_{ph}(\epsilon)$ is the seed photon density (Böttcher et al., 2013). The different cooling timescales and the acceleration timescale are shown in Fig. 5.21 (top panel).

In the hadronic solution, synchrotron radiation by the highest energy relativistic protons (few EeV in the co-moving frame) can satisfactorily reproduce the second SED peak located at few hundreds of GeV (see Sec. 5.4.1). The synchrotron radiation of the ultra-relativistic electrons still gives rise to the first peak of the SED. The proton-synchrotron solutions are shown in Fig. 5.22. The proton-synchrotron component is denoted by the dot-dashed blue line. The photo-meson cascade component is denoted by the dot-dot-dashed orange line. It arises due to emission by the secondary e^+/e^- pairs that are generated when a high-energy proton interacts with the low-energy soft photon field composed of the electron synchrotron emission. The photo-meson cascade (or p- γ cascade) component gives a sub-dominant contribution to the overall SED in the chosen parameter space.

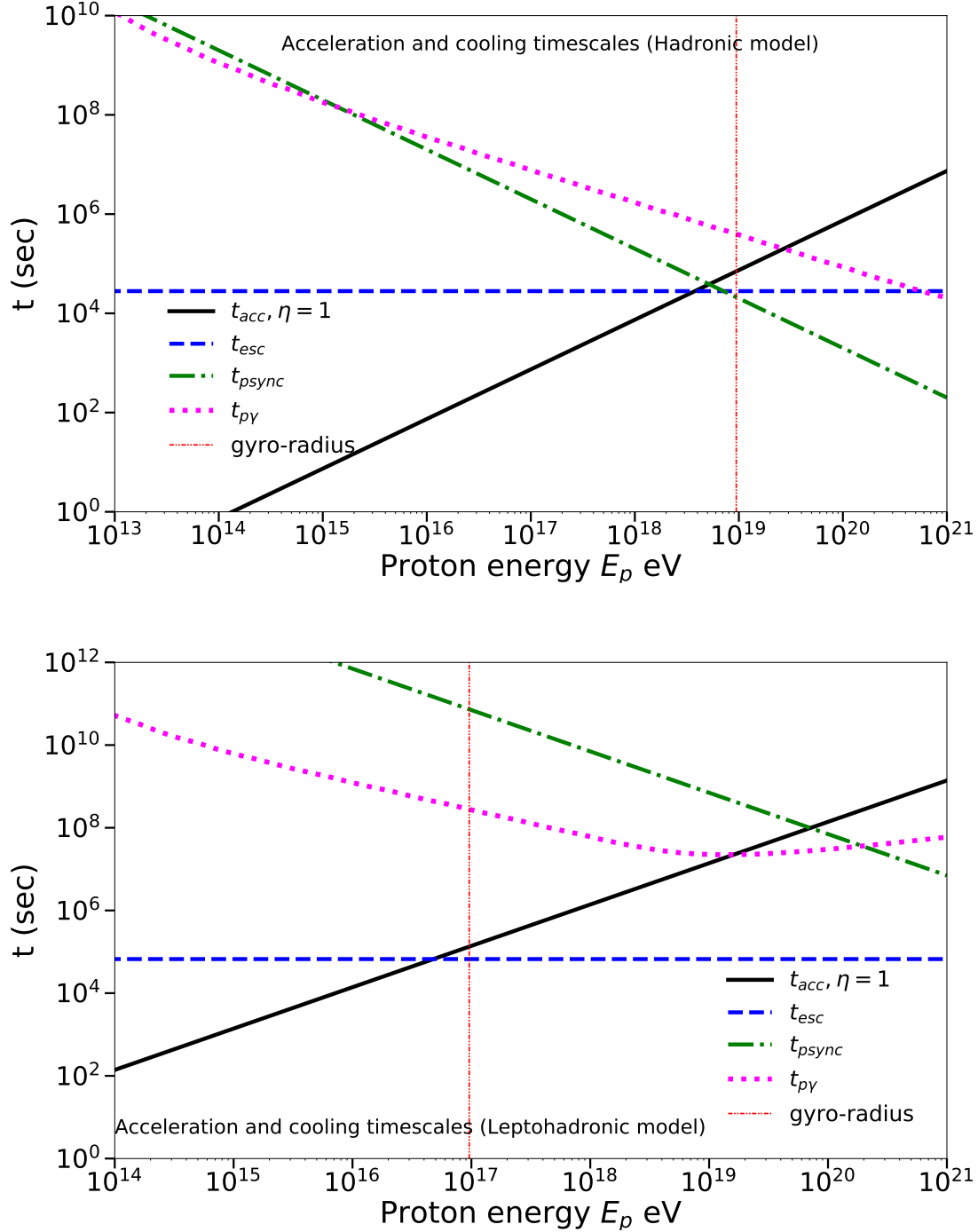


Figure 5.21: Comparison between the acceleration (t_{acc}) and cooling timescales ($t_{esc}, t_{psync}, t_{p\gamma}$) for the hadronic (top panel) and mixed lepto-hadronic (bottom panel) models for 13th June 2016. The acceleration efficiency η_{acc} was chosen to be 1. The energy corresponding to which the proton gyro-radius becomes equal to the size of the emission zone is shown with the red dot-dashed line.

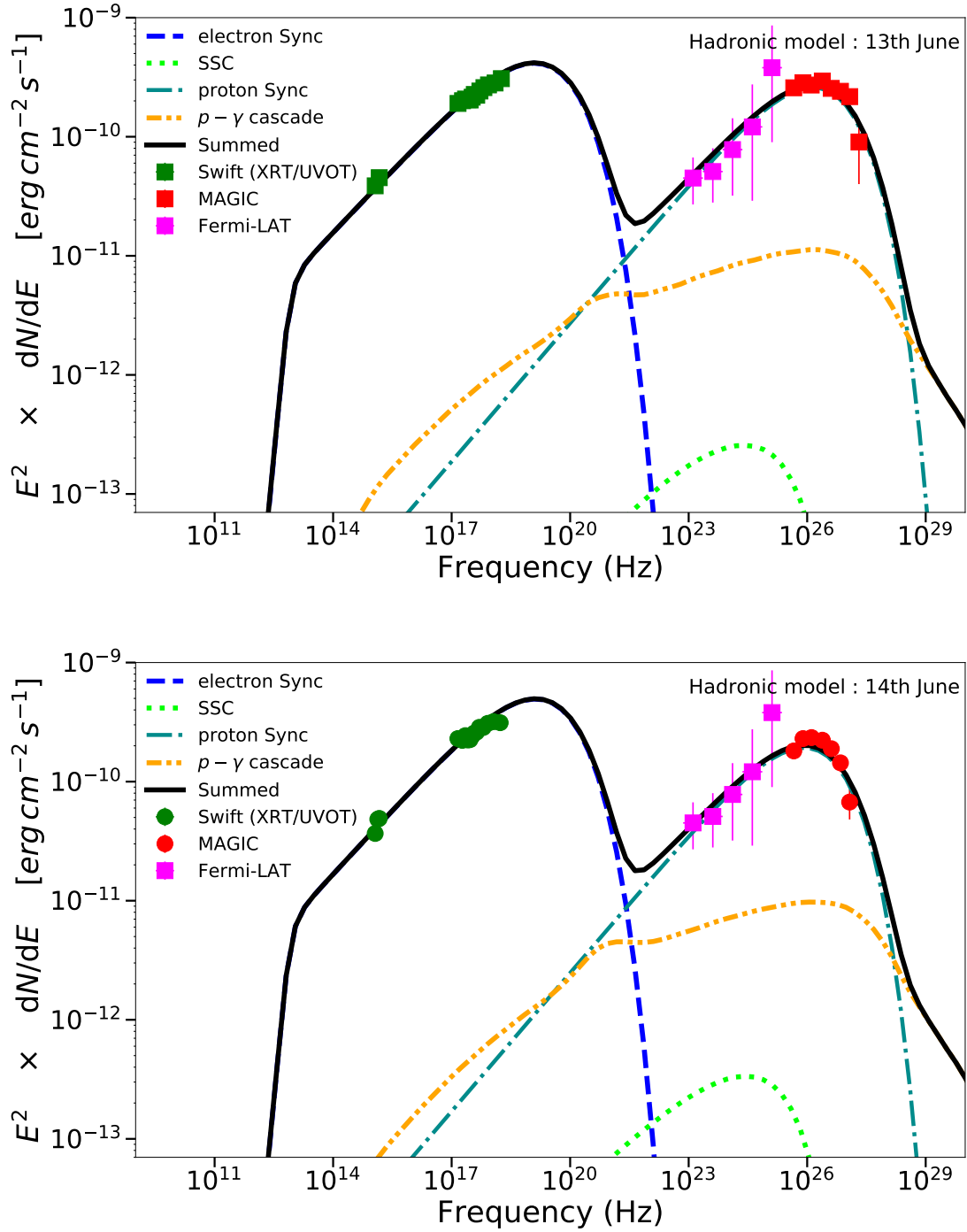


Figure 5.22: Hadronic model fits to the broadband SEDs of 13th June (top panel) and 14th June (bottom panel) 2016. The data from different instruments are indicated in the legend. Black solid line: summed SED; blue dashed line: electron synchrotron; green dotted line: SSC; green dot-dashed line: proton synchrotron; orange dot-dot-dashed line: $p-\gamma$ cascade. Synchrotron radiation by ultra-relativistic protons give a dominant contribution to the higher energy SED peak with parameters $B \sim 100$ G, $E_{p,max} > 10^{18}$ eV and overall jet power $L_j \sim 10^{46}$ erg/s ($\sim L_{Edd}$). The model parameters are given in Table 5.3.

To achieve a satisfactory description of the VHE γ -ray data, the protons have to be accelerated up to extremely high energies (EeV scale). Proton acceleration up to EeV energies is possible if the source possesses very high acceleration efficiency ($\eta_{acc} = 1$) and high values of the magnetic field (see the timescale plots in Fig. 5.21 (top panel)). Large values of the magnetic fields (>100 G) are required in order to overcome the slow cooling time of protons which is generally insufficient to explain sub-hour scale variability as observed during the 2016 flares. Under these conditions the proton cooling time is $t_{psync} \sim 2.5 \times 10^4$ s, which is shorter than the co-moving frame variability timescales ($\Delta t_{jet} = \delta \Delta t_{var}$) observed in the VHE band by MAGIC. Moreover, the magnetic field strength is a function of the distance from the central core which is defined by:

$$d = \frac{\delta c t_{var}}{(1+z)\theta_j} \quad (5.31)$$

where θ_j represents the jet-opening angle. For our choice of $R \sim 2 \times 10^{14}$ cm and assuming a typical value of the jet-opening angle ~ 1 degree, the distance from the central core becomes $d \sim \text{few } 10^{16}$ cm. At such distances from the central core, $B \sim 100$ G can be expected (e.g. Barkov et al. 2012).

No break is assumed in the stationary proton spectrum since the cooling time of the protons is slow and the propagated spectrum essentially remains uncooled for the adopted choice of parameters. For the chosen large value of the magnetic field (~ 150 G), the primary electrons are in the fast cooling regime and can be parametrized by a simple power law function. The complete list of model parameters for 13th and 14th June can be found in Table 5.3. The required value of the Doppler factor in the proton-synchrotron solutions is considerably less ($\delta \sim 25$) compared to the one-zone SSC models, especially for 13th June. The difference between the VHE spectra from 13th June and 14th June can be mainly attributed to the slightly different values of $\gamma_{p,max}$ in the proton-synchrotron solutions (14th June requires smaller values of $\gamma_{p,max}$ than 13th June: $\sim 5 \times 10^9$ and $\sim 7 \times 10^9$ respectively).

Large value of the total jet power dominated by the kinetic energy density of the protons is required for the proton-synchrotron dominated solutions ($L_j \sim 2 \times 10^{46}$ erg/s). This is comparable to the Eddington luminosity ($L_{Edd} \sim 10^{46}$ erg/s) of the source (assuming $M_{BH} = 10^8 M_{solar}$; Falomo et al. 2002). The requirement of high jet power is one of the common problems of hadronic models.

Lepto-hadronic model and implications for neutrino emission

The proton-synchrotron models usually predict neutrino fluxes falling below the sensitivity limit of the current generation of neutrino telescopes. An alternative lepto-hadronic solution was thus investigated. Similar to the hadronic model, here also injection of a stationary population of ultra-relativistic protons having the same functional form is assumed along with the primary electrons. In the lepto-hadronic solutions the second SED peak is attributed to a joint contribution of the SSC and the p- γ cascade component as shown in Fig. 5.23 (top panel). Here, the maximum proton energy is determined by the particle escape timescale, as shown in the timescale plot of Fig. 5.21 (bottom panel) ($\gamma_{p,max} \sim 6 \times 10^7$). All the other model parameters obtained from the fit are tabulated in Table 5.3.

The maximum proton energy primarily determines the peak energy of the predicted neutrino spectra. As seen in the previous section, the proton-synchrotron solutions require fairly large values of the $E_{p,max}$. Hence the inferred neutrino spectra from such a model peak at $>\text{EeV}$ energies in the frame of the observer and the obtained neutrino flux is also quite low. In case of the lepto-hadronic solution, due to the requirement of much lower values of $\gamma_{p,max}$ the neutrino spectra peak about two orders of magnitude lower. The predicted neutrino spectra from the lepto-hadronic and proton synchrotron solutions are shown in Fig. 5.23 (bottom panel). The black steps shown in the figure represent the IceCube sensitivity curve, calculated for 8 years of operation and at the declination of 1ES 1959+650 (Aartsen et al., 2018). It is to be noted that it is difficult to directly compare the derived neutrino spectra obtained from the modelling of 2016 VHE flares and the IceCube sensitivity, due to a variable nature of the 1ES 1959+650 electro-magnetic emission. The neutrino spectra, calculated for a short-lasting high emission state, falls slightly short of the IceCube sensitivity limit. Therefore it can be expected that on average the neutrino emission from 1ES 1959+650 will be much lower than that derived during the 2016 flares. The integrated neutrino flux from the lepto-hadronic model in the 600 GeV–100 TeV (i.e. central 90% confidence level (C.L.) neutrino energy range for the declination of $\sim 65^\circ$, calculated from Fig. 1, bottom panel in Aartsen et al. 2018) is $\sim 5.5 \times 10^{-13} \text{ TeV cm}^{-2} \text{ s}^{-1}$. The derived value is comparable to the upper limit flux obtained by

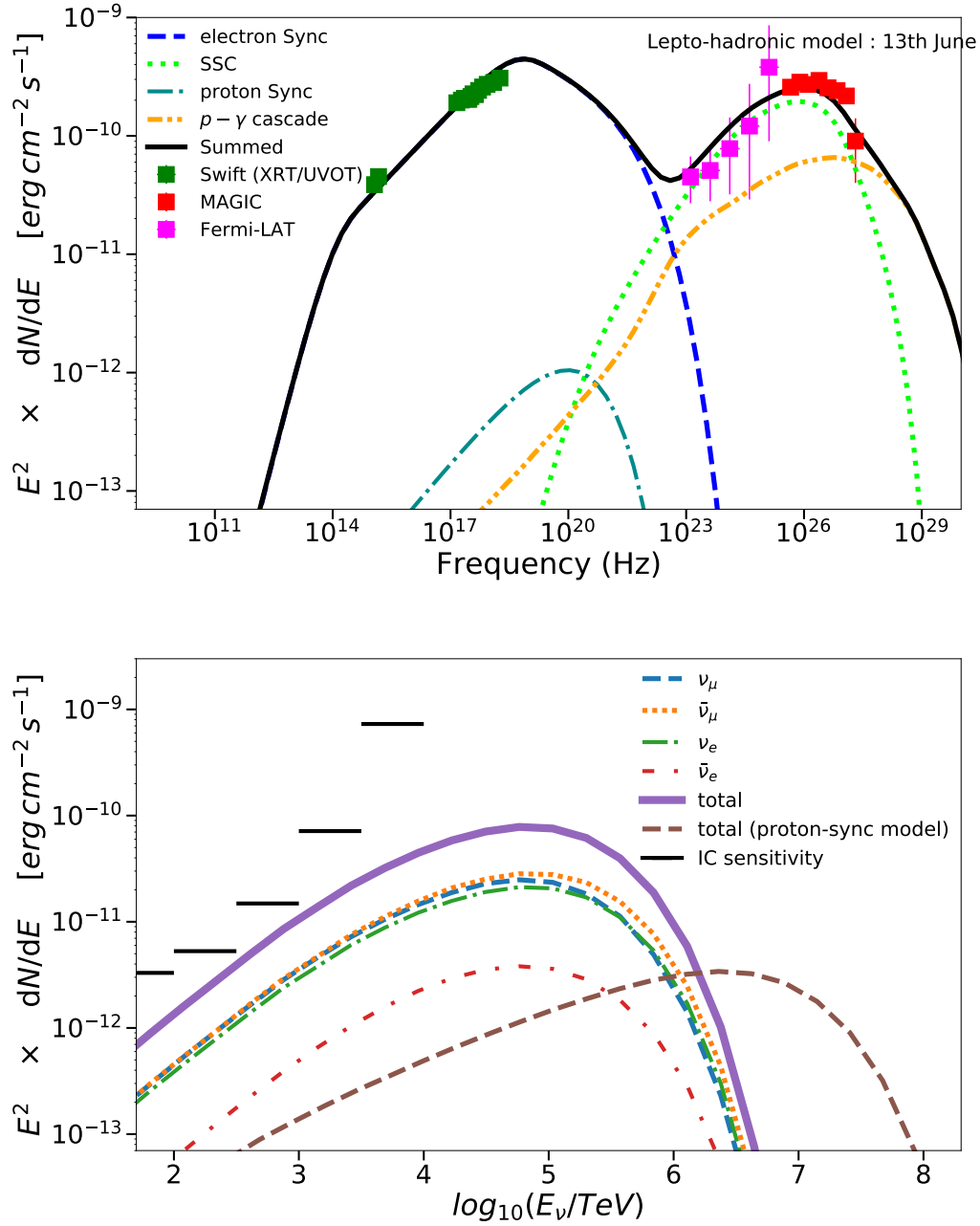


Figure 5.23: Lepto-hadronic model fit to the broadband SED of 13th June 2016 (top panel) and the predicted neutrino fluxes (bottom panel). The meanings of the symbols and lines in the top panel are same as in Fig. 5.22. The high-energy SED peak in this case arises from a combination of SSC and p- γ cascade component (with parameter values $B \sim 1$ G, $E_{p,max} > 10^{16}$ eV and overall high jet power $L_j > 10^{48}$ erg/s $\gg L_{Edd}$). The meanings of the different curves in the neutrino spectra (bottom) are explained in the legend. The black steps show the IceCube sensitivity curve (Aartsen et al., 2018) corresponding to declination 60°. Neutrino spectrum obtained from the proton-synchrotron model (Fig. 5.22) peak at very high energies and gives low neutrino flux in 0.1–100 PeV energy range (brown dashed line). The lepto-hadronic model provides slightly higher neutrino flux peaking at much lower energies (violet solid line represents the summed component) at the cost of very high values of the jet power. The model parameters are given in Table 5.3.

IceCube at the location of 1ES 1959+650 ($9.86 \times 10^{-13} \text{ TeV cm}^{-2} \text{ s}^{-1}$ at 90% C.L.²). From the lepto-hadronic model predictions it can be inferred that it is difficult to produce detectable neutrino emission during the 2016 VHE flares of 1ES 1959+650, which is in agreement with the non-detection of significant neutrino excess in the IceCube data analysis (Kintscher et al., 2018). In this work, three independent search methods were used to look for neutrino excess during the γ -ray flaring phase: time-integrated search over the entire flaring window (29th April-26th July 2016), search for clusters over shorter timescales, correlation of neutrino arrival time with the γ -ray flares by combining the data from MAGIC (data analyzed by the author) and FACT (Anderhub et al., 2013) telescopes. No indications for neutrino excess coincident with the γ -ray flares has been found in either of the search methods.

An important caveat of the lepto-hadronic solutions is that it requires very high values of the total jet power ($L_j > 10^{48} \text{ erg/s}$) exceeding the Eddington luminosity by more than 2 orders of magnitude. Hence the lepto-hadronic solutions are energetically less favourable (see however Barkov et al. 2012). For the soft proton spectra as adopted in the model, the proton luminosity is largely dependent on the minimum proton energy which is conservatively chosen as 1 here. Choosing higher values of $\gamma_{p,min}$ can reduce the overall luminosity to some extent, but it is still insufficient to achieve sub-Eddington values. Super-Eddington jet power have been predicted for many other blazars (e.g. Barkov et al. 2012, Basumallick and Gupta 2017 etc. and the references therein). The jet power can also be significantly reduced by assuming external photon fields inside the emission region as in the structured jet scenario (Tavecchio et al. (2014); see also Righi et al. 2017).

5.5 Summary

The results from the MAGIC and multi-wavelength monitoring campaign of the blazar 1ES 1959+650 during 2016 is presented. The blazar is a bright and well known source observed by several instruments spanning the entire electromagnetic spectrum since a long time. During 2016, it entered into a very active state in several wavebands, including optical, X-rays and γ rays. The MAGIC telescopes started monitoring the source since 29th April 2016 following a high-activity alert from *Fermi* (Buson et al., 2016). It continued monitoring the source in synergy with multi-wavelength instruments up to November 2016.

The long-term multi-wavelength light curves of the source showed wide range of flux variations, especially in the X-ray and the VHE γ -ray band. A hint of correlation was found between the fluxes in these two wave bands. The spectral index in the X-ray band becomes harder with increasing flux and a hint of a similar trend was also visible in the VHE γ -ray band.

The MAGIC light curve calculated above 300 GeV exhibited three remarkably bright flares on 13th June, 14th June and 1st July, with the flux level reaching up to 2.5-3 times the Crab Nebula flux above the same threshold. This represents the highest VHE state of the source since its extreme activity period in 2002 (when it also showed an orphan flaring behaviour). The MAGIC observations clearly resolved fast intra-night variability within sub-hour timescales during the intense flaring states. The VHE spectra were also quite hard extending up to several TeV. The source spectra in the X-ray and high-energy γ -ray band were also found to show hardness compared to the historical values.

The broadband SEDs during the two flaring nights of 13th June and 14th June were investigated in terms of three theoretical models: leptonic, hadronic and mixed lepto-hadronic. The leptonic model requires high values of Doppler factor to explain the flat VHE spectra up to multi-TeV energies. Alternatively in the hadronic model, the high-energy SED peak could be attributed to proton synchrotron radiation, requiring comparatively smaller Doppler factor and large value of the magnetic field strength. To investigate the level of neutrino emission from the source, a lepto-hadronic model was also studied. The lepto-hadronic model requires large values of the jet power exceeding the Eddington luminosity of the source. The neutrino fluxes predicted from the hadronic and mixed lepto-hadronic models during the intense flares, falls below the sensitivity of the IceCube neutrino telescope. Hence it can be expected that on average the neutrino emission from the source will be much lower during quiescent states and hence cannot reach the sensitivity of current generation of neutrino detectors.

The future CTA observations will be very crucial to constrain the underlying physical conditions of the source. Moreover, due to the brightness and proximity ($z \sim 0.047$) of the source, it can be an interesting target for the commissioning observations of the LST prototype telescope, to test the telescope performance, validate the data

²(Aartsen et al., 2018), Table 2

analysis chain and propose improvements. Since the second SED peak of the source lies in the VHE band during extreme flaring states like 2016, an instrument with a low energy threshold as the CTA will be of paramount importance to perform proper measurements of the peak characteristics. Moreover, the measurement of the spectrum up to several tens of TeV can also have profound implications for high-energy cosmic-ray acceleration within the source.

Chapter 6

Development of a new stationary lepto-hadronic SED modelling tool

In this chapter, the development of a new stationary lepto-hadronic code for modelling the broadband SED of blazars will be discussed. The code implements the relevant leptonic as well as hadronic emission processes. It uses mostly simple semi-analytical frameworks that can calculate the non-thermal emission spectra from AGNs with accuracy comparable to Monte Carlo simulations.

The code is written in the programming language Python. The leptonic part of the code is an evolution of the *Naïma* package (Zabalza (2015); see also Appendix B) that was mainly developed for Galactic astrophysical sources. The hadronic part of the code is a novel implementation by the author. The code thus allows for a fully self-consistent and comprehensive study of purely leptonic, purely hadronic or mixed lepto-hadronic solutions for modelling of the electromagnetic and neutrino emission from AGNs.

First, the leptonic part of the code will be discussed in Sec. 6.1, where the main improvements and additions with respect to the *Naïma* package will be presented. This will be followed by the discussion in Sec. 6.2 about the implementation of the hadronic non-thermal radiative processes. In order to test the code implementation, a comparison with previously existing lepto-hadronic code (Cerruti et al., 2012) will be discussed in Sec. 6.3. The developed code has been used to investigate the broadband SEDs and neutrino emission during the VHE flaring states of 1ES 1959+650 in 2016 (see Chapter 5) and the broadband electromagnetic and neutrino emission of the "neutrino blazar" TXS 0506+056 (see Chapter 7).

6.1 Leptonic emission processes

In this section, the main improvements and additions in the leptonic part of the code with respect to the *Naïma* package will be discussed. *Naïma* already provides the non-thermal radiative models for the following processes exhibited by a population of relativistic electrons - synchrotron and inverse Compton emission. The primary modifications with respect to the original code are the following:

- Introduction of an emission volume defined by a size parameter R
- Implementation of Doppler boosting
- Implementation of the Synchrotron-Self-Absorption (SSA) process
- Implementation of the γ - γ pair-production process

Each of the improvements will be discussed in the subsequent subsections 6.1.1 to 6.1.4. For more details about the computation of the individual leptonic emission components, see Zabalza (2015).

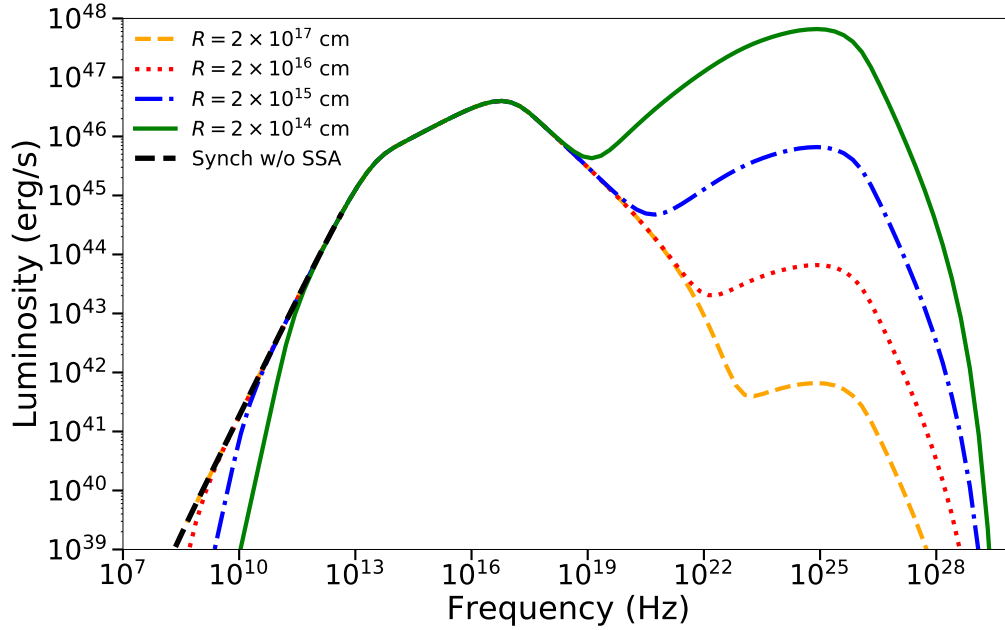


Figure 6.1: The impact of variation of the radius of the emitting region assuming a spherical geometry of the emission region (equivalent to the variation in the source *compactness*; see Eqn. 6.1) on the spectra of a simple SSC model. With increasing *compactness* or decreasing radius, the inverse Compton component (second bump) starts dominating and the cut-off energy of the SSA also increases.

6.1.1 Introduction of an emission volume

In the original version of the Naïma code, the distribution of the primary particles is defined over an arbitrary emission region (i.e. number of particles per unit energy). For blazars, it is necessary to define a shape of the emission region since the non-thermal radiative components depend on the exact geometry of the source. Hence in the modified code, the particle distribution is defined in terms of its number density i.e. the number of primary particles per unit energy per unit volume taking into account the assumption on the geometry of the emitting region. No a-priori shape of the emission region is assumed in the code and it is adjusted according to the assumed modelling framework. The most commonly used assumption is a uniform spherical emission volume having a radius R . However in reality, the emission region can also possess a cylindrical geometry (e.g.: [Tavecchio et al. \(2014\)](#)) or a much more complex geometry.

Another, important aspect of defining a shape of the emission region is that it provides a measure of the *compactness*, which is a dimensionless parameter defined as:

$$l = \frac{L\sigma_T}{4\pi Rmc^3} \quad (6.1)$$

where L denotes the luminosity of the source, R denotes the radius of the emission region (by assuming a uniform spherical geometry) and m is the mass of the primary particle. For a fixed value of the source luminosity, the *compactness* parameter increases with decreasing radius and its effect on the spectra of a simple SSC model is shown in Fig. 6.1.

6.1.2 Relativistic beaming effect

Jetted AGNs, particularly blazars possess ultra-relativistic jets that are oriented very closely to the line of sight of an observer on Earth. Due to this geometry, the intrinsic emission component in the frame of the jet appears highly boosted in the observers' frame due to relativistic beaming effects. This effect was not taken into account in the

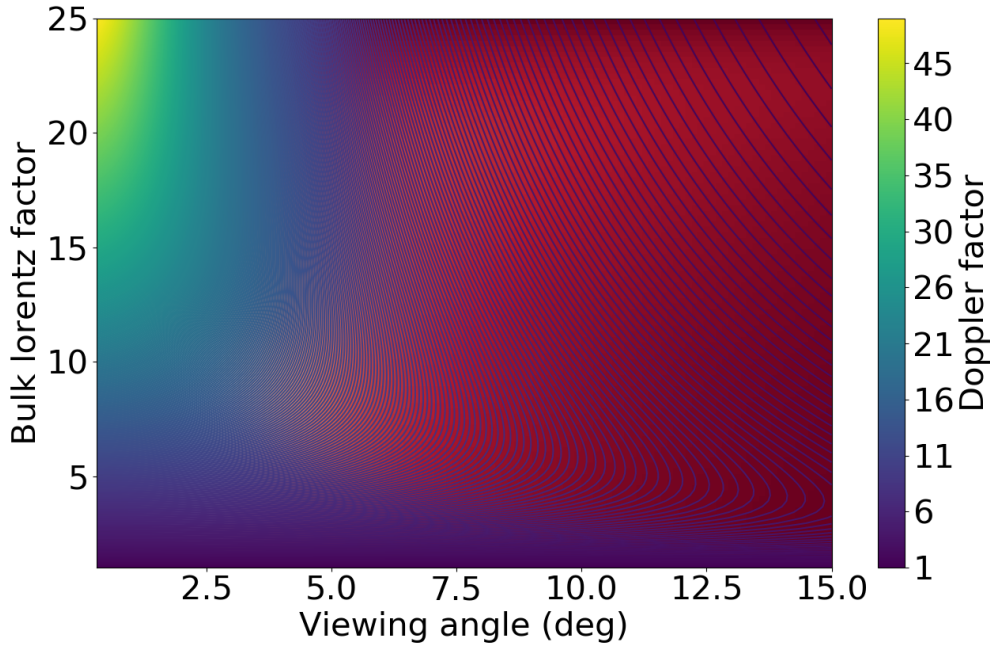


Figure 6.2: The dependence of Doppler factor δ on the bulk Lorentz factor Γ and viewing angle θ of the jet with respect to an observer on Earth.

original Naima code which was mainly designed to model Galactic sources such as pulsars, SNRs etc that do not possess jets. The formalism adopted in the modified code for the implementation of the relativistic beaming (also known as Doppler boosting) is discussed below. For more details the reader is referred to (Dermer and Menon, 2009).

The relativistic motion of the particles inside the blazar jet are characterized by the bulk Lorentz factor Γ which is defined by:

$$\Gamma = (1 - \beta^2)^{-1/2} \quad (6.2)$$

where $\beta = v/c$ and v is the velocity of the emitting region in the jet rest frame and c is the speed of light in vacuum. If an observer is at a viewing angle θ with respect to the jet axis, then the relativistic beaming factor (so called Doppler factor) is defined as:

$$\delta = \frac{1}{\Gamma(1 - \beta \cos(\theta))} \quad (6.3)$$

For high bulk Lorentz factors, $\Gamma \gg 1$ and small viewing angles $\theta \ll 1$ the Doppler factor only depends on the combination of θ and Γ :

$$\delta \longrightarrow \frac{2\Gamma}{1 + \Gamma^2 \theta^2} \quad (6.4)$$

Assuming $\theta = 0$, the maximum Doppler factor is determined by 2Γ . The dependence of the Doppler factor on θ and Γ is shown in Fig. 6.2. As can be seen from the colour-scale, for blazars that have a small viewing angle (typically $< 2.5^\circ$) and high bulk Lorentz factor ($\Gamma > 15$), the Doppler factor can easily reach a magnitude more than 20.

Due to the Doppler boosting the radiation intensity and the energy appears boosted and the time shortened in the observers' frame compared to the co-moving frame of the jet. Let us consider an observer receiving photons at an angle θ with respect to a frame K' , that is moving at a velocity βc with respect to a stationary frame K .

If the frequency of the photon in the frames K and K' are denoted by ν and ν' respectively, they are related according to the following equation:

$$\nu' = \delta \nu \quad (6.5)$$

Since the energy is proportional to frequency, the energy transformations also follow the same principle. The integrated radiation luminosities L and L' transform as:

$$L' = \delta^4 L \quad (6.6)$$

A time interval dt in the stationary frame K appears shortened in the frame K' according to the following relation:

$$dt' = \frac{dt}{\delta} \quad (6.7)$$

In leptonic AGN models where the second SED peak is attributed to inverse Compton upscattering of external photons by the jet-frame electrons, a higher Doppler boosting in γ -rays is expected due to an additional Lorentz transformation of the external photons to the frame of the jet (Dermer, 1995). This causes a higher Compton dominance (predominance of the inverse Compton SED component over the synchrotron SED component) for small viewing angles (termed as the "Dermer effect"). In the models where the internal synchrotron photons of the jet are upscattered by the jet-frame electrons, both the SED peaks are boosted uniformly by the same factor.

6.1.3 Implementation of Synchrotron-Self Absorption

The synchrotron emission of the primary electrons is accompanied by absorption, in which the emitted synchrotron photons interact with the same electrons that produced them and get absorbed by transferring their energy to the electrons. This process is known as Synchrotron-Self Absorption (SSA). The process becomes dominant when the synchrotron photons reach the energy close to the critical energy of the electron $\nu_c = \frac{3eB\sin\theta}{2mc} \gamma^2$. The process plays an important role especially towards the lower energy tail of the synchrotron emission. The formalism adopted for the implementation of the SSA process is described below.

When the interaction between a primary electron and synchrotron photon takes place, the electron can either absorb the photon completely or emit stimulated emission. The probability of each process is governed by the Einstein's coefficients. Taking into account both these processes, the synchrotron absorption cross-section was derived by Ghisellini and Svensson (1991) and have the following functional form (see their Eqn. 2.7):

$$\frac{d\sigma_s(\nu, \gamma)}{d\Omega} = \frac{1}{2m\nu^2} \frac{1}{\gamma p} \frac{\partial}{\partial \gamma} [\gamma p j(\nu, \gamma, \psi)] \quad (6.8)$$

where ν and γ are the frequency of the interacting photon and Lorentz factor of the electron respectively, $p = \sqrt{\gamma^2 - 1}$ is the particle momentum in units of mc and $j(\nu, \gamma, \psi)$ is the single particle emissivity dependent on ν, γ and the pitch angle ψ .

For an isotropic distribution of electrons in a tangled magnetic field of strength B , the particle emissivity in the above expression can be averaged over an isotropic distribution of pitch angle to obtain the total cross-section of SSA. In the ultra-relativistic regime where $\gamma \gg 1$, the total cross-section is given by Eqn. 2.17 of Ghisellini and Svensson (1991) having the following form:

$$\sigma_s(\nu, \gamma) = \frac{\sqrt{3}\pi}{10} \frac{\sigma_T}{\sigma_f} \frac{B_{cr}}{B} \frac{x}{\gamma^5} [K_{4/3}^2(\frac{x}{2}) - K_{1/3}^2(\frac{x}{2})], \quad \gamma \gg 1 \quad (6.9)$$

where $x = \nu/\nu_c$, $\nu_c = \frac{3}{2}\gamma^2\nu_L$ where ν_L is the cyclotron frequency, $B_{cr} = 4.4 \times 10^{13}$ G, $\alpha_f = 1/137$ (fine structure constant) and $K_{4/3}, K_{1/3}$ represent the Bessel functions of fourth and first order respectively.

In the sub-relativistic regime, the total cross-section can be expressed using Eqn. 2.23 of Ghisellini and Svensson (1991) having the following form:

$$\begin{aligned} \sigma_s(\nu, \gamma) = & \frac{3\pi^2}{8} \frac{\sigma_T}{\sigma_f} \frac{B_{cr}}{B} \left(\frac{\nu_L}{\nu}\right)^2 \exp\left(-2\frac{\nu}{\nu_L} \left[\gamma \ln\left(\frac{\gamma+1}{p}\right) - 1\right]\right) \\ & \times \left(\frac{C}{G} - \frac{G'}{G^2}\right), \quad \nu/\nu_L \gg \gamma^2 \end{aligned} \quad (6.10)$$

where

$$C = \frac{2\gamma^2 - 1}{\gamma p^2} + 2\frac{\nu}{\nu_L} \left[\frac{\gamma}{p^2} - \ln\left(\frac{\gamma+1}{p}\right)\right] \quad (6.11)$$

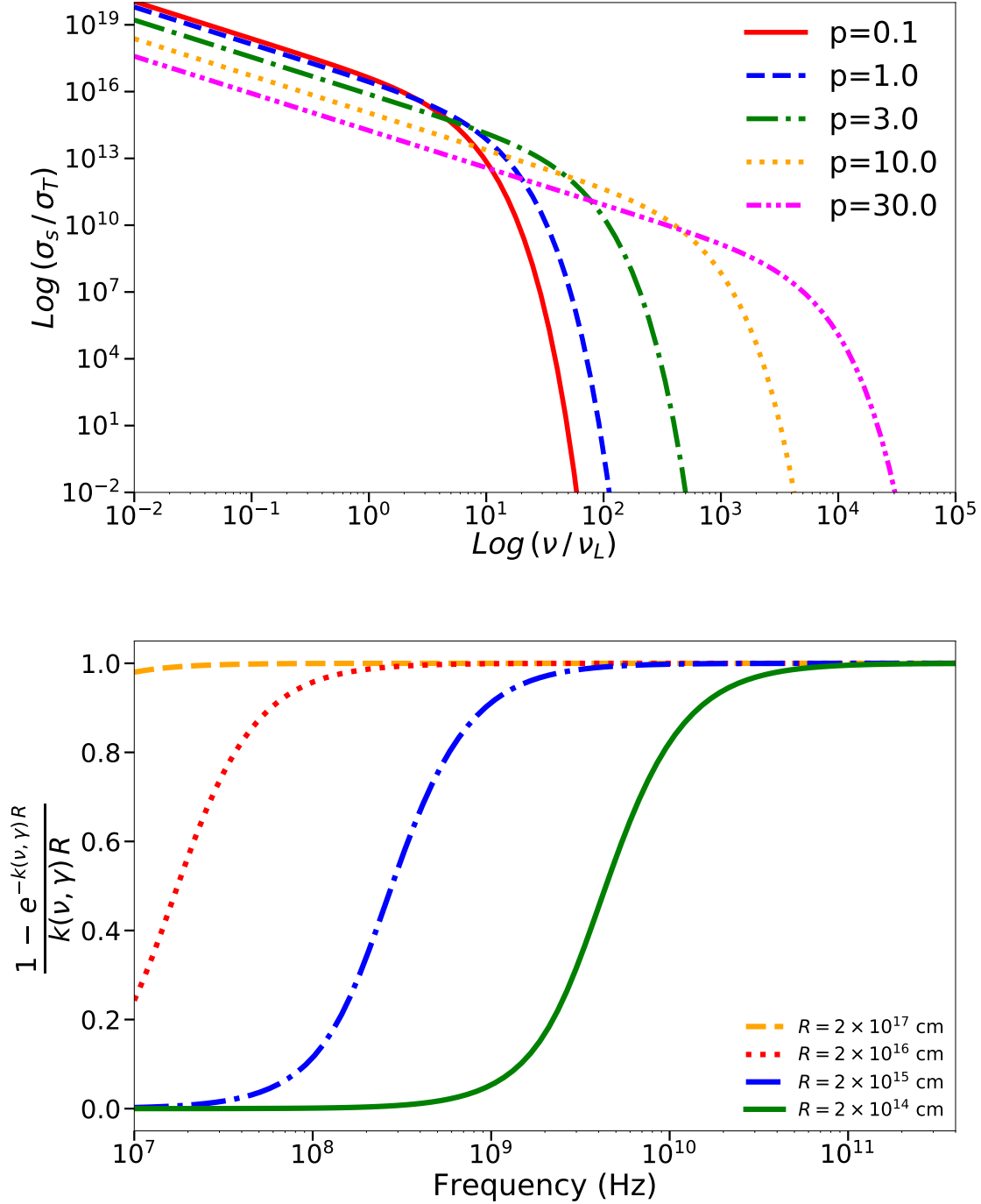


Figure 6.3: Top panel: The total cross-section (normalized over σ_T) of the SSA process for different values of the particle's dimensionless momentum p (Eqn. 6.9 for $p > 3$ and Eqn. 6.10 for $p < 3$) as a function of the synchrotron photon frequency ν/ν_L . Bottom panel: The SSA attenuation factor C_{att} for different values of the source radius R (and hence varying compactness) as a function of the the co-moving frame photon frequency. The radius and compactness values correspond to Fig. 6.1.

$$G = [1 - 2p^2 \gamma \ln[(\gamma + 1)/p] - 1]^{1/2} \quad (6.12)$$

$$G' = 3\gamma - (3\gamma^2 - 1) \ln[(\gamma + 1)/p] / G \quad (6.13)$$

The corresponding SSA absorption coefficient for a distribution of particles $N(\gamma)$ confined within a volume of radius R is then defined by (Eqn. 1.3 of [Ghisellini and Svensson \(1991\)](#)):

$$k(\nu) = \frac{1}{2m\nu^2} \int_1^\infty N(\gamma) \sigma(\nu, \gamma) d\gamma \quad (6.14)$$

The attenuation factor can be defined as $C_{att} = (1 - e^{-\tau})/\tau$ ([Dermer and Menon, 2009](#)) where $\tau = Rk(\nu)$ is the optical depth for absorption.

The SSA cross-section as a function of the synchrotron photon frequency (normalized over the cyclotron frequency) is shown in Fig. 6.3 (top panel) for different values of the particle momentum p (for the cases with $p > 3$, Eqn. 6.9 have been used for the computation, whereas for the cases with $p < 3$, Eqn. 6.10 have been used).

The effect of SSA on the primary synchrotron emission can be seen from the lower energy tail of the synchrotron spectra (first SED hump) in Fig. 6.1. For comparison, the unattenuated synchrotron spectrum without the SSA effect is also shown with the black-dotted line. In the bottom panel of Fig. 6.3, the dependence of the attenuation factor C_{att} on ν (in the co-moving frame) is shown for different values of the source radius (and hence varying compactness) corresponding to Fig. 6.1. One can see that with increasing compactness of the source (i.e. with decreasing radius), the attenuation factor of SSA becomes stronger (as can also be seen in the lower energy synchrotron tail from Fig. 6.1).

6.1.4 Implementation of γ - γ pair production

When a high energy photon of dimensionless energy $\varepsilon_1 = h\nu_1/mc^2$ interacts with another low energy photon having a dimensionless energy $\varepsilon_2 = h\nu_2/mc^2$ and if the total energy available for interaction is greater than $2m_e c^2$, secondary pairs of e^+/e^- are produced. This process thus provides an attenuation factor and becomes relevant especially for the highest energy emission from blazars (in the γ -ray energy regime), which can interact with other low energy photon fields present within the emission region. The low energy photons can be supplied by the synchrotron emission of the electrons or can originate from outside the jet.

For an incident high energy photon of energy ε_1 interacting with uniform isotropic radiation field (in the co-moving frame) having a number density $n_{ph}(\varepsilon_2)$, the pair-production optical depth is defined as ([Dermer and Menon, 2009](#)):

$$\tau_{\gamma\gamma}(\varepsilon_1) = R \int_0^\infty d\varepsilon_2 \sigma_{\gamma\gamma}(\varepsilon_1 \varepsilon_2) n_{ph}(\varepsilon_2) \quad (6.15)$$

where R is the dimension of the source and $\sigma_{\gamma\gamma}(\varepsilon_1 \varepsilon_2)$ is the pair-production cross-section.

Two formalism have been adopted in the numerical code to evaluate the γ - γ cross-section. One of them is given by [Dermer and Menon \(2009\)](#) as:

$$\sigma_{\gamma\gamma}(s) = \frac{8}{16} \sigma_T (1 - \beta_{cm}^2) [(3 - \beta_{cm}^4) \ln\left(\frac{1 + \beta_{cm}}{1 - \beta_{cm}}\right) - 2\beta_{cm}(2 - \beta_{cm}^2)] \quad (6.16)$$

where $s = \varepsilon_1 \varepsilon_2$ and $\beta_{cm} = \sqrt{1 - s^{-1}}$. For an isotropic photon field, the pair-production cross-section can be expressed in the following form ([Aharonian et al., 2008](#)):

$$\sigma_{\gamma\gamma}(s) = \frac{3\sigma_T}{2s^2} \left[\left(s + \frac{1}{2} \ln s - \frac{1}{6} + \frac{1}{2s} \right) \ln(\sqrt{s} + \sqrt{s-1}) - \left(s + \frac{4}{9} - \frac{1}{9s} \right) \sqrt{1 - \frac{1}{s}} \right] \quad (6.17)$$

The later formalism is used in most of the work done in this thesis assuming an isotropic target photon field. The two formulae are comparable with only a minute difference in the cross-section, especially near the threshold $s \sim 1$

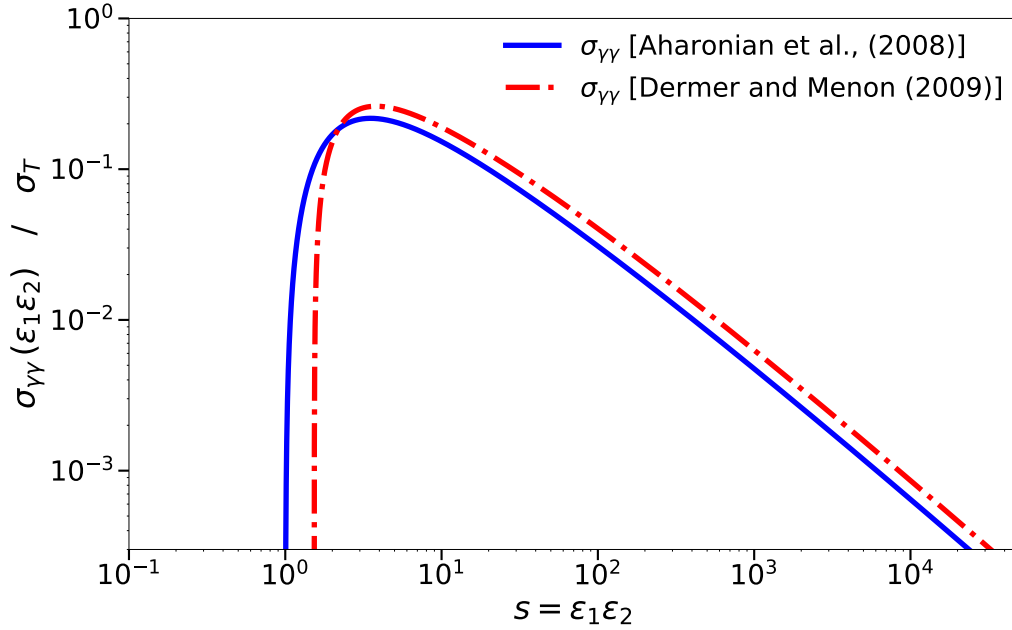


Figure 6.4: $\gamma\text{-}\gamma$ pair production cross section $\sigma_{\gamma\gamma}(s)$ as a function of the quantity s . Blue solid curve: $\sigma_{\gamma\gamma}(s)$ following Aharonian et al. (2008); red dot-dashed curve: $\sigma_{\gamma\gamma}(s)$ following Dermer and Menon (2009).

(see Fig. 6.4). The cross-section only depends on the product s . It attains the maximum value of $\sim 0.2 - 0.3\sigma_T$ at $s \sim 3.5$.

To demonstrate the numerical calculations, Fig. 6.5 shows the attenuation factor $\exp(-\tau_{\gamma\gamma})$ for γ -ray photons (of energy between few tens of GeV to tens of TeV) interacting with a black body photon field. The target field is described by a Planckian distribution with three different values of the temperature: $T = 10^3\text{K}$, 10^4K , 10^5K (similar to Aharonian et al. (2008)). The dips in the curve represent the optical depths for the maximum absorption which occurs at $E^* = m_e^2 c^4 / kT$. The curves are thus identical with only a shift in the maximum absorption energy corresponding to the black body temperature.

6.2 Hadronic emission processes

The numerical code developed for this thesis also calculates the relevant hadronic processes for the blazar electromagnetic emission, along with the leptonic processes described in Sec. 6.1. To model the emission expected when hadronic interactions are relevant, the author have implemented in the code the following processes:

- Proton-synchrotron radiation
- Proton-proton interactions
- Photo-meson interactions
- Pair cascades (itself a leptonic process generated as a by-product of hadronic interactions)

The basic semi-analytical framework used for the development of each of these processes will be described in the subsections below.

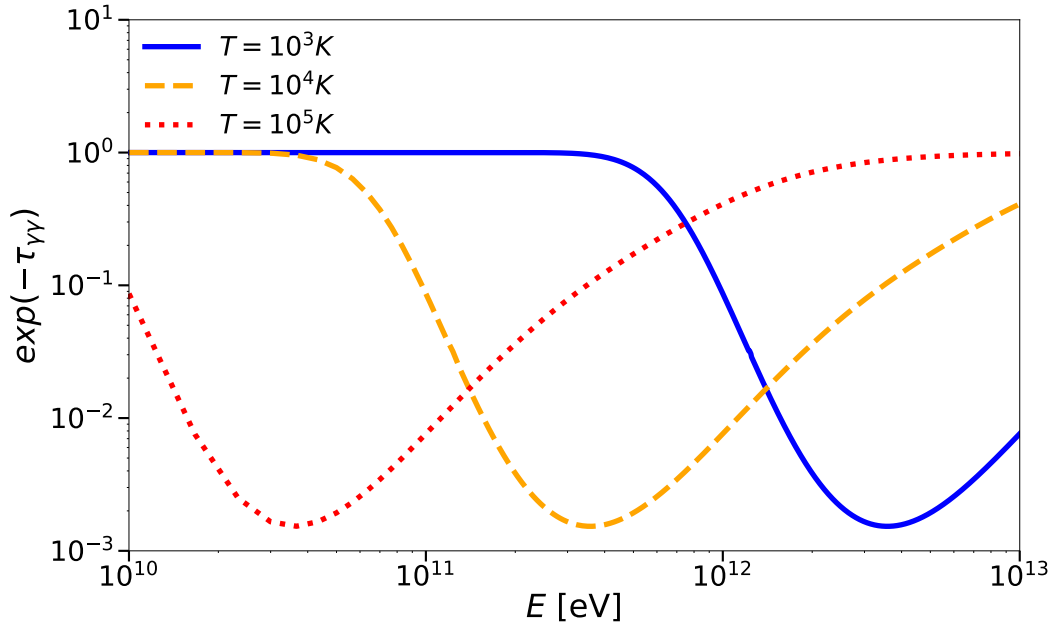


Figure 6.5: The attenuation factor $\exp(-\tau_{\gamma\gamma})$ for a γ -ray photon field interacting with a black body target (shown for three different values of the black body temperature $T = 10^3\text{K}$, 10^4K , 10^5K). The energy corresponding to the maximum attenuation is a function of the black body temperature, given by $E^* = m_e^2 c^4 / kT$ as can be seen from the dips in the different curves corresponding to different black body temperatures.

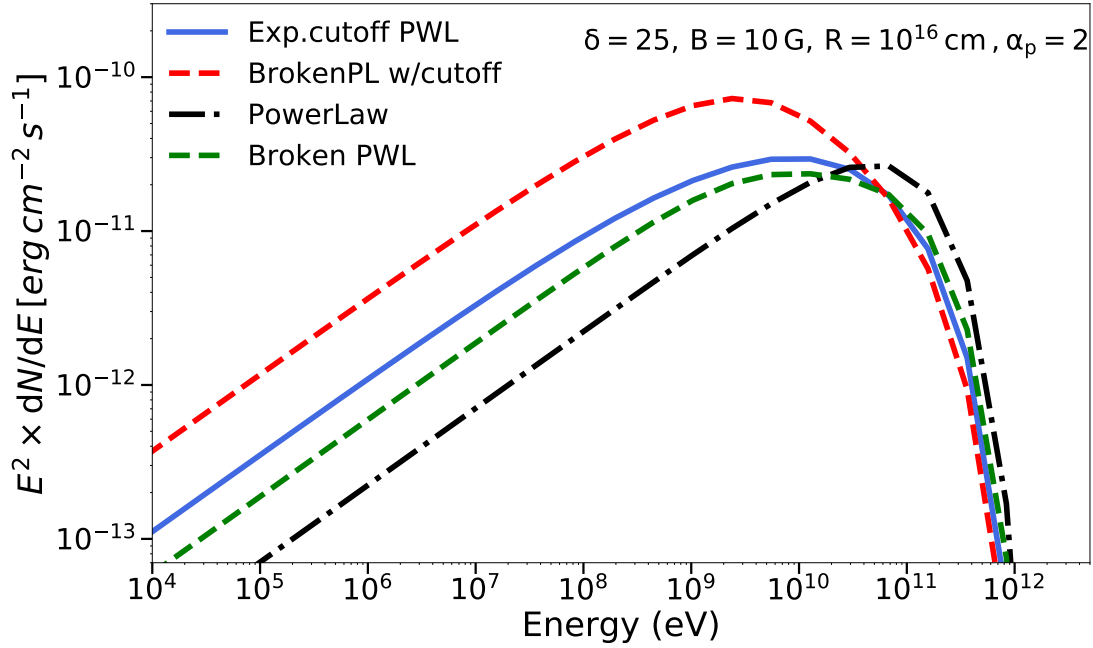


Figure 6.6: Proton synchrotron emission components for different proton distribution functions for randomly selected emission parameters. Assumed parameters: $z=0.1$, $\delta = 25$, $B=10\text{ G}$, $R=10^{16}\text{ cm}$, $\alpha_p = 2$

6.2.1 Implementation of the proton-synchrotron radiation

In hadronic models, the high-energy hump of the SED is often attributed to synchrotron radiation of ultra-relativistic protons. Proton-synchrotron emission can give a dominant contribution to the highest energy photons (up to TeV energies) observed in the blazar electromagnetic emission in highly magnetized environments (with magnetic field strength of few 10 – 100 G), if the protons can be accelerated to energies greater than a few EeV. This can be achieved if the proton acceleration efficiency $\eta_{acc} \sim 1$, i.e. close to the maximum theoretical limit (where the acceleration timescale is given by $t_{acc} = \eta_{acc} r_g / c$, r_g being the gyro-radius of the proton) (Aharonian, 2000).

In order to implement the proton-synchrotron interaction, the same formalism as described in Aharonian et al. (2010) for electrons is used by replacing the electron mass with the proton mass.

The single proton emissivity function of synchrotron emission is described by:

$$\frac{dN_\gamma}{dE_\gamma dt} = \frac{\sqrt{3}}{2\pi} \frac{e^3 B}{m_p c^2 \hbar E_\gamma} F\left(\frac{E_\gamma}{E_c}\right) \quad (6.18)$$

where

$$F(x) = x \int_x^\infty K_{5/3}(\tau) d\tau, \quad \text{and} \quad E_c = \frac{3eB\gamma_p^2}{2m_p c} \quad (6.19)$$

In the equations above, e, m_p, c, \hbar have their usual meanings, B denotes the strength of the magnetic field, E_γ the energy of the emitted photon and γ_p the Lorentz factor of the proton population.

For a tangled magnetic field, the emissivity has to be averaged over the directions of the magnetic field which modifies the function $F(x)$ to the following form in terms of modified Bessel functions:

$$G(x) = \frac{x}{20} [(8 + 3x^2)(K_{1/3}(x/2))^2 + xK_{2/3}(x/2)(2K_{1/3}(x/2) - 3xK_{2/3}(x/2))] \quad (6.20)$$

In order to express the function $G(x)$ in a simpler form without using special functions, Aharonian et al. (2010) derived an approximation which provides an accuracy better than 0.2% for the entire range of x . This simplified form is used in the discussed numerical code for the computation of proton-synchrotron radiation and can be given in the following form:

$$\tilde{G}(x) \sim \frac{1.808x^{1/2}}{\sqrt{1 + 3.4x^{2/3}}} \frac{1 + 2.21x^{2/3} + 0.347x^{4/3}}{1 + 1.353x^{2/3} + 0.217x^{4/3}} e^{-x} \quad (6.21)$$

For a broadband distribution of protons, the emissivity can be convolved with the particle distribution function and integrated over the entire range of Lorentz factors γ_p for protons to obtain the final emission component.

Fig. 6.6 shows the numerical simulations of proton-synchrotron emission for four different proton distributions (power law, power law with exponential cutoff, broken power law, broken power law with exponential cutoff) and for randomly chosen parameters. The assumed parameters are redshift $z=0.1$, Doppler factor $\delta = 25$, magnetic field strength $B = 10$ G, source radius $R = 10^{16}$ cm, the maximum proton energy $E_{p,max} = 3 \times 10^{18}$ eV and proton spectral index at injection $\alpha_p = 2$. It should be noted however, that for most practical purposes the proton spectrum essentially remains unbroken, in the form of a simple power law. This is due to the fact, that the maximum proton energy is usually much lower than the value where cooling starts to become important (assuming that the spectral break is produced due to radiative cooling). For a power law distribution of protons, the peak frequency of the proton synchrotron component can be given as (Cerruti et al., 2015):

$$\frac{\nu_{peak,p}}{10^{27}\text{Hz}} = \frac{1.25 \times 10^{-3}}{1+z} \frac{3 - \alpha_p}{1.5} \frac{\delta}{10} \left(\frac{B}{1\text{G}}\right)^3 \left(\frac{R}{10^{17}\text{cm}}\right)^2 \quad (6.22)$$

For the chosen parameters, $\nu_{peak,p} \sim 8 \times 10^{10}$ eV. Thus the analytical estimate is in agreement with the numerical simulations shown in Fig. 6.6.

6.2.2 Implementation of the photo-meson interactions

If an ultra-relativistic proton population is present inside the emission region, it interacts with the low energy photon field via the photo-meson (or $p-\gamma$) process to produce charged and neutral pions (π^0, π^\pm), which further

decay to produce secondary γ rays and e^+e^- pairs and neutrinos respectively. To implement the photo-meson interactions in the developed numerical code, the analytical approximations of [Kelner and Aharonian \(2008\)](#) have been used. These approximations pose an alternative approach to Monte Carlo simulations ([Mücke et al., 2000](#)) and provides a simple and accurate framework to calculate the spectra of the final decay products.

In this formalism, the final energy spectra of the secondary photons and leptons are expressed as:

$$\frac{dN}{dE} = \int_{\eta_0}^{\infty} H(\eta, E) d\eta \quad (6.23)$$

where

$$H(\eta, E) = \frac{m_p^2 c^4}{4} \int_E^{\infty} \frac{dE_p}{E_p^2} f_p(E_p) f_{ph}\left(\frac{\eta m_p^2 c^4}{4E_p}\right) \Phi\left(\eta, \frac{E}{E_p}\right) \quad (6.24)$$

Here, η is a product of the soft photon energy ε and proton energy E_p defined as $\eta = \frac{4\varepsilon E_p}{m_p^2 c^4}$, $\eta_0 = 0.313$ denotes the interaction threshold, $f_p(E_p)$ and $f_{ph}(\varepsilon)$ denote the energy distribution of the initial protons and photons respectively. $\Phi\left(\eta, \frac{E}{E_p}\right)$ characterizes the spectra of the decay particles for interaction of a proton with a fixed energy and an isotropic mono-energetic target photon field.

The function $\Phi\left(\eta, \frac{E}{E_p}\right)$ has been approximated by simple analytical formulae for the different decay products. For the production of γ rays where $x = \frac{E_\gamma}{E_p}$ (fraction of the parent proton energy carried by the γ rays), the function is defined in the range $x_- < x < x_+$ (for the definition of x_-, x_+ , see [Kelner and Aharonian \(2008\)](#)) as:

$$\Phi_\gamma(\eta, x) = B_\gamma \exp\left\{-s_\gamma \left[\ln\left(\frac{x}{x_-}\right)\right]^{\delta_\gamma}\right\} \times \left[\ln\left(\frac{2}{1+y^2}\right)\right]^{2.5+0.4\ln(\eta/\eta_0)} \quad (6.25)$$

and at lower energies for $x < x_-$ as:

$$\Phi(\eta, x) = B_\gamma (\ln 2)^{2.5+0.4\ln(\eta/\eta_0)} \quad (6.26)$$

The reader is referred to [Kelner and Aharonian \(2008\)](#) for the definition of y . In the range $x > x_+$, the function $\Phi_\gamma(\eta, x)$ is zero. Here $B_\gamma, s_\gamma, \delta_\gamma$ are functions of η . Their values are tabulated in Tables I, II and III of [Kelner and Aharonian \(2008\)](#) for all the relevant secondary particles produced in a p- γ interaction including γ rays and leptons. They are quite smooth functions of η (as shown in Fig. 6.7). Hence for intermediate values of η , a linear interpolation is performed in order to evaluate them.

Fig. 6.8 shows the function $H(\eta, E_\gamma)$ for a power law distribution of protons with spectral index α_p interacting with a black body radiation field (described by a Planckian distribution) having a characteristic energy kT , for a fixed value of the γ -ray energy $E_\gamma = 0.5E^*$. Here E^* represents the threshold proton energy for the p- γ interaction, defined as $E^* = m_p c^2 \left(\frac{m_p c^2}{4kT}\right) \eta_0$. The function is evaluated for three different values of α_p . At low energy the function drops very quickly. At high energies, the function becomes harder with decreasing spectral index of the parent proton. In the above calculation a single photon energy is assumed. For a broadband distribution of target photons, the spectra can be integrated over the entire energy range of the target photon distribution by convolving with its differential flux, to obtain the final spectra of the decay products.

Similar to the γ rays, the function $\Phi_\gamma(\eta, x)$ can be also evaluated for the secondary electrons, positrons, muon neutrinos and anti-neutrinos, electron neutrinos and anti-neutrinos. For more details regarding the expression of their energy spectra, please see [Kelner and Aharonian \(2008\)](#) and Appendix B.

Fig. 6.9 shows a comparison of the energy spectra of the decay products ($\gamma, e^\pm, \nu_\mu, \bar{\nu}_\mu, \nu_e, \bar{\nu}_e$) from photo-meson interactions between an arbitrary power law distribution of protons characterized by a spectral index $\alpha_p = 2$ and a maximum proton energy $E_{p,max} = 10^{16}$ eV (in the co-moving frame) and an arbitrary soft photon target described by a broken power law distribution. For simulating the curves, a blazar located at a redshift $z = 0.1$ was assumed. The emission region was characterized by a uniform spherical volume of radius $R = 10^{16}$ cm and having a Doppler factor $\delta = 25$.

The assumed distribution of protons and the soft photon field is of great practical relevance in blazar environments. Particularly for most BL Lacs, the low energy photons are often supplied by the synchrotron photons present inside the jet, that can be parametrized by a broken power law distribution. The secondary pairs and γ rays further interact with the soft photons triggering an electromagnetic cascade. The neutrinos freely escape the source carrying 0.05 times the parent proton energy (roughly the location of the neutrino peak, in the co-moving frame) and thus act as direct messengers of cosmic-ray sources.

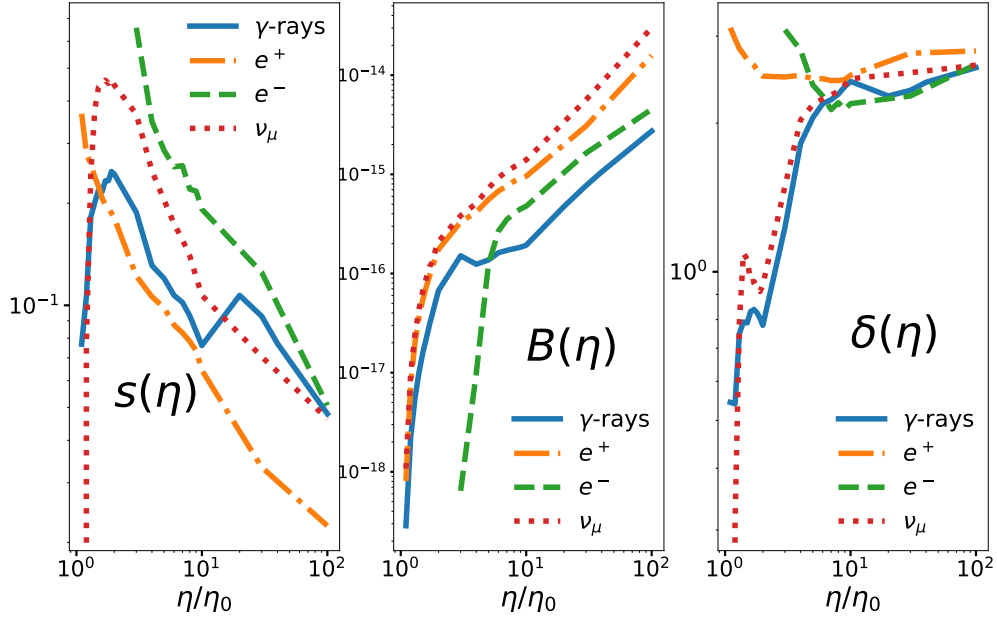


Figure 6.7: The smoothness of the functional parameters $s(\eta)$, $B(\eta)$, $\delta(\eta)$ plotted from Tables I, II and III of Kelner and Aharonian (2008) for some of the secondary decay products of photo-meson interactions.

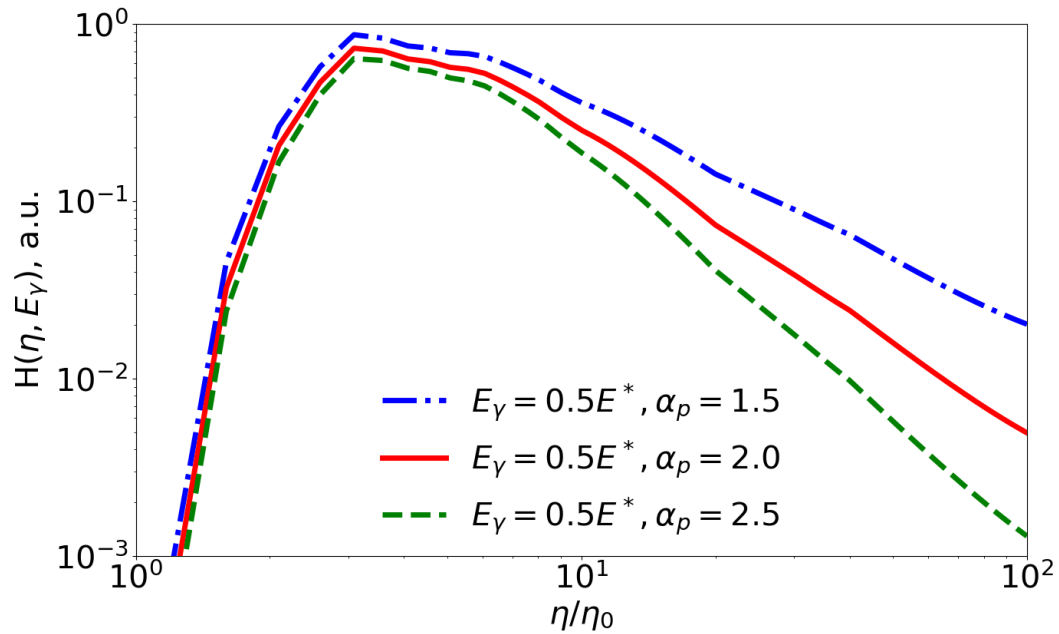


Figure 6.8: The function $H(\eta, E_\gamma)$ calculated for a fixed γ -ray energy $E_\gamma = 0.5E^*$, with three different values of the parent proton's spectral index α_p . The target is assumed to be a black body described by a Planckian distribution (as in Kelner and Aharonian (2008)).

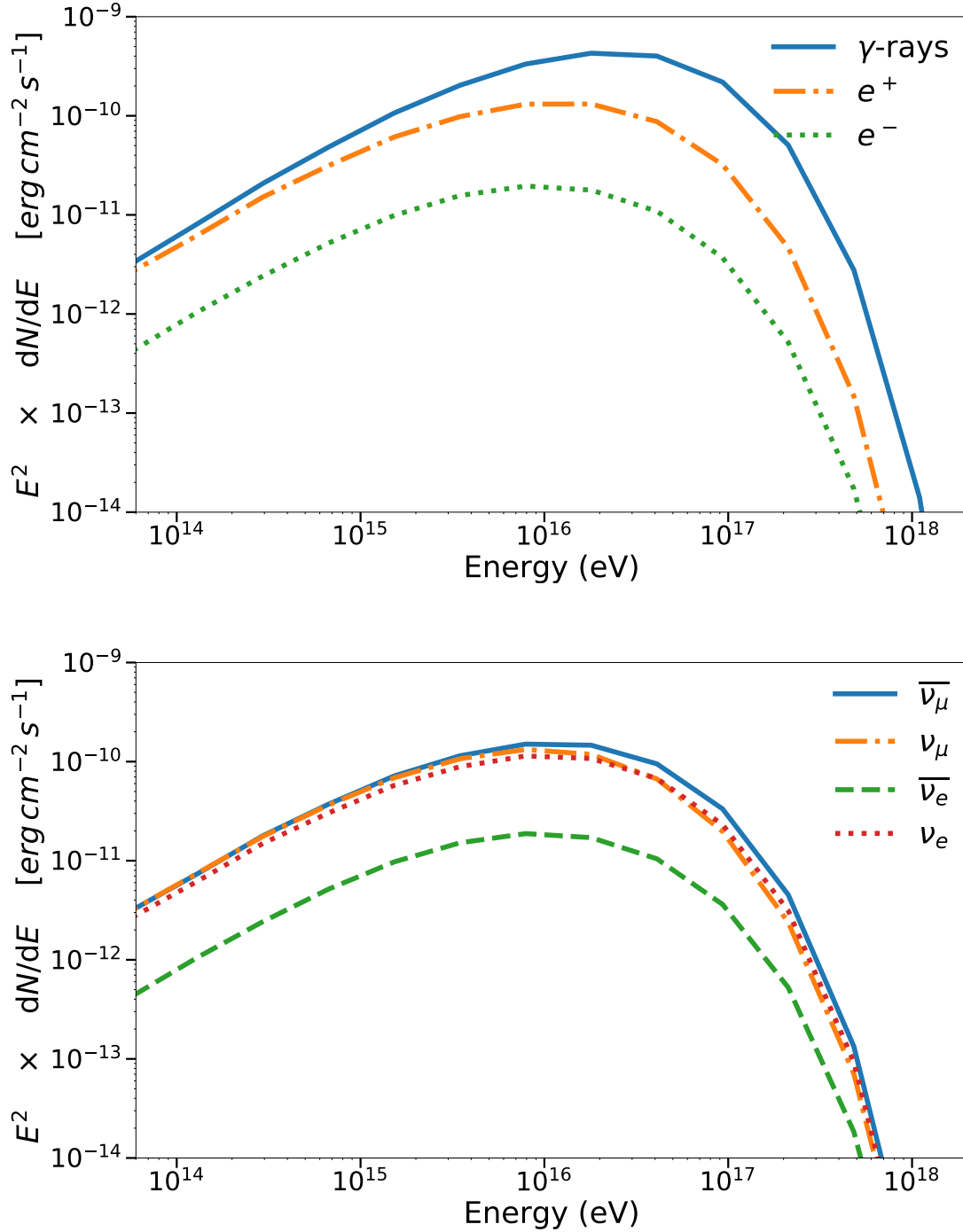


Figure 6.9: The energy spectrum of decay products from photo-meson interactions: γ -rays, e^+ and e^- (top panel) and electron and muon neutrinos (and antineutrinos; bottom panel). The proton distribution is assumed to be a power law with index 2 and maximum energy 10^{16} eV (in the co-moving frame). The target field is assumed to be described by an arbitrary broken power law distribution.

6.2.3 Implementation of proton-proton interactions

In some astrophysical environments where the density of soft photons is low compared to the density of the gas (mostly for Galactic sources like SNRs, pulsars etc), proton-proton (or p-p) interactions become important. When an ultra-relativistic proton interacts with the ambient gas, it produces charged and neutral pions (and also some other secondaries like η mesons). The neutral pions decay to generate γ rays while the charged pions decay to produce secondary e^+/e^- pairs and neutrinos. The p-p interactions have been implemented in the code developed by the author for the sake of completeness and future use. But blazars being the main source class of scientific study in this thesis (where p- γ interactions are more dominant), the p-p interactions have not been investigated in terms of any source interpretation.

The p-p interactions are numerically evaluated in the code following the formalism developed in [Kelner et al. \(2006\)](#). In this formalism, the energy spectra of the final decay products (γ rays, electrons and neutrinos) have been parametrized in terms of simple but accurate analytic approximations. The total energy spectra of γ rays resulting from an interaction of a mono-energetic proton beam of energy E_p with the ambient gas is given by:

$$F_\gamma(x, E_p) = B_\gamma \frac{\ln(x)}{x} \left[\frac{1 - x^{\beta_\gamma}}{1 + k_\gamma x^{\beta_\gamma} (1 - x^{\beta_\gamma})} \right]^4 \left[\frac{1}{\ln(x)} - \frac{4\beta_\gamma x^{\beta_\gamma}}{1 - x^{\beta_\gamma}} - \frac{4k_\gamma \beta_\gamma x^{\beta_\gamma} (1 - 2x^{\beta_\gamma})}{1 + k_\gamma x^{\beta_\gamma} (1 - x^{\beta_\gamma})} \right] \quad (6.27)$$

where $x = E_\gamma/E_p$ is the fraction of energy of the incident proton carried by the γ ray. B_γ , β_γ and k_γ are functions of the proton energy and are defined as:

$$B_\gamma = 1.30 + 0.14L + 0.011L^2 \quad (6.28)$$

$$\beta_\gamma = \frac{1}{1.79 + 0.11L + 0.008L^2} \quad (6.29)$$

$$k_\gamma = \frac{1}{0.801 + 0.049L + 0.014L^2} \quad (6.30)$$

where $L = \ln(E_p/1\text{TeV})$. For a broadband distribution of protons $dN_p = J_p(E_p)dE_p$ interacting with an ambient hydrogen gas of density n_H , the spectrum of γ rays is given by:

$$\frac{dN_\gamma}{dE_\gamma} = cn_H \int_{E_\gamma}^{\infty} \sigma_{inel}(E_p) J_p(E_p) F_\gamma\left(\frac{E_\gamma}{E_p}\right) \frac{dE_p}{E_p} \quad (6.31)$$

where $\sigma_{inel}(E_p)$ is the inelastic cross-section of p-p interactions (see [Kelner et al. \(2006\)](#)). It is to be noted that the formalism described above is only valid for $E_p > 0.1$ TeV and $x_i = E_i/E_p \geq 10^{-3}$. The numerical calculations for lower values of energy are implemented in the code for a particular distribution of protons, given by a power law with exponential cutoff (which can be assumed as a reasonable distribution for most practical applications), following the approximate approach described in [Kelner et al. \(2006\)](#).

Similar to the γ rays, the energy spectra of the charged leptons and the neutrinos are also given in [Kelner et al. \(2006\)](#) in simple analytic forms, for a fixed energy of the parent proton. For a broadband proton distribution, those spectra can be integrated over the entire range of proton energy convolving with the proton energy distribution function with an equation analogous to 6.31 in order to obtain their final energy spectra.

Fig. 6.10 shows the energy spectra of γ rays, $e^+ + e^-$, $\nu_\mu^{(1)}$ (from decay of muons) and ν_μ (total contribution, including the one from direct pion decay). The assumed hydrogen gas density has a value of 1 cm^{-3} . The assumed parent proton distribution has the form of power law with an exponential cutoff having spectral index α_p and cutoff energy $E_{p,cut}$ (fixed at 700 TeV). In order to perform the calculations for $E_p < 0.1$ TeV, the delta-function approximation given in [Kelner et al. \(2006\)](#) have been used. In the top panel the spectra have been evaluated for $\alpha_p = 1.5$ and in the bottom panel for $\alpha_p = 2$. With a harder proton spectrum, the spectra of the decay products also become harder at lower energies. It can be seen from Fig. 6.10, that the spectrum of the secondaries start cutting off near $E_i = 7$ TeV. As explained by [Kelner et al. \(2006\)](#), this is due to the presence of a cutoff in the secondary spectra, given by $\exp[-(16\gamma/E_{p,cut})^{1/2}]$. This term becomes important already at $E_i \geq 0.01E_{p,cut}$, thus giving rise to the cutoff.

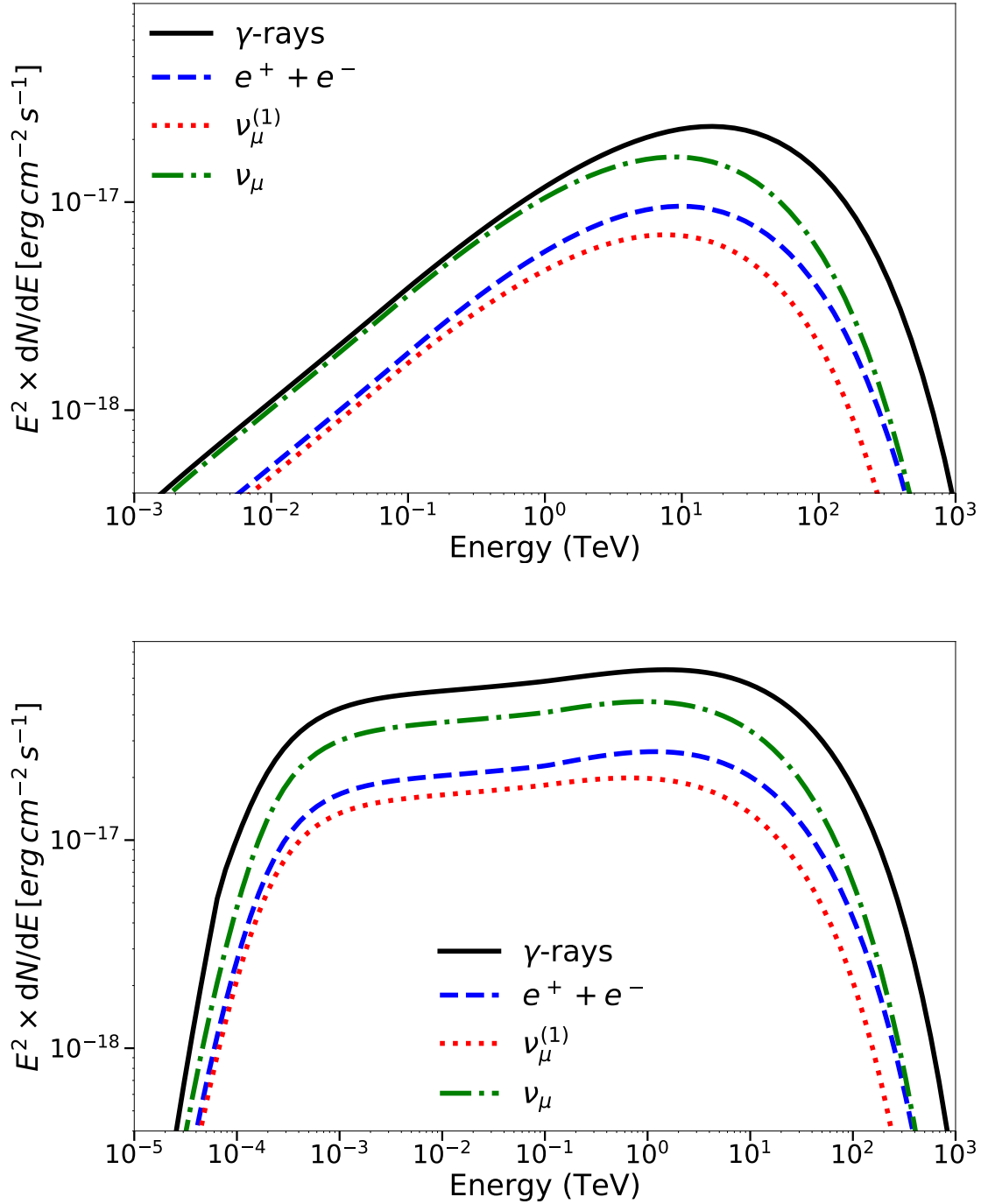


Figure 6.10: Energy spectra of secondary decay products from p-p interaction between a proton distribution of power law with exponential cutoff form and a hydrogen gas with density $n_H = 1 \text{ cm}^{-3}$. Decay products: γ rays, $e^+ + e^-$, $\nu_\mu^{(1)}$ (neutrinos from muonic decay), ν_μ (total muon neutrino spectra including the contribution from direct pion decay). The spectra has been calculated for a fixed cutoff energy of the parent proton of 700 TeV and spectral index $\alpha_p = 1.5$ (top panel) and $\alpha_p = 2$ (bottom panel).

6.2.4 Implementation of photo-meson pair cascades

The pair cascade process is itself not hadronic, but a by-product of a process that started hadronically. The photons coming from the π^0 decay during a photo-meson interaction and the synchrotron and inverse Compton emission from the secondary e^+/e^- pairs, appear in the energy regime at which the dense soft radiation fields in the emission region are opaque to $\gamma\text{-}\gamma$ pair production. Hence these secondary by-products of p- γ processes trigger an electromagnetic cascade upon interaction with the soft photon fields.

To implement the photo-meson pair cascade process, the semi-analytical treatment of [Böttcher et al. \(2013\)](#) have been used. It has been assumed that the injection rates of the first generation of γ rays, \dot{N}_e and $e^+ + e^-$ pairs, $Q_e(\gamma)$ are known from the analytical approximations of [Kelner and Aharonian \(2008\)](#), as described in Sec 6.2.2. The low energy photons as targets can be provided by the internal synchrotron photons inside the emission region or can be injected from an external source. From the known soft photon target density, the opacity for $\gamma\text{-}\gamma$ pair production $\tau_{\gamma\gamma}(\varepsilon)$ is pre-calculated following the method described in Sec. 6.1.4. The low energy radiation field is assumed to be isotropic in the developed numerical code. The final escaping photon distribution is then described with the following equation:

$$\dot{N}_\varepsilon^{esc} = \dot{N}_\varepsilon^{em} \left(\frac{1 - e^{-\tau_{\gamma\gamma}(\varepsilon)}}{\tau_{\gamma\gamma}(\varepsilon)} \right) \quad (6.32)$$

Here \dot{N}_ε^{em} contains the contribution from both the initial π^0 decay photons and the emission from the secondary e^+/e^- pairs.

To obtain the equilibrium electron distribution $N_e(\gamma)$, the isotropic Fokker-Planck equation in equilibrium is solved:

$$\frac{\partial}{\partial \gamma} (\dot{\gamma} N_e(\gamma)) = Q_e(\gamma) + \dot{N}_e^{\gamma\gamma}(\gamma) + \dot{N}_e(\gamma)^{esc} \quad (6.33)$$

$\dot{N}_e(\gamma)^{esc}$ represents the escape term which has been parametrized as:

$$\dot{N}_e(\gamma)^{esc} = -N_e(\gamma)/t_{esc} \quad (6.34)$$

where $t_{esc} = \eta_{esc} R/c$ and η_{esc} denotes the efficiency of escape.

The cooling term in [Böttcher et al. \(2013\)](#) has only the contribution from synchrotron losses included. However, in some environments where the soft photon field is very dense, inverse Compton losses can also give a non-negligible contribution to the electron loss term. The inverse Compton losses for the highly energetic secondary electrons will mostly be in the Klein-Nishina regime, where the available target photon energy density can be approximated by a term $U_{rad,avail}$ (see Eqn. 19 of [Tavecchio et al. \(1998\)](#)). Hence the net cooling term is parametrized in the code as:

$$\dot{\gamma} = \frac{4\sigma_T \gamma^2}{3m_e c} \left(\frac{B^2}{8\pi} + U_{rad,avail} \right) = v_0 \gamma^2 \quad (6.35)$$

The term $\dot{N}_e^{\gamma\gamma}(\gamma)$ represents the injection rate of pairs due to $\gamma\text{-}\gamma$ pair production. This term has also been modified with respect to [Böttcher et al. \(2013\)](#) to include the pair injection contribution from inverse Compton $\dot{N}_{\varepsilon_i}^{IC}$ along with the contribution from synchrotron ($\dot{N}_{\varepsilon_i}^{sy}$) and π^0 decay ($\dot{N}_{\varepsilon_i}^0$) photons:

$$\dot{N}_e^{\gamma\gamma}(\gamma) = f_{abs}(\varepsilon_1) (\dot{N}_{\varepsilon_1}^0 + \dot{N}_{\varepsilon_1}^{sy} + \dot{N}_{\varepsilon_1}^{IC}) + f_{abs}(\varepsilon_2) (\dot{N}_{\varepsilon_2}^0 + \dot{N}_{\varepsilon_2}^{sy} + \dot{N}_{\varepsilon_2}^{IC}) \quad (6.36)$$

The target energy density of $U_{rad,avail}$ is used for the computation of \dot{N}_ε^{IC} . In the above formula, $\varepsilon_1 = \gamma/f_\gamma$ and $\varepsilon_2 = \gamma/(1-f_\gamma)$, where f_γ is the fraction of energy carried by a pair during a e^+/e^- pair production and has been fixed to 0.9 as given in [Böttcher et al. \(2013\)](#).

To obtain the solution to Eqn. 6.33, a modified scheme from the one discussed in [Chiaberge and Ghisellini \(1999\)](#) (see also [Chang and Cooper \(1970\)](#)) has been adopted. This is slightly different from the [Böttcher et al. \(2013\)](#) approach who use a direct numerical integration of Eqn. 6.33. Note that although this scheme is not strictly required in the considered scenario, it can be easily extrapolated to solve a time-dependent Fokker-Planck equation and also requires significantly reduced number of mesh points to obtain accurate numerical solutions. In the numerical calculation for this thesis, the Eqn. 6.33 is discretized in the following way:

$$\frac{F_{j+1/2} - F_{j-1/2}}{\Delta \gamma_j} = Q_j + \dot{N}_{\gamma j} - \frac{N_j}{t_{esc}} \quad (6.37)$$

where $F_{j\pm 1/2} = \dot{\gamma}_{j\pm 1/2} N_{j\pm 1/2}$. Following [Chang and Cooper \(1970\)](#), $N_{j+1/2} = N_{j+1}$ and $N_{j-1/2} = N_j$. Now Eqn. 6.37 can be cast into a triadiagonal form given by:

$$V_{3j}N_{j+1} + V_{2j}N_j + V_{1j}N_{j-1} = S_j \quad (6.38)$$

where

$$\begin{aligned} V_{3j} &= \frac{\dot{\gamma}_{j+1/2}}{\Delta\gamma_j} = -\frac{v_0\gamma_{j+1/2}^2}{\Delta\gamma_j} \\ V_{2j} &= \frac{1}{t_{esc}} - \frac{\dot{\gamma}_{j-1/2}}{\Delta\gamma_j} = \frac{1}{t_{esc}} + \frac{v_0\gamma_{j-1/2}^2}{\Delta\gamma_j} \\ V_{1j} &= 0 \\ S_j &= Q_j + \dot{N}_{\gamma j} \end{aligned} \quad (6.39)$$

As described in [Böttcher et al. \(2013\)](#), the solution obtained for $N_e(\gamma)$ is implicit since $N_e(\gamma)$ occurs on both sides of the equation. Hence for the numerical computation using the above discretized method, the total energy grid in γ (starting from the highest energy where either $\dot{N}_{e1,2}$ or $Q_e(\gamma) \neq 0$) is broken into number of fine sub-grids. The solution obtained for the first highest energy sub-grid (assuming $N_e(\gamma) = 0$ initially) is then passed as input to the lower-energy sub-grid and so on, to obtain the final equilibrium pair distribution.

6.3 Test applications

As a first application of the developed lepto-hadronic code, in this section the multi-wavelength SED of the BL Lac object PKS 2155-304 is modelled. A detailed study of the SED of PKS 2155-304 have been performed in [Cerruti et al. \(2012\)](#). In this work the same dataset has been used to model the SED in order to compare the results with an existing code. In their work [Cerruti et al. \(2012\)](#) have modelled the SED using four different scenarios - purely leptonic, purely hadronic and two mixed lepto-hadronic scenarios. In the applications shown below, only two of the cases have been considered since the main purpose is to compare the different emission components in the same parameter regime. In all the applications, the EBL model of [Dominguez et al. \(2011\)](#) has been used.

6.3.1 PKS 2155-304

PKS 2155-304 is one of the brightest TeV BL Lac objects in the southern sky. It is classified as an HBL and located at a redshift $z=0.117$ ([Charles et al., 1979](#)). It was first discovered as a VHE γ -ray emitter by the University of Durham Mark 6 γ -ray telescope in Australia ([Chadwick et al., 1999](#)) and later detected by various other instruments such as CANGAROO, H.E.S.S. establishing it as one of the most prominent VHE γ -ray emitter. An exceptional flaring activity was reported by the H.E.S.S. collaboration in 2006 ([Aharonian et al., 2007](#)) where the VHE γ -ray flux reached 11 times the Crab Nebula flux. Following this exceptional flare, the MAGIC telescopes were also able to detect the source at large zenith angles ([Aleksić et al., 2012b](#)). In 2008, a MWL campaign led by the H.E.S.S. collaboration ([Aharonian et al., 2009](#)) reported the full characterization of the SED in a lowstate with data ranging from radio up to TeV γ rays. This dataset has been used in [Cerruti et al. \(2012\)](#) for the modelling and is also used in the work presented in this thesis.

The radio data in BL Lacs is usually attributed to an extended region of the jet, which is not responsible for the high-energy emission. For this purpose, the radio data is not included in the modelling. It has been reported in [Cerruti et al. \(2012\)](#) that no clear correlation of the optical data has been found with the high-energy emission ([Abramowski et al., 2012](#)), which might suggest that the optical emission originates from a different emission zone. For this reason it was not included in the modelling of [Cerruti et al. \(2012\)](#).

The results of the modelling obtained from the developed lepto-hadronic code along with the results from the original model are shown in Figs. 6.12 and 6.13. The model parameters from [Cerruti et al. \(2012\)](#) that were used for the code comparison are listed in Table 6.1. The different individual and summed emission components are shown for both the cases. For the SED modelling results produced with the code developed in this thesis, the photo-meson cascade component (denoted by the orange dot-dot-dashed lines in the top panels of Fig. 6.12 and Fig. 6.13) includes the contribution from the initial π^0 decay photons as well as synchrotron photons radiated by

Table 6.1: Parameters for the mixed lepto-hadronic model 1 and the hadronic model from Cerruti et al. (2012), that were used to compare the results from their code with the code developed by the author

Model parameters	Symbol	Hadronic	Mixed 1
Doppler factor	δ	30	30
Emission region size	R (cm)	5.2×10^{14}	1.8×10^{16}
Magnetic field strength	B (G)	80	0.065
Min. e^\pm Lorentz factor	$\gamma_{e,min}$	1	5×10^2
Max. e^\pm Lorentz factor	$\gamma_{e,max}$	6×10^4	2.5×10^6
e^\pm break Lorentz factor	$\gamma_{e,brk}$	4×10^3	1.5×10^5
e^\pm injection spectral index	n_1	2.0	2.4
e^\pm after-break spectral index	n_2	4.32	4.32
Min. p^+ Lorentz factor	$\gamma_{p,min}$	1	1×10^5
Max. p^+ Lorentz factor	$\gamma_{p,max}$	1×10^9	8×10^7
p^+ injection spectral index	n_p	2.0	2.4

the secondary e^+/e^- pairs from π^\pm decay. These two emission components are separately shown in the modelling of Cerruti et al. (2012) (with the orange and pink dashed lines).

The main difference between the two results arises from the decay of intermediate π^\pm . The charged pions decay to produce μ^\pm which can further cool down by radiating synchrotron emission. This muonic synchrotron component can give a dominant contribution to the SED as apparent in the hadronic model of Cerruti et al. (2012). This component is not implemented in our code, since the analytical parametrizations of Aharonian et al. (2008) on which this code is based on, assumes that the intermediate products of photo-meson interactions decay instantaneously before cooling. Hence the muon-synchrotron component is neglected. However, the analytical parametrizations of Aharonian et al. (2008) are still valid if one of the following two conditions are satisfied as shown by Böttcher et al. (2013):

- The proton-synchrotron losses are strongly dominant over the photo-meson losses
- The secondary pions and muons cool down slower than their decay timescale, which leads to the following constraint on the magnetic field strength for a given γ_p (proton Lorentz factor):

$$B\gamma_p \ll \begin{cases} 7.8 \times 10^{11} \text{ G} & \text{for pions} \\ 5.6 \times 10^{10} \text{ G} & \text{for muons} \end{cases} \quad (6.40)$$

For the range of parameters considered here, the synchrotron cooling of the protons is indeed faster than their photo-meson cooling timescales as shown in Fig. 6.11. Hence the analytical treatment can be considered a valid approach for the parameter regime considered here. In this work, the contribution from the cascade emission induced by the γ - γ absorption of the high-energy tail of the proton-synchrotron emission is also neglected (which is shown by the blue dotted lines in the results from Cerruti et al. (2012)) since it does not impact the summed SED component at all in all the cases considered here.

6.4 Summary

A new stationary lepto-hadronic code is developed during the course of this thesis for modelling the broadband electromagnetic and neutrino emission from AGNs. Apart from the conventional leptonic emission processes such as synchrotron and inverse Compton, the code also implements the relevant hadronic emission processes including proton synchrotron, photo-meson interactions, proton-proton interactions and pair cascades. The code thus permits a wide scan of parameters within a self-consistent framework, spanning the particle distributions of both electrons and protons along with the parameters specific to the emission region, such as its size, Doppler factor, magnetic field strength etc. The Bethe-Heitler pair production is not yet implemented in the code and set as a future goal. In order to neglect the contribution from this process, we define a characteristic proton energy given

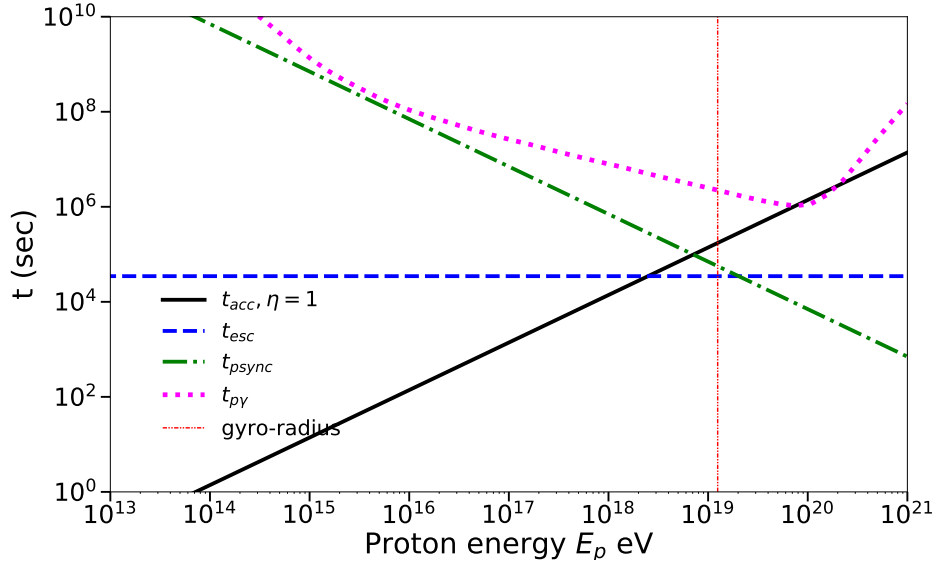


Figure 6.11: The acceleration and cooling timescales for the hadronic model of PKS 2155-304 as shown in Fig. 6.13. The green-dotted line denotes the proton-synchrotron cooling timescale and the pink-dotted line shows the photo-meson cooling timescale as a function of the proton energy. As can be seen from the figure, the proton synchrotron cooling dominates over the photo-meson cooling for a wide range of proton energies.

by (Dimitrakoudis et al., 2012):

$$\gamma_{p,meson} = \left(\frac{1}{b} \frac{m_p m_\pi}{m_e^2} \left(1 + \frac{m_p}{2m_\pi} \right) \right)^{1/3} \quad (6.41)$$

where m_e, m_p, m_π are the rest mass for electrons, protons and pions respectively and $b = B/B_c$, where B is the assumed magnetic field strength and $B_c = m_e^2 c^3 / e \hbar$. If the maximum proton Lorentz factor $\gamma_{p,max} > \gamma_{p,meson}$, then photo-meson process dominates over the Bethe-Heitler process. Hence neglecting the Bethe-Heitler process provides a lower limit to the maximum proton energy assumed for the modelling.

One of the main drawbacks of the code is that, in the formulation of Kelner and Aharonian (2008) that is used as the main reference for photo-meson interactions, the intermediate decay products such as muons and pions are assumed to decay instantly. Since the synchrotron cooling of the intermediate muons and pions are neglected, a restriction to the assumed magnetic field strength and the maximum proton energy is imposed, as discussed in Sec. 6.3. Another drawback of the code is the slow computation time of some of the hadronic emission processes, especially the pair cascades (which takes roughly 30 minutes). Profiling and optimization of the code is set as a future goal.

The code has been tested with the code of Cerruti et al. (2012) as shown in Sec. 6.3. The comparison between the two codes show a good degree of agreement. The code developed by the author is used to model the SEDs and multi-messengers observations for the blazars 1ES 1959+650 and TXS 0506+056, that will be discussed in Chapters 5 and 7 respectively.

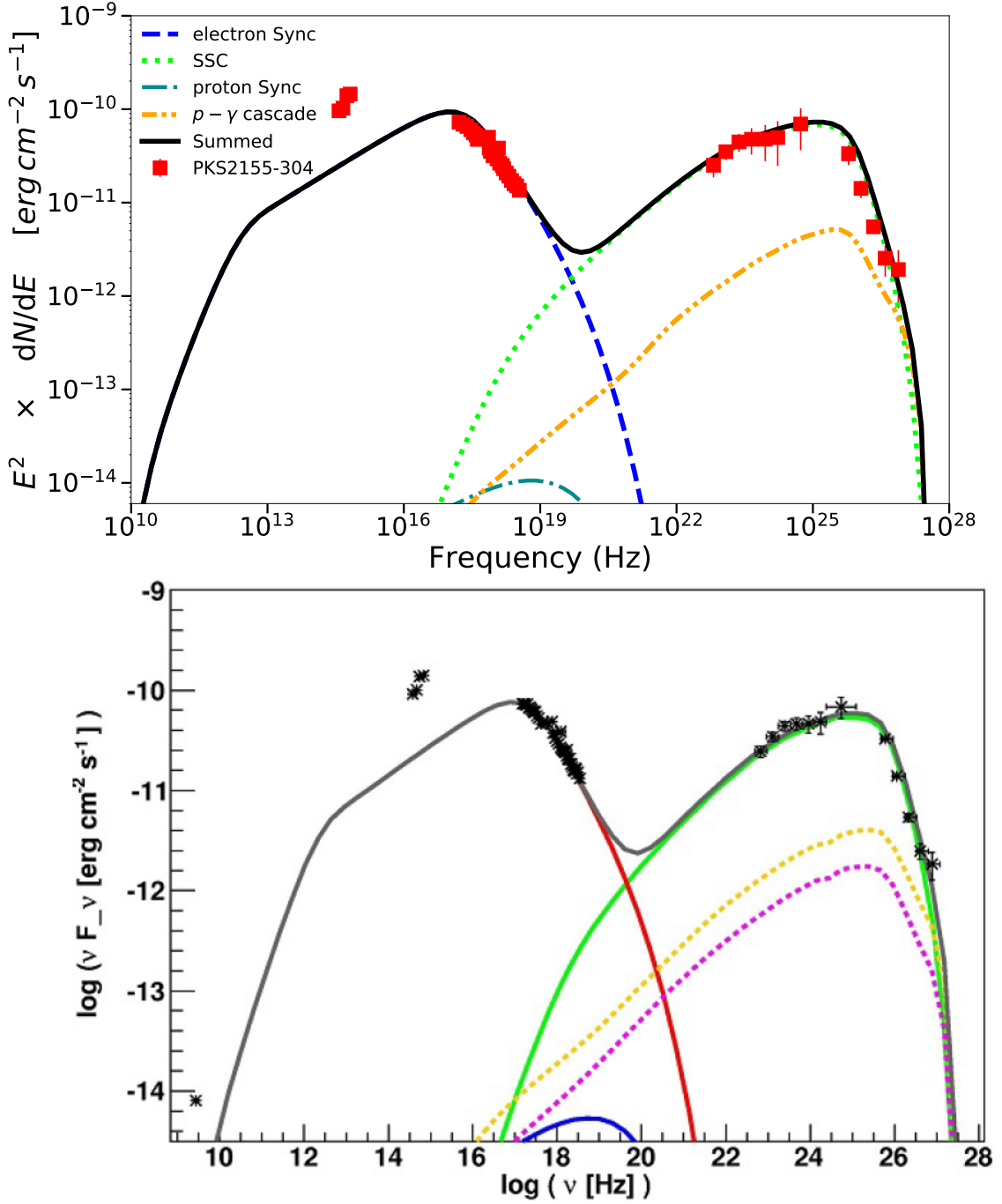


Figure 6.12: The mixed lepto-hadronic model 1 of the MWL SED of PKS 2155-304. The top panel shows the results obtained with the lepto-hadronic emission model developed for this thesis. The bottom panel shows the SED model from the original work of [Cerruti et al. \(2012\)](#). The colour code for the figure is: red-primary electron synchrotron; green-inverse Compton; blue-proton synchrotron; yellow-photons from π^0 decay; pink-synchrotron emission from secondary e^\pm coming from π^\pm decay (for the list of parameters see Table 6.1).

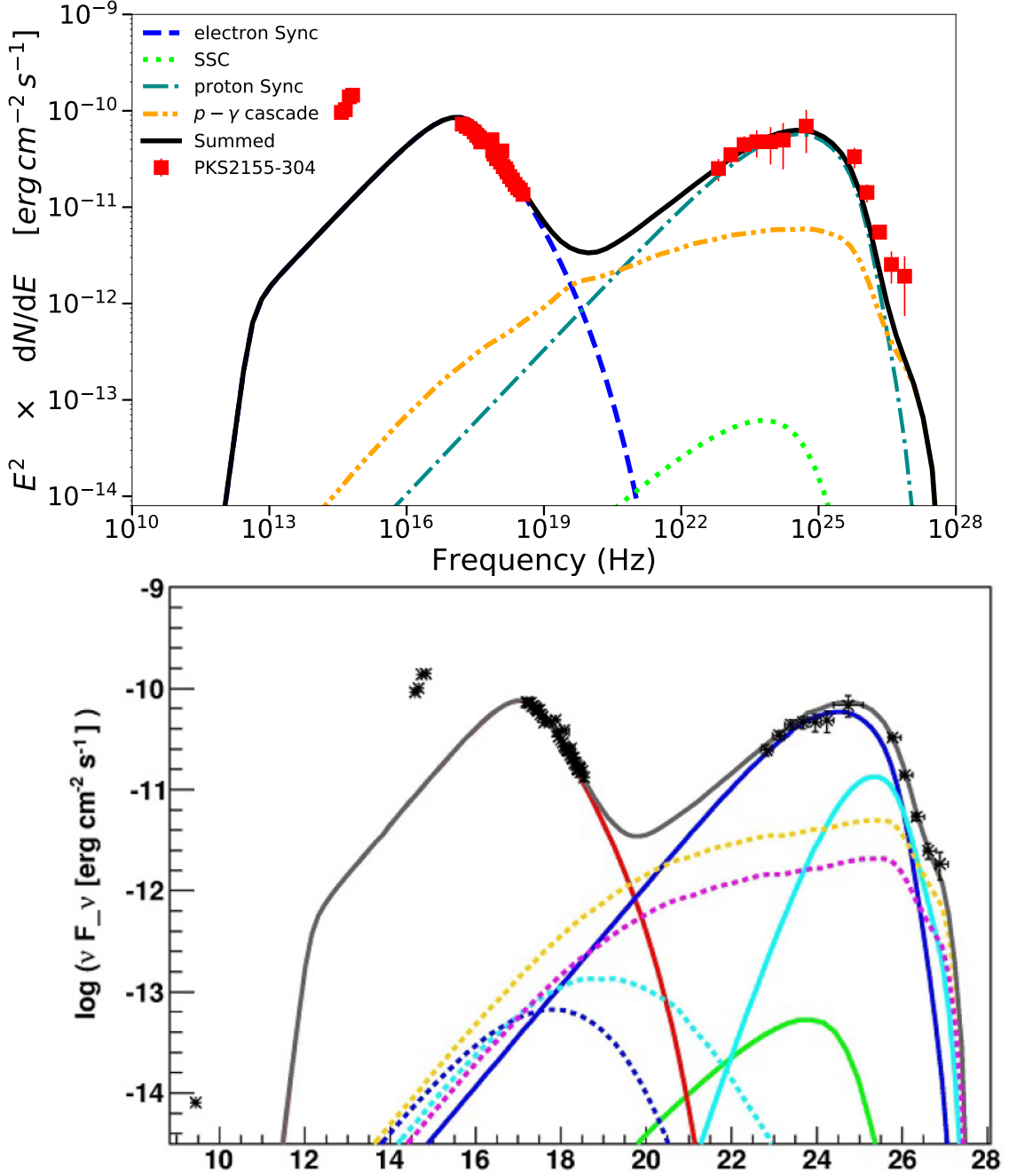


Figure 6.13: The hadronic model of the MWL SED of PKS 2155-304. The top panel shows the results obtained with the lepto-hadronic emission model developed for this thesis. The bottom panel shows the SED model from the original work of [Cerruti et al. \(2012\)](#). The colour code for the figure is same as in Fig. 6.12. Additionally, the light blue solid line represents muon synchrotron emission, the light blue and dark blue dotted lines represent the electromagnetic cascade associated with muon synchrotron and proton synchrotron respectively (for the list of parameters see Table 6.1).

Chapter 7

Multi-messenger association of a high-energy neutrino event with a flaring blazar TXS 0506+056

In this chapter, the observation of a high-energy neutrino event dubbed IC 170922A by the IceCube neutrino observatory and its association with a flaring blazar named TXS 0506+056, will be discussed. Those multi-messenger observations, for the first time, points towards a potential association of an extraterrestrial neutrino with an extragalactic source that also emits photons across the entire electromagnetic spectrum. These observations allow a comprehensive study of the astrophysical emission engine and links it to sources accelerating high-energy cosmic rays.

The analysis of the VHE γ -ray and multi-wavelength data presented in this chapter is not performed by the author. The main contribution of the author was to the investigation of plausible theoretical frameworks that can explain the multi-messenger observations and the neutrino-blazar association. The numerical code used for the evaluation of the basic radiative processes for this work, is discussed in Chapter 6. The results of the theoretical interpretation obtained from this study have been published in The Astrophysical Journal Letters ([Ansoldi et al., 2018](#)).

First, a brief description of the IceCube detection of the neutrino event IC 170922A will be given. This will be followed by a description of the electromagnetic observations in Sec. 7.1, from the *Fermi*-LAT, MAGIC and other multi-wavelength instruments (for more details, please see [IceCube Collaboration et al. \(2018b\)](#), [Ansoldi et al. \(2018\)](#)). The theoretical framework adopted for the interpretation will be discussed in Sec. 7.2, followed by a discussion of the results from the theoretical interpretation. The implications for neutrino emission obtained from the theoretical interpretation are compared with the results from IceCube, which show a good degree of agreement.

7.1 The neutrino and electromagnetic observations

To understand the sources of origin, the acceleration mechanisms and the interaction processes of cosmic rays, a combination of multiple cosmic messengers such as photons and neutrinos can be used. In contrast to cosmic rays which are deflected by the intervening magnetic fields during propagation towards the Earth, photons and neutrinos are electrically neutral and point back to the source. This is the essence of multi-messenger astronomy (see Chapter 2, Sec 2.4). While electromagnetic observations in the X-ray– γ -ray regime can arise due to both leptonic and hadronic emission processes, the coincident observation of a high-energy neutrino can be considered a "smoking gun" signature of hadronic acceleration.

In the subsections below, the coincident detection of a high-energy astrophysical neutrino with a γ -ray flaring blazar called TXS 0506+056 will be discussed. The compelling evidence of the observed correlation is the strongest of its kind so far and strengthens the importance of multi-messenger astronomy to understand the long-standing mystery about the origin of the ultra-high-energy-cosmic-rays.

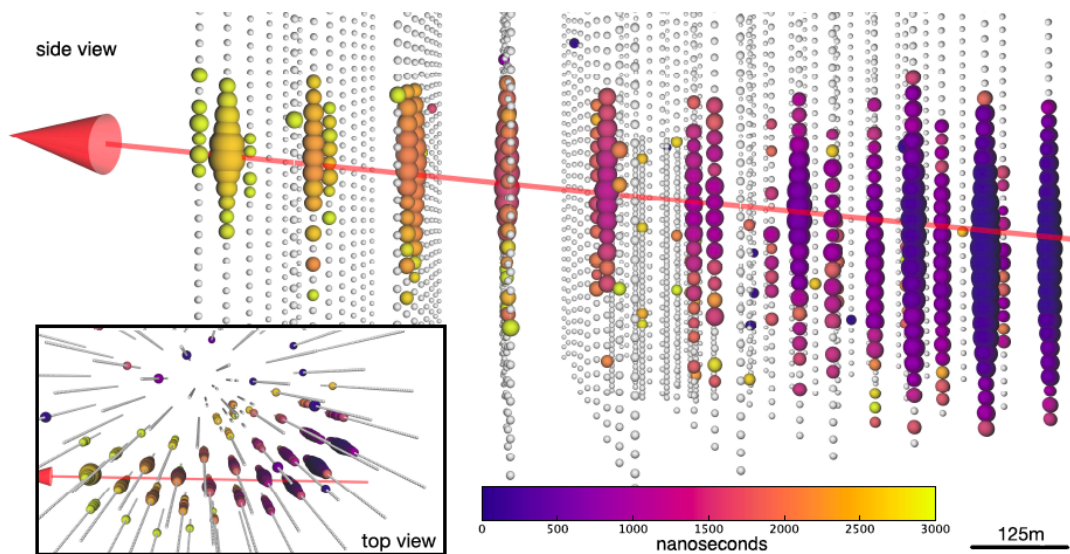


Figure 7.1: The event display of IC 170922A. The times at which the different DOMs of the IceCube detector observed the signal is indicated by the colorbar, with blue signifying the earliest time and yellow the latest time with respect to the first DOM hit of the signal. The inset shows a top view of the event. Figure taken from [IceCube Collaboration et al. \(2018b\)](#).

7.1.1 The IceCube detection of the astrophysical neutrino event IC 170922A

IceCube is a neutrino observatory of volume 1 km^3 located in Antarctica, at the geographic South Pole ([Aartsen et al., 2017b](#)). On 22nd September 2017, IceCube reported the detection of a high-energy neutrino event dubbed IC 170922A which had 56.5% probability of being truly astrophysical ([IceCube Collaboration et al., 2018b](#)). 43 seconds after detecting the high-energy neutrino-induced muon track on 22nd September, the IceCube real-time alert system sent an automated alert¹ to the observers, providing an initial estimate of the event direction and energy. A refined directional estimate (0.14° offset from the initial direction) was sent as a Gamma-ray Coordinates Network (GCN) circular 4 hours after the automatic alert². The event display of IC 170922A, depicting the times at which the signal was detected by the different digital optical modules (DOMs) of the detector is shown in Fig. 7.1. The prompt alert sent by IceCube right after the detection triggered intense multi-wavelength follow-up observations by various instruments observing photons across a wide energy range. On 28th September 2017, the *Fermi*-LAT collaboration reported that a catalogued γ -ray source named TXS 0506+056 located 0.1° away from the best-fit reconstructed direction of the IceCube event, was showing an enhanced activity in the GeV band ([IceCube Collaboration et al., 2018b](#)). Thanks to the precise estimation of the direction of the IceCube neutrino event, the probability of chance coincidence with a flaring blazar from the *Fermi*-LAT catalogue was disfavoured with a confidence level of $\sim 3.5\sigma$. Hence these observations for the first time, point towards a possible correlation between an astrophysical neutrino and an extragalactic source, that was also observed to be flaring in γ -rays. An independent estimate confirming the blazar TXS 0506+056 as a high-energy neutrino source came from an a-posteriori measurement by the IceCube Collaboration ([IceCube Collaboration et al., 2018a](#)). Investigating 9.5 years of IceCube data, the collaboration found an excess of high-energy neutrino events above the atmospheric background at the position of the blazar, between September 2014 and March 2015. These observations suggest that blazars are the first identifiable class of sources producing high-energy astrophysical neutrino flux.

The reconstructed energy of the neutrino event detected in 2017 was reported to be 290 TeV (311 TeV) with the 90% C.L. upper and lower limits to be 4.3 PeV (7.5 PeV) and 183 TeV (200 TeV) respectively, with an assumed spectral index for the diffuse astrophysical muon neutrino spectrum of 2.13 (2.0) ([Aartsen et al., 2014a](#)). No additional excess of lower energy neutrino events was detected from the direction of TXS 0506+056 during 2017

¹https://gcn.gsfc.nasa.gov/notices_amon/50579430_130033.amon

²<https://gcn.gsfc.nasa.gov/gcn3/21916.gcn3>

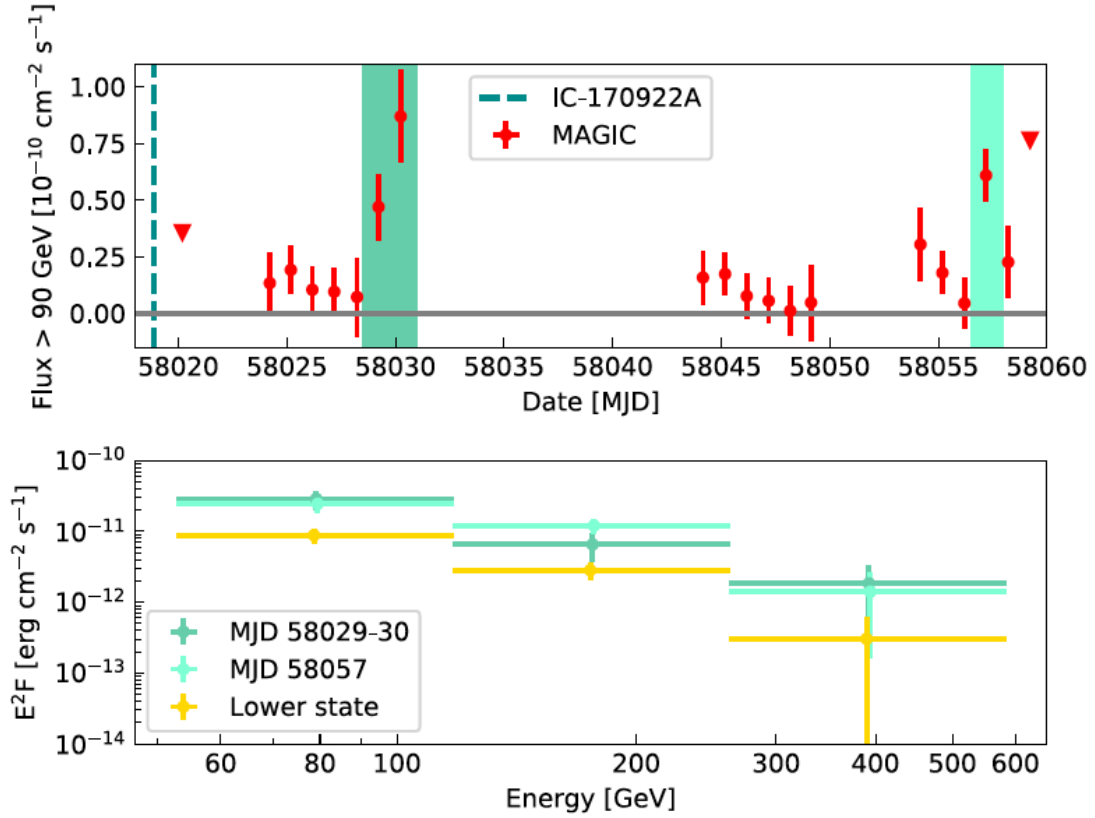


Figure 7.2: Top panel: The VHE γ -ray light curve above 90 GeV obtained by MAGIC. The data from MJD 58020-58030 has been presented in [IceCube Collaboration et al. \(2018b\)](#). The green shaded regions denote the two periods of enhanced activity observed by MAGIC on 3-4th October 2017 and 31st October 2017. MAGIC could also detect the source in a low VHE emission state excluding the two flaring activities mentioned above. Bottom panel: The VHE γ -ray spectrum ($E^2 \times \frac{dF}{dE}$) of TXS 0506+056 observed by MAGIC during different emission states. Figure taken from [Ansoldi et al. \(2018\)](#).

([IceCube Collaboration et al., 2018b](#)).

7.1.2 The γ -ray and multi-wavelength observations

Following the IceCube neutrino detection on 22nd September 2017, a number of multi-wavelength observations were performed across the entire electromagnetic spectrum spanning from radio up to VHE γ -rays. The source was found to be active in all energy bands, most notably in the HE γ -rays observed by *Fermi*-LAT and the VHE γ -rays, detected for the first time from this object by the MAGIC telescopes. The source was also later detected by VERITAS as a VHE γ -ray emitter ([Abeysekara et al., 2018](#)). The counts map of γ -rays above 1 GeV from *Fermi*-LAT and the detection significance map of MAGIC above 90 GeV following the flare has been reported in [IceCube Collaboration et al. \(2018b\)](#). For the work presented in this thesis, additional MAGIC and multi-wavelength data spanning 24th September (MJD 58020) - 2nd November (MJD 58060) 2017 have been used.

The light curve and spectra above 90 GeV obtained by the VHE MAGIC observations are shown in [Fig. 7.2](#). The VHE flux was found to be variable on daily timescales with an enhancement of factor up to ~ 6 within one day. Two periods of enhanced γ -ray activity, on 3-4th October 2017 (MJD 58029-58030) and 31st October 2017 (MJD 58057), could be clearly resolved. Excluding these two periods, MAGIC could also detect the source in a low VHE state with a significance of 5.7σ by stacking the rest of the data. The measured differential photon spectrum was found to be compatible with a power law of index 4.0 ± 0.3 to 3.5 ± 0.4 irrespective of the activity state, which is significantly steeper than the quasi-simultaneous spectrum measured from *Fermi*-LAT observations

(2.0 ± 0.2) .

To obtain quasi-simultaneous multi-wavelength coverage of the MAGIC observations, open access data from the instruments KVA (optical band), Ultraviolet and Optical Telescope (UVOT) and X-ray Telescope (XRT) on board the Neil Gehrels *Swift* observatory (UV and soft X-ray band), NuStar (hard X-ray band) and *Fermi*-LAT (HE γ -ray band) were analyzed with public tools. The data within 24 hours of the MAGIC observations were considered quasi-simultaneous. Good multi-wavelength coverage could be obtained for the VHE flare on 3-4th October 2017 and during the low VHE emission state. Due to lack of a good multi-wavelength coverage for the 31st October 2017 flare, it was excluded from the modelling discussed in Sec. 7.2.

It is to be noted that the low VHE emission state referred to here does not correspond to the typical quiescent state of the source as apparent from the archival data taken from the ASI Science Data Center, shown in Fig. 7.4 (bottom panel). Comparison of the light curve shown in Fig. 7.2 (top panel) and the results from *Fermi*-LAT (IceCube Collaboration et al., 2018b) show that the low state represents rather an average emission state during the 6 months of enhanced GeV activity from the source observed by *Fermi*-LAT.

7.2 Interpretation of the broadband electromagnetic and neutrino emission

It is believed that the production of neutrinos in BL Lac objects occur through the decay of charged pions produced by the interaction of ultra-relativistic protons with the target radiation fields present within the emission region (p- γ interactions). For the production of a 290 TeV neutrino, the parent proton energy in the observer's frame should be $E'_p = 20E'_\nu \approx 6$ PeV. From the photo-meson interaction threshold, the energy of the target photons in the observers' frame, required to produce the neutrino is given by $\epsilon' = m_\pi m_p c^4 / E'_p \approx 440 - 870$ eV (depending on the Doppler factor $\delta=20-40$), i.e. in the UV to soft X-ray region.

FSRQs are generally considered good candidates for efficient neutrino production (Murase et al., 2014) due to the presence of high density of target photons for p- γ interactions in such environments. However, the target photons in such environments peaking at much lower energies, produce a hard spectrum of neutrinos with a maximum yield at ~ 10 PeV which is higher than that inferred from the IceCube observations (IceCube Collaboration et al. (2013); Aartsen et al. (2014b)). Murase et al. (2014) inferred that non-standard assumptions have to be added to the standard scenario to explain the IceCube results.

BL Lacs usually have a low density of target photons for p- γ interactions and hence a large power in the ultra-relativistic protons are required in the hadronic scenarios to produce neutrinos (Cerruti et al., 2018). However high efficiency of the p- γ interactions at the cost of low power injected into the protons, can be achieved by considering photons external to the jet. One such scenario is the so-called spine-layer model (Ghisellini et al. (2005); Tavecchio et al. (2014); see Sec. 7.2.1 for a brief description of the model).

The p- γ interaction process on the target photon fields are also accompanied by γ - γ absorption of the photons emitted in the VHE γ -ray regime, best accessible to MAGIC. Hence the spectral features at a few hundred GeV as observed by MAGIC serve as important constraints for the density of the target radiation field adopted in the model.

In the subsections below, a brief description of the spine-layer scenario and the model assumptions will be presented.

7.2.1 The spine-layer framework

In this section the theoretical framework used for the TXS 0506+056 modelling will be briefly discussed. The model adopted for the theoretical interpretation is the so-called spine-layer model (Tavecchio et al., 2014). The essential features of this model will be re-called and for more details, the reader is referred to the main reference.

The spine-layer model postulates the existence of a velocity structure in the blazar jets, with a fast moving spine surrounded by a slower layer. Such a stratified velocity profile of the jet is directly inferred from very long baseline interferometry observations in the radio band, where a "limb-brightened" structure was observed in the jets of some blazars and radio galaxies (Giroletti et al. (2008); Nagai et al. (2014)). The direct consequence of the existence of such a velocity structure in the jet, is a radiative coupling between the spine and the layer which results in relativistic amplification of the radiation field of the layer in the frame of the spine (and vice versa).

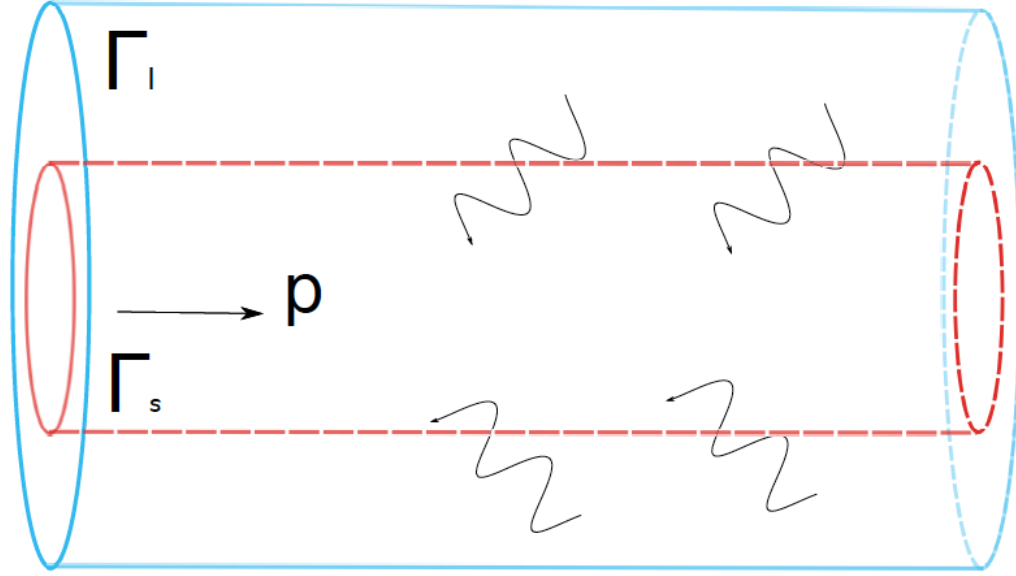


Figure 7.3: Schematic representation of the spine-layer model. The blazar jet is assumed to be composed of a fast-moving spine surrounded by a slower layer having bulk Lorentz factor Γ_s and Γ_l respectively. The relative motion between the two regions leads to a relativistic amplification of the density of the radiation field and photon energy of the layer in the frame of the spine by a relativistic Lorentz factor Γ_{rel} (see the text below). Figure taken from [Righi et al. \(2017\)](#).

Due to the relativistic amplification, the boosted layer radiation in the spine frame can easily dominate over the intrinsic radiation field of the spine. A schematic representation of the velocity structure of the jet postulated in the spine-layer model, is shown in Fig. 7.3.

Let us assume that the bulk Lorentz factor of the spine is Γ_s and that of the layer is $\Gamma_l \ll \Gamma_s$. The Doppler factors are denoted by δ_s and δ_l for each component, respectively. If the luminosity of the layer in the observer's frame is denoted as $L(\epsilon_l)$, then the photon number density in the layer frame is defined as:

$$n(\epsilon_l'') = \frac{L(\epsilon_l)}{4\pi R^2 c \delta_l^3 \epsilon_l''} \quad (7.1)$$

where R denotes the radius of the emission region (the emission region is assumed to possess a cylindrical geometry). Due to relative motion between the spine and the layer, the number density and energy of the layer photons will appear boosted in the spine frame by a relative Lorentz factor $\Gamma_{\text{rel}} = \Gamma_s \Gamma_l (1 - \beta_s \beta_l)$ according to the following transformations: $n(\epsilon_s'') d\epsilon_s'' = \Gamma_{\text{rel}} n(\epsilon_l'') d\epsilon_l''$ and $\epsilon_s'' = \Gamma_{\text{rel}} \epsilon_l''$.

When the boosted radiation field of the layer is the dominant soft photon field in the frame of the spine, it can significantly increase the efficiency of the inverse Compton and neutrino emission of the spine, compared to the conventional one-zone models. Thus the spine-layer model provides a theoretically-driven and observationally-motivated framework for efficient neutrino production in the jets of BL Lacs ([Tavecchio et al. \(2014\)](#), [Tavecchio and Ghisellini \(2015\)](#), [Righi et al. \(2017\)](#)), which usually are considered as insufficient neutrino emitters due to their intrinsically low target radiation field.

The spine-layer scenario has been used to explain the electromagnetic SED of various astrophysical objects such as BL Lacs and radio galaxies ([Ghisellini et al. \(2005\)](#), [Tavecchio and Ghisellini \(2008\)](#), [Tavecchio and Ghisellini \(2014\)](#)). The previous works treated the leptonic emission components and/or neutrino emission, but lacked an explicit treatment of the hadronic emission processes. This work is the first extension of the model to also include the relevant hadronic radiative processes along with the leptonic processes inside AGN jets.

Table 7.1: Model parameters for the high and low VHE state using the spine layer model (for the maximum proton energy $E_{p,max} = 10^{16}$ eV and the proton spectral index $n_p = 2$)

Parameters	Symbols	MJD 58029-30	Low state
Magnetic field strength	B (G)	2.6	2.6
Min. e^\pm energy	$E_{e,min}$ (eV)	3.2×10^8	2.0×10^8
e^\pm break energy	$E_{e,brk}$ (eV)	7.0×10^8	9.0×10^8
Max. e^\pm energy	$E_{e,max}$ (eV)	8.0×10^{11}	8.0×10^{11}
e^\pm injection spectral index	n_1	2	2
e^\pm after-break spectral index	n_2	3.9	4.4
Electron luminosity	P_e (erg s $^{-1}$)	2×10^{42}	1.6×10^{42}
Proton luminosity	P_p (erg s $^{-1}$)	8×10^{45}	3×10^{45}
Magnetic field luminosity	P_B (erg s $^{-1}$)	1.2×10^{45}	1.2×10^{45}

7.2.2 Model description

This subsection discusses the basic model assumptions used for the interpretation of the observed multi-messenger signal.

The emission region is assumed to possess a cylindrical geometry. The spine is assumed to be a solid cylinder with radius R_s and length $H_s = R_s$. The layer, which surrounds the spine is a hollow cylinder with inner radius $R_{l,i} = R_s$, outer radius $R_{l,o} = 1.5 \times R_s$ and length $H_l = R_l$. The volume of the spine is $V_s = \pi R_s^2 H_s$ and that of the layer is $V_l = \pi H_l (R_{l,o}^2 - R_{l,i}^2)$. The spine and the layer possess bulk Lorentz factors Γ_s and Γ_l such that $\Gamma_s > \Gamma_l$. The boosted radiation field from the layer is used as target photon field in the spine frame. The radiative components are calculated in the frame of the spine and then transformed to the frame of the observer by relativistic Doppler transformations.

The emission region is assumed to be filled with a tangled magnetic field of strength B and contain a population of co-accelerated ultra-relativistic electrons and protons. The electrons follow a broken power law distribution with spectral indices n_1 and n_2 before and after break, energy of the break $E_{e,brk}$ and minimum and maximum energy $E_{e,min}$ and $E_{e,max}$. The protons follow a power law with exponential-cutoff distribution with spectral index n_p and maximum proton energy $E_{p,max}$.

The angular distribution of the boosted seed photons from the layer for inverse Compton scattering are highly anisotropic in the frame of the spine. For small viewing angle of the jet with respect to the observer, such anisotropy effect induces a narrower beaming pattern (the so-called "Dermer effect") in the external Compton component with respect to the SSC component (Dermer (1995), Ghisellini et al. (2005)), which has been taken into account in the model. The same argument can be extended for the neutrino production. The seed photons being highly anisotropic in the spine-frame, the charged pions and muons produced in photo-meson interactions with the protons, also have an anisotropic angular distribution in the spine frame. If the magnetic field is not too large (i.e. $<$ few tens of Gauss), then under the assumption that the charged pions and muons are not significantly deflected by the field before decaying, the produced neutrinos also follow an anisotropic distribution in the jet rest frame. This should induce a similar narrowly beamed neutrino spectrum in the observer's frame in analogy with the external Compton component. However, due to the complexity in the trajectory of propagation of the charged particles, detailed Monte Carlo simulations are required to quantify the effect. This is beyond the scope of the current work and hence not explicitly included in the calculations. On the other hand, the anisotropy does not affect the photo-meson cascade spectra, since the secondary leptons produced in such interactions are expected to be isotropized by the magnetic field as they degrade in energy.

The main parameters of the model (i.e. the particle distributions, magnetic field, Doppler factor) are varied to consistently interpret the multi-messenger electromagnetic and neutrino observations. The absorption of the γ rays by the EBL during its propagation towards the Earth is modelled following Dominguez et al. (2011). Recently the redshift of the source was measured to be $z = 0.3365 \pm 0.0010$ (Paiano et al., 2018). At such redshift, the absorption due to the EBL does not significantly affect the γ rays observed below 400 GeV from this source (the absorption factor is expected to be $\sim 10\%$ at 400 GeV).

7.3 Results

The results obtained for the multi-messenger interpretation of the observed broadband electromagnetic SED of TXS 0506+056 and the observed neutrino signal is discussed in this section.

The results of the modelling for the high and low VHE emission states are shown in Fig. 7.4 (top panel: modelling for the high VHE state; middle panel: modelling for the low VHE state) and the model parameters are given in Table 7.1. The assumed spectral index for the electrons before break is $n_1 = 2$, which is also equal to the index of the proton distribution assuming a co-acceleration scenario. The size of the emission region is fixed to $R = 10^{16}$ cm by assuming a variability timescale of 1 day as observed in the VHE energy band by MAGIC. The bulk Lorentz factor of the spine and layer are assumed to be $\Gamma_s = 22$ and $\Gamma_l = 2.2$ respectively and the viewing angle $\theta_{view} = 0.8^\circ$ is the same for both the regions. At such small viewing angles ($\theta_{view} < \frac{1}{\Gamma_j}$) the intensity of the external Compton spectrum is expected to be more than the synchrotron, SSC, cascade components due to the anisotropic beaming effect (Dermer, 1995). The total jet power is calculated using the formula $L_{jet} = \pi R^2 \Gamma_s^2 c (u_e + u_p + u_B)$ where u_e, u_p, u_B are the co-moving energy densities of the electrons, protons and the magnetic field. The contribution of the individual components to the total jet power, L_e, L_p, L_B are given in Table 7.1.

7.3.1 Radiative components and their contribution to the overall SED

The main radiative components arising from the modelling are: synchrotron radiation, SSC, external Compton and photo-meson cascade. The later is the most important hadronic component in our modelling (direct synchrotron radiation by ultra-relativistic protons is expected to give a negligible contribution to the overall SED for the magnetic field strength chosen for the modelling). The neutrino spectra predicted from the modelling are shown with the solid brown lines in Fig. 7.4. The muon and pion synchrotron radiation losses are neglected in our model under the assumption that they decay instantaneously before interacting. As shown by Böttcher et al. (2013), this assumption imposes a constraint in the magnetic field for an assumed maximum proton energy. This condition is always respected in our model as shown in Fig. 7.5. In the chosen parameter regime (shaded pink region in Fig. 7.5), the decay timescales of the muons and pions are always smaller than their cooling timescales.

The lower energy hump arises due to synchrotron radiation by the primary electrons in the spine and the second SED hump arises due to external Compton scattering of the boosted layer photons by the electrons in the spine. The hadronic cascade component is mostly subdominant, but gives a non-negligible contribution especially in the X-ray and the VHE γ -ray band. As can be seen from Fig. 7.4, the observed data from optical up to the VHE γ -ray regime can be predominantly explained with leptonic emission. This is in contrast with the commonly accepted view that neutrino emission predicts hadronically-dominated γ -rays. Our models show that neutrino emission from blazars can be in agreement with a leptonic dominated electromagnetic SED. This is in agreement with many previous studies that predict that the broadband electromagnetic emission from blazars is typically leptonic in origin.

If a comparison is drawn for the model parameters for the high and low VHE emission states (the comparison plot is shown in the bottom panel of Fig. 7.4), the high state can be explained by a harder electron spectrum after break, a larger average energy and an increased proton luminosity with respect to the high state. Such a variability is consistent with the commonly observed activity states of BL Lac objects. The total jet power for both the states is in the range $10^{45} - 4 \times 10^{46}$ erg/s, which is slightly higher than purely leptonic models where no ultra-relativistic proton population is considered (Ghisellini et al., 2009). The ratio of the energy densities of protons and electrons in the jet frame are ~ 3600 and ~ 1700 respectively for the high and low states, similar to those inferred from various astrophysical environments.

Finally, a spectral steepening could be observed in the VHE γ -ray band observed by MAGIC, above ~ 100 GeV. This steepening could be attributed to the internal γ - γ absorption. The photon-meson efficiency $f_{p\gamma}$ defined as the ratio of the adiabatic and photo-meson cooling timescales, $f_{p\gamma} = \frac{t_{adia}}{t_{p\gamma}}$, is $\sim 10^{-4}$ for the production of a 290 TeV neutrino. The p- γ efficiency can be directly connected to the γ - γ optical depth according to the following relations (Murase et al., 2016):

$$\tau_{\gamma\gamma}(\varepsilon_\gamma) \sim 10 \left(\frac{f_{p\gamma}(\varepsilon_p)}{0.01} \right) \quad (7.2)$$

where $\varepsilon_\gamma \sim \text{GeV} \left(\frac{\varepsilon_\nu}{25 \text{ TeV}} \right)$. For the case under consideration, $\varepsilon_\nu = 290$ TeV and $f_{p\gamma} = 10^{-4}$, which gives $\tau_{\gamma\gamma} \sim 0.1$ for $\varepsilon_\gamma \sim 10$ GeV. The γ - γ absorption only starts becoming important for $\varepsilon_\gamma > 100$ GeV, which matches the spectral

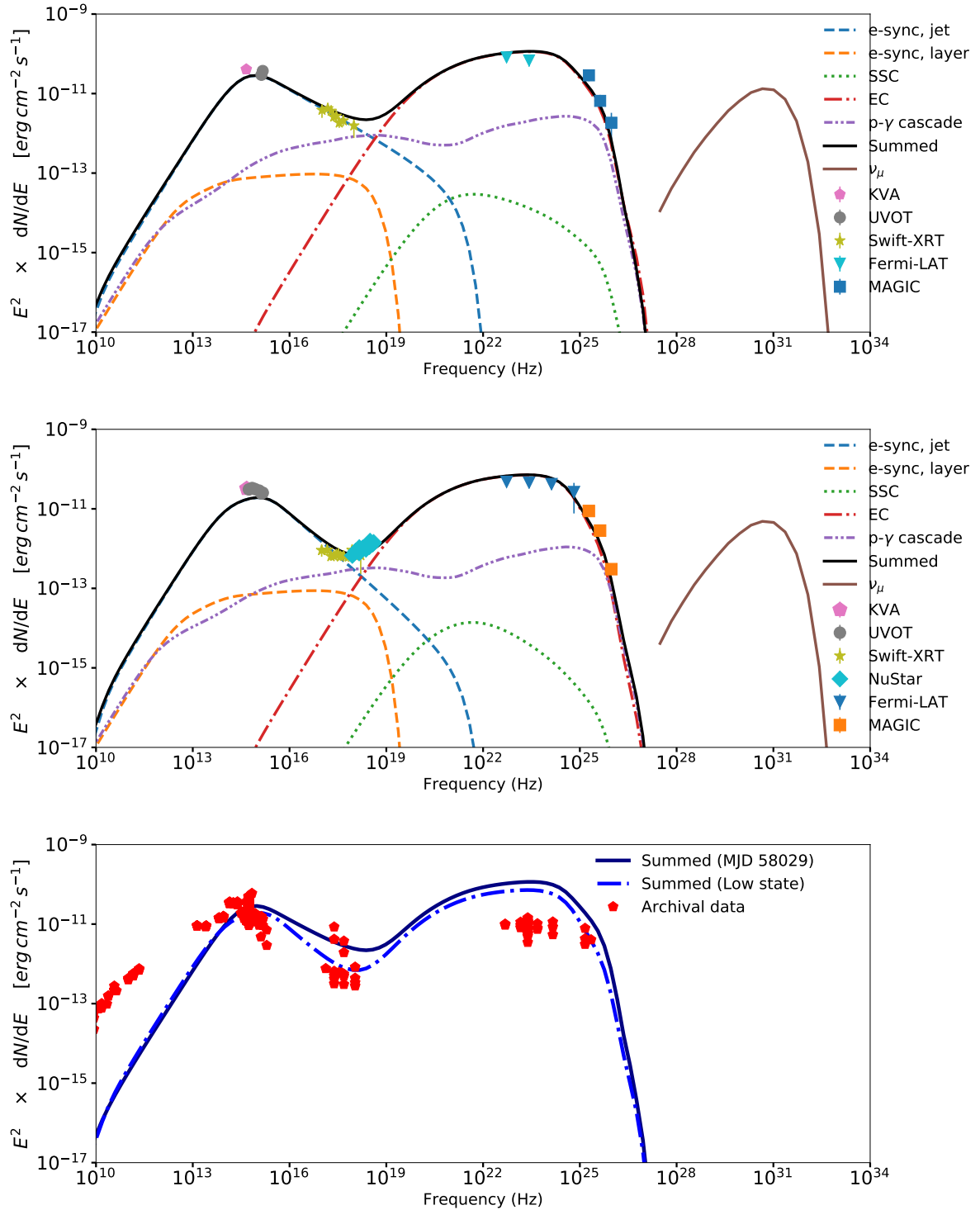


Figure 7.4: SED modelling for the multi-messenger observations of TXS 0506+056 in the framework of the spine-layer model, using $E_{p,max} = 10^{16}$ eV. The data from different instruments and the contribution of individual non-thermal components to the total SED are described in the legend. Top panel: High state (MJD 58029 to 58030). Middle panel: Low state. Bottom panel: Comparison of the high and low VHE states and the archival data from the ASI Science Data Center.

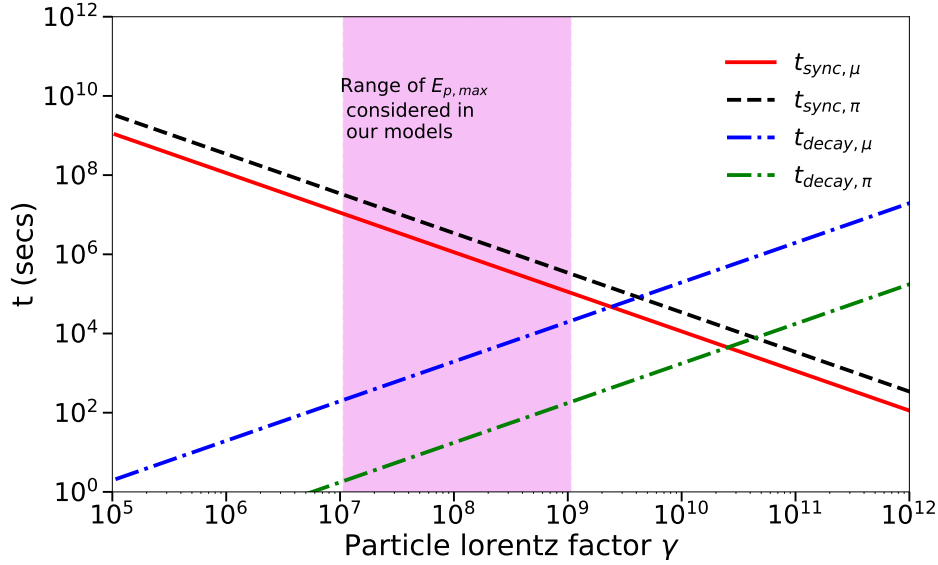


Figure 7.5: Comparison of the decay and cooling timescales of the intermediate muons and pions produced in the photo-meson interactions responsible for the high-energy neutrino emission. In the chosen parameter regime (the shaded pink region), the muons and pions decay much faster before cooling. Thus the cooling of the intermediate products can be neglected.

steepening observed by MAGIC with respect to the *Fermi*-LAT spectrum. The absorption due to the EBL plays a negligible role at such energies for the redshift of the source ($z \sim 0.34$), as pointed out earlier in Sec. 7.2.2.

7.3.2 The neutrino event rates and neutrino energy

The muon neutrino fluxes predicted from the theoretical modelling are shown with the solid brown lines in Fig. 7.4. The neutrino flux is then convolved with the IceCube effective area reported in IceCube Collaboration et al. (2018b) at the declination of the source and the cumulative distribution of the convolved quantity is derived in order to obtain the confidence bands for the neutrino energy. The obtained cumulative distribution is shown in Fig. 7.6. The derived 80% and 90% C.L. energy containment interval of the model-predicted neutrino spectra are shown with the shaded green and red regions respectively in Fig. 7.6. The theoretically obtained 90% C.L. energy band, 206 TeV - 6.3 PeV is in good agreement with the observationally-derived 90% C.L. energy interval reported by IceCube: 183 TeV (200 TeV) and 4.3 PeV (7.5 PeV) for an assumed index of -2.13 (2.0) (IceCube Collaboration et al., 2018b).

The neutrino rates are derived by assuming an activity period of 6 months, which is motivated by the duration of the high activity state observed by *Fermi*-LAT. The neutrino flux (and hence the event rate) is constrained by the limits on the hadronic cascade emission imposed by the electromagnetic SED, especially in the X-ray and VHE γ -ray bands. The obtained neutrino event rates for a 6 months period are 0.17 for the high state and 0.06 for the low state. Both these numbers are consistent with the detection of one neutrino event by IceCube. If the anisotropy of the target photon field is taken into account analogous to the external Compton emission, the rates can be boosted by a factor of 2-3.

7.3.3 Constraints on the maximum proton energy

The observation of a single neutrino event with energy of 290 TeV, implies the presence of ultra-relativistic protons with maximum energy of at least $E_{p,max} = 5.8$ PeV (in the observers' frame). The combination of the observed neutrino signal and the electromagnetic data help us to scan the parameter space of the maximum proton energy to obtain the limits on $E_{p,max}$.

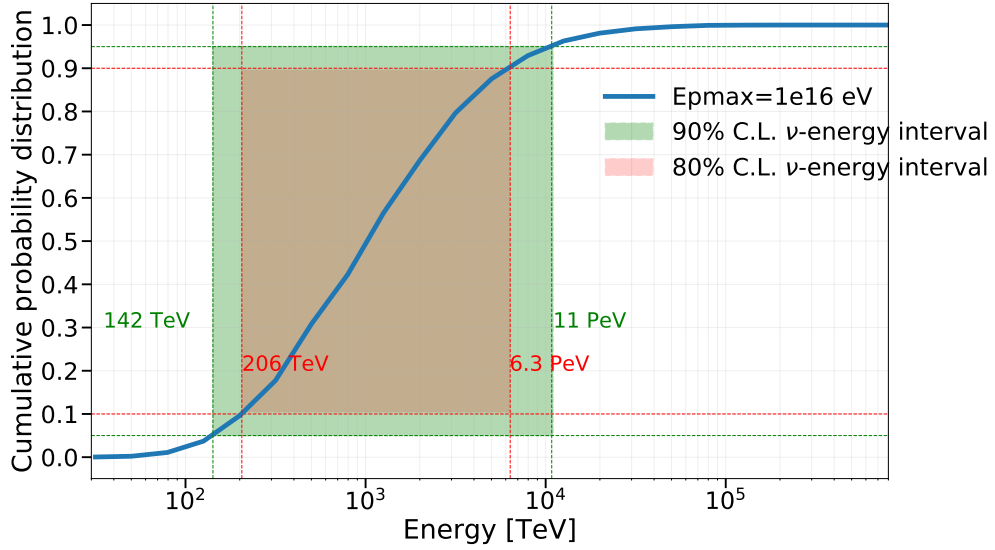


Figure 7.6: The cumulative distribution function of the neutrino flux (obtained from the spine-layer SED modelling, shown in Fig. 7.4) convolved with the IceCube effective area, as a function of the neutrino energy. The green and red shaded region indicate the 90% and 80% containment neutrino energy interval as predicted by the theoretical modelling (142 TeV - 11 PeV and 206 TeV - 6.3 PeV, respectively).

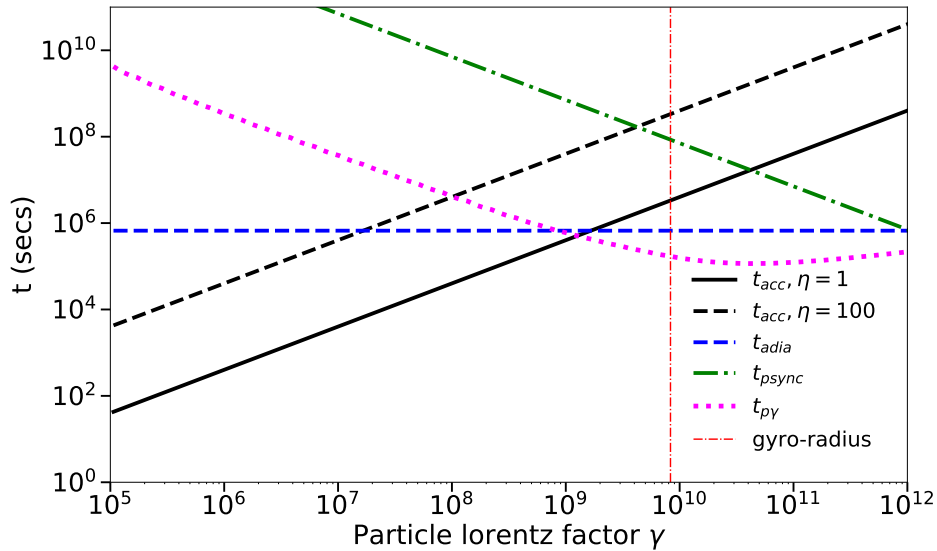


Figure 7.7: The comparison of the proton acceleration timescale (t_{acc}) and the cooling timescales - adiabatic loss (t_{adia}), synchrotron loss (t_{psync}), p- γ loss ($t_{p\gamma}$) as a function of the proton Lorentz factor in the co-moving frame. As shown, the energy corresponding to the gyro-radius is greater than the maximum allowed proton energy (defined as the energy where the acceleration timescales is equal to the minimum cooling timescale - in this case t_{adia} and $t_{p\gamma}$).

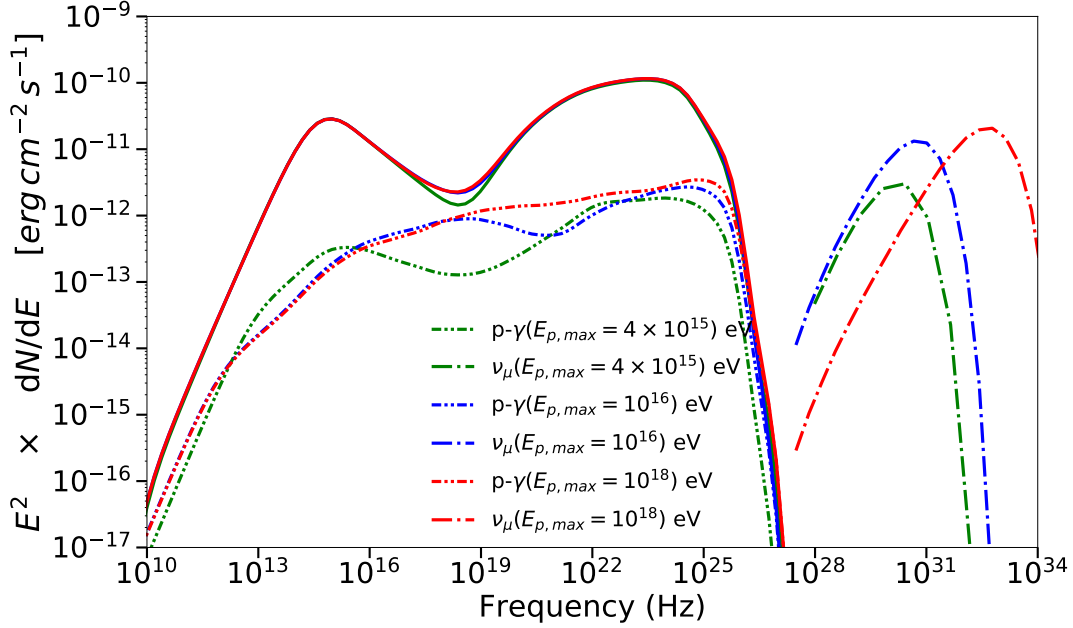


Figure 7.8: The effect of variation of the maximum proton energy $E_{p,max}$ on the overall SED (solid lines), the hadronic p- γ cascade component (dot-dot-dashed lines) and neutrino emission (dot-dashed lines) for the high state.

As mentioned earlier, the most important hadronic component for broadband SED of TXS 0506+056 is the photo-meson cascade component, which constraints also the contribution of the neutrino fluxes. A coarse scan of the $E_{p,max}$ parameter space was performed and the contribution from the photo-meson component was evaluated at each energy along with the predicted neutrino flux. The aim of the work was to achieve an acceptable neutrino event rate compatible with the IceCube observations within Poissonian fluctuations, without violation of the X-ray and VHE γ -ray constraints on the photo-meson cascade component.

By considering a balance between the acceleration timescale and different cooling timescales (Cerruti et al., 2015), it was found that the maximum proton energy can reach up to $\sim 10^{18}$ eV (in the co-moving frame), as shown in Fig. 7.7. The efficiency of acceleration is characterized by the η_{acc} parameter. As shown in the figure, for $\eta_{acc} = 1$ (most efficient acceleration), the proton Lorentz factor can reach values up to $\sim 10^9$ (corresponding to $E_{p,max} = 10^{18}$ eV), governed by the adiabatic and photo-meson cooling timescales (t_{adia} and $t_{p\gamma}$ respectively).

Lower values of $E_{p,max}$ are still possible by considering a less efficient acceleration (e.g.: $\eta_{acc} = 100$). With the above constraints, $E_{p,max}$ was varied between few times 10^{15} to 10^{18} eV and contribution to the photo-meson cascade and neutrino emission are shown in Fig. 7.8 for the high VHE emission states. From the obtained neutrino event rates, we can infer that the maximum proton energy can be anywhere between $10^{15} - 10^{18}$ eV. We note that the Bethe-Heitler contribution was neglected for this work, since at energies well above the threshold for photo-meson interactions, the photo-meson process dominates over the Bethe-Heitler process, which is true at least up to $E_{p,max} \sim$ few times 10^{15} eV for the parameter regime considered here. At lower energies, the Bethe-Heitler process can give a dominant contribution over the photo-meson cascade, especially at the X-ray band energies, but can still achieve acceptable neutrino rates in conformity with the IceCube measurements (Ansoldi et al., 2018).

To an observer on Earth, the maximum proton energy will appear boosted due to relativistic beaming, i.e. $E_{p,observed} = \Gamma_j f_{el} E_{p,max}$, where $f_{el} \leq 1$ is an energy loss factor due to escape. Assuming $f_{el} \sim 1$, $\Gamma_j = 22$, $E_{p,observed} \sim 2 \times 10^{16} - 2 \times 10^{19}$ eV. The upper limit of the observed maximum proton energy falls well within the regime of UHECRs.

Chapter 8

Summary and conclusions

The goal of this thesis was to investigate the non-thermal emission mechanisms in Active Galactic Nuclei (AGNs) particularly blazars, especially in the context of hadronic processes leading to neutrino and cosmic-ray production. Observation of very-high-energy (VHE) γ rays in synergy with observation at larger wavelengths (the so-called multi-wavelength observations) were used to construct the complete broadband spectral energy distribution (SED) for two AGNs: 1ES 1959+650 and TXS 0506+056. A detailed characterization of the broadband SED spanning 20 orders of magnitude from radio up to VHE γ rays is of paramount importance to understand the operating non-thermal emission mechanisms, nature of the emitting particles, physical properties of the central engine, energetics of the source etc. This is one of the fundamental steps to identify extreme astrophysical environments where high-energy cosmic-ray can be accelerated. The sources of origin of these high-energy particles that we frequently detect on Earth, pose one of the biggest challenges in the field of Astroparticle Physics. A combination of multiple cosmic messengers, namely cosmic rays, photons and neutrinos provide a very powerful method to identify potential cosmic-ray accelerators. Since charged cosmic rays do not point back to the progenitor due to deflections in the cosmic magnetic fields, electromagnetic and neutrino observations can be used as direct messengers of the sources of origin. High-energy photons can originate due to both leptonic and hadronic interaction processes within the source while neutrinos can only be produced by hadronic mechanisms. Simultaneous photon and neutrino observations (so-called multi-messenger observation strategy) and their interpretation within a self-consistent scenario are thus crucial to constrain the source characteristics and provide a firm evidence for high-energy cosmic-ray acceleration.

Interpretation of the broadband electromagnetic SED of AGNs in the framework of hadronic or lepto-hadronic emission models, also predict a flux of high-energy neutrinos. The predicted flux can be compared with the observations by neutrino telescopes, or in case of non-observations can be used to constrain the level of neutrino emission from the source. For the interpretation purpose, a new stationary lepto-hadronic SED modelling code was developed. The code can perform detailed numerical calculations for all the relevant leptonic non-thermal emission processes such as synchrotron radiation, inverse Compton up-scattering as well as the hadronic emission components such as proton synchrotron, photo-meson interactions, proton-proton interactions and pair cascades. The code thus allows for a complete self-consistent study of the broadband SED from AGNs over a wide range of parameters within a reasonable amount of time. Apart from modelling the electromagnetic SED, the code can also compute the neutrino spectra for all flavours. The hadronic non-thermal emission mechanisms implemented in the code can thus play an important role to investigate plausible cosmic-ray sources via modelling of multi-messenger photon and neutrino observations.

VHE γ -ray measurements are the key to constrain the emission mechanisms responsible for the second SED hump of AGNs, that typically exhibit a two-hump structure. The origin of the first hump is unambiguously attributed to synchrotron radiation by ultra-relativistic electrons present within the emission region. The origin of the high-energy hump is debatable and can originate due to both hadronic or leptonic radiation processes. Hence strong implications regarding cosmic-ray and neutrino production can be derived from interpretation of the second SED hump of AGNs, which relies upon detailed measurement of the VHE γ -ray spectra for a complete characterization. In this thesis the interpretation of two AGNs are discussed, namely the blazars 1ES 1959+650 and TXS 0506+056.

1ES 1959+650 is a bright and nearby object, which showed in the past peculiar features like the "orphan" VHE

γ -ray flare in 2002 and is considered a strong candidate for hadronic particle acceleration. In this thesis the 2016 monitoring campaign with the MAGIC telescopes is discussed. It is complemented with observations across a wide range of frequencies including optical/UV (*Swift*-UVOT), X-ray (*Swift*-XRT) and high-energy γ rays (*Fermi*-LAT). MAGIC observed the source during different activity periods throughout 2016 accumulating a total of > 63 hours of data.

The long-term X-ray and VHE γ -ray data collected during 2016 showed a mild hint of correlation with zero time lag. The X-ray spectral index becomes harder with increasing flux and a similar trend is also visible in the VHE γ -ray band. The source entered into a very active state from June 2016. Three remarkable VHE flares were observed by MAGIC on 13th June, 14th June and 1st July 2016, with flux levels reaching ~ 3 times the flux of Crab Nebula, our standard candle in the γ -ray sky. The de-absorbed VHE spectra above 300 GeV was quite hard and extended up to several TeV. The spectra in the X-ray band and high-energy γ -ray band also showed considerable hardness. Two of the three brightest flaring nights, 13th June and 1st July showed rapid variations of the VHE flux within sub-hour timescales (flux doubling time ~ 35 mins). The characteristic fast variability timescale was used to constrain the size of the emission region during the flares within a few $10^{14} - 10^{15}$ cm.

The rich multi-wavelength data collected during the γ -ray activity period of 13th June and 14th June allowed a detailed investigation of the emission properties of the source. A simple one-zone synchrotron self-Compton (SSC) model can describe the data requiring moderate to high values of the Doppler factor ($\delta > 35 - 50$). Alternatively, the high-energy emission component can also be attributed to synchrotron radiation by extremely energetic protons present within the jet, if the strength of the magnetic field is sufficiently high ($B \sim 100$ G). A mixed lepto-hadronic scenario was also investigated where the high-energy emission arises by a combination of SSC and photo-meson pair cascade process, but it requires extremely high values of the total jet power ($L_{jet} > 10^{48}$ erg/s).

1ES 1959+650 had been considered in the past as a prime candidate source of high-energy neutrinos. In 2005, the AMANDA neutrino observatory reported the detection of three neutrinos in spatial and temporal correlation with the source (Halzen and Hooper (2005), Bernardini et al. (2005), Ackermann et al. (2005)), although the statistical significance of the association was not possible to estimate a-posteriori. From the hadronic and lepto-hadronic SED modelling of the 2016 VHE flares performed in this thesis, it was inferred that the source cannot produce detectable neutrino emission in accordance with the sensitivity of the current generation of neutrino telescopes.

The final part of the thesis deals with interpretation of the multi-messenger observations of a high-energy neutrino event in coincidence with a flaring BL Lac object (see however Padovani et al. (2019)), that provides the first compelling evidence of an extragalactic high-energy cosmic-ray source. In September 2017, the IceCube neutrino observatory detected a high-energy neutrino event dubbed IC 170922A in possible positional correlation with a catalogued γ -ray source named TXS 0506+056, which was also observed to be flaring in γ rays as observed by the *Fermi*-LAT and MAGIC telescopes (IceCube Collaboration et al., 2018b). For interpretation of the multi-messenger signal from the source, multi-wavelength data spanning optical to VHE γ rays was accumulated from 22nd September 2017 following the IceCube detection, up to 2nd November 2017. The interpretation was performed for the flaring VHE state of the source in October 2017 and also a low VHE state excluding the high activity periods. A theoretical framework known as the spine-layer model (Tavecchio et al., 2014) was adopted for this work, where the jet is postulated to possess a velocity structure, having a fast spine surrounded by a slower layer. BL Lacs are generally considered inefficient neutrino emitters due to lack of a dense internal target photon field for photo-meson interactions. Due to the relativistic amplification of the layer photons in the spine frame, it can act as the dominant source of soft photons within the spine exceeding its internal photon density. Such a geometry thereby boosts the potential for neutrino emission from BL Lac objects. The previous works with the spine-layer model included either the leptonic processes and/or neutrino emission, but did not explicitly treat the hadronic processes. This work represents the first extension of the spine-layer model for a self-consistent treatment of both the leptonic and hadronic emission components.

The lepto-hadronic modelling showed that the first SED hump originates due to the usual electron synchrotron radiation while the second SED hump arises due to inverse Compton up-scattering of the boosted layer photon by the electrons in the spine frame. The neutrino emission arises due to photo-meson interactions of the boosted layer photons with an assumed population of ultra-relativistic protons. The photo-meson interactions also give rise to a photo-meson pair cascade component in the electromagnetic SED, whose contribution is however sub-dominant with respect to the inverse Compton contribution, but non-negligible especially in the X-ray and VHE γ -ray band. The steep VHE spectra observed by MAGIC was found to be consistent with internal γ - γ absorption in the same photon field responsible for the high-energy neutrino production. The inferred neutrino rates from the modelling

(0.17), assuming a six month long activity period of the source as observed by *Fermi*-LAT, is in agreement with the IceCube measurements. The model-predicted 90% containment interval of the neutrino energy (142 TeV - 11 PeV) is also in good agreement with the IceCube predictions. While the observation of a single neutrino by IceCube having energy ~ 290 TeV infers the presence of relativistic protons with atleast energy of 6 PeV, the combined electromagnetic and neutrino observations allowed us to constrain a range of the maximum proton energy. From the lepto-hadronic modelling of the multi-messenger signal, we can infer that the maximum proton energy can be anywhere between $10^{15} - 10^{18}$ eV. The higher end of the derived maximum proton energy is well within the range of UHECRs.

In conclusion, the power of VHE γ -ray observations performed jointly with multi-wavelength photon and high-energy neutrino observations, was demonstrated to identify and investigate potential cosmic-ray sources. The future Cherenkov Telescope Array (CTA) will extend the energy spectrum of γ -rays up to ~ 100 TeV. Such observations will be crucial to identify potential spectral signatures of cosmic-ray acceleration in the γ -ray band. Leptonic processes will have difficulty to explain the spectra up to such high energies due to the Klein-Nishina suppression. CTA will improve the γ -ray flux sensitivity by almost ten times compared to the current generation of instruments. It will help us to detect new sources and perform follow-up observations of neutrino events, AGN flares and other transient sources. Such globally coordinated network of neutrino and electromagnetic follow-up observations will increase the discovery potential of high-energy cosmic-ray sources and probe new Physics. The dawn of multi-messenger astronomy has already been inaugurated following the first potential coincidence of a neutrino event with a flaring blazar, TXS 0506+056. Future upgrades of the IceCube detector (IceCube-Gen2) are planned that will further increase the collection area and improve the event reconstruction.

It was demonstrated that the modelling of the broadband electromagnetic spectra from AGNs/blazars can provide a wealth of information regarding their inner acceleration engines and composition, energetics and physical conditions in the jets. In future, the author will work towards development of a time-dependent SED modelling code that will allow to follow time evolution of the source and transition between its different emission states.

Appendix A

γ -ray and multi-wavelength tables for 1ES 1959+650 2016 monitoring campaign

In this section, the data for the 1ES 1959+650 multi-wavelength campaign during 2016 is presented. The corresponding figure for the multi-wavelength light curve of the source during 2016 can be found in Chapter 5, Sec 5.3. Three nights having the highest fluxes (i.e. 13th June, 14th June, 1st July 2016) were investigated in details in terms of the intranight variability and/or broadband SED modelling (see Chapter 5, Sec. 5.4). The broadband SED data during the flares from the instruments *Swift*, *Fermi*-LAT and MAGIC are also tabulated below.

A.1 Multi-wavelength long-term light curves during 2016

Table A.1: The VHE γ -ray light curve above 300 GeV observed by MAGIC from the blazar 1ES 1959+650 during 2016

starting MJD	ending MJD	flux ($\text{cm}^{-2} \text{s}^{-1}$)	flux-error ($\text{cm}^{-2} \text{s}^{-1}$)
57507.172419	57507.214013	1.61×10^{-10}	8.49×10^{-12}
57508.169373	57508.215136	1.12×10^{-10}	6.54×10^{-12}
57509.157644	57509.213828	1.38×10^{-10}	6.32×10^{-12}
57510.155835	57510.211966	7.98×10^{-11}	4.92×10^{-12}
57511.152414	57511.210251	4.13×10^{-11}	3.74×10^{-12}
57512.149488	57512.168191	4.03×10^{-11}	6.11×10^{-12}
57513.145524	57513.154163	4.95×10^{-11}	9.33×10^{-12}
57514.139414	57514.151015	2.37×10^{-11}	6.91×10^{-12}
57515.141636	57515.152296	2.98×10^{-11}	7.30×10^{-12}
57517.18044	57517.208341	5.01×10^{-11}	5.65×10^{-12}
57521.162645	57521.174858	3.82×10^{-11}	8.59×10^{-12}
57522.121861	57522.128805	4.74×10^{-11}	9.89×10^{-12}
57523.114426	57523.198782	8.90×10^{-11}	4.56×10^{-12}
57524.134935	57524.198715	6.92×10^{-11}	5.03×10^{-12}
57536.11324	57536.151142	1.09×10^{-10}	7.23×10^{-12}
57537.111766	57537.153781	4.54×10^{-11}	4.40×10^{-12}
57538.114167	57538.152386	5.24×10^{-11}	5.28×10^{-12}
57539.161216	57539.195388	5.12×10^{-11}	5.17×10^{-12}
57540.161389	57540.19614	1.31×10^{-10}	8.83×10^{-12}
57541.161167	57541.195469	9.27×10^{-11}	7.12×10^{-12}
57542.159571	57542.194722	1.14×10^{-10}	8.00×10^{-12}
57543.155836	57543.194086	1.20×10^{-10}	8.11×10^{-12}

Continued on next page

Table A.1 – *Continued from previous page*

starting MJD	ending MJD	flux (cm ⁻² s ⁻¹)	flux-error (cm ⁻² s ⁻¹)
57544.154599	57544.193275	1.32×10 ⁻¹⁰	8.36×10 ⁻¹²
57545.155717	57545.192489	2.02×10 ⁻¹⁰	1.18×10 ⁻¹¹
57546.137746	57546.193923	2.18×10 ⁻¹⁰	1.08×10 ⁻¹¹
57547.135058	57547.19434	1.96×10 ⁻¹⁰	9.20×10 ⁻¹²
57548.131303	57548.194097	1.98×10 ⁻¹⁰	9.11×10 ⁻¹²
57549.126706	57549.193972	2.34×10 ⁻¹⁰	1.02×10 ⁻¹¹
57550.136368	57550.194323	2.16×10 ⁻¹⁰	1.04×10 ⁻¹¹
57552.039972	57552.19218	3.77×10 ⁻¹⁰	9.37×10 ⁻¹²
57553.059741	57553.149356	3.28×10 ⁻¹⁰	1.03×10 ⁻¹¹
57554.095937	57554.134236	1.10×10 ⁻¹⁰	7.98×10 ⁻¹²
57567.056149	57567.098264	1.01×10 ⁻¹⁰	7.37×10 ⁻¹²
57568.087694	57568.128883	6.61×10 ⁻¹¹	5.42×10 ⁻¹²
57569.008884	57569.159191	9.36×10 ⁻¹¹	4.39×10 ⁻¹²
57569.9992	57570.206661	3.79×10 ⁻¹⁰	8.32×10 ⁻¹²
57570.997504	57571.053715	2.30×10 ⁻¹⁰	9.43×10 ⁻¹²
57571.989404	57572.045556	1.27×10 ⁻¹⁰	6.41×10 ⁻¹²
57572.987293	57573.045324	1.40×10 ⁻¹⁰	6.96×10 ⁻¹²
57573.979917	57574.029247	1.21×10 ⁻¹⁰	6.63×10 ⁻¹²
57574.998619	57575.012373	1.40×10 ⁻¹⁰	1.29×10 ⁻¹¹
57582.023628	57582.064213	1.16×10 ⁻¹⁰	8.51×10 ⁻¹²
57583.045913	57583.087905	1.23×10 ⁻¹⁰	7.98×10 ⁻¹²
57597.063935	57597.152838	1.24×10 ⁻¹⁰	6.30×10 ⁻¹²
57598.997086	57599.019181	4.94×10 ⁻¹⁰	6.99×10 ⁻¹²
57609.958411	57609.989975	2.97×10 ⁻¹⁰	4.09×10 ⁻¹²
57610.988263	57611.027129	2.30×10 ⁻¹⁰	3.45×10 ⁻¹²
57612.013158	57612.055258	2.75×10 ⁻¹⁰	3.74×10 ⁻¹²
57621.92065	57621.934348	4.86×10 ⁻¹¹	8.78×10 ⁻¹²
57623.982826	57624.024836	5.90×10 ⁻¹¹	4.94×10 ⁻¹²
57638.868466	57638.910817	5.40×10 ⁻¹¹	5.03×10 ⁻¹²
57639.860626	57639.902823	7.39×10 ⁻¹¹	5.87×10 ⁻¹²
57640.864714	57640.888937	3.00×10 ⁻¹¹	5.55×10 ⁻¹²
57652.970209	57652.99595	5.10×10 ⁻¹¹	6.04×10 ⁻¹²
57693.818655	57693.888894	5.41×10 ⁻¹¹	3.53×10 ⁻¹²
57694.836176	57694.846422	3.22×10 ⁻¹¹	7.31×10 ⁻¹²
57708.818864	57708.842104	6.50×10 ⁻¹¹	6.52×10 ⁻¹²
57709.820074	57709.840368	4.07×10 ⁻¹¹	5.67×10 ⁻¹²
57710.819895	57710.8415	4.85×10 ⁻¹¹	6.24×10 ⁻¹²
57711.816606	57711.839737	3.81×10 ⁻¹¹	4.90×10 ⁻¹²
57712.819842	57712.821367	2.79×10 ⁻¹¹	1.66×10 ⁻¹¹

Table A.2: The *Swift*-XRT light curve in the energy range 0.5–5 keV observed for the blazar 1ES 1959+650 during 2016

MJD	flux ($\text{erg cm}^{-2} \text{s}^{-1}$)	flux-error ($\text{erg cm}^{-2} \text{s}^{-1}$)
56779.28959	4.85×10^{-11}	1.99×10^{-12}
56786.8817	3.43×10^{-11}	2.09×10^{-12}
56793.73326	3.31×10^{-11}	1.77×10^{-12}
56807.95131	3.25×10^{-11}	1.65×10^{-12}
56821.13938	5.16×10^{-11}	3.27×10^{-12}
56842.19216	6.87×10^{-11}	2.60×10^{-12}
56848.55767	4.48×10^{-11}	2.49×10^{-12}
56856.74353	6.03×10^{-11}	1.97×10^{-12}
56863.53227	8.49×10^{-11}	2.93×10^{-12}
56868.73564	5.51×10^{-11}	1.80×10^{-12}
56871.95776	5.00×10^{-11}	1.76×10^{-12}
56874.1867	7.01×10^{-11}	1.94×10^{-12}
56877.85872	9.53×10^{-11}	2.27×10^{-12}
56880.39	8.14×10^{-11}	2.13×10^{-12}
56913.44652	7.30×10^{-11}	3.30×10^{-12}
56917.14497	7.51×10^{-11}	2.25×10^{-12}
56917.18321	6.37×10^{-11}	2.83×10^{-12}
56922.14299	7.80×10^{-11}	1.94×10^{-12}
56922.24655	7.48×10^{-11}	3.41×10^{-12}
57045.20393	5.51×10^{-11}	1.33×10^{-12}
57052.08457	5.36×10^{-11}	1.49×10^{-12}
57068.11212	8.02×10^{-11}	2.75×10^{-12}
57071.54096	7.22×10^{-11}	2.02×10^{-12}
57073.90654	6.85×10^{-11}	1.93×10^{-12}
57080.15654	5.56×10^{-11}	1.55×10^{-12}
57087.90033	1.38×10^{-10}	2.92×10^{-12}
57091.49299	1.63×10^{-10}	4.59×10^{-12}
57097.51162	1.30×10^{-10}	3.08×10^{-12}
57099.47032	7.12×10^{-11}	1.83×10^{-12}
57150.24324	8.88×10^{-11}	2.79×10^{-12}
57171.61731	8.77×10^{-11}	3.06×10^{-12}
57178.93579	6.92×10^{-11}	3.63×10^{-12}
57185.71687	5.86×10^{-11}	2.25×10^{-12}
57227.85682	5.27×10^{-11}	5.68×10^{-12}
57235.9371	7.79×10^{-11}	5.02×10^{-12}
57249.52633	1.04×10^{-10}	3.05×10^{-12}
57254.93512	1.33×10^{-10}	3.53×10^{-12}
57259.36063	1.35×10^{-10}	02×10^{-12}
57270.81777	1.86×10^{-10}	3.85×10^{-12}
57273.04941	2.26×10^{-10}	4.65×10^{-12}
57274.21351	1.71×10^{-10}	4.31×10^{-12}
57276.83205	1.59×10^{-10}	8.29×10^{-12}
57281.88372	1.83×10^{-10}	4.28×10^{-12}
57302.15478	2.62×10^{-10}	4.80×10^{-12}
57304.14263	1.84×10^{-10}	4.03×10^{-12}
57306.17371	2.99×10^{-10}	5.88×10^{-12}
57307.14272	1.64×10^{-10}	5.20×10^{-12}
57308.13614	2.22×10^{-10}	4.85×10^{-12}

Continued on next page

Table A.2 – Continued from previous page

MJD	flux ($\text{erg cm}^{-2} \text{s}^{-1}$)	flux-error ($\text{erg cm}^{-2} \text{s}^{-1}$)
57311.99795	2.41×10^{-10}	5.03×10^{-12}
57314.28369	1.75×10^{-10}	2.78×10^{-12}
57322.85702	1.41×10^{-10}	3.69×10^{-12}
57326.48336	2.28×10^{-10}	3.81×10^{-12}
57328.54332	1.27×10^{-10}	3.36×10^{-12}
57332.09051	1.87×10^{-10}	3.67×10^{-12}
57333.0894	2.32×10^{-10}	1.12×10^{-11}
57334.11305	1.90×10^{-10}	2.87×10^{-12}
57335.74427	1.66×10^{-10}	5.54×10^{-12}
57338.67342	1.64×10^{-10}	8.00×10^{-12}
57341.93422	3.50×10^{-10}	7.00×10^{-12}
57342.98207	1.49×10^{-10}	3.63×10^{-12}
57344.05859	2.36×10^{-10}	4.46×10^{-12}
57347.91316	1.07×10^{-10}	3.01×10^{-12}
57350.89764	1.04×10^{-10}	3.15×10^{-12}
57353.35091	4.23×10^{-10}	6.54×10^{-12}
57354.08173	2.97×10^{-10}	8.95×10^{-12}
57355.07673	2.25×10^{-10}	4.80×10^{-12}
57356.81364	1.51×10^{-10}	3.86×10^{-12}
57359.59952	1.43×10^{-10}	3.26×10^{-12}
57363.06142	1.79×10^{-10}	5.57×10^{-12}
57373.98151	1.92×10^{-10}	4.46×10^{-12}
57379.36365	1.84×10^{-10}	4.00×10^{-12}
57382.7505	5.40×10^{-10}	7.59×10^{-12}
57384.91451	3.99×10^{-10}	6.38×10^{-12}
57386.80381	2.11×10^{-10}	4.30×10^{-12}
57388.07527	2.80×10^{-10}	6.33×10^{-12}
57389.46798	1.31×10^{-10}	3.41×10^{-12}
57390.47001	1.25×10^{-10}	3.63×10^{-12}
57391.38886	1.82×10^{-10}	4.16×10^{-12}
57394.076	9.29×10^{-11}	2.38×10^{-12}
57397.10141	1.71×10^{-10}	4.11×10^{-12}
57400.76404	1.47×10^{-10}	5.76×10^{-12}
57403.61347	6.50×10^{-11}	2.03×10^{-12}
57409.00748	1.53×10^{-10}	4.69×10^{-12}
57413.68653	3.97×10^{-11}	1.26×10^{-12}
57416.57426	4.59×10^{-11}	2.24×10^{-12}
57427.73281	1.17×10^{-10}	2.51×10^{-12}
57431.12002	1.28×10^{-10}	3.18×10^{-12}
57433.45157	1.23×10^{-10}	2.57×10^{-12}
57436.60663	1.43×10^{-10}	3.23×10^{-12}
57440.7212	1.21×10^{-10}	2.67×10^{-12}
57442.9783	1.82×10^{-10}	3.19×10^{-12}
57445.77006	1.54×10^{-10}	2.92×10^{-12}
57448.20146	1.61×10^{-10}	3.07×10^{-12}
57451.52385	1.72×10^{-10}	3.20×10^{-12}
57454.80857	9.83×10^{-11}	2.45×10^{-12}
57461.71325	9.30×10^{-11}	2.24×10^{-12}
57508.16711	2.77×10^{-10}	5.51×10^{-12}
57508.4027	2.83×10^{-10}	4.92×10^{-12}

Continued on next page

Table A.2 – *Continued from previous page*

MJD	flux ($\text{erg cm}^{-2} \text{s}^{-1}$)	flux-error ($\text{erg cm}^{-2} \text{s}^{-1}$)
57509.17797	2.70×10^{-10}	5.64×10^{-12}
57509.42941	1.96×10^{-10}	4.66×10^{-12}
57510.16268	1.51×10^{-10}	3.92×10^{-12}
57510.43393	1.00×10^{-10}	2.92×10^{-12}
57511.16072	1.14×10^{-10}	3.21×10^{-12}
57511.42958	1.10×10^{-10}	2.91×10^{-12}
57512.16453	1.16×10^{-10}	3.32×10^{-12}
57512.42662	1.43×10^{-10}	5.75×10^{-12}
57514.7563	1.43×10^{-10}	4.12×10^{-12}
57517.13613	1.65×10^{-10}	4.70×10^{-12}
57531.18114	1.65×10^{-10}	4.00×10^{-12}
57535.63744	2.07×10^{-10}	4.35×10^{-12}
57543.27916	2.02×10^{-10}	6.09×10^{-12}
57545.06848	2.96×10^{-10}	5.73×10^{-12}
57545.65534	4.10×10^{-10}	6.40×10^{-12}
57546.22837	3.39×10^{-10}	5.46×10^{-12}
57546.569	3.14×10^{-10}	5.61×10^{-12}
57547.16714	3.46×10^{-10}	5.81×10^{-12}
57547.99476	3.82×10^{-10}	6.49×10^{-12}
57548.05967	4.11×10^{-10}	6.46×10^{-12}
57548.8455	4.45×10^{-10}	6.86×10^{-12}
57549.71252	2.79×10^{-10}	6.31×10^{-12}
57550.18827	2.95×10^{-10}	5.80×10^{-12}
57550.97974	4.19×10^{-10}	7.68×10^{-12}
57552.14032	4.35×10^{-10}	7.22×10^{-12}
57552.76389	4.87×10^{-10}	7.58×10^{-12}
57553.10118	4.88×10^{-10}	8.04×10^{-12}
57553.33375	4.41×10^{-10}	8.03×10^{-12}
57553.9698	3.75×10^{-10}	7.06×10^{-12}
57554.39631	3.55×10^{-10}	4.69×10^{-12}
57555.36384	5.16×10^{-10}	5.40×10^{-12}
57557.77959	4.04×10^{-10}	7.27×10^{-12}
57564.0561	2.67×10^{-10}	8.57×10^{-12}
57566.99493	2.14×10^{-10}	9.21×10^{-12}
57569.77012	4.86×10^{-10}	1.48×10^{-11}
57570.7062	5.51×10^{-10}	7.94×10^{-12}
57571.24042	5.84×10^{-10}	1.23×10^{-11}
57580.36487	3.74×10^{-10}	7.01×10^{-12}
57582.29332	2.82×10^{-10}	5.24×10^{-12}
57584.32203	2.32×10^{-10}	4.53×10^{-12}
57586.61391	2.43×10^{-10}	4.78×10^{-12}
57589.47238	1.76×10^{-10}	5.18×10^{-12}
57592.52425	1.62×10^{-10}	3.93×10^{-12}
57598.16905	4.13×10^{-10}	5.35×10^{-12}
57599.69291	2.47×10^{-10}	4.99×10^{-12}
57600.89266	3.51×10^{-10}	5.07×10^{-12}
57602.15025	3.82×10^{-10}	6.32×10^{-12}
57603.77852	1.76×10^{-10}	3.38×10^{-12}
57606.99664	5.16×10^{-11}	2.45×10^{-12}
57609.99174	1.59×10^{-10}	3.90×10^{-12}

Continued on next page

Table A.2 – *Continued from previous page*

MJD	flux ($\text{erg cm}^{-2} \text{s}^{-1}$)	flux-error ($\text{erg cm}^{-2} \text{s}^{-1}$)
57612.24617	1.02×10^{-10}	2.22×10^{-12}
57618.49371	1.55×10^{-10}	3.19×10^{-12}
57621.21312	1.26×10^{-10}	4.55×10^{-12}
57631.79911	1.47×10^{-10}	5.03×10^{-12}
57634.09223	6.89×10^{-11}	2.03×10^{-12}
57654.7584	1.76×10^{-10}	4.11×10^{-12}
57656.10975	1.73×10^{-10}	4.28×10^{-12}
57657.29332	2.03×10^{-10}	4.22×10^{-12}
57660.29175	7.77×10^{-10}	2.34×10^{-12}
57663.01616	2.07×10^{-10}	4.54×10^{-12}
57668.66453	1.47×10^{-10}	3.31×10^{-12}
57670.41967	9.74×10^{-11}	2.64×10^{-12}
57682.69758	1.34×10^{-10}	3.52×10^{-12}
57684.19523	1.69×10^{-10}	3.98×10^{-12}
57691.52604	3.05×10^{-10}	5.54×10^{-12}
57692.52986	3.52×10^{-10}	5.46×10^{-12}
57693.11963	1.74×10^{-10}	8.65×10^{-12}
57694.06296	2.32×10^{-10}	7.10×10^{-12}
57695.24866	1.33×10^{-10}	3.11×10^{-12}
57696.17526	1.62×10^{-10}	3.64×10^{-12}
57697.23869	2.21×10^{-10}	4.57×10^{-12}
57700.36119	1.15×10^{-10}	3.89×10^{-12}

Table A.3: The *Fermi*-LAT light curve in the energy range 0.3–300 GeV from the blazar 1ES 1959+650 during 2016

starting MJD	ending MJD	photon flux ($\text{cm}^{-2} \text{s}^{-1}$)	photon flux-error ($\text{cm}^{-2} \text{s}^{-1}$)
57512.0	57515.0	3.13341489676e-08	1.26831062879e-08
57515.0	57518.0	4.76809039749e-08	1.46667761407e-08
57518.0	57521.0	3.29270956133e-08	1.0942086684e-08
57521.0	57524.0	4.05147326288e-08	1.51787637466e-08
57524.0	57527.0	4.90529183883e-08	1.613906042e-08
57527.0	57530.0	5.43611015692e-08	1.76307676887e-08
57530.0	57533.0	5.35955404662e-08	1.88010928871e-08
57533.0	57536.0	3.6e-08	1.53863334991e-08
57536.0	57539.0	6.87396705971e-08	1.8282232821e-08
57539.0	57542.0	7.33179497203e-08	1.83141229805e-08
57542.0	57545.0	9.32831232449e-08	1.79370033955e-08
57545.0	57548.0	9.54843123451e-08	1.84351053363e-08
57548.0	57551.0	8.05536860016e-08	1.73664155051e-08
57551.0	57554.0	1.11921897023e-07	2.27062674427e-08
57554.0	57557.0	4.7e-08	1.77598192171e-08
57557.0	57560.0	7.94607381337e-08	2.59496393306e-08
57560.0	57563.0	8.78141458941e-08	2.38354319362e-08
57563.0	57566.0	9.70533744968e-08	2.10774961927e-08
57566.0	57569.0	4.5e-08	1.58538622692e-08
57569.0	57572.0	1.02054461962e-07	2.36329062522e-08
57572.0	57575.0	9.24355546548e-08	2.41336879648e-08
57575.0	57578.0	5.45382205954e-08	1.6e-08
57578.0	57581.0	5.82073486881e-08	1.67289980619e-08
57581.0	57584.0	8.1109562565e-08	1.86600955259e-08
57584.0	57587.0	6.56850816185e-08	1.97554034053e-08
57587.0	57590.0	2.30504653272e-08	1.43180553837e-08
57590.0	57593.0	8.40626343756e-13	8.68445659179e-10
57593.0	57596.0	3.85024966761e-08	1.37081441774e-08
57596.0	57599.0	8.02142198368e-08	1.73990052809e-08
57599.0	57602.0	5.53989767075e-08	1.62370041751e-08
57602.0	57605.0	9.88703958425e-08	4.56051133764e-08
57608.0	57611.0	6.41846922928e-08	2.15887555626e-08
57611.0	57614.0	8.22732733494e-09	6.40703186361e-09
57614.0	57617.0	5.64680520845e-08	1.933039994e-08
57617.0	57620.0	5.36560267268e-08	2.1147084788e-08
57620.0	57623.0	5.57601692306e-08	1.9e-08
57623.0	57626.0	1.39259749724e-08	9.8956891899e-09
57626.0	57629.0	5.2e-08	1.80784300515e-08
57629.0	57632.0	5.26278249238e-08	1.98293552086e-08
57632.0	57635.0	3.50980059884e-08	1.53849775379e-08
57635.0	57638.0	3.82328433678e-08	1.48937256874e-08
57638.0	57641.0	3.63921644084e-08	1.37364125786e-08
57641.0	57644.0	4.90727027553e-08	1.53783318596e-08
57644.0	57647.0	3.26434665635e-08	1.23281043948e-08
57647.0	57650.0	5e-08	1.55699050948e-08
57650.0	57653.0	2.51408985833e-08	1.14400362207e-08
57653.0	57656.0	3.28368997113e-08	1.18657310947e-08
57656.0	57659.0	2.80979293051e-08	1.02719508825e-08
57659.0	57662.0	6.65663361742e-08	1.88907716715e-08

Continued on next page

Table A.3 – *Continued from previous page*

starting MJD	ending MJD	photon flux ($\text{cm}^{-2} \text{s}^{-1}$)	error in photon flux ($\text{cm}^{-2} \text{s}^{-1}$)
57662.0	57665.0	3.25360309466e-08	1.48538015583e-08
57665.0	57668.0	6.25037201152e-08	2.36282172197e-08
57668.0	57671.0	3.27245992885e-08	1.4157702751e-08
57671.0	57674.0	6.25727297123e-08	1.84112539356e-08
57674.0	57677.0	8.7e-08	2.1e-08
57677.0	57680.0	1.06234974743e-08	7.58878823574e-09
57680.0	57683.0	7.9e-08	2.2835118661e-08
57683.0	57686.0	1.95484936945e-08	1.24898674086e-08
57686.0	57689.0	3.61704414129e-08	1.65550714434e-08
57689.0	57692.0	6.3161627441e-08	1.82925768404e-08
57692.0	57695.0	8.51631294776e-08	2.25439187749e-08
57695.0	57698.0	1.24e-07	3.34261974216e-08
57698.0	57701.0	2.9081664325e-08	1.63883225474e-08
57701.0	57704.0	6.04746871447e-08	1.73505019216e-08
57704.0	57707.0	4.4e-08	1.55860904018e-08
57707.0	57710.0	5.22632289989e-08	1.5e-08
57710.0	57713.0	5.33522946817e-08	1.55927417108e-08
57713.0	57716.0	9.89122999391e-08	2.26182318271e-08
57716.0	57719.0	2.39449477172e-08	1.14832726654e-08
57719.0	57722.0	6.21096952079e-08	1.68216363716e-08

A.2 Spectra in the optical, X-ray, HE and VHE γ -ray bands during the brightest flaring nights from 2016

Table A.4: The EBL-deabsorbed SED of MAGIC for 13th June 2016

Energy and energy error (GeV)	flux and flux error ($\text{TeV cm}^{-2} \text{s}^{-1}$)
192.1-(43.2)+(49.7)	$1.58 \times 10^{-10} - (9.32 \times 10^{-12}) + (9.30 \times 10^{-12})$
309.7-(67.9)+(83.0)	$1.65 \times 10^{-10} - (9.44 \times 10^{-12}) + (9.44 \times 10^{-12})$
483.1-(90.4)+(154.6)	$1.70 \times 10^{-10} - (9.68 \times 10^{-12}) + (9.68 \times 10^{-12})$
851.7-(214.0)+(183.8)	$1.87 \times 10^{-10} - (1.20 \times 10^{-11}) + (1.20 \times 10^{-11})$
1359.7-(324.2)+(321.7)	$1.50 \times 10^{-10} - (1.20 \times 10^{-11}) + (1.20 \times 10^{-11})$
2197.4-(516.0)+(532.8)	$1.71 \times 10^{-10} - (1.514 \times 10^{-11}) + (1.51 \times 10^{-11})$
3559.5-(829.4)+(873.6)	$1.42 \times 10^{-10} - (1.57 \times 10^{-11}) + (1.57 \times 10^{-11})$
5768.8-(1335.6)+(1429.7)	$1.23 \times 10^{-10} - (1.85 \times 10^{-11}) + (1.85 \times 10^{-11})$
9353.7-(2155.3)+(2334.9)	$8.77 \times 10^{-11} - (2.82 \times 10^{-11}) + (2.82 \times 10^{-11})$

Table A.5: The EBL-deabsorbed SED of MAGIC for 14th June 2016

Energy and energy error (GeV)	flux and flux error ($\text{TeV cm}^{-2} \text{s}^{-1}$)
196.0-(47.0)+(45.9)	$1.25 \times 10^{-10} - (8.51 \times 10^{-12}) + (8.51 \times 10^{-12})$
314.7-(72.9)+(78.0)	$1.31 \times 10^{-10} - (8.41 \times 10^{-12}) + (8.41 \times 10^{-12})$
501.7-(109.0)+(136.0)	$1.43 \times 10^{-10} - (9.47 \times 10^{-12}) + (9.47 \times 10^{-12})$
883.1-(245.4)+(152.3)	$1.44 \times 10^{-10} - (1.12 \times 10^{-11}) + (1.12 \times 10^{-11})$
1373.9-(338.4)+(307.4)	$1.32 \times 10^{-10} - (1.28 \times 10^{-11}) + (1.28 \times 10^{-11})$
2207.8-(526.5)+(522.3)	$1.02 \times 10^{-10} - (1.26 \times 10^{-11}) + (1.26 \times 10^{-11})$
3554.4-(824.3)+(878.7)	$7.16 \times 10^{-11} - (1.24 \times 10^{-11}) + (1.24 \times 10^{-11})$
5705.2-(1272.0)+(1493.3)	$3.53 \times 10^{-11} - (1.35 \times 10^{-11}) + (1.35 \times 10^{-11})$

Table A.6: The EBL-deabsorbed SED of MAGIC for 1st July 2016

Energy and energy error (GeV)	flux and flux error ($\text{TeV cm}^{-2} \text{s}^{-1}$)
192.4-(43.5)+(49.4)	$1.49 \times 10^{-10} - (5.80 \times 10^{-12}) + (5.80 \times 10^{-12})$
309.1-(67.3)+(83.6)	$1.60 \times 10^{-10} - (5.53 \times 10^{-12}) + (5.53 \times 10^{-12})$
495.1-(102.4)+(142.6)	$1.58 \times 10^{-10} - (5.64 \times 10^{-12}) + (5.64 \times 10^{-12})$
847.3-(209.6)+(188.1)	$1.60 \times 10^{-10} - (6.77 \times 10^{-12}) + (6.77 \times 10^{-12})$
1363.6-(328.1)+(317.8)	$1.55 \times 10^{-10} - (7.67 \times 10^{-12}) + (7.67 \times 10^{-12})$
2203.7-(522.3)+(526.5)	$1.43 \times 10^{-10} - (8.58 \times 10^{-12}) + (8.58 \times 10^{-12})$
3564.6-(834.5)+(868.5)	$1.01 \times 10^{-10} - (8.50 \times 10^{-12}) + (8.50 \times 10^{-12})$
5757.7-(1324.6)+(1440.7)	$6.93 \times 10^{-11} - (8.89 \times 10^{-12}) + (8.89 \times 10^{-12})$
9277.4-(2079.0)+(2411.2)	$1.81 \times 10^{-11} - (1.10 \times 10^{-11}) + (1.10 \times 10^{-11})$

Table A.7: The SED from *Swift*-UVOT and *Swift*-XRT for 13th June 2016

Frequency (Hz)	Frequency error (Hz)	flux ($\text{erg cm}^{-2} \text{s}^{-1}$)	flux error ($\text{erg cm}^{-2} \text{s}^{-1}$)
1.47×10^{15}	0.0	4.53×10^{-11}	1.61638×10^{-12}

Continued on next page

Table A.7 – Continued from previous page

Frequency (Hz)	Frequency error (Hz)	flux (erg cm ⁻² s ⁻¹)	flux error (erg cm ⁻² s ⁻¹)
1.16×10^{15}	0.0	3.87×10^{-11}	1.55587×10^{-12}
1.4508×10^{17}	2.418×10^{16}	1.90401×10^{-10}	5.42282×10^{-12}
1.88604×10^{17}	1.9344×10^{16}	2.00632×10^{-10}	5.61331×10^{-12}
2.24874×10^{17}	1.6926×10^{16}	2.073×10^{-10}	5.83627×10^{-12}
2.58726×10^{17}	1.6926×10^{16}	2.0461×10^{-10}	5.74001×10^{-12}
2.93787×10^{17}	1.8135×10^{16}	2.03483×10^{-10}	5.69679×10^{-12}
3.31266×10^{17}	1.9344×10^{16}	2.14816×10^{-10}	6.07431×10^{-12}
3.73581×10^{17}	2.2971×10^{16}	2.26363×10^{-10}	6.44363×10^{-12}
4.31613×10^{17}	3.5061×10^{16}	2.23144×10^{-10}	6.30509×10^{-12}
5.18661×10^{17}	5.1987×10^{16}	2.42026×10^{-10}	6.88478×10^{-12}
6.55278×10^{17}	8.463×10^{16}	2.58524×10^{-10}	7.36694×10^{-12}
8.57181×10^{17}	1.17273×10^{17}	2.72412×10^{-10}	7.77698×10^{-12}
1.25736×10^{18}	2.82906×10^{17}	2.82744×10^{-10}	8.05907×10^{-12}
1.81592×10^{18}	2.75652×10^{17}	3.07465×10^{-10}	2.02754×10^{-11}

Table A.8: The SED from *Swift*-UVOT and *Swift*-XRT for 14th June 2016

Frequency (Hz)	Frequency error (Hz)	flux (erg cm ⁻² s ⁻¹)	flux error (erg cm ⁻² s ⁻¹)
1.47×10^{15}	0.0	4.91×10^{-11}	1.7674×10^{-12}
1.35×10^{15}	0.0	4.83×10^{-11}	1.75757×10^{-12}
1.16×10^{15}	0.0	3.67×10^{-11}	1.65422×10^{-12}
1.43871×10^{17}	2.2971×10^{16}	2.30023×10^{-10}	4.13894×10^{-13}
1.86186×10^{17}	1.9344×10^{16}	2.22041×10^{-10}	5.66725×10^{-13}
2.22456×10^{17}	1.6926×10^{16}	2.43345×10^{-10}	7.06323×10^{-13}
2.56308×10^{17}	1.6926×10^{16}	2.23745×10^{-10}	7.51756×10^{-13}
2.91369×10^{17}	1.8135×10^{16}	2.25167×10^{-10}	8.1419×10^{-13}
3.28848×10^{17}	1.9344×10^{16}	2.41347×10^{-10}	9.24179×10^{-13}
3.71163×10^{17}	2.2971×10^{16}	2.55379×10^{-10}	1.03068×10^{-12}
4.25568×10^{17}	3.1434×10^{16}	2.6016×10^{-10}	1.12229×10^{-12}
5.02944×10^{17}	4.5942×10^{16}	2.85706×10^{-10}	1.26801×10^{-12}
6.31098×10^{17}	8.2212×10^{16}	2.84762×10^{-10}	1.34776×10^{-12}
8.23329×10^{17}	1.10019×10^{17}	3.08564×10^{-10}	1.54586×10^{-12}
1.14613×10^{18}	2.12784×10^{17}	3.18971×10^{-10}	1.71857×10^{-12}
1.69381×10^{18}	3.34893×10^{17}	3.12513×10^{-10}	3.12861×10^{-12}

Table A.9: The SED from *Fermi*-LAT for 13th June and 14th June 2016

Energy and energy error (GeV)	flux and flux error ($\text{erg cm}^{-2} \text{s}^{-1}$)
0.533-(0.233)+(0.415)	$4.5 \times 10^{-11} - (1.8 \times 10^{-11}) + (2.2 \times 10^{-11})$
1.69-(0.74)+(1.31)	$5.1 \times 10^{-11} - (2.3 \times 10^{-11}) + (2.9 \times 10^{-11})$
5.33-(2.33)+(4.15)	$7.8 \times 10^{-11} - (4.6 \times 10^{-11}) + (6.5 \times 10^{-11})$
16.9-(7.4)+(13.3)	$1.21 \times 10^{-10} - (9.2 \times 10^{-11}) + (1.54 \times 10^{-10})$
53.3-(23.3)+(41.5)	$3.8 \times 10^{-10} - (2.9 \times 10^{-10}) + (4.8 \times 10^{-10})$

Observation dates for the OFF data sample

- RBS 0970: 30/05/2016, 01/06/2016, 04/06/2016, 07/06/2016, 08/06/2016
- 3C 371: 08/09/2016
- Triangulum II: 27/09/2016
- M87: 09/06/2016

Appendix B

Supplementary materials for the lepto-hadronic code development

B.1 The Naima package

Naima is a python package for calculation of non-thermal radiative processes from ultra-relativistic particles in various astrophysical environments [Zabalza \(2015\)](#). Naima is mainly written for Galactic sources. The basic radiative processes implemented in the Naima tcode are the following: synchrotron radiation ([Aharonian, 2000](#)), inverse Compton radiation ([Khangulyan et al., 2014](#)), neutral pion decay from proton-proton interactions ([Kafexhiu et al., 2014](#)) and non-thermal bremsstrahlung ([Baring et al., 1999](#)). The main uses of the original code for the work done in this thesis is described below.

In this thesis, the synchrotron and inverse Compton modules of the original code were modified along with several improvements (see Chapter 6). Apart from the modifications and improvements of the leptonic code based on Naima, novel implementations of the various relevant hadronic emission processes were also done, including proton synchrotron, photo-meson interactions, proton-proton interactions and pair cascades (more details can be found in Chapter 6).

The Naima package also includes several mathematical models that were used in the code developed in this thesis, to parametrize the energy distribution of the parent population of electrons and protons, namely power law, power law with exponential cutoff, broken power law functions. To define the particle distributions, the proper geometry of the emission region has been taken into account in the code developed by the author.

B.2 Energy spectra of leptons from photo-meson interactions

The energy spectra of leptons from photo-meson interactions for a fixed value of the proton proton energy E_p and the soft photon target ε can be parametrized in simple analytical form ([Kelner and Aharonian, 2008](#)). If x denotes the fraction of the parent proton energy carried by the lepton E_l i.e. $x = \frac{E_l}{E_p}$ and $\eta = \frac{4\varepsilon E_p}{m_p^2 c^4}$, the energy spectra for a fixed proton and target photon energy can be given in the following form:

In the range $x'_- < x < x'_+$:

$$\Phi_l(\eta, x) = B_l \exp \left\{ -s_l \left[\ln \left(\frac{x}{x'_-} \right) \right]^{\delta_l} \right\} \left[\ln \left(\frac{2}{1+y^2} \right) \right]^\psi \quad (\text{B.1})$$

and in the range $x < x'_-$:

$$\Phi_l(\eta, x) = B_l (\ln 2)^\psi \quad (\text{B.2})$$

where

$$y' = \frac{x - x'_-}{x'_+ - x'_-} \quad (\text{B.3})$$

For $x > x'_+$, the function $\Phi_l(\eta, x) = 0$. B_l, s_l, δ_l are function of η , as given in Table II and Table III of [Kelner and Aharonian \(2008\)](#). The value of the parameters ψ and x'_\pm are given below for each type of leptons.

B.2.1 Energy spectra for positrons, muon anti-neutrinos and electron neutrinos

The parameter ψ is defined for positrons (e^+), muon anti-neutrinos ($\bar{\nu}_\mu$) and electron neutrinos (ν_e) in the following form:

$$\psi = 2.5 + 1.4 \ln\left(\frac{\eta}{\eta_0}\right) \quad (\text{B.4})$$

and

$$x'_- = \frac{x_-}{4} \quad x'_+ = x_+ \quad (\text{B.5})$$

x_- and x_+ are defined in Eqn. 19 of [Kelner and Aharonian \(2008\)](#).

B.2.2 Energy spectra of muon neutrinos

The parameter ψ for muon neutrinos (ν_μ) is same as for e^+ , $\bar{\nu}_\mu$, ν_e defined above. The definition of x'_\pm is given below:

$$x'_+ = \begin{cases} 0.427x_+, & \rho < 2.14 \\ (0.427 + 0.0729(\rho - 2.14))x_+, & 2.14 < \rho < 10 \\ x_+, & \rho > 10 \end{cases} \quad (\text{B.6})$$

where $\rho = \frac{\eta}{\eta_0}$ and $\eta_0 = 0.313$ (threshold criterion) and

$$x'_- = 0.427x_- \quad (\text{B.7})$$

B.2.3 Energy spectra for electrons and electron anti-neutrinos

The definitios for ψ and x'_\pm for electrons (e^-) and electron anti-neutrinos ($\bar{\nu}_e$) are given below:

$$\psi = 6(1 - e^{1.5(4-\rho)})\Theta(\rho - 4), \quad \rho = \frac{\eta}{\eta_0} \quad (\text{B.8})$$

where $\Theta(\rho)$ is the Heaviside step function defined as: $\Theta(\rho) = 0$ if $\rho < 0$ and $\Theta(\rho) = 1$ if $\rho \geq 0$.

$$x'_\pm = \frac{1}{2(1+\eta)} (\eta - 2r \pm \sqrt{\eta(\eta - 4r(1+r))}) \quad (\text{B.9})$$

where r denotes the mass ratio of a charged pion and a proton, $r = \frac{m_\pi}{m_p} \sim 0.146$

Appendix C

Parametrization of Cherenkov shower images

In experiments using the IACT technique (such as CTA, H.E.S.S., VERITAS, MAGIC), the shower induced by a cosmic particle interaction with the Earth's atmosphere, projects an image in the camera. After calibration and pedestal subtraction, the image is represented by the number of Cherenkov photons for each pixel. For further analysis, the image is parametrized using simple parameters (for more details, see Chapter 3, Sec. 3.4.3).

The author contributed to the parametrization of Cherenkov shower image for the ctapipe software, that will be used for the low-level data processing of the upcoming CTA (discussed briefly in Chapter 3). The ctapipe software¹ is developed and maintained in Github. The repository to which the author had contributed to was called ctapipe/image. Below a brief description is given for the adopted formalism for Cherenkov image parametrization. The main contribution of the author was to the higher order image moments (such as asymmetry, skewness, kurtosis), implementing a few bug fixes and sanity checks in the existing version of the ctapipe code.

C.1 Image parametrization:

(x_i, y_i) : coordinates of the pixel i in the camera coordinates

(x_0, y_0) : reference point (for e.g.: center of the camera)

N_i : number of Cherenkov photons in pixel i

w_i : weight for pixel $i = \frac{N_i}{\sum N_k}$

A new coordinate system is introduced by rotating the camera coordinate system by an angle δ (as shown in Fig. C.1). (x, y) represents the original camera coordinate system and (x', y') represents the rotated coordinate system.

The definition of the correlations in the original camera coordinates are given below (mean of a quantity X is denoted by $\bar{X} = \sum w_i X_i$):

$$c_{xx} = \overline{(x - \bar{x})^2} \quad c_{yy} = \overline{(y - \bar{y})^2} \quad (\text{C.1})$$

$$c_{xy} = \overline{(x - \bar{x})(y - \bar{y})} \quad (\text{C.2})$$

$$c_{x^3} = \overline{(x - \bar{x})^3} \quad c_{y^3} = \overline{(y - \bar{y})^3} \quad (\text{C.3})$$

$$c_{xy^2} = \overline{(x - \bar{x})(y - \bar{y})^2} \quad c_{x^2y} = \overline{(x - \bar{x})^2(y - \bar{y})} \quad (\text{C.4})$$

In the rotated coordinate the image parameters can be defined in the following manner:

¹<https://github.com/cta-observatory/ctapipe>

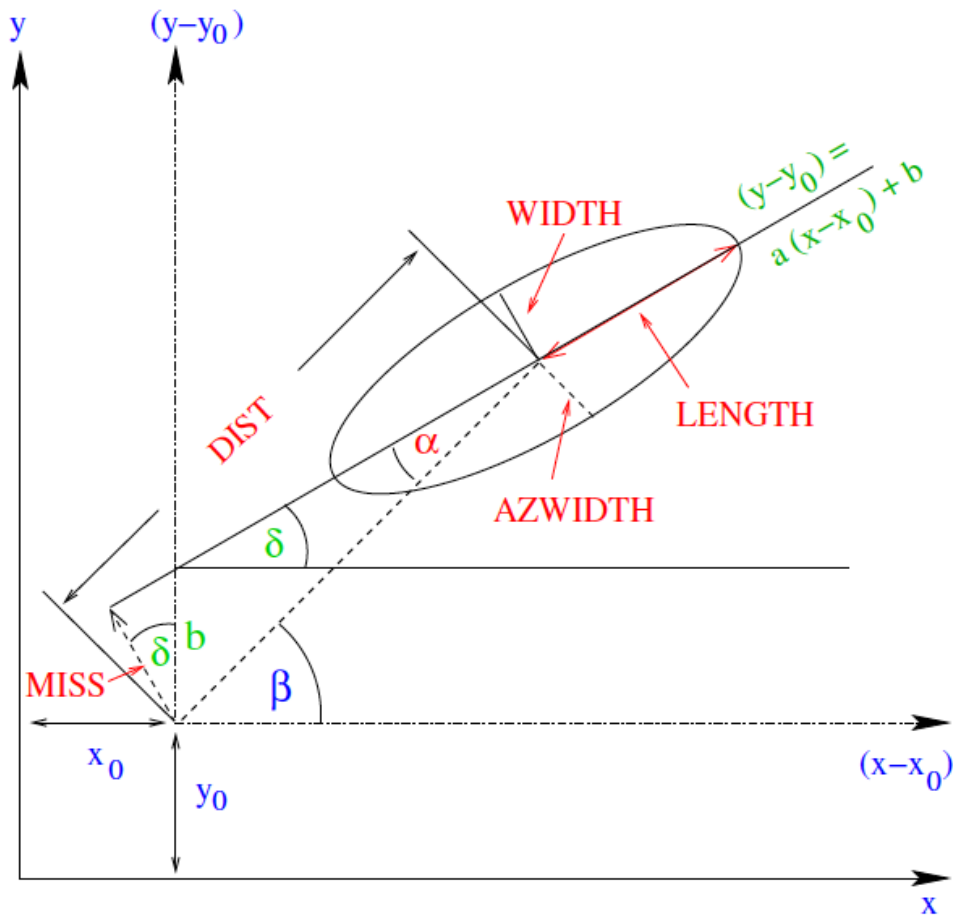


Figure C.1: Cherenkov shower image parametrization. The Hillas ellipse (Chapter 3, Sec. 3.4.3) is characterized by simple image parameters. (x, y) represents the camera coordinate system, (x_0, y_0) is a reference point. The camera coordinates are rotated by an angle δ .

$$\text{size} = \Sigma w_i \quad (\text{C.5})$$

$$\text{length}^2 = c_{x'x'} = (c_{xx} + 2a.c_{xy} + a^2.c_{yy})/(1 + a^2) \quad (\text{C.6})$$

$$\text{width}^2 = c_{y'y'} = (a^2.c_{xx} + 2a.c_{xy} + c_{yy})/(1 + a^2) \quad (\text{C.7})$$

$$\text{dist}^2 = (\bar{x} - x_0)^2 + (\bar{y} - y_0)^2 \quad (\text{C.8})$$

$$\text{miss} = \frac{b}{\sqrt{1 + a^2}} \quad (\text{C.9})$$

$$\text{asymmetry}^3 = c_{x'x'x'} = \cos^3 \delta . c_{x^3} + 3\cos^2 \delta \sin \delta . c_{x^2y} + 3\sin^2 \delta \cos \delta . c_{xy^2} + \sin^3 \delta . c_{y^3} \quad (\text{C.10})$$

Here $a = \tan \delta$ with $b = (\bar{y} - y_0) - a.(\bar{x} - x_0)$.

Let $Q_i = \cos \delta (x_i - \bar{x}) + \sin \delta (y_i - \bar{y})$. Then skewness and kurtosis can be defined as:

$$\text{skewness} = \frac{\Sigma(w_i Q_i^3)/\text{size}}{(\Sigma(w_i Q_i^2)/\text{size})^{3/2}} \quad (\text{C.11})$$

$$\text{kurtosis} = \frac{\Sigma(w_i Q_i^4)/\text{size}}{(\Sigma(w_i Q_i^2)/\text{size})^2} \quad (\text{C.12})$$

Bibliography

- A. Aab et al. Observation of a large-scale anisotropy in the arrival directions of cosmic rays above 8×10^{18} eV. *Science*, 357(6357):1266–1270, 2017.
- M. G. Aartsen et al. Searches for extended and point-like neutrino sources with four years of IceCube data. *The Astrophysical Journal*, 796(2):109, 2014a.
- M. G. Aartsen et al. Observation of high-energy astrophysical neutrinos in three years of IceCube data. *Physical review letters*, 113(10):101101, 2014b.
- M. G. Aartsen et al. All-sky search for time-integrated neutrino emission from astrophysical sources with 7 yr of IceCube data. *The Astrophysical Journal*, 835(2):151, 2017a.
- M. G. Aartsen et al. The IceCube Neutrino Observatory: instrumentation and online systems. *Journal of Instrumentation*, 12(03):P03012, 2017b.
- M. G. Aartsen et al. Extending the search for muon neutrinos coincident with gamma-ray bursts in IceCube data. *The Astrophysical Journal*, 843(2):112, 2017c.
- M. G. Aartsen et al. The contribution of FERMI-2LAC blazars to diffuse TeV-PeV neutrino flux. *The Astrophysical Journal*, 835(1):45, 2017d.
- M. G. Aartsen et al. Constraints on galactic neutrino emission with seven years of IceCube data. *The Astrophysical Journal*, 849(1):67, 2017e.
- M. G. Aartsen et al. All-sky search for time-integrated neutrino emission from astrophysical sources with 7 yr of IceCube data. *The Astrophysical Journal*, 835(2):151, 2017f.
- M. G. Aartsen et al. The IceCube realtime alert system. *Astroparticle Physics*, 92:30–41, 2017g.
- M. G. Aartsen et al. Search for steady point-like sources in the astrophysical muon neutrino flux with 8 years of IceCube data. *arXiv e-prints*, art. arXiv:1811.07979, November 2018.
- R. U. Abbasi et al. Monocular measurement of the spectrum of UHE cosmic rays by the FADC detector of the HiRes experiment. *Astroparticle Physics*, 23:157–174, Mar 2005. doi: 10.1016/j.astropartphys.2004.12.006.
- R. U. Abbasi et al. Search for cross-correlations of ultrahigh-energy cosmic rays with BL Lacertae objects. *The Astrophysical Journal*, 636(2):680, 2006.
- R. U. Abbasi et al. First Observation of the Greisen-Zatsepin-Kuzmin Suppression. , 100:101101, Mar 2008. doi: 10.1103/PhysRevLett.100.101101.
- R. U. Abbasi et al. Publisher’s Note: Indications of Proton-Dominated Cosmic-Ray Composition above 1.6 EeV [Phys. Rev. Lett. 104, 161101 (2010)]. , 104:199902, May 2010. doi: 10.1103/PhysRevLett.104.199902.
- B. P. Abbott et al. Observation of gravitational waves from a binary black hole merger. *Physical review letters*, 116(6):061102, 2016.
- B. P. Abbott et al. Gravitational waves and gamma-rays from a binary neutron star merger: GW170817 and GRB 170817A. *The Astrophysical Journal Letters*, 848(2):L13, 2017a.

BIBLIOGRAPHY

- B. P. Abbott et al. GW170817: Observation of gravitational waves from a binary neutron star inspiral. *Physical Review Letters*, 119(16):161101, 2017b.
- B. P. Abbott et al. Multi-messenger observations of a binary neutron star merger. *Astrophys. J. Lett*, 848(2):L12, 2017c.
- H. Abdalla et al. The HESS Galactic plane survey. *Astronomy & Astrophysics*, 612:A1, 2018.
- A. A. Abdo et al. Fermi Gamma-Ray Imaging of a Radio Galaxy. *Science*, 328:725, May 2010a. doi: 10.1126/science.1184656.
- A. A. Abdo et al. Fermi Large Area Telescope constraints on the gamma-ray opacity of the universe. *The Astrophysical Journal*, 723(2):1082, 2010b.
- A. A. Abdo et al. Fermi Large Area Telescope observations of Markarian 421: The missing piece of its spectral energy distribution. *The Astrophysical Journal*, 736(2):131, 2011.
- A. U. Abeysekara et al. Gamma-Rays from the Quasar PKS 1441+ 25: Story of an Escape. *The Astrophysical Journal Letters*, 815(2):L22, 2015.
- A. U. Abeysekara et al. The 2HWC HAWC observatory gamma-ray catalog. *The Astrophysical Journal*, 843(1):40, 2017.
- A. U. Abeysekara et al. VERITAS observations of the BL Lac object TXS 0506+ 056. *The Astrophysical Journal Letters*, 861(2):L20, 2018.
- J. Abraham et al. Properties and performance of the prototype instrument for the Pierre Auger Observatory. *Nuclear Instruments and Methods in Physics Research Section A: Accelerators, Spectrometers, Detectors and Associated Equipment*, 523(1-2):50–95, 2004.
- A. Abramowski et al. A multiwavelength view of the flaring state of PKS 2155-304 in 2006. *Astronomy & Astrophysics*, 539:A149, 2012.
- P. Abreu et al. Update on the correlation of the highest energy cosmic rays with nearby extragalactic matter. *Astroparticle Physics*, 34:314–326, Jan 2010. doi: 10.1016/j.astropartphys.2010.08.010.
- T. Abu-Zayyad et al. The Cosmic-Ray Energy Spectrum Observed with the Surface Detector of the Telescope Array Experiment. , 768(1):L1, May 2013. doi: 10.1088/2041-8205/768/1/L1.
- F. Acero et al. Fermi Large Area Telescope third source catalog. *The Astrophysical Journal Supplement Series*, 218(2):23, 2015.
- M. Ackermann. Searches for signals from cosmic point-like sources of high energy neutrinos in 5 years of AMANDA-II data. 2006.
- M. Ackermann et al. Multiwavelength comparison of selected neutrino point source candidates. Technical report, astro-ph/0509330, 2005.
- M. Ackermann et al. The third catalog of active galactic nuclei detected by the Fermi Large Area Telescope. *The Astrophysical Journal*, 810(1):14, 2015.
- M. Actis et al. Design concepts for the Cherenkov Telescope Array CTA: an advanced facility for ground-based high-energy gamma-ray astronomy. *Experimental Astronomy*, 32(3):193–316, 2011.
- F. A. Aharonian. TeV gamma rays from BL Lac objects due to synchrotron radiation of extremely high energy protons. *New Astronomy*, 5(7):377–395, 2000.
- F. A. Aharonian. *Very high energy cosmic gamma radiation: a crucial window on the extreme Universe*. World Scientific, 2004.

- F. A. Aharonian, P. S. Coppi, and H. J. Völk. Very High Energy Gamma-Rays from AGN: Cascading on the Cosmic Background Radiation Fields and the Formation of Pair Halos. *arXiv preprint astro-ph/9312045*, 1993.
- F. A. Aharonian, D. Khangulyan, and L. Costamante. Formation of hard very high energy gamma-ray spectra of blazars due to internal photon–photon absorption. *Monthly Notices of the Royal Astronomical Society*, 387(3): 1206–1214, 2008.
- F. A. Aharonian, S. R. Kelner, and A. Y. Prosekin. Angular, spectral, and time distributions of highest energy protons and associated secondary gamma rays and neutrinos propagating through extragalactic magnetic and radiation fields. *Physical Review D*, 82(4):043002, 2010.
- F. A. Aharonian et al. The potential of ground based arrays of imaging atmospheric Cherenkov telescopes. I. Determination of shower parameters. *Astroparticle Physics*, 6(3-4):343–368, 1997.
- F. A. Aharonian et al. Detection of TeV gamma-rays from the BL Lac 1ES 1959+650 in its low states and during a major outburst in 2002. , 406:L9–L13, July 2003. doi: 10.1051/0004-6361:20030838.
- F. A. Aharonian et al. Observations of the Crab nebula with HESS. *Astronomy & Astrophysics*, 457(3):899–915, 2006.
- F. A. Aharonian et al. An exceptional very high energy Gamma-Ray flare of PKS 2155–304. *The Astrophysical Journal Letters*, 664(2):L71, 2007.
- F. A. Aharonian et al. Simultaneous Observations of PKS 2155–304 with HESS, Fermi, RXTE, and Atom: Spectral Energy Distributions and Variability in a Low State. *The Astrophysical Journal Letters*, 696(2):L150, 2009.
- Q. R. Ahmad et al. Measurement of the Rate of $\nu_e + d \rightarrow p + p + e^-$ Interactions Produced by 8B Solar Neutrinos at the Sudbury Neutrino Observatory. *Phys. Rev. Lett.*, 87:071301, Jul 2001. doi: 10.1103/PhysRevLett.87.071301.
- Q. R. Ahmad et al. Direct Evidence for Neutrino Flavor Transformation from Neutral-Current Interactions in the Sudbury Neutrino Observatory. *Phys. Rev. Lett.*, 89:011301, Jun 2002. doi: 10.1103/PhysRevLett.89.011301.
- M. L. Ahnen et al. Very High Energy γ -Rays from the Universe’s Middle Age: Detection of the $z=0.940$ Blazar PKS 1441+ 25 with MAGIC. *The Astrophysical Journal Letters*, 815(2):L23, 2015.
- M. L. Ahnen et al. Detection of very high energy gamma-ray emission from the gravitationally lensed blazar QSO B0218+ 357 with the MAGIC telescopes. *Astronomy & Astrophysics*, 595:A98, 2016.
- M. L. Ahnen et al. Performance of the MAGIC telescopes under moonlight. *Astroparticle Physics*, 94:29–41, Sep 2017. doi: 10.1016/j.astropartphys.2017.08.001.
- M. L. Ahnen et al. Extreme HBL behavior of Markarian 501 during 2012. *Astronomy & Astrophysics*, 620:A181, 2018.
- J. Albert et al. Observation of very high energy gamma-ray emission from the active galactic nucleus 1ES 1959+ 650 using the magic telescope. *The Astrophysical Journal*, 639(2):761, 2006.
- J. Albert et al. Observations of Markarian 421 with the MAGIC Telescope. *The Astrophysical Journal*, 663(1): 125, 2007a.
- J. Albert et al. Variable very high energy γ -ray emission from Markarian 501. *The Astrophysical Journal*, 669(2): 862, 2007b.
- J. Albert et al. Unfolding of differential energy spectra in the MAGIC experiment. *Nuclear Instruments and Methods in Physics Research Section A: Accelerators, Spectrometers, Detectors and Associated Equipment*, 583(2-3):494–506, 2007c.
- J. Albert et al. Very-high-energy gamma rays from a distant quasar: How transparent is the universe? *Science*, 320 (5884):1752–1754, 2008.

BIBLIOGRAPHY

- J. Aleksić et al. Search for an extended VHE γ -ray emission from Mrk 421 and Mrk 501 with the MAGIC Telescope. *Astronomy & Astrophysics*, 524:A77, 2010.
- J. Aleksić et al. Performance of the MAGIC stereo system obtained with Crab Nebula data. *Astroparticle Physics*, 35:435–448, Feb 2012a. doi: 10.1016/j.astropartphys.2011.11.007.
- J. Aleksić et al. High zenith angle observations of PKS 2155-304 with the MAGIC-I telescope. *Astronomy & Astrophysics*, 544:A75, 2012b.
- J. Aleksić et al. The major upgrade of the MAGIC telescopes, Part II: A performance study using observations of the Crab Nebula. *Astroparticle Physics*, 72:76–94, 2016a.
- J. Aleksić et al. The major upgrade of the MAGIC telescopes, Part I: The hardware improvements and the commissioning of the system. *Astroparticle Physics*, 72:61–75, Jan 2016b. doi: 10.1016/j.astropartphys.2015.04.004.
- K. D. Alexander et al. The electromagnetic counterpart of the binary neutron star merger LIGO/VIRGO GW170817. VI. Radio constraints on a relativistic jet and predictions for late-time emission from the kilonova ejecta. *The Astrophysical Journal Letters*, 848(2):L21, 2017.
- E. N. Alexeyev et al. Detection of the neutrino signal from SN 1987A in the LMC using the INR Baksan underground scintillation telescope. *Physics Letters B*, 205(2-3):209–214, 1988.
- E. Aliu et al. Multiwavelength observations and modeling of 1ES 1959+ 650 in a low flux state. *The Astrophysical Journal*, 775(1):3, 2013.
- E. Aliu et al. Investigating broadband variability of the TeV blazar 1ES 1959+ 650. *The Astrophysical Journal*, 797(2):89, 2014.
- D. Allard, E. Parizot, and A. V. Olinto. On the transition from galactic to extragalactic cosmic-rays: Spectral and composition features from two opposite scenarios. *Astroparticle Physics*, 27(1):61–75, 2007.
- H. Anderhub et al. Design and operation of FACT—the first G-APD Cherenkov telescope. *Journal of Instrumentation*, 8(06):P06008, 2013.
- J. R. P. Angel and H. S. Stockman. Optical and infrared polarization of active extragalactic objects. *Annual Review of Astronomy and Astrophysics*, 18(1):321–361, 1980.
- S. Ansoldi et al. The Blazar TXS 0506+ 056 Associated with a High-energy Neutrino: Insights into Extragalactic Jets and Cosmic-Ray Acceleration. *The Astrophysical Journal Letters*, 863(1):L10, 2018.
- W. D. Apel et al. Kneelike structure in the spectrum of the heavy component of cosmic rays observed with KASCADE-Grande. *Physical Review Letters*, 107(17):171104, 2011.
- W. D. Apel et al. Ankle-like feature in the energy spectrum of light elements of cosmic rays observed with KASCADE-Grande. *Physical Review D*, 87(8):081101, 2013.
- C. Arbeiter, M. Pohl, and R. Schlickeiser. The influence of dust on the inverse Compton emission from jets in Active Galactic Nuclei. *Astronomy & Astrophysics*, 386(2):415–426, 2002.
- I. Arcavi et al. Optical emission from a kilonova following a gravitational-wave-detected neutron-star merger. *Nature*, 551(7678):64, 2017.
- A. Atayan and C. D. Dermer. High-energy neutrinos from photomeson processes in blazars. *Physical Review Letters*, 87(22):221102, 2001.
- M. Backes. Long-term observations of the TeV blazar 1ES1959+ 650. 2011.
- J. A. Baldwin, M. M Phillips, and R. Terlevich. CLASSIFICATION PARAMETERS FOR THE EMISSION-LINE SPECTRA OF EXTRAGALACTIC OBJECTS. *Publications of the Astronomical Society of the Pacific*, 93(551):5, 1981.

- K. S. Baliyan et al. Optical/NIR Observations of HBL 1ES 1959+625 from Mt Abu IR Observatory(MIRO), India. *The Astronomer's Telegram*, 9070:1, May 2016.
- M. G. Baring et al. Radio to gamma-ray emission from shell-type supernova remnants: predictions from nonlinear shock acceleration models. *The Astrophysical Journal*, 513(1):311, 1999.
- M. V. Barkov et al. Rapid TeV Variability in Blazars as a Result of Jet-Star Interaction. *The Astrophysical Journal*, 749(2):119, 2012.
- P. P. Basumallick and N. Gupta. A single zone synchrotron model for flares of PKS1510-089. *Astroparticle Physics*, 88:1–6, February 2017. doi: 10.1016/j.astropartphys.2016.12.005.
- J. K. Becker. High-energy neutrinos in the context of multimessenger astrophysics. , 458:173–246, Mar 2008. doi: 10.1016/j.physrep.2007.10.006.
- V. Berezhinsky, A. Gazizov, and S. Grigorieva. On astrophysical solution to ultrahigh energy cosmic rays. *Physical Review D*, 74(4):043005, 2006.
- E. Bernardini et al. Multi-Messenger Studies with AMANDA/IceCube: Observations and Strategies. *arXiv preprint astro-ph/0509396*, 2005.
- P. L. Biermann et al. Active Galactic Nuclei: Sources for Ultra High Energy Cosmic Rays. *International Journal of Modern Physics D*, 18:1577–1581, Jan 2009. doi: 10.1142/S0218271809015369.
- A. Biland and R. Mirzoyan. FACT and MAGIC measure an increased gamma-ray flux from the HBL 1ES 1959+650. *The Astronomer's Telegram*, 9203:1, July 2016.
- A. Biland, D. Dorner, R. Mirzoyan, R. Mukherjee, S. Buson, and B. Kapanazde. Further increase of gamma-ray emission from the HBL 1ES 1959+650. *The Astronomer's Telegram*, 9148:1, June 2016.
- R. M. Bionta et al. Observation of a neutrino burst in coincidence with supernova 1987A in the Large Magellanic Cloud. *Phys. Rev. Lett.*, 58:1494–1496, Apr 1987. doi: 10.1103/PhysRevLett.58.1494.
- M. Bitossi. Ultra-fast sampling and readout for the MAGIC-II telescope Data Acquisition system. 2009.
- M. Böttcher. A Hadronic Synchrotron Mirror Model for the “Orphan” TeV Flare in 1ES 1959+650. , 621:176–180, March 2005. doi: 10.1086/427430.
- M. Böttcher et al. Leptonic and hadronic modeling of Fermi-detected blazars. *The Astrophysical Journal*, 768(1): 54, 2013.
- J. H. Boyer et al. FADC-based DAQ for HiRes Fly's Eye. *Nuclear Instruments and Methods in Physics Research Section A: Accelerators, Spectrometers, Detectors and Associated Equipment*, 482(1-2):457–474, 2002.
- M. Branchesi. Multi-messenger astronomy: gravitational waves, neutrinos, photons, and cosmic rays. In *Journal of Physics: Conference Series*, volume 718, page 022004. IOP Publishing, 2016.
- S. Buson, J. D. Magill, D. Dorner, A. Biland, R. Mirzoyan, and R. Mukherjee. Fermi-LAT, FACT, MAGIC and VERITAS detection of increasing gamma-ray activity from the high-energy peaked BL Lac object 1ES 1959+650. *The Astronomer's Telegram*, 9010:1, April 2016.
- A. Caccianiga and M. J. M. Marcha. The CLASS blazar survey: testing the blazar sequence. *Monthly Notices of the Royal Astronomical Society*, 348(3):937–954, 2004.
- M. Cerruti et al. A mixed lepto-hadronic scenario for PKS 2155-304. In *AIP Conference Proceedings*, volume 1505, pages 635–638. AIP, 2012.
- M. Cerruti et al. A hadronic origin for ultra-high-frequency-peaked BL Lac objects. *Monthly Notices of the Royal Astronomical Society*, 448(1):910–927, 2015.

BIBLIOGRAPHY

- M. Cerruti et al. Leptohadronic single-zone models for the electromagnetic and neutrino emission of TXS 0506+056. *Monthly Notices of the Royal Astronomical Society: Letters*, 483(1):L12–L16, 2018.
- P. M. Chadwick et al. Very High Energy Gamma Rays from PKS 2155–304. *The Astrophysical Journal*, 513(1):161, 1999.
- J. S. Chang and G. Cooper. A practical difference scheme for Fokker-Planck equations. *Journal of Computational Physics*, 6(1):1–16, 1970.
- P. Charles, J. Thorstensen, and S. Bowyer. H2155–304: a highly luminous BL Lac object. *Nature*, 281(5729):285, 1979.
- P. A. Cherenkov. Visible emission of clean liquids by action of radiation. *Doklady Akademii Nauk SSSR*, 2:451+, 1934.
- M. Chiaberge and G. Ghisellini. Rapid variability in the synchrotron self-Compton model for blazars. *Monthly Notices of the Royal Astronomical Society*, 306(3):551–560, 1999.
- N. Chiba et al. Possible evidence for 10 GeV neutrons associated with the solar flare of 4 June 1991. *Astroparticle Physics*, 1(1):27–32, 1992.
- V. Chmill et al. On the characterisation of SiPMs from pulse-height spectra. *Nuclear Instruments and Methods in Physics Research Section A: Accelerators, Spectrometers, Detectors and Associated Equipment*, 854:70–81, 2017.
- R. Chornock et al. The electromagnetic counterpart of the binary neutron star merger LIGO/VIRGO GW170817. IV. Detection of near-infrared signatures of r-process nucleosynthesis with Gemini-south. *The Astrophysical Journal Letters*, 848(2):L19, 2017.
- L. Costamante et al. Extreme synchrotron BL Lac objects—Stretching the blazar sequence. *Astronomy & Astrophysics*, 371(2):512–526, 2001.
- R. M. Crocker et al. A lower limit of 50 microgauss for the magnetic field near the Galactic Centre. *Nature*, 463(7277):65, 2010.
- CTA Consortium et al. The Cherenkov Telescope Array: Science Goals and Current Status. *arXiv preprint arXiv:1904.12196*, 2019.
- J. M. Davies and E. S. Cotton. Design of the quartermaster solar furnace. *Solar Energy*, 1(2-3):16–22, 1957.
- A. De Angelis and M. Mallamaci. Gamma-ray astrophysics. *The European Physical Journal Plus*, 133(8):324, 2018.
- C. D. Dermer. On the beaming statistics of gamma-ray sources. *The Astrophysical Journal*, 446:L63, 1995.
- C. D. Dermer and G. Menon. *High energy radiation from black holes: gamma rays, cosmic rays, and neutrinos*, volume 17. Princeton University Press, 2009.
- C. D. Dermer and S. Razzaque. Acceleration of Ultra-high-energy Cosmic Rays in the Colliding Shells of Blazars and Gamma-ray Bursts: Constraints from the Fermi Gamma-ray Space Telescope. , 724:1366–1372, Dec 2010. doi: 10.1088/0004-637X/724/2/1366.
- S. Dimitrakoudis et al. The time-dependent one-zone hadronic model—First principles. *Astronomy & Astrophysics*, 546:A120, 2012.
- A. Djannati-Atai et al. Very High Energy Gamma-ray spectral properties of Mrk 501 from CAT Cerenkov telescope observations in 1997. *arXiv preprint astro-ph/9906060*, 1999.
- A. Dominguez et al. Extragalactic background light inferred from AEGIS galaxy-SED-type fractions. *Monthly Notices of the Royal Astronomical Society*, 410(4):2556–2578, 2011.

- A. Domínguez et al. DETECTION OF THE COSMIC γ -RAY HORIZON FROM MULTIWAVELENGTH OBSERVATIONS OF BLAZARS. *The Astrophysical Journal*, 770(1):77, may 2013. doi: 10.1088/0004-637x/770/1/77.
- D. Donato et al. Hard X-ray properties of blazars. *Astronomy & Astrophysics*, 375(3):739–751, 2001.
- R. A. Edelson and J. H. Krolik. The discrete correlation function—A new method for analyzing unevenly sampled variability data. *The Astrophysical Journal*, 333:646–659, 1988.
- F. Eisenhauer et al. SINFONI in the Galactic center: young stars and infrared flares in the Central Light-Month. *The Astrophysical Journal*, 628(1):246, 2005.
- M. Elvis et al. The Einstein Slew Survey. *The Astrophysical Journal Supplement Series*, 80:257, May 1992. doi: 10.1086/191665.
- P. A. Evans et al. Swift and NuSTAR observations of GW170817: detection of a blue kilonova. *Science*, 358(6370):1565–1570, 2017.
- R. Falomo, J. K. Kotilainen, and A. Treves. The black hole mass of BL Lacertae objects from the stellar velocity dispersion of the host galaxy. *The Astrophysical Journal Letters*, 569(1):L35, 2002.
- R. Falomo et al. Black hole masses and the fundamental plane of BL Lacertae objects. *The Astrophysical Journal*, 595(2):624, 2003.
- E. Fermi. On the origin of the cosmic radiation. *Physical Review*, 75(8):1169, 1949.
- Fermi-LAT Collaboration et al. Fermi Large Area Telescope Fourth Source Catalog. *arXiv preprint arXiv:1902.10045*, 2019.
- A. Fernández Barral. Extreme particle acceleration in microquasars jets and pulsar wind nebulae with the MAGIC telescopes. 2017.
- D. Fidalgo et al. Data processing activities at the MAGIC site. In *The 34th International Cosmic Ray Conference*, volume 236, page 742. SISSA Medialab, 2016.
- J. D. Finke, S. Razzaque, and C. D. Dermer. Modeling the extragalactic background light from stars and dust. *The Astrophysical Journal*, 712(1):238, 2010.
- G. Fossati et al. A unifying view of the spectral energy distributions of blazars. *Monthly Notices of the Royal Astronomical Society*, 299(2):433–448, 1998.
- A. Franceschini, G. Rodighiero, and M. Vaccari. Extragalactic optical-infrared background radiation, its time evolution and the cosmic photon-photon opacity. *Astronomy & Astrophysics*, 487(3):837–852, 2008.
- C. Fruck et al. A novel LIDAR-based atmospheric calibration method for improving the data analysis of MAGIC. *arXiv preprint arXiv:1403.3591*, 2014.
- Y. Fukuda et al. Evidence for oscillation of atmospheric neutrinos. *Physical Review Letters*, 81(8):1562, 1998.
- T. K. Gaisser. Book-Review-Cosmic-Rays and Particle Physics. *Journal of the British Astronomical Association*, 101:128, 1991.
- J. R. García et al. Status of the new Sum-Trigger system for the MAGIC telescopes. *arXiv preprint arXiv:1404.4219*, 2014.
- K. Gebhardt et al. Black hole mass estimates from reverberation mapping and from spatially resolved kinematics. *The Astrophysical Journal Letters*, 543(1):L5, 2000.
- G. Ghisellini. Extragalactic relativistic jets. In *AIP Conference Proceedings*, volume 1381, pages 180–198. AIP, 2011.

BIBLIOGRAPHY

- G. Ghisellini and R. Svensson. The synchrotron and cyclo-synchrotron absorption cross-section. *Monthly Notices of the Royal Astronomical Society*, 252(3):313–318, 1991.
- G. Ghisellini and F. Tavecchio. The blazar sequence: a new perspective. *Monthly Notices of the Royal Astronomical Society*, 387(4):1669–1680, 2008.
- G. Ghisellini, F. Tavecchio, and M. Chiaberge. Structured jets in TeV BL Lac objects and radiogalaxies. Implications for the observed properties. , 432:401–410, Mar 2005. doi: 10.1051/0004-6361:20041404.
- G. Ghisellini, L. Maraschi, and F. Tavecchio. The Fermi blazars’ divide. *Monthly Notices of the Royal Astronomical Society: Letters*, 396(1):L105–L109, 2009.
- G. Ghisellini et al. A theoretical unifying scheme for gamma-ray bright blazars. *Monthly Notices of the Royal Astronomical Society*, 301(2):451–468, 1998.
- G. Ghisellini et al. The transition between BL Lac objects and flat spectrum radio quasars. *Monthly Notices of the Royal Astronomical Society*, 414(3):2674–2689, 2011.
- G. Ghisellini et al. The Fermi blazar sequence. *Monthly Notices of the Royal Astronomical Society*, 469(1):255–266, 2017.
- R. C. Gilmore et al. Semi-analytic modelling of the extragalactic background light and consequences for extragalactic gamma-ray spectra. *Monthly Notices of the Royal Astronomical Society*, 422(4):3189–3207, 2012.
- C. Gini. Measurement of inequality of incomes. *The Economic Journal*, 31(121):124–126, 1921.
- P. Giommi, M. T. Menna, and P. Padovani. The sedentary multifrequency survey—I. Statistical identification and cosmological properties of high-energy peaked BL Lacs. *Monthly Notices of the Royal Astronomical Society*, 310(2):465–475, 1999.
- P. Giommi et al. The sedentary survey of extreme high energy peaked BL Lacs. *Astronomy & Astrophysics*, 434(1):385–396, 2005.
- P. Giommi et al. A simplified view of blazars: clearing the fog around long-standing selection effects. *Monthly Notices of the Royal Astronomical Society*, 420(4):2899–2911, 2012.
- M. Giroletti et al. The jet of Markarian 501 from millions of Schwarzschild radii down to a few hundreds. *Astronomy & Astrophysics*, 488(3):905–914, 2008.
- D. Glawion. Contemporaneous Multi-Wavelength Observations of the Gamma-Ray Emitting Active Galaxy IC 310—New Clues on Particle Acceleration in Extragalactic Jets. 2014.
- A. Goldstein et al. An ordinary short gamma-ray burst with extraordinary implications: Fermi-GBM detection of GRB 170817A. *The Astrophysical Journal Letters*, 848(2):L14, 2017.
- P. Gorenstein, F. R. Harnden, and D. G. Fabricant. In orbit performance of the Einstein Observatory/HEAO-2 imaging proportional counter. *IEEE Transactions on Nuclear Science*, 28(1):869–874, 1981.
- P. C. Gregory and J. J. Condon. The 87GB Catalog of Radio Sources Covering 0 degrees δ +75 degrees at 4.85 GHz. *The Astrophysical Journal Supplement Series*, 75:1011, April 1991. doi: 10.1086/191559.
- J. Greiner et al. The redshift and afterglow of the extremely energetic gamma-ray burst GRB 080916C. *Astronomy & Astrophysics*, 498(1):89–94, 2009.
- K. Greisen. End to the Cosmic-Ray Spectrum? , 16:748–750, Apr 1966. doi: 10.1103/PhysRevLett.16.748.
- P. K. F. Grieder. *Extensive Air Showers: High Energy Phenomena and Astrophysical Aspects—A Tutorial, Reference Manual and Data Book*. Springer Science & Business Media, 2010.
- D. A. Guberman. *MAGIC observations with bright Moon and their application to measuring the VHE gamma-ray spectral cut-off of the PeVatron candidate Cassiopeia A*. PhD thesis, Universitat Autònoma de Barcelona, 2018.

- K. Gültekin et al. The M - σ and ML relations in galactic bulges, and determinations of their intrinsic scatter. *The Astrophysical Journal*, 698(1):198, 2009.
- F. Halzen and D. Hooper. High energy neutrinos from the TeV Blazar 1ES 1959 + 650. *Astroparticle Physics*, 23: 537–542, July 2005. doi: 10.1016/j.astropartphys.2005.03.007.
- W. F. Hanlon. Updated Cosmic Ray Spectrum, 2010. <https://www.physics.utah.edu/~whanlon/spectrum.html>.
- D. E. Harris and H. Krawczynski. X-ray emission processes in radio jets. *The Astrophysical Journal*, 565(1):244, 2002.
- J. Heidt et al. High-resolution imaging of Einstein slew survey bl lacertae objects. *arXiv preprint astro-ph/9811050*, 1998.
- C. A. Heisler, S. L. Lumsden, and J. A. Bailey. Visibility of scattered broad-line emission in Seyfert 2 galaxies. *Nature*, 385(6618):700, 1997.
- V. F. Hess. Über Beobachtungen der durchdringenden Strahlung bei sieben Freiballonfahrten. *Z. Phys.*, 13:1084, 1912.
- High Resolution Fly’S Eye Collaboration et al. Search for correlations between HiRes stereo events and active galactic nuclei. *Astroparticle Physics*, 30:175–179, Nov 2008. doi: 10.1016/j.astropartphys.2008.08.004.
- A. M. Hillas. The origin of ultra-high-energy cosmic rays. *Annual review of astronomy and astrophysics*, 22(1): 425–444, 1984.
- A. M. Hillas. Cerenkov light images of EAS produced by primary gamma. 1985.
- K. S. Hirata et al. Observation in the Kamiokande-II detector of the neutrino burst from supernova SN1987A. *Phys. Rev. D*, 38:448–458, Jul 1988. doi: 10.1103/PhysRevD.38.448.
- W. Hofmann et al. Comparison of techniques to reconstruct VHE gamma-ray showers from multiple stereoscopic Cherenkov images. *Astroparticle Physics*, 12(3):135–143, 1999.
- J. Holder. VERITAS: status and performance. In *Science With The New Generation Of High Energy Gamma-Ray Experiments: The Variable Gamma-Ray Sources: Their Identifications and Counterparts*, pages 69–76. World Scientific, 2007.
- J. Holder et al. Detection of TeV gamma rays from the BL Lacertae object 1ES 1959+ 650 with the Whipple 10 meter telescope. *The Astrophysical Journal Letters*, 583(1):L9, 2002.
- IceCube Collaboration et al. Evidence for high-energy extraterrestrial neutrinos at the IceCube detector. *Science*, 342(6161):1242856, 2013.
- IceCube Collaboration et al. Neutrino emission from the direction of the blazar TXS 0506+ 056 prior to the IceCube-170922A alert. *Science*, 361(6398):147–151, 2018a.
- IceCube Collaboration et al. Multimessenger observations of a flaring blazar coincident with high-energy neutrino IceCube-170922A. *Science*, 361(6398):eaat1378, 2018b.
- IceCube-Gen2 Collaboration et al. IceCube-Gen2: a vision for the future of neutrino astronomy in Antarctica. *arXiv preprint arXiv:1412.5106*, 2014.
- D. Ivanov. TA spectrum summary. *PoS*, page 349, 2015.
- W. Jaffe et al. A large nuclear accretion disk in the active galaxy NGC4261. *Nature*, 364(6434):213, 1993.
- M. Kadler et al. Coincidence of a high-fluence blazar outburst with a PeV-energy neutrino event. *Nature Physics*, 12(8):807, 2016.

BIBLIOGRAPHY

- E. Kafexhiu et al. Parametrization of gamma-ray production cross sections for p p interactions in a broad proton energy range from the kinematic threshold to PeV energies. *Physical Review D*, 90(12):123014, 2014.
- B. Kapanadze. A strong X-ray Flare in TeV blazar 1ES 1959+650. *The Astronomer's Telegram*, 8289:1, November 2015.
- B. Kapanadze, D. Dorner, and S. Kapanadze. A new highest historical X-ray State in 1ES 1959+650. *The Astronomer's Telegram*, 9205:1, July 2016.
- D. Kasen et al. Origin of the heavy elements in binary neutron-star mergers from a gravitational-wave event. *Nature*, 551(7678):80, 2017.
- M. M. Kasliwal et al. Illuminating gravitational waves: a concordant picture of photons from a neutron star merger. *Science*, 358(6370):1559–1565, 2017.
- K. L. Kellermann et al. VLA observations of objects in the Palomar Bright Quasar Survey. *The Astronomical Journal*, 98:1195–1207, 1989.
- S. R. Kelner and F. A. Aharonian. Energy spectra of gamma rays, electrons, and neutrinos produced at interactions of relativistic protons with low energy radiation. *Physical Review D*, 78(3):034013, 2008.
- S. R. Kelner, F. A. Aharonian, and V. V. Bugayov. Energy spectra of gamma rays, electrons, and neutrinos produced at proton-proton interactions in the very high energy regime. *Physical Review D*, 74(3):034018, 2006.
- D. Khangulyan, F. A. Aharonian, and S. R. Kelner. Simple analytical approximations for treatment of inverse Compton scattering of relativistic electrons in the blackbody radiation field. *The Astrophysical Journal*, 783(2): 100, 2014.
- J. Kildea et al. The Whipple Observatory 10 m gamma-ray telescope, 1997–2006. *Astroparticle Physics*, 28(2): 182–195, 2007.
- T. Kintscher et al. IceCube Search for Neutrinos from 1ES 1959+650: Completing the Picture. *PoS, ICRC2017*: 969, 2018. doi: 10.22323/1.301.0969.
- T. M. Kneiske and H. Dole. A lower-limit flux for the extragalactic background light. *Astronomy & Astrophysics*, 515:A19, 2010.
- A. Konigl. Relativistic jets as X-ray and gamma-ray sources. , 243:700–709, February 1981. doi: 10.1086/158638.
- K. Kotera, D. Allard, and A. V. Olinto. Cosmogenic neutrinos: parameter space and detectability from PeV to ZeV. *Journal of Cosmology and Astroparticle Physics*, 2010(10):013, 2010.
- H. Krawczynski et al. Multiwavelength observations of strong flares from the TeV blazar 1ES 1959+ 650. *The Astrophysical Journal*, 601(1):151, 2004.
- J. H. Krolik and M. C. Begelman. Molecular tori in Seyfert galaxies—Feeding the monster and hiding it. *The Astrophysical Journal*, 329:702–711, 1988.
- J. P. Leahy and R. A. Perley. VLA images of 23 extragalactic radio sources. *The Astronomical Journal*, 102: 537–561, 1991.
- T. P. Li and Y. Q. Ma. Analysis methods for results in gamma-ray astronomy. *The Astrophysical Journal*, 272: 317–324, 1983.
- N. H. Liao, S. Li, and Y. Z. Fan. Fermi-LAT Detection of a Transient γ -Ray Source in the Direction of a Distant Blazar B3 1428+ 422 at $z=4.72$. *The Astrophysical Journal Letters*, 865(2):L17, 2018.
- M. S. Longair. *High energy astrophysics. Vol. 1: Particles, photons and their detection*. 1992.
- M. S. Longair. *High energy astrophysics*. Cambridge university press, 2011.

- R. López-Coto et al. The Topo-trigger: a new concept of stereo trigger system for imaging atmospheric Cherenkov telescopes. *Journal of Instrumentation*, 11(04):P04005, 2016.
- Rubén López Coto. Very-high-energy-ray observations of pulsar wind nebulae and cataclysmic variable stars with MAGIC and development of trigger systems for IACTs. 2015.
- M. Lyutikov and M. Lister. Resolving doppler-factor crisis in active galactic nuclei: Non-steady magnetized outflows. *The Astrophysical Journal*, 722(1):197, 2010.
- L. Ma et al. CCD photometry of five X-ray selected BL Lacertae objects. *Astrophysics and Space Science*, 327(1): 35–58, 2010.
- G. Madejski and M. Sikora. Gamma-ray observations of active galactic nuclei. *Annual Review of Astronomy and Astrophysics*, 54:725–760, 2016.
- K. Mannheim. The proton blazar. *Astronomy and Astrophysics*, 269:67–76, 1993.
- L. Maraschi, G. Ghisellini, and A. Celotti. A jet model for the gamma-ray emitting blazar 3C 279. *The Astrophysical Journal*, 397:L5–L9, 1992.
- M. J. M. Marcha et al. Optical spectroscopy and polarization of a new sample of optically bright flat radio spectrum sources. *Monthly Notices of the Royal Astronomical Society*, 281(2):425–448, 1996.
- E. Massaro et al. Log-parabolic spectra and particle acceleration in the BL Lac object Mkn 421: Spectral analysis of the complete BeppoSAX wide band X-ray data set. *Astronomy & Astrophysics*, 413(2):489–503, 2004.
- E. Massaro et al. Roma-BZCAT: a multifrequency catalogue of blazars. *Astronomy & Astrophysics*, 495(2): 691–696, 2009.
- R. A. Millikan and G. H. Cameron. High frequency rays of cosmic origin III. Measurements in snow-fed lakes at high altitudes. *Physical Review*, 28(5):851, 1926.
- R. Mirzoyan. On the calibration accuracy of light sensors in atmospheric Cherenkov fluorescence and neutrino experiments. In *International Cosmic Ray Conference*, volume 7, page 265, 1997.
- R. Mirzoyan. First-time detection of VHE gamma rays by MAGIC from a direction consistent with the recent EHE neutrino event IceCube-170922A. *The Astronomer's Telegram*, 10817:1, Oct 2017.
- R. Mirzoyan. First time detection of a GRB at sub-TeV energies; MAGIC detects the GRB 190114C. *The Astronomer's Telegram*, 12390:1, Jan 2019.
- R. Mirzoyan et al. The first telescope of the HEGRA air Cherenkov imaging telescope array. *Nuclear Instruments and Methods in Physics Research Section A: Accelerators, Spectrometers, Detectors and Associated Equipment*, 351(2-3):513–526, 1994.
- A. Mücke et al. Monte Carlo simulations of photohadronic processes in astrophysics. *Computer Physics Communications*, 124(2-3):290–314, 2000.
- A. Mücke et al. BL Lac objects in the synchrotron proton blazar model. *Astroparticle Physics*, 18:593–613, March 2003. doi: 10.1016/S0927-6505(02)00185-8.
- C. Müller et al. Dual-frequency VLBI study of Centaurus A on sub-parsec scales-The highest-resolution view of an extragalactic jet. *Astronomy & Astrophysics*, 530:L11, 2011.
- K. Murase, Y. Inoue, and C. D. Dermer. Diffuse neutrino intensity from the inner jets of active galactic nuclei: Impacts of external photon fields and the blazar sequence. *Physical Review D*, 90(2):023007, 2014.
- K. Murase, D. Guetta, and M. Ahlers. Hidden cosmic-ray accelerators as an origin of TeV-PeV cosmic neutrinos. *Physical Review Letters*, 116(7):071101, 2016.

BIBLIOGRAPHY

- H. Nagai et al. Limb-brightened jet of 3C 84 revealed by the 43 GHz very-long-baseline-array observation. *The Astrophysical Journal*, 785(1):53, 2014.
- R. Narayan and I. Yi. Advection-dominated accretion: Underfed black holes and neutron stars. *arXiv preprint astro-ph/9411059*, 1994.
- M. Nenkova et al. AGN dusty tori. I. Handling of clumpy media. *The Astrophysical Journal*, 685(1):147, 2008.
- T. Nishiyama. Detection of a new TeV gamma-ray source of BL Lac object 1ES 1959+650. *International Cosmic Ray Conference*, 3:370, August 1999.
- T. Nonaka et al. The present status of the Telescope Array experiment. *Nuclear Physics B-Proceedings Supplements*, 190:26–31, 2009.
- D. E. Osterbrock and R. W. Pogge. The spectra of narrow-line Seyfert 1 galaxies. *The Astrophysical Journal*, 297:166–176, 1985.
- P. Padovani, F. Oikonomou, M. Petropoulou, P. Giommi, and E. Resconi. TXS 0506+ 056, the first cosmic neutrino source, is not a BL Lac. *Monthly Notices of the Royal Astronomical Society: Letters*, 484(1):L104–L108, 2019.
- P. Padovani et al. Extreme blazars as counterparts of IceCube astrophysical neutrinos. *Monthly Notices of the Royal Astronomical Society*, 457(4):3582–3592, 2016.
- S. Paiano et al. The redshift of the BL Lac object TXS 0506+ 056. *The Astrophysical Journal Letters*, 854(2):L32, 2018.
- R. Paoletti et al. The global trigger system of the magic telescope array. In *2008 IEEE Nuclear Science Symposium Conference Record*, pages 2781–2783. IEEE, 2008.
- E. S. Perlman et al. The EINSTEIN slew survey sample of BL Lacertae objects. *The Astrophysical Journal Supplement Series*, 104:251, 1996.
- E. S. Perlman et al. Surveys and the Blazar parameter space. *arXiv preprint astro-ph/0012185*, 2000.
- E. Pian et al. Spectroscopic identification of r-process nucleosynthesis in a double neutron-star merger. *Nature*, 551(7678):67, 2017.
- E. A. Pier and J. H. Krolik. Infrared spectra of obscuring dust tori around active galactic nuclei. I-Calculational method and basic trends. *The Astrophysical Journal*, 401:99–109, 1992.
- Pierre Auger Collaboration et al. Correlation of the Highest-Energy Cosmic Rays with Nearby Extragalactic Objects. *Science*, 318:938, Nov 2007. doi: 10.1126/science.1151124.
- Pierre Auger Collaboration et al. Correlation of the highest-energy cosmic rays with the positions of nearby active galactic nuclei. *Astroparticle Physics*, 29:188–204, Apr 2008. doi: 10.1016/j.astropartphys.2008.01.002.
- Pierre Auger Collaboration et al. The Pierre Auger Observatory II: Studies of Cosmic Ray Composition and Hadronic Interaction models. *arXiv e-prints*, art. arXiv:1107.4804, Jul 2011.
- T. S. Poole et al. Photometric calibration of the Swift ultraviolet/optical telescope. *Monthly Notices of the Royal Astronomical Society*, 383(2):627–645, 2007.
- A. S. Pozanenko et al. GRB 170817A associated with GW170817: multi-frequency observations and modeling of prompt gamma-ray emission. *The Astrophysical Journal Letters*, 852(2):L30, 2018.
- G. Pühlhofer et al. The technical performance of the HEGRA system of imaging air Cherenkov telescopes. *Astroparticle Physics*, 20(3):267–291, 2003.
- A. Reimer, M. Böttcher, and S. Postnikov. Neutrino emission in the hadronic Synchrotron Mirror Model: the “orphan” TeV flare from 1ES 1959+ 650. *The Astrophysical Journal*, 630(1):186, 2005.

- R. C. Reis et al. Reflection from the strong gravity regime in a lensed quasar at redshift $z=0.658$. *Nature*, 507 (7491):207, 2014.
- C. Righi, F. Tavecchio, and D. Guetta. High-energy emitting BL Lacs and high-energy neutrinos-Prospects for the direct association with IceCube and KM3NeT. *Astronomy & Astrophysics*, 598:A36, 2017.
- I. Robson. An Overview of AGN. In *Symposium-International Astronomical Union*, volume 194, pages 3–11. Cambridge University Press, 1999.
- W. A. Rolke, A. M. López, and J. Conrad. Limits and Confidence Intervals in the Presence of Nuisance Parameters. In Louis Lyons and Müge Karagöz Ünel, editors, *Statistical Problems in Particle Physics, Astrophysics and Cosmology*, page 97, Jan 2006. doi: 10.1142/9781860948985_0021.
- P. W. A. Roming et al. The Swift ultra-violet/optical telescope. *Space Science Reviews*, 120(3-4):95–142, 2005.
- M. Santander. The dawn of multi-messenger astronomy. In *neutrino astronomy: current status, future prospects*, pages 125–140. World Scientific, 2017.
- K. Satalecka. *Multimessenger studies of point-sources using the IceCube neutrino telescope and the MAGIC gamma-ray telescope*. PhD thesis, Humboldt-Universität zu Berlin, Mathematisch-Naturwissenschaftliche Fakultät I, 2010.
- K. Satalecka et al. Cluster Search for neutrino flares from pre-defined directions. In *Proc. 30th International Cosmic Ray Conference, Merida, 2007*.
- R. Scarpa et al. The Hubble space Telescope Survey of BL lacertae objects: Gravitational lens candidates and other unusual sources. *The Astrophysical Journal*, 521(1):134–144, aug 1999. doi: 10.1086/307552.
- J. F. Schachter et al. Ten new BL Lacertae objects discovered by an efficient X-ray/radio/optical technique. *The Astrophysical Journal*, 412:541–549, 1993.
- P. Schneider. *Einführung in die extragalaktische Astronomie und Kosmologie*. Springer-Verlag, 2006.
- C. K. Seyfert. Nuclear Emission in Spiral Nebulae. *The Astrophysical Journal*, 97:28, 1943.
- N. I. Shakura and R. A. Sunyaev. Black holes in binary systems. Observational appearance. *Astronomy and Astrophysics*, 24:337–355, 1973.
- M. S. Shaw et al. Spectroscopy of the largest ever γ -ray-selected BL Lac sample. *The Astrophysical Journal*, 764 (2):135, 2013.
- F. W. Stecker, M. A. Malkan, and S. T. Scully. A Determination of the Intergalactic Redshift-dependent Ultraviolet-Optical-NIR Photon Density Using Deep Galaxy Survey Data and the Gamma-Ray Opacity of the Universe. *The Astrophysical Journal*, 761(2):128, 2012.
- M. Su, T. R. Slatyer, and D. P. Finkbeiner. Giant gamma-ray bubbles from Fermi-LAT: active galactic nucleus activity or bipolar galactic wind? *The Astrophysical Journal*, 724(2):1044, 2010.
- Ignacio Taboada. A view of the universe with the IceCube and ANTARES neutrino telescopes. In *XXVIII International Conference on Neutrino Physics and Astrophysics*, 2018.
- G. Tagliaferri et al. Wide band X-ray and optical observations of the BL Lac object 1ES 1959+ 650 in high state. *Astronomy & Astrophysics*, 412(3):711–720, 2003.
- G. Tagliaferri et al. Simultaneous multiwavelength observations of the blazar 1ES 1959+ 650 at a low TeV flux. *The Astrophysical Journal*, 679(2):1029, 2008.
- Y. T. Tanaka, S. Buson, and D. Kocevski. Fermi-LAT detection of increased gamma-ray activity of TXS 0506+056, located inside the IceCube-170922A error region. *The Astronomer's Telegram*, 10791:1, Sep 2017.

BIBLIOGRAPHY

- F. Tavecchio and G. Ghisellini. Spine–sheath layer radiative interplay in subparsec-scale jets and the TeV emission from M87. *Monthly Notices of the Royal Astronomical Society: Letters*, 385(1):L98–L102, 2008.
- F. Tavecchio and G. Ghisellini. On the spine-layer scenario for the very high-energy emission of NGC 1275. *Monthly Notices of the Royal Astronomical Society*, 443(2):1224–1230, 2014.
- F. Tavecchio and G. Ghisellini. High-energy cosmic neutrinos from spine-sheath BL Lac jets. *Monthly Notices of the Royal Astronomical Society*, 451(2):1502–1510, 2015.
- F. Tavecchio, L. Maraschi, and G. Ghisellini. Constraints on the physical parameters of TeV blazars. *The Astrophysical Journal*, 509(2):608, 1998.
- F. Tavecchio, G. Ghisellini, and D. Guetta. Structured jets in BL Lac objects: efficient PeV neutrino factories? *The Astrophysical Journal Letters*, 793(1):L18, 2014.
- F. Tavecchio et al. TeV BL Lac objects at the dawn of the Fermi era. *Monthly Notices of the Royal Astronomical Society*, 401(3):1570–1586, 2010a.
- F. Tavecchio et al. Constraining the location of the emitting region in Fermi blazars through rapid γ -ray variability. *Monthly Notices of the Royal Astronomical Society: Letters*, 405(1):L94–L98, 2010b.
- A. Tchekhovskoy, R. Narayan, and J. C. McKinney. Black hole spin and the radio loud/quiet dichotomy of active galactic nuclei. *The Astrophysical Journal*, 711(1):50, 2010.
- A. Terliuk. *Measurement of atmospheric neutrino oscillations and search for sterile neutrino mixing with IceCube DeepCore*. PhD thesis, Humboldt-Universität zu Berlin, Mathematisch-Naturwissenschaftliche Fakultät, 2018.
- M. Unger, Pierre Auger Collaboration, et al. Highlights from the Pierre Auger Observatory. In *35th International Cosmic Ray Conference*, volume 301, page 1102. SISSA Medialab, 2018.
- C. M. Urry and P. Padovani. Unified schemes for radio-loud active galactic nuclei. *Publications of the Astronomical Society of the Pacific*, 107(715):803, 1995.
- M. Usner et al. Improving Future High-Energy Tau Neutrino Searches in IceCube. In *35th International Cosmic Ray Conference*, volume 301, page 973. SISSA Medialab, 2018.
- S. Valenti et al. The discovery of the electromagnetic counterpart of GW170817: kilonova AT 2017gfo/DLT17ck. *The Astrophysical Journal Letters*, 848(2):L24, 2017.
- S. Vaughan et al. On characterizing the variability properties of X-ray light curves from active galaxies. *Monthly Notices of the Royal Astronomical Society*, 345(4):1271–1284, 2003.
- S. Veilleux and D. E. Osterbrock. Spectral classification of emission-line galaxies. *The Astrophysical Journal Supplement Series*, 63:295–310, 1987.
- R. C. Vermeulen et al. When Is BL Lac Not a BL Lac? *The Astrophysical Journal Letters*, 452(1):L5, 1995.
- V. Verzi, D. Ivanov, and Y. Tsunesada. Measurement of energy spectrum of ultra-high energy cosmic rays. *Progress of Theoretical and Experimental Physics*, 2017(12):12A103, 2017.
- H. H. Voigt et al. *Landolt-Börnstein: Numerical Data and Functional Relationships in Science and Technology - New Series Gruppe/Group 6 Astronomy and Astrophysics Volume 3 Voigt: Extension and Supplement to Volume 2 Interstellar Matter, Galaxy, Universe*. 1999.
- I. Vovk and A. Neronov. Variability of gamma-ray emission from blazars on black hole timescales. *The Astrophysical Journal*, 767(2):103, 2013.
- N. Wandkowsky. Latest results on astrophysical neutrinos using high-energy events with contained vertices, June 2018.
- T. C. Weekes. *Very high energy gamma-ray astronomy*. CRC Press, 2003.

- B. Wiebel-Sooth, P. L. Biermann, and H. Meyer. Cosmic rays. VII. Individual element spectra: prediction and data. , 330:389–398, Feb 1998.
- L. Wille et al. Search for Astrophysical Tau Neutrinos with the IceCube Waveforms. In *35th International Cosmic Ray Conference*, volume 301, page 1009. SISSA Medialab, 2018.
- T. Yamamoto. The UHECR spectrum measured at the Pierre Auger Observatory and its astrophysical implications. *International Cosmic Ray Conference*, 4:335–338, Jan 2008.
- S. Yoshida et al. The cosmic ray energy spectrum above $3 \cdot 10^{18}$ eV measured by the Akeno Giant Air Shower Array. *Astroparticle Physics*, 3:105–123, Mar 1995. doi: 10.1016/0927-6505(94)00036-3.
- V. Zabalza. naima: a Python package for inference of relativistic particle energy distributions from observed nonthermal spectra. *arXiv preprint arXiv:1509.03319*, 2015.
- R. Zanin. MARS, the MAGIC analysis and reconstruction software. In *Proceedings, 33rd International Cosmic Ray Conference (ICRC2013): Rio de Janeiro, Brazil, July 2-9, 2013*, page 0773, 2013.
- G. T. Zatsepin and V. A. Kuz'min. Upper Limit of the Spectrum of Cosmic Rays. *Soviet Journal of Experimental and Theoretical Physics Letters*, 4:78, Aug 1966.
- Y. H. Zhang et al. Rapid X-Ray Variability of the BL Lacertae Object PKS 2155–304. *The Astrophysical Journal*, 527(2):719, 1999.

List of Figures

2.1	Spectrum of cosmic rays as observed from the Earth (Hanlon, 2010)	15
2.2	Spectrum of UHECRs measured by HiRes and Pierre Auger experiments overlaid with different cosmic-ray models of Galactic to extragalactic transition and different injected chemical composition. Image taken from Kotera et al. (2010) and the references therein.	17
2.3	The mass fractions of cosmic rays obtained by fitting the distribution of atmospheric depth (height at which the number of particles in the cosmic-ray induced air shower reaches its maximum) obtained from simulations of proton (p), helium (He), nitrogen (N) and iron (Fe)-induced air showers to the data (goodness of fit is shown in the lowest panel). Image taken from Unger et al. (2018).	17
2.4	The contribution of various galactic sources to the cosmic-ray luminosity from the Milky Way. The solid black curve provides the cosmic-ray luminosity above the minimum energy, $E > E_{min}$. The blue shaded region shows the contribution from SNRs, the red hatched region (lines) shows the contribution from X-ray binaries and the green hatched region (open circles) show the contribution from pulsars. Figure taken from Becker (2008).	18
2.5	Magnetic field strength as a function of the typical size of various potential cosmic-ray sources. The lines indicate the upper bound to the energy up to which cosmic rays (protons or heavier nuclei such as iron (Fe)) can be accelerated while still remaining confined within the source (Hillas, 1984).	19
2.6	Schematic representation of the penetration depth of photons to the Earth's atmosphere as a function of wavelength, for satellite or ground-based detection methods. Figure taken from Backes (2011).	21
2.7	List of the VHE ($E > 100$ GeV) γ -ray emitting sources (Galactic and extragalactic) from the TeVCat catalog. Image taken from http://tevcat.uchicago.edu/	26
2.8	The IceCube neutrino detector located at South Pole, Antarctica. Image taken from Taboada (2018).	27
2.9	Left: Neutral current interaction of a muon neutrino and a proton. Right: Charged current interaction of a muon neutrino and a proton. Image adapted from Satalecka (2010).	28
2.10	Left panel: The arrival time and energies of the neutrinos observed from SN1987A by Kamiokande, IMB and Baskan. The figure is taken from the thesis of Andrii Terliuk (Terliuk, 2018). Right panel: Flux of the astrophysical neutrinos measured in 7.5 years of IceCube data (Wandkowsky, 2018). The blue band shows a single power law fit to the data and the pink band denotes the 8 years up-going muons best fit.	29
2.11	A schematic sketch of multi-messenger astronomy: the different messengers of Astroparticle Physics, their propagation towards the Earth and detection methods. Figure taken from Backes (2011).	31
3.1	Polarization induced by a charged particle moving inside a dielectric medium with a certain velocity v . If this velocity is lower than the speed of light in the medium (denoted by c_n in the figure), the polarization induced is symmetric (left). If on the other hand the velocity is greater than the velocity of light in the medium, the polarization is asymmetric along the direction of the particle (right) and Cherenkov light is emitted. Figure taken from Weekes (2003).	34
3.2	Schematic representation of the Cherenkov cone formation. A relativistic particle with a velocity v moves down the z -axis through a medium of refractive index n and emits Cherenkov light with a cone of angle θ . Image taken from Grieder (2010).	34

3.3	Left panel: Schematic representation of electromagnetic shower development. Right panel: Schematic representation of hadronic shower development. Image credit: Weekes (2003)	35
3.4	Left panel: A Monte Carlo simulation of an electromagnetic cascade generated by a 100 GeV γ ray. Right panel: A Monte Carlo simulation of a cascade generated by a 100 GeV proton. Top panel: The vertical profile of the showers. Bottom panel: The transverse profile of the showers. The red lines correspond to e^\pm or γ -ray tracks and the green and blue lines correspond to muons and hadrons respectively. Image taken from López Coto (2015)	36
3.5	Schematic representation of the Imaging Air Cherenkov Technique. Image adapted from www.ctaobservatory.org	38
3.6	The MAGIC telescopes. Images credit: Daniel López	39
3.7	Left panel: An image of one of the MAGIC cameras. Right panel: An image of the MAGIC I mirror panels. Images taken from https://magic.mpp.mpg.de/	39
3.8	Schematic representation of the wobble mode of observation. The camera center (black dot) is located 0.4° away from the source (green dot). As the source moves in the camera plane it follows a circular trajectory. The OFF is calculated simultaneously to the data from a region / regions 0.4° at the same distance from the camera center as the source. The chosen number of OFF regions can be one (left panel) or three (right panel) and up to five. Figure taken from López Coto (2015)	42
3.9	The Hillas ellipse fitted to the surviving pixels after image cleaning and a schematic view of the main Hillas parameters. For simplicity, the image represents an ON-mode observation where the source is expected to be at the center of the camera. Image taken from Fernández Barral (2017)	44
3.10	Schematic representation of the stereoscopic parameters. Image taken from Guberman (2018)	45
3.11	Dependence of the MAGIC data on weather conditions on the MAGIC site. Left: The measured event rates (black points) by MAGIC under good weather conditions, indicated by low "cloudiness" parameter (red) (obtained from Pyrometer) and high number of stars (obtained by the Starguider camera). Right (the color code is same): The measured events under bad weather conditions (resulting in low event rates, high clouds and low number of detected stars in the field of view). Image credit: Glawion (2014)	46
3.12	Left panel: The two possible reconstructed directions of a single telescope image estimated using the <i>disp</i> parameter. Right panel: All possible combinations of the distances between the different reconstructed source positions from images produced in both the telescopes. The closest distance is chosen and the reconstructed position is a weighted average of the two chosen positions. Figure taken from Fernández Barral (2017)	48
3.13	θ^2 distribution for a sample of Crab Nebula data amounting to effective observation time of 1.7 hours. The black points are the number of observed events and the gray shaded region show the expected background / OFF events, which are expected to be flat for different values of θ^2 . The region towards the left of the dotted horizontal line is defined as the signal region. The excess events are calculated from this signal region.	49
3.14	Dependence of the energy threshold (energy corresponding to the peak of the differential event rate) of MAGIC on the zenith angle of observations for a hypothetical source with spectral index -2.6. Solid crosses: Zenith $0 - 30^\circ$. Dotted crosses: Zenith $30 - 45^\circ$. Image credit: Aleksić et al. (2016a)	49
3.15	Sensitivity curves of MAGIC for low ($< 30^\circ$; red line) and medium ($30 - 45^\circ$; blue line) zenith angle. For comparison, the sensitivity of MAGIC before installation of the DRS4 readout (grey curve) and in single-telescope mode readouts (before 2009) are also shown. Image credit: Aleksić et al. (2016a)	50
3.16	Distribution of the pedestal events for dark (black histogram) and different moon (colored histograms) levels. During moon observation, the NSB increases and as a result the pedestal mean and RMS also increases. The PMT after-pulse tail is also enlarged for large charge values. Credit: Ahnen et al. (2017)	53
3.17	Design of the three prototype telescopes of CTA. From left to right: the SSTs, the MSTs and the LST. Image adapted from https://www.cta-observatory.org/	55

3.18	Differential flux sensitivity of CTA North (blue line) and CTA South (black line) for 50 hours of observation in comparison with the current generation of γ -ray instruments. Image taken from https://www.cta-observatory.org/	56
4.1	Schematic representation of an AGN. The central region consist of a supermassive black hole. It is surrounded by an accretion disk (in red) and a dusty torus (in pink). The black and blue dots represent the gas clouds present in the broad line and the narrow line region. The position of the eyes shows the unification scheme of AGNs based on the viewing angle by an observer on Earth. Figure adapted from Urry and Padovani (1995)	59
4.2	Schematic representation of an AGN jet showing the characteristic magnetic field strength B and bulk Lorentz factor Γ as a function of distance from the central black hole ($M_{BH} = 10^8$ solar mass). Image adapted from Barkov et al. (2012)	61
4.3	Morphology of radio galaxies. Left panel: Image of the FR I radio galaxy 3C 296. Right panel: Image of the FR II radio galaxy 3C 457. Image taken from Leahy and Perley (1991)	62
4.4	The active galactic nucleus of the AGN NGC 4261. Left: optical image of the galaxy with the relativistic jets observed in radio. Right: A zoomed plot of the central region showing the dusty torus obscuring the central engine of the active galactic nucleus. Credits: HST/NASA/ESA, adapted from Jaffe et al. (1993)	63
4.5	Left: Orbital motion of stars around $SgrA^*$. Right: Radial velocity of the six stars shown in the left panel. Image taken from Eisenhauer et al. (2005)	64
4.6	An image of the <i>Fermi bubble</i> in the Milky way. The image represents the sky in galactic coordinates. Image: https://apod.nasa.gov/apod/ap101110.html	65
4.7	Example of the optical spectrum of blazars. Left panel: spectrum of the FSRQ 1FGL J1209.7+1806. Right panel: Spectrum of the BL Lac PKS 0516-621 (1FGL J0516.7-6207). Images taken from Shaw et al. (2013)	66
4.8	An SSC model successfully explaining the data from the HBL Mrk 421. The grey dashed line shows the SSC model fitted to the observational data. The lower energy hump in the SED arises from synchrotron radiation of relativistic electrons within the jet in presence of a magnetic field. The high-energy peak is attributed to inverse Compton upscattering of the synchrotron photons by the same population of electrons. For more details, see Albert et al. (2007a)	67
4.9	A hadronic model fitting the data for the IBL BL Lacertae. The lower energy hump is attributed to synchrotron radiation of the relativistic electrons. The high-energy part is attributed to contributions from the proton synchrotron, photo-meson cascade and SSC radiation components. For more details, see Böttcher et al. 2013	68
4.10	The CGRH obtained by comparison of the intrinsic/unattentauted spectrum from the SSC modelling of a sample of blazars and the observations from IACTs. The sample of blazars used in the modelling is shown in the left panel. For comparison (left panel) the CGRH predicted from the EBL model of D11 is also shown by the red shaded region. The results from the comparison of SED models and observational data, are in agreement with the prediction from D11 within the uncertainties. Right panel: The CGRH for the sample of blazars in left panel calculated for different values of the optical depth (indicated in the legend).	69
4.11	FSRQs (open squares) and BL Lacs (open circles) selected from the simulated radio flux density limited sample (red) and the X-ray flux limited sample (green) of Giommi et al. (2012) . The filled circles represent BL Lacs with very weak emission lines or featureless spectra, that in a real survey would most likely not have a redshift estimate and hence would not have a luminosity value.	71
4.12	The new blazar sequence for different γ -ray luminosity bins (indicated by the respective labels) for different sources - FSRQs (top), BL Lacs (middle), BL Lac and FSRQs combined (bottom). With increasing bolometric luminosity, the peak position in the SEDs of the FSRQs does not change much (unlike the original sequence), but the "Compton dominance" increases and the X-ray spectrum becomes harder. In BL Lacs a clear trend exists as in the original blazar sequence i.e. with increasing bolometric luminosity, the peak frequencies of the synchrotron and inverse Compton bump becomes smaller (and the Compton dominance increases). The blazar sequence can be clearly seen by merging BL Lacs and FSRQs, with FSRQs occupying the highest luminosity bins and the BL Lacs occupying the lowest luminosity bins. Image credit: Ghisellini et al. (2017)	72

5.1	The optical spectrum of 1ES 1959+650 obtained from the <i>Einstein</i> Slew Survey during 1993. The spectra is featureless with no emission lines and only a few absorption lines. Image taken from Schachter et al. (1993)	75
5.2	Light curves obtained from the 2002 multi-wavelength campaign (May 16 - August 14 2002). (a) The Whipple (star) and HEGRA (open circles) integrated TeV flux above 600 GeV and 2 TeV respectively. The Whipple data is binned with 20 mins while the HEGRA data is in daily bins. (b) RXTE X-ray flux at 10 keV. (c) RXTE photon index between 3-25 keV. (d) Absolute V-band magnitudes from Boltwood. (e) Absolute R-band magnitudes from Boltwood (crosses) and Abastumani (circles). (f) Relative I-band magnitude (Boltwood). (g) 14.5 GHz flux density from UMRAO. (h) 4.8 GHz flux density from UMRAO. Image taken from Krawczynski et al. (2004)	77
5.3	Zoomed image of the TeV orphan flare observed by Whipple on 4th June 2002. The meaning of the symbols are same as in Fig. 5.2. Image taken from Krawczynski et al. (2004)	78
5.4	The arrival times of the neutrino events coming from the direction of 1ES 1959+650 (green lines) detected by AMANDA-II, superimposed on the multi-wavelength light curve after Modified Julian Date (MJD) 52410. Image taken from Ackermann (2006)	78
5.5	The distribution of median DC of the MAGIC I camera as a function of Modified Julian Date (MJD) for the 1ES 1959+650 2016 MAGIC data set. The horizontal lines indicate the DC categories (according to the label) in which the data set is divided.	80
5.6	Dependence of the energy threshold at the reconstruction level as a function of the sky brightness (in units of NSB_{Dark}). Blue points: nominal HV, green points: Reduced HV, red points: UV-pass filter. Dotted and solid gray lines: Analytic approximations given by Eqn. 5.1 for zenith angle below 30° and $30 - 45^\circ$ respectively. Image credit: Ahn et al. (2017)	81
5.7	Distribution of the data quality parameters to assess the data quality cut for 1ES 1959+650 2016 MAGIC data analysis. Top left: Cut on mean DC of MAGIC I camera ($< 4.5\mu A$), top right: cut on zenith angle from $35 - 45^\circ$, bottom left: cut on the atmospheric transmission at 9 km above the ground-level of MAGIC at 0.75, bottom right: cut based on the average number of stars > 40	83
5.8	Relative error in A_{eff} due to azimuth-binning vs statistical error in the γ -ray excess for 14th June and 1st July 2016 (as an example). The black circles and black open squares represent the relative error in A_{eff} due to 12 and 1 azimuth bins respectively and the red circles and red open squares represent the errors in the excess (independent of azimuth). The errors in A_{eff} are always below (or comparable to) the statistical errors up to 12 azimuth bins. Hence 12 azimuth bins have been used in our work as a compromise between keeping sufficient Monte Carlo statistics and decreasing the systematics due to azimuth-dependence of A_{eff}	85
5.9	The daily-binned VHE light curve of 1ES 1959+650 above 300 GeV from 29th April (MJD 57507) to 21st November (MJD 57713) 2016. The red-dashed and the blue-dashed lines show the integral flux and three times the integral flux of Crab Nebula above 300 GeV respectively. Fits with constant functions and their respective $\chi^2/d.o.f$ are shown with the orange (including all points) and green (excluding the three brightest flares) solid lines.	86
5.10	Zoomed light curves for 2nd June-14th June 2016 (left panel) and 1st July-28th July 2016 (right panel). The flux doubling timescales for the rising and falling parts obtained by fitting Eqns. 5.6 and 5.7 are of the order of $\sim 6-7$ days and $\sim 0.5-1$ day respectively.	87
5.11	The multi-wavelength light curve of 1ES 1959+650 for the period 28th April-24th November 2016. Topmost panel: the VHE flux above 300 GeV measured by MAGIC. Second panel: The HE γ -ray photon flux from <i>Fermi</i> -LAT in the energy range 0.3-300 GeV. Third panel: X-ray energy flux from <i>Swift</i> -XRT in the energy range 0.5-5 keV. Bottom panel: UV/Optical energy flux from the <i>Swift</i> -UVOT instrument.	89
5.12	Long-term X-ray to VHE γ -ray correlation study. Top panel: Quasi-simultaneous X-ray and VHE flux (normalized to the highest flux in the respective energy band) vs MJD. Bottom panel: Correlation plot for the fluxes measured in the two energy bands.	91
5.13	Discrete Correlation Function (DCF) plotted a function of time-lag in the range [-100, 100] days for the VHE γ -ray and X-ray light curves of 1ES 1959+650 during 2016 monitoring campaign. The VHE γ rays show a hint of long-term correlation with the X-rays with zero time lag.	92

5.14	The α index of a LogP spectrum as a function of the MAGIC flux (left panel) and the XRT flux (right panel). The normalization energy was set to $E_0 = 300$ GeV for MAGIC and 1 keV for <i>Swift</i> -XRT. α gives a measure of the local spectral index at E_0	92
5.15	The SEDs from 13th June, 14th June, 1st July 2016 (top to bottom) obtained from MAGIC observations. The black points are the EBL-deabsorbed SEDs (with the model of Dominguez et al. (2011)) and the red points are the observed SEDs. The differential spectral functions fitted to the SEDs are shown with the solid, dashed, dotted and dot-dashed lines (see figure legend).	93
5.16	Intra-night variability observed in the VHE band on 13th June 2016. Solid-red curve: fit with the function given in Eqn. 5.21; green-dashed curve: fit with the function given in Eqn. 5.6. Rise and decay times of the individual substructures in the light curve are indicated in the legend.	97
5.17	Intra-night variability observed in the VHE band on 1st July 2016. Solid-red curve: fit with the function given in Eqn. 5.21. Rise and decay times of the individual substructures in the light curve are indicated in the legend.	97
5.18	The fixed time-binned light curve above 300 GeV on 14th June 2016. The flux of 14th June was more or less a constant. blue-dashed curve: constant fit.	98
5.19	The power spectrum of the 2016 flares of 1ES 1959+650. Red squares: power spectrum of 13th June 2016; black circles: that of 14th June 2016; blue triangles: that of 1st July 2016.	98
5.20	SSC model fits to the broadband SEDs of 13th June (top panel) and 14th June (bottom panel) 2016. The data from different instruments are indicated in the legend. The historical data taken from Tagliaferri et al. (2008) is shown in grey. The dashed blue, dot-dashed brown and black solid curves represent the summed SED model in increasing order of Doppler factor δ . The multi-wavelength data from 13th June requires high values of $\delta > 45$. The SED from 14th June could be explained with comparatively moderate values, $\delta \sim 30$ -50. The model parameters are given in Table 5.3.	102
5.21	Comparison between the acceleration (t_{acc}) and cooling timescales ($t_{esc}, t_{psync}, t_{p\gamma}$) for the hadronic (top panel) and mixed lepto-hadronic (bottom panel) models for 13th June 2016. The acceleration efficiency η_{acc} was chosen to be 1. The energy corresponding to which the proton gyro-radius becomes equal to the size of the emission zone is shown with the red dot-dashed line.	104
5.22	Hadronic model fits to the broadband SEDs of 13th June (top panel) and 14th June (bottom panel) 2016. The data from different instruments are indicated in the legend. Black solid line: summed SED; blue dashed line: electron synchrotron; green dotted line: SSC; green dot-dashed line: proton synchrotron; orange dot-dot-dashed line: p- γ cascade. Synchrotron radiation by ultra-relativistic protons give a dominant contribution to the higher energy SED peak with parameters $B \sim 100$ G, $E_{p,max} > 10^{18}$ eV and overall jet power $L_j \sim 10^{46}$ erg/s ($\sim L_{Edd}$). The model parameters are given in Table 5.3.	105
5.23	Lepto-hadronic model fit to the broadband SED of 13th June 2016 (top panel) and the predicted neutrino fluxes (bottom panel). The meanings of the symbols and lines in the top panel are same as in Fig. 5.22. The high-energy SED peak in this case arises from a combination of SSC and p- γ cascade component (with parameter values $B \sim 1$ G, $E_{p,max} > 10^{16}$ eV and overall high jet power $L_j > 10^{48}$ erg/s $\gg L_{Edd}$). The meanings of the different curves in the neutrino spectra (bottom) are explained in the legend. The black steps show the IceCube sensitivity curve (Aartsen et al., 2018) corresponding to declination 60° . Neutrino spectrum obtained from the proton-synchrotron model (Fig. 5.22) peak at very high energies and gives low neutrino flux in 0.1–100 PeV energy range (brown dashed line). The lepto-hadronic model provides slightly higher neutrino flux peaking at much lower energies (violet solid line represents the summed component) at the cost of very high values of the jet power. The model parameters are given in Table 5.3.	107
6.1	The impact of variation of the radius of the emitting region assuming a spherical geometry of the emission region (equivalent to the variation in the source <i>compactness</i> ; see Eqn. 6.1) on the spectra of a simple SSC model. With increasing <i>compactness</i> or decreasing radius, the inverse Compton component (second bump) starts dominating and the cut-off energy of the SSA also increases.	111
6.2	The dependence of Doppler factor δ on the bulk Lorentz factor Γ and viewing angle θ of the jet with respect to an observer on Earth.	112

6.3	Top panel: The total cross-section (normalized over σ_T) of the SSA process for different values of the particle's dimensionless momentum p (Eqn. 6.9 for $p > 3$ and Eqn. 6.10 for $p < 3$) as a function of the synchrotron photon frequency ν/ν_L . Bottom panel: The SSA attenuation factor C_{att} for different values of the source radius R (and hence varying compactness) as a function of the the co-moving frame photon frequency. The radius and compactness values correspond to Fig. 6.1.	114
6.4	γ - γ pair production cross section $\sigma_{\gamma\gamma}(s)$ as a function of the quantity s . Blue solid curve: $\sigma_{\gamma\gamma}(s)$ following Aharonian et al. (2008) ; red dot-dashed curve: $\sigma_{\gamma\gamma}(s)$ following Dermer and Menon (2009)	116
6.5	The attenuation factor $\exp(-\tau_{\gamma\gamma})$ for a γ -ray photon field interacting with a black body target (shown for three different values of the black body temperature $T = 10^3\text{K}, 10^4\text{K}, 10^5\text{K}$). The energy corresponding to the maximum attenuation is a function of the black body temperature, given by $E^* = m_e^2 c^4 / kT$ as can be seen from the dips in the different curves corresponding to different black body temperatures.	117
6.6	Proton synchrotron emission components for different proton distribution functions for randomly selected emission parameters. Assumed parameters: $z=0.1, \delta = 25, B=10\text{ G}, R=10^{16}\text{ cm}, \alpha_p = 2$	117
6.7	The smoothness of the functional parameters $s(\eta), B(\eta), \delta(\eta)$ plotted from Tables I, II and III of Kelner and Aharonian (2008) for some of the secondary decay products of photo-meson interactions.	120
6.8	The function $H(\eta, E_\gamma)$ calculated for a fixed γ -ray energy $E_\gamma = 0.5E^*$, with three different values of the parent proton's spectral index α_p . The target is assumed to be a black body described by a Planckian distribution (as in Kelner and Aharonian (2008)).	120
6.9	The energy spectrum of decay products from photo-meson interactions: γ -rays, e^+ and e^- (top panel) and electron and muon neutrinos (and antineutrinos; bottom panel). The proton distribution is assumed to be a power law with index 2 and maximum energy 10^{16} eV (in the co-moving frame). The target field is assumed to be described by an arbitrary broken power law distribution.	121
6.10	Energy spectra of secondary decay products from p-p interaction between a proton distribution of power law with exponential cutoff form and a hydrogen gas with density $n_H = 1\text{ cm}^{-3}$. Decay products: γ rays, $e^+ + e^-$, $\nu_\mu^{(1)}$ (neutrinos from muonic decay), ν_μ (total muon neutrino spectra including the contribution from direct pion decay). The spectra has been calculated for a fixed cutoff energy of the parent proton of 700 TeV and spectral index $\alpha_p = 1.5$ (top panel) and $\alpha_p = 2$ (bottom panel).	123
6.11	The acceleration and cooling timescales for the hadronic model of PKS 2155-304 as shown in Fig. 6.13. The green-dotted line denotes the proton-synchrotron cooling timescale and the pink-dotted line shows the photo-meson cooling timescale as a function of the proton energy. As can be seen from the figure, the proton synchrotron cooling dominates over the photo-meson cooling for a wide range of proton energies.	127
6.12	The mixed lepto-hadronic model 1 of the MWL SED of PKS 2155-304. The top panel shows the results obtained with the lepto-hadronic emission model developed for this thesis. The bottom panel shows the SED model from the original work of Cerruti et al. (2012) . The colour code for the figure is: red-primary electron synchrotron; green-inverse Compton; blue-proton synchrotron; yellow-photons from π^0 decay; pink-synchrotron emission from secondary e^\pm coming from π^\pm decay (for the list of parameters see Table 6.1).	128
6.13	The hadronic model of the MWL SED of PKS 2155-304. The top panel shows the results obtained with the lepto-hadronic emission model developed for this thesis. The bottom panel shows the SED model from the original work of Cerruti et al. (2012) . The colour code for the figure is same as in Fig. 6.12. Additionally, the light blue solid line represents muon synchrotron emission, the light blue and dark blue dotted lines represent the electromagnetic cascade associated with muon synchrotron and proton synchrotron respectively (for the list of parameters see Table 6.1).	129
7.1	The event display of IC 170922A. The times at which the different DOMs of the IceCube detector observed the signal is indicated by the colorbar, with blue signifying the earliest time and yellow the latest time with respect to the first DOM hit of the signal. The inset shows a top view of the event. Figure taken from IceCube Collaboration et al. (2018b)	131

7.2	Top panel: The VHE γ -ray light curve above 90 GeV obtained by MAGIC. The data from MJD 58020-58030 has been presented in IceCube Collaboration et al. (2018b) . The green shaded regions denote the two periods of enhanced activity observed by MAGIC on 3-4th October 2017 and 31st October 2017. MAGIC could also detect the source in a low VHE emission state excluding the two flaring activities mentioned above. Bottom panel: The VHE γ -ray spectrum ($E^2 \times \frac{dF}{dE}$) of TXS 0506+056 observed by MAGIC during different emission states. Figure taken from Ansoldi et al. (2018)	132
7.3	Schematic representation of the spine-layer model. The blazar jet is assumed to be composed of a fast-moving spine surrounded by a slower layer having bulk Lorentz factor Γ_s and Γ_l respectively. The relative motion between the two regions leads to a relativistic amplification of the density of the radiation field and photon energy of the layer in the frame of the spine by a relativistic Lorentz factor Γ_{rel} (see the text below). Figure taken from Righi et al. (2017)	134
7.4	SED modelling for the multi-messenger observations of TXS 0506+056 in the framework of the spine-layer model, using $E_{p,max} = 10^{16}$ eV. The data from different instruments and the contribution of individual non-thermal components to the total SED are described in the legend. Top panel: High state (MJD 58029 to 58030). Middle panel: Low state. Bottom panel: Comparison of the high and low VHE states and the archival data from the ASI Science Data Center.	137
7.5	Comparison of the decay and cooling timescales of the intermediate muons and pions produced in the photo-meson interactions responsible for the high-energy neutrino emission. In the chosen parameter regime (the shaded pink region), the muons and pions decay much faster before cooling. Thus the cooling of the intermediate products can be neglected.	138
7.6	The cumulative distribution function of the neutrino flux (obtained from the spine-layer SED modelling, shown in Fig. 7.4) convolved with the IceCube effective area, as a function of the neutrino energy. The green and red shaded region indicate the 90% and 80% containment neutrino energy interval as predicted by the theoretical modelling (142 TeV - 11 PeV and 206 TeV - 6.3 PeV, respectively).	139
7.7	The comparison of the proton acceleration timescale (t_{acc}) and the cooling timescales - adiabatic loss (t_{adia}), synchrotron loss (t_{psync}), p- γ loss ($t_{p\gamma}$) as a function of the proton Lorentz factor in the co-moving frame. As shown, the energy corresponding to the gyro-radius is greater than the maximum allowed proton energy (defined as the energy where the acceleration timescales is equal to the minimum cooling timescale - in this case t_{adia} and $t_{p\gamma}$).	139
7.8	The effect of variation of the maximum proton energy $E_{p,max}$ on the overall SED (solid lines), the hadronic p- γ cascade component (dot-dot-dashed lines) and neutrino emission (dot-dashed lines) for the high state.	140
C.1	Cherenkov shower image parametrization. The Hillas ellipse (Chapter 3, Sec. 3.4.3) is characterized by simple image parameters. (x, y) represents the camera coordinate system, (x_0, y_0) is a reference point. The camera coordinates are rotated by an angle δ	158

List of Tables

2.1	A comparison of the characteristics of the <i>Fermi</i> satellite, IACTs and EAS arrays.	24
3.1	Typical NSB levels during MAGIC observations under different sky brightness and the adopted cleaning levels. Reference: Ahnen et al. (2017)	53
5.1	VHE fit parameters for the nights of 13th June, 14th June, 1st July 2016.	95
5.2	Results from fitting the individual substructures in the intra-night light curve of 13th June and 1st July with the functional forms given in Eqn. 7 and 8. $t_{rise} = t_r \times \log(2)$ and $t_{fall} = t_f \times \log(2)$. . .	99
5.3	Parameters for the SSC, hadronic and lepto-hadronic modelling of the 13th and 14th June flares of 1ES 1959+650.	103
6.1	Parameters for the mixed lepto-hadronic model 1 and the hadronic model from Cerruti et al. (2012) , that were used to compare the results from their code with the code developed by the author . . .	126
7.1	Model parameters for the high and low VHE state using the spine layer model (for the maximum proton energy $E_{p,max} = 10^{16}$ eV and the proton spectral index $n_p = 2$)	135
A.1	The VHE γ -ray light curve above 300 GeV observed by MAGIC from the blazar 1ES 1959+650 during 2016	144
A.2	The <i>Swift</i> -XRT light curve in the energy range 0.5–5 keV observed for the blazar 1ES 1959+650 during 2016	146
A.3	The <i>Fermi</i> -LAT light curve in the energy range 0.3–300 GeV from the blazar 1ES 1959+650 during 2016	150
A.4	The EBL-deabsorbed SED of MAGIC for 13th June 2016	152
A.5	The EBL-deabsorbed SED of MAGIC for 14th June 2016	152
A.6	The EBL-deabsorbed SED of MAGIC for 1st July 2016	152
A.7	The SED from <i>Swift</i> -UVOT and <i>Swift</i> -XRT for 13th June 2016	152
A.8	The SED from <i>Swift</i> -UVOT and <i>Swift</i> -XRT for 14th June 2016	153
A.9	The SED from <i>Fermi</i> -LAT for 13th June and 14th June 2016	154

Declaration

I declare that I have completed the thesis independently using only the aids and tools specified. I have not applied for a doctor's degree in the doctoral subject elsewhere and do not hold a corresponding doctor's degree. I have taken due note of the Faculty of Mathematics and Natural Sciences PhD Regulations, published in the Official Gazette of Humboldt-Universität zu Berlin no. 42/2018 on 11/07/2018.

Date:

Signature

Place:

